ACS OMEGA

http://pubs.acs.org/journal/acsodf

Article

Highlighting the Anti-Synergy between Adsorption and Diffusion in Cation-Exchanged Faujasite Zeolites

Rajamani Krishna* and Jasper M. van Baten

Cite This: *ACS Omega* 2022, 7, 13050−13056

Read Online

ACCESS | Metrics & More | Article Recommendations | Supporting Information

ABSTRACT: Using configurational-bias Monte Carlo simulations of adsorption equilibrium and molecular dynamics simulations of guest diffusivities of CO_2, CH_4, N_2, and O_2 in FAU zeolites with varying amounts of extra-framework cations (Na^+ or Li^+), we demonstrate that adsorption and diffusion do not, in general, proceed hand-in-hand. Stronger adsorption often implies reduced mobility. The anti-synergy between adsorption and diffusion has consequences for the design and development of pressure-swing adsorption and membrane separation technologies for CO_2 capture and N_2/O_2 separations.

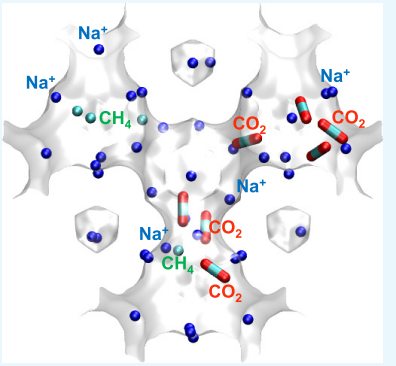

1. INTRODUCTION

Despite the burgeoning research and development activities on novel metal−organic frameworks (MOFs) in separation applications, cation-exchanged zeolites remain viable contenders for use as adsorbents in the industrial practice. For post-combustion CO_2 capture, Na^+ cation-exchanged FAU (faujasite) zeolite, NaX, also commonly known by its trade name 13X (with Si/Al ≈ 1.2), is considered to be the benchmark adsorbent, with the ability to meet government targets for CO_2 purity and recovery.[1] NaX zeolites are also of potential use in natural gas purification,[2,3] alkane/alkene separations,[4−8] and hydrogen purification processes.[3,9−23] Coulombic interactions of CO_2 and unsaturated alkenes with the extra-framework cations (e.g., Na^+, Ca^{++}, Li^+, and Ba^{++}) result in strong binding; the binding strength and selectivity can be tuned by the appropriate choice of the extra-framework cations and the adjustment of the Si/Al ratios.[9,11,20,24−26]

Li^+ cation-exchanged FAU (faujasite) zeolite is commercially used for separation of N_2/O_2 mixtures.[23,27,28] For supplying medical grade oxygen to prevent hypoxemia-related complications related to COVID-19, portable medical oxygen concentrators commonly use LiLSX (LS = low silica; Si/Al ≈ 1) to achieve high N_2/O_2 adsorption selectivities, ensuring enhanced rejection of purified O_2, the desired product.[29,30]

For separation applications using pressure-swing adsorption (PSA) technology, consisting of adsorption/desorption cycles, there is often a mismatch between the requirements of strong adsorption and ease of desorption.[31] For example, NaX has a very strong affinity for CO_2, but the regeneration requires application of deep vacuum. For CO_2 capture from flue gases, Prats et al.[25,26] have used molecular simulations of mixture adsorption in FAU to determine the optimum Si/Al ratio for PSA operations.

In the design and development of PSA technologies employing cation-exchanged zeolite adsorbents, we also require data on the intracrystalline diffusivities of guest molecules. Most commonly, diffusion limitations cause distended breakthrough characteristics and reduction in the purities of the desired products.[31−36] Diffusivity data are also of vital importance in the development of zeolite membrane constructs for mixture separations in which cation-exchanged zeolites are used as thin layers or as fillers in mixed-matrix configurations.[37−43]

The primary objective of this communication is to gain some fundamental thermodynamic insights into the adsorption and diffusion characteristics of a variety of guest molecules such as CO_2, CH_4, N_2, and O_2 in FAU zeolites with varying amounts of extra-framework cations: Na^+ and Li^+. The desired insights are obtained by performing configurational-bias Monte Carlo (CBMC) simulations of adsorption and molecular dynamics (MD) simulations of diffusion in Na- and Li-exchanged FAU zeolites with varying Si/Al ratios. The CBMC and MD simulation methodologies, along with details of the force field implementations, are detailed in the Supporting Information accompanying this publication. We aim to demonstrate the

Received: January 21, 2022
Accepted: March 14, 2022
Published: April 8, 2022

anti-synergy between adsorption and diffusion; the stronger the binding of a guest molecule, the lower is its mobility. Such insights are of vital importance in determining the optimum Si/Al ratio of zeolite for use in PSA technologies or in membrane constructs.

2. THE GIBBSIAN CONCEPT OF SPREADING PRESSURE

The spreading pressure, π, is related to the molar chemical potential, μ_i, by the Gibbs adsorption equation[44]

$$A\mathrm{d}\pi = \sum_{i=1}^{n} q_i \mathrm{d}\mu_i \tag{1}$$

where A represents the surface area per kg of framework, and q_i is the component molar loading in the adsorbed phase mixture. At thermodynamic equilibrium, the μ_i are related to the partial fugacities in the bulk fluid mixture

$$\mathrm{d}\mu_i = RT\mathrm{d}\ln f_i \tag{2}$$

In developing the ideal adsorbed solution theory (IAST), Myers and Prausnitz[45] write the following expression relating the partial fugacities in the bulk gas mixture

$$f_i = P_i^0 x_i; \quad i = 1, 2, ..., n \tag{3}$$

to the mole fractions, x_i, in the adsorbed phase mixture

$$x_i = \frac{q_i}{q_1 + q_2 + ... + q_n}; \quad i = 1, 2, ..., n \tag{4}$$

In eq 3, P_i^0 is the pressure for sorption of every component i, which yields the same spreading pressure, π, for each of the pure components as that for the n-component mixture:

$$\frac{\pi A}{RT} = \int_0^{P_1^0} \frac{q_1^0(f)}{f}\mathrm{d}f = \int_0^{P_2^0} \frac{q_2^0(f)}{f}\mathrm{d}f = \int_0^{P_3^0} \frac{q_3^0(f)}{f}\mathrm{d}f \tag{5}$$

In eq 5, $q_i^0(f)$ is the pure component adsorption isotherm. Since the surface area A is not directly accessible from experimental data, the surface potential $\pi A/RT \equiv \Phi$, with the units mol kg^{-1}, serves as a convenient and practical proxy for the spreading pressure π.[46−49] As derived in detail in the Supporting Information, the fractional pore occupancy, θ, is related to the surface potential by

$$\theta = 1 - \exp\left(-\frac{\Phi}{q_{\mathrm{sat,mix}}}\right) \tag{6}$$

where $q_{\mathrm{sat,\,mix}}$ is the saturation capacity for mixture adsorption. Equation 6 implies that Φ may also be interpreted as a proxy for the pore occupancy; it is the fundamentally correct yardstick to compare the adsorption and diffusion characteristics of different host materials.[41,48−50]

In view of eq 3, we may express the adsorption selectivity for the i−j pair as follows

$$S_{\mathrm{ads}} = \frac{q_i/q_j}{f_i/f_j} = \frac{x_i/f_i}{x_j/f_j} = \frac{P_j^0}{P_i^0} \tag{7}$$

Applying the restriction specified by eq 5, it follows that S_{ads} is uniquely determined by the surface potential Φ, irrespective of the mixture composition and total fugacity, f_t.

3. RESULTS AND DISCUSSION

3.1. CO_2 Capture Using Na-Exchanged FAU. Figure 1a plots the CBMC data on isosteric heats of adsorption, Q_{st}, a measure of the binding energies, of CO_2 and CH_4 in FAU (0 Al, all-silica), NaY (54 Al uc^{-1}), and NaX (86 Al uc^{-1}) zeolites, plotted as a function of the surface potential Φ. For CO_2, the hierarchy of Q_{st} is NaX > NaY > FAU; this hierarchy reflects the strong electrostatic interactions with the extra-framework cations, engendered by the large quadrupole moment of CO_2. For CH_4, the differences in the Q_{st} in the three different hosts are considerably smaller because the adsorption of CH_4 is due to van der Waals interactions that also increase with increasing number of cations.

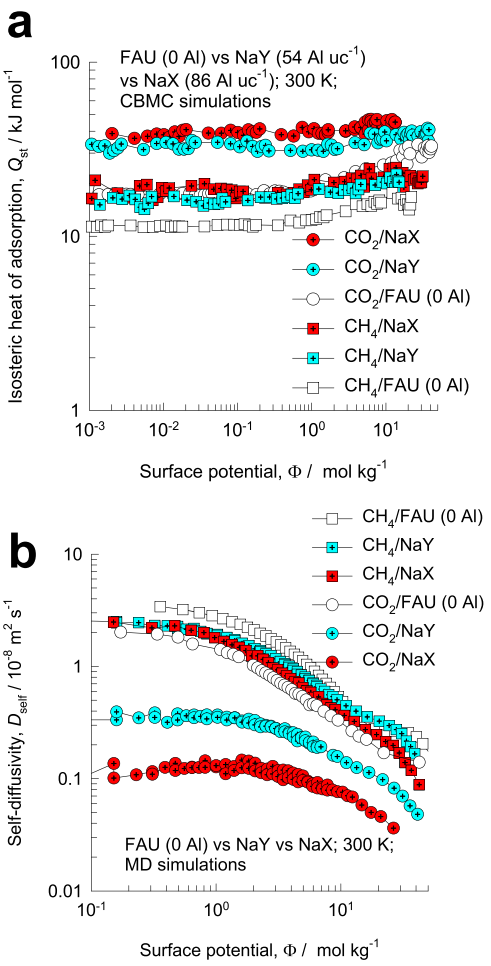

Figure 1. (a) CBMC simulations of the isosteric heats of adsorption, Q_{st}, of CO_2 and CH_4 in FAU (0 Al, all-silica), NaY (54 Al uc^{-1}), and NaX (86 Al uc^{-1}) zeolites, determined at 300 K, plotted as a function of the surface potential Φ. (b) MD simulations of the self-diffusivities, $D_{i,\,self}$, of CO_2 and CH_4 in FAU, NaY, and NaX zeolites, determined at 300 K, plotted as a function of the surface potential Φ. All simulation details and input data are provided in the Supporting Information accompanying this publication.

Strong binding of guest molecules also implies a higher degree of "stickiness" and, consequently, lower mobility.[51,52] To demonstrate this, Figure 1b presents the MD simulations of

https://doi.org/10.1021/acsomega.2c00427
ACS Omega 2022, 7, 13050−13056

the unary self-diffusivities, $D_{i,\,self}$, of CO_2 and CH_4 in FAU (0 Al), NaY, and NaX zeolites. Compared at the same surface potential Φ, the hierarchy of self-diffusivities is precisely reverse of the hierarchy of Q_{st}. Noteworthily, CH_4, the guest with the larger kinetic diameter of 3.8 Å, has a higher mobility than CO_2, which has a smaller kinetic diameter of 3.3 Å. The fallacy of using kinetic diameters to anticipate hierarchies in the diffusivity values has been underscored in published works.[15,51]

CBMC simulations were carried out for equimolar ($f_1 = f_2$) $CO_2(1)/CH_4(2)$ mixtures in FAU (0 Al), NaY, and NaX zeolites. The values of the adsorption selectivities, S_{ads}, are plotted in Figure 2a as a function of Φ. The hierarchy of S_{ads} values is NaX > NaY > FAU (0 Al), reflecting the stronger binding of CO_2. The corresponding hierarchy of diffusion selectivities, $S_{diff} = D_{1,\,self}/D_{2,\,self}$, is precisely the reverse of S_{ads}; evidently, mixture adsorption and diffusion do not proceed hand-in-hand. This anti-synergy has important consequences of use of cation-exchanged zeolites in membrane constructs. If the partial fugacities of the components at the downstream face are negligibly small in comparison with those at the upstream face, the component permeabilities may be estimated from the following expression[41]

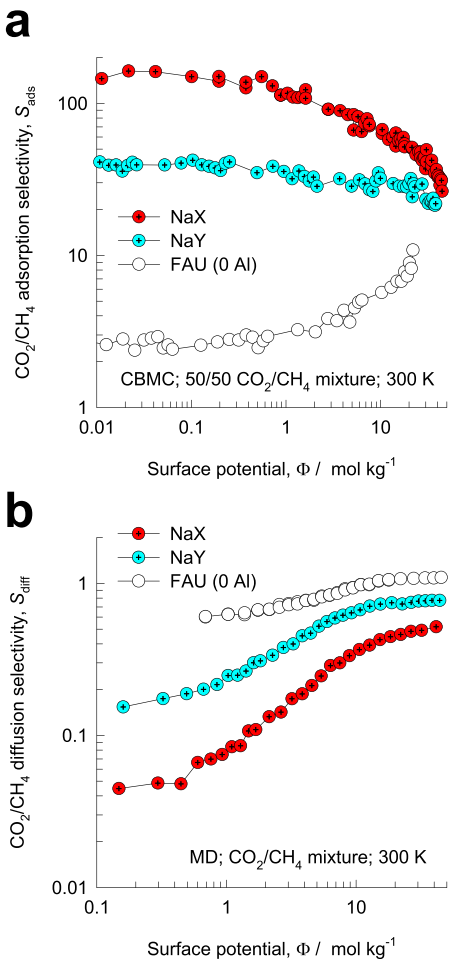

Figure 2. Comparison of CBMC/MD simulations of (a) adsorption selectivities, S_{ads}, and (b) diffusion selectivities, S_{diff}, of CO_2/CH_4 mixtures in FAU (0 Al), NaY, and NaX zeolites at 300 K. The selectivities are plotted as a function of the surface potential Φ. All simulation details and input data are provided in the Supporting Information accompanying this publication.

$$\Pi_i = \frac{\rho D_{i,\mathrm{self}} q_i}{f_i} \tag{8}$$

For FAU (0 Al), NaY, and NaX zeolites, Figure 3a,b compares the values of the CO_2 permeabilities, Π_1, and the permeation selectivity

$$S_{perm} = \Pi_1/\Pi_2 = S_{ads} \times S_{perm} \tag{9}$$

The CO_2 permeabilities, Π_1, decrease with increasing values of Φ. The S_{perm} is a product of the adsorption selectivity and diffusion selectivity (cf. Figure 2a,b). While the S_{diff} increases with Φ for all three hosts, the S_{ads} increases with Φ until a maximum is reached for NaX and NaY and decreases on a further increase in Φ. Consequently, the S_{perm} also shows a maximum value for NaX and NaY. For the specific choice of upstream operating conditions, $f_t = f_1 + f_2 = 10^6$ Pa, Figure 3c shows the Robeson[53] plot of S_{perm} vs Π_1 for the three host structures. We note that the performances of both NaY and NaX lie above the line representing the Robeson upper bound.[53] Since both S_{perm} and Π_1 are important metrics governing the choice of the appropriate membrane material, there is room for optimization of the Si/Al ratio depending on the relative weightage to be assigned to permeation selectivity and permeability. CBMC/MD data that are analogous to those presented in Figures 2 and 3 are obtained for CO_2/N_2, CO_2/H_2, CH_4/H_2, CH_4/C_2H_6, and CH_4/C_3H_8 mixtures in FAU (0 Al), NaY, and NaX (see Figures S60−S64 of the Supporting Information).

3.2. N_2/O_2 Separations Using Li-FAU and Na-FAU.

Figure 4a presents MD simulations of the unary self-diffusivities, $D_{i,\,self}$, for N_2, at 300 K in Li-exchanged FAU zeolites, with different Al contents per unit cell: 0, 48, 54, 86, and 96, plotted as functions of the surface potential Φ; the contents of Li^+ are equal to that of Al. The magnitudes of $D_{i,\,self}$ decrease with increasing values of Φ, which also serves as a proxy for the pore occupancy. At any specified value of Φ, the values of the self-diffusivity, $D_{i,\,self}$, show the following trend: FAU (0 Al) ≫ FAU (48 Al) ≈ FAU (54 Al) > FAU (86 Al) ≈ FAU (96 Al). This hierarchy of $D_{i,\,self}$ values correlates, inversely, with the corresponding values of the isosteric heats of adsorption of N_2 (cf. Figure 4b). N_2 has a significant quadrupole moment, and the electrostatic interaction potentials increase with increasing Al content, leading to increasing binding energies. The data in Figure 4a,b confirm that the diffusional mobility of N_2 is reduced with increased binding energy.

On the other hand, we note from Figure 4b that the isosteric heats of adsorption of O_2 are practically uninfluenced by the addition of extra-framework cations due to the significantly lower quadrupole moment of O_2. Therefore, we should anticipate that the mobility of O_2 should be practically independent of the degree of Li exchange; this expectation is fulfilled by the MD simulations of the self-diffusivities of O_2 in Li-FAU (see Figure 4c).

For 80/20 N_2/O_2 mixture adsorption, Figure 5a plots the adsorption selectivities, S_{ads}, of Li-exchanged FAU zeolites, with different Al contents. We note that the S_{ads} increases with increasing Al content. MD simulations of the N_2/O_2 diffusion selectivities, S_{diff}, plotted in Figure 5b, demonstrate the anti-synergy between adsorption and diffusion; the higher the

https://doi.org/10.1021/acsomega.2c00427
ACS Omega 2022, 7, 13050−13056

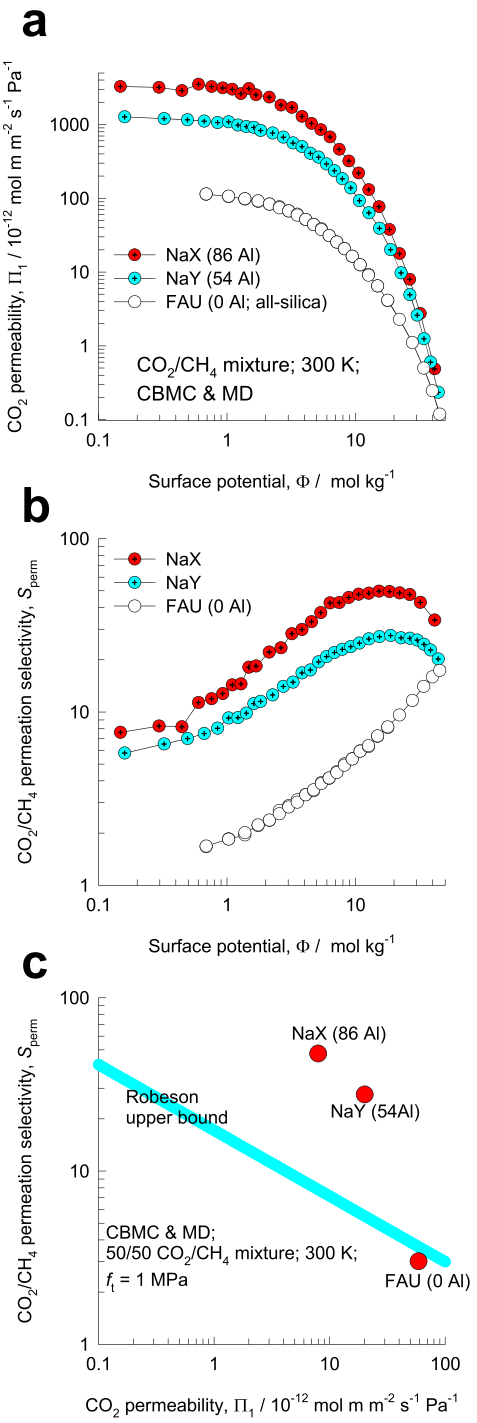

Figure 3. Comparison of (a) CO_2 permeability, Π_1, and (b) permeation selectivity, S_{perm}, for $CO_2(1)/CH_4(2)$ mixtures in FAU (0 Al), NaY, and NaX zeolites at 300 K; the x-axis represents the surface potential Φ. (c) Robeson plot of S_{perm} vs Π_1 data at $f_t = f_1 + f_2 = 10^6$ Pa and 300 K. All simulation details and input data are provided in the Supporting Information accompanying this publication.

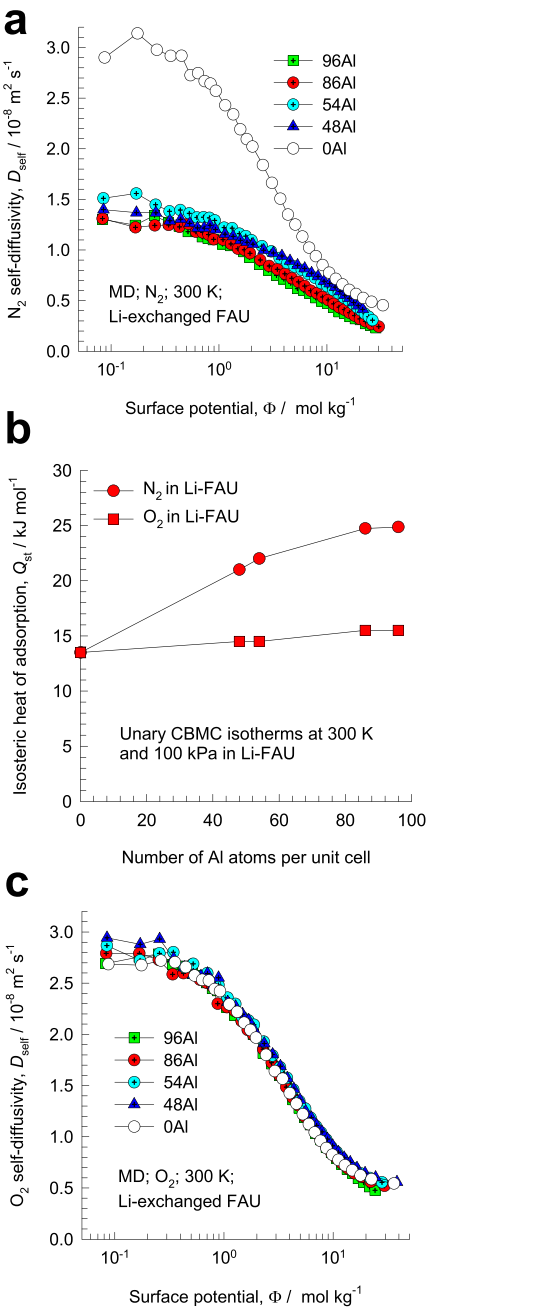

Figure 4. (a) MD simulations of the unary self-diffusivities for N_2 at 300 K in Li-exchanged FAU zeolites, with different Al contents per unit cell: 0, 48, 54, 86, and 96, plotted as a function of the surface potential Φ. (b) Isosteric heats of adsorption, Q_{st}, plotted as a function of the number of Al atoms per unit cell. (c) MD simulations of the unary self-diffusivities for O_2 at 300 K in Li-exchanged FAU zeolites, with different Al contents per unit cell: 0, 48, 54, 86, and 96, plotted as a function of the surface potential Φ. All simulation details and input data are provided in the Supporting Information accompanying this publication.

adsorption selectivity, the lower is the corresponding diffusion selectivity. Analogous CBMC and MD simulations with Na-exchanged FAU zeolites were also carried out; the results are provided in Figures S73−S81 of the Supporting Information.

For 80/20 N_2/O_2 mixture separations at a total fugacity of 100 kPa, Figure 6a compares the adsorption selectivities of Li-FAU and Na-FAU. For the same Al content, we note that the S_{ads} values with Li-FAU are significantly higher than for Na-FAU. The interaction potential, engendered by the quadrupole moment, is inversely proportional to the cube of the center-to-center distance between nitrogen molecules and the extra-framework cation (see the detailed explanation provided in Chapter 2 of the Supporting Information). Due to the smaller ionic radius of Li^+, compared to Na^+, the N_2-Li^+ distances are smaller than the N_2-Na^+ distances; this is confirmed by radial

https://doi.org/10.1021/acsomega.2c00427
ACS Omega 2022, 7, 13050−13056

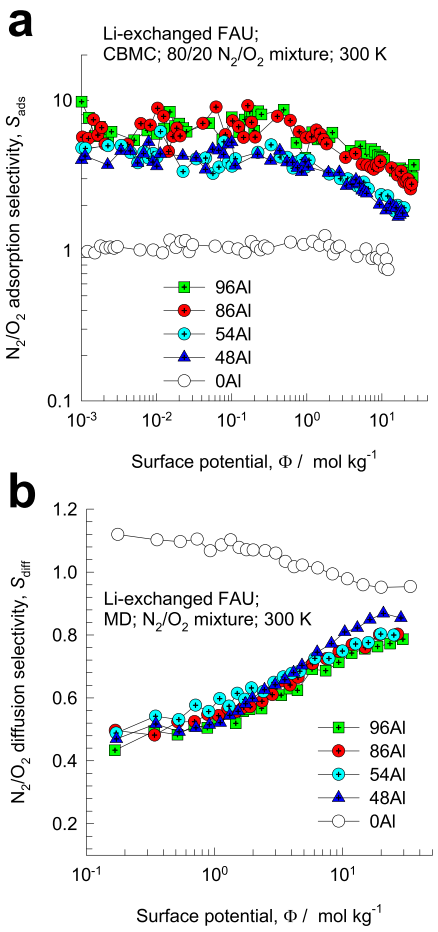

Figure 5. (a) CBMC simulations of the adsorption selectivity, S_{ads}, for binary 80/20 N_2/O_2 mixture adsorption in Li-FAU, with different Al contents per unit cell: 0, 48, 54, 86, and 96. (b) MD simulations of the N_2/O_2 diffusion selectivity, S_{diff}, at 300 K in Li-FAU zeolites. All simulation details and input data are provided in the Supporting Information accompanying this publication.

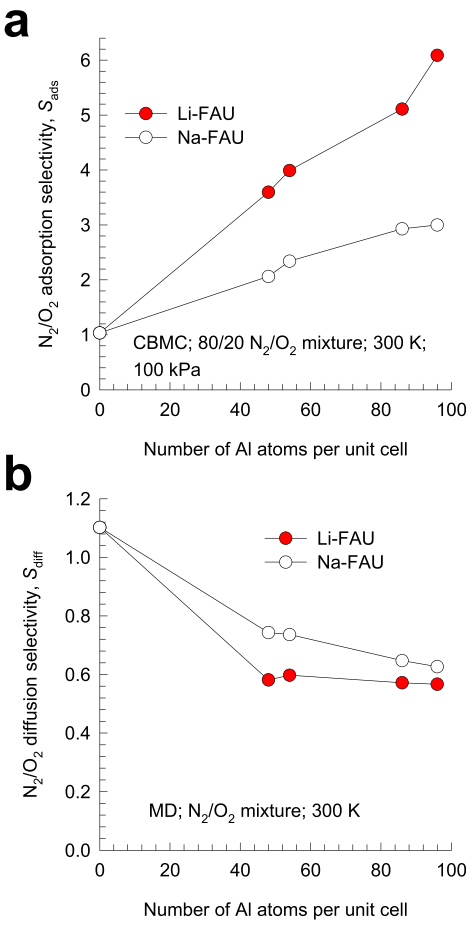

Figure 6. Comparison of the (a) adsorption selectivity and (b) diffusion selectivity for 80/20 N_2/O_2 separations using either Li-exchanged or Na-exchanged FAU zeolites, with different Al contents per unit cell: 0, 48, 54, 86, and 96. All simulation details and input data are provided in the Supporting Information accompanying this publication.

distribution functions for N_2−Li^+ and N_2−Na^+ pairs for 80/20 N_2/O_2 mixture adsorption in Li-FAU(96Al) and Na-FAU-(96Al) (see Figure 7).

The N_2/O_2 diffusion selectivities for Na-FAU are only slightly higher than those of Li-FAU (see Figure 6b). The CBMC/MD data rationalize the use of LiX, with Al ≈ 96 uc^{-1}, in the industrial practice.[29,30]

Figure 8 shows a Robeson plot of S_{perm} vs N_2 permeabilities of N_2 for binary 80/20 N_2/O_2 mixture permeation across the Li-FAU zeolite membrane at an upstream total pressure of 100 kPa. We note that the separation performance increases monotonously with increasing degrees of Li^+ exchange; the permeabilities are significantly higher than the values reported in the literature[54] for polymeric and mixed-matrix membranes.

4. CONCLUSIONS

A combination of CBMC and MD simulations for adsorption and diffusion of guest molecules CO_2, CH_4, N_2, and O_2 in FAU zeolites with varying amounts of extra-framework cations (Na^+ or Li^+) was carried out to investigate the influence of varying Si/Al ratios on mixture separations. Stronger adsorption, with increasing amounts of extra-framework cations, results in lowered diffusivities. For CO_2/CH_4 and N_2/O_2 mixture separations, the adsorption selectivity, S_{ads}, and diffusion selectivity, S_{diff}, do not proceed hand-in-hand. The anti-synergy between adsorption and diffusion has important consequences for the choice of the extra-framework cation, Na^+ or Li^+, and the Si/Al ratio for use in PSA and membrane separation technologies.

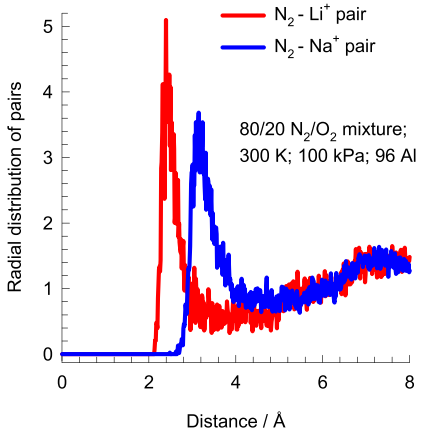

Figure 7. Radial distribution functions for N_2−Li^+ and N_2−Na^+ pairs for 80/20 N_2/O_2 mixture adsorption in Li-FAU (96Al) and Na-FAU (96Al) at 100 kPa and 300 K.

https://doi.org/10.1021/acsomega.2c00427
ACS Omega 2022, 7, 13050−13056

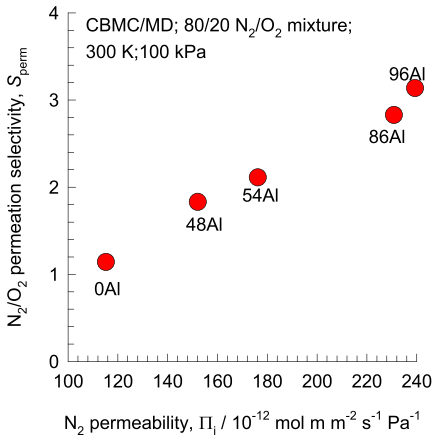

Figure 8. Robeson plot of S_{perm} vs N_2 permeabilities for binary 80/20 N_2/O_2 mixture permeation across the Li-exchanged FAU zeolite membrane, with different Al contents per unit cell: 0, 48, 54, 86, and 96. All simulation details and input data are provided in the Supporting Information accompanying this publication.

■ ASSOCIATED CONTENT

Supporting Information

The Supporting Information is available free of charge at https://pubs.acs.org/doi/10.1021/acsomega.2c00427.

CBMC and MD simulation methodologies; details of IAST calculations; Maxwell−Stefan formulation for mixture diffusion; CBMC data on unary isotherms and isotherm fits; CBMC and MD data on adsorption, diffusion, and permeation of mixtures in various cation-exchanged FAU zeolites (PDF)

■ AUTHOR INFORMATION

Corresponding Author

Rajamani Krishna − *Van't Hoff Institute for Molecular Sciences, University of Amsterdam, 1098 XH Amsterdam, The Netherlands;* orcid.org/0000-0002-4784-8530; Email: r.krishna@contact.uva.nl

Author

Jasper M. van Baten − *Van't Hoff Institute for Molecular Sciences, University of Amsterdam, 1098 XH Amsterdam, The Netherlands*

Complete contact information is available at: https://pubs.acs.org/10.1021/acsomega.2c00427

Notes

The authors declare no competing financial interest.

■ ACKNOWLEDGMENTS

The authors acknowledge Dr. Richard Baur for helpful discussions.

■ NOMENCLATURE

Latin Alphabet

A surface area per kg of framework, $m^2\ kg^{-1}$
$D_{i,self}$ self-diffusivity of species i, $m^2\ s^{-1}$
f_i partial fugacity of species i, Pa
f_t total fugacity of bulk gas mixture, Pa
P_i^0 sorption pressure, Pa
q_i component molar loading of species i, $mol\ kg^{-1}$
$q_{i,sat}$ molar loading of species i at saturation, $mol\ kg^{-1}$
Q_{st} isosteric heat of adsorption, $J\ mol^{-1}$
R gas constant, 8.314 $J\ mol^{-1}\ K^{-1}$
S_{ads} adsorption selectivity, dimensionless
S_{diff} diffusion selectivity, dimensionless
S_{perm} permeation selectivity, dimensionless
T absolute temperature, K
x_i mole fraction of species i in the adsorbed phase, dimensionless

Greek Alphabet

μ_i molar chemical potential of component i, $J\ mol^{-1}$
π spreading pressure, $N\ m^{-1}$
θ fractional occupancy, dimensionless
Π_i membrane permeability of species i, $mol\ m\ m^{-2}\ s^{-1}\ Pa^{-1}$
ρ crystal framework density, $kg\ m^{-3}$
Φ surface potential, $mol\ kg^{-1}$

■ REFERENCES

(1) Wilkins, N. S.; Rajendran, A. Measurement of competitive CO_2 and N_2 adsorption on Zeolite 13X for post-combustion CO_2 capture. *Adsorption* **2019**, *25*, 115−133.

(2) Wu, H.; Yao, K.; Zhu, Y.; Li, B.; Shi, Z.; Krishna, R.; Li, J. Cu-TDPAT, an *rht*-type Dual-Functional Metal−Organic Framework Offering Significant Potential for Use in H_2 and Natural Gas Purification Processes Operating at High Pressures. *J. Phys. Chem. C* **2012**, *116*, 16609−16618.

(3) Belmabkhout, Y.; Pirngruber, G.; Jolimaitre, E.; Methivier, A. A complete experimental approach for synthesis gas separation studies using static gravimetric and column breakthrough experiments. *Adsorption* **2007**, *13*, 341−349.

(4) He, Y.; Krishna, R.; Chen, B. Metal-Organic Frameworks with Potential for Energy-Efficient Adsorptive Separation of Light Hydrocarbons. *Energy Environ. Sci.* **2012**, *5*, 9107−9120.

(5) Da Silva, F. A.; Rodrigues, A. E. Vacuum swing adsorption for propylene/propane separation with 4A zeolite. *Ind. Eng. Chem. Res.* **2001**, *40*, 5758−5774.

(6) Grande, C. A.; Poplow, F.; Rodrigues, A. E. Vacuum pressure swing adsorption to produce polymer-grade polypropylene. *Sep. Sci. Technol.* **2010**, *45*, 1252−1259.

(7) Divekar, S.; Nanoti, A.; Dasgupta, S.; Aarti; Chauhan, R.; Gupta, P.; Garg, M. O.; Singh, S. P.; Mishra, I. M. Adsorption Equilibria of Propylene and Propane on Zeolites and Prediction of Their Binary Adsorption with the Ideal Adsorbed Solution Theory. *J. Chem. Eng. Data* **2016**, *61*, 2629−2637.

(8) Da Silva, F. A.; Rodrigues, A. E. PropylenePropane Separation by Vacuum Swing Adsorption Using 13X Zeolite. *AIChE J.* **2001**, *47*, 341−357.

(9) Pirngruber, G. D.; Carlier, V.; Leinekugel-le-Cocq, D. Post-Combustion CO_2 Capture by Vacuum Swing Adsorption Using Zeolites − a Feasibility Study. *Oil Gas Sci. Technol.* **2014**, *69*, 989−1003.

(10) Yang, J.; Krishna, R.; Li, J.; Li, J. Experiments and Simulations on Separating a CO_2/CH_4 Mixture using K-KFI at Low and High Pressures. *Microporous Mesoporous Mater.* **2014**, *184*, 21−27.

(11) Palomino, M.; Corma, A.; Rey, F.; Valencia, S. New Insights on CO_2−Methane Separation Using LTA Zeolites with Different Si/Al Ratios and a First Comparison with MOFs. *Langmuir* **2010**, *26*, 1910−1917.

(12) Krishna, R.; van Baten, J. M. In Silico Screening of Zeolite Membranes for CO_2 Capture. *J. Membr. Sci.* **2010**, *360*, 323−333.

(13) Krishna, R.; van Baten, J. M. In silico screening of metal-organic frameworks in separation applications. *Phys. Chem. Chem. Phys.* **2011**, *13*, 10593−10616.

(14) Krishna, R.; van Baten, J. M. A comparison of the CO_2 capture characteristics of zeolites and metal-organic frameworks. *Sep. Purif. Technol.* **2012**, *87*, 120−126.

(15) Krishna, R. Methodologies for Screening and Selection of Crystalline Microporous Materials in Mixture Separations. *Sep. Purif. Technol.* **2018**, *194*, 281−300.
(16) Hudson, M. R.; Murray, L.; Mason, J. A.; Fickel, D. W.; Lobo, R. F.; Queen, W. L.; Brown, C. M. Unconventional and Highly Selective CO_2 Adsorption in Zeolite SSZ-13. *J. Am. Chem. Soc.* **2012**, *134*, 1970−1973.
(17) Gholipour, F.; Mofarahi, M. Adsorption Equilibrium of Methane and Carbon Dioxide on Zeolite13X: Experimental and Thermodynamic Modeling. *J. Supercrit. Fluids* **2016**, *111*, 47−54.
(18) Hefti, M.; Marx, D.; Joss, L.; Mazzotti, M. Adsorption Equilibrium of Binary Mixtures of Carbon Dioxide and Nitrogen on Zeolites ZSM-5 and 13X. *Microporous Mesoporous Mater.* **2015**, *215*, 215−228.
(19) Mofarahi, M.; Gholipour, F. Gas Adsorption Separation of CO_2/CH_4 System using Zeolite 5A. *Microporous Mesoporous Mater.* **2014**, *200*, 47−54.
(20) Bae, T.-H.; Hudson, M. R.; Mason, J. A.; Queen, W. L.; Dutton, J. J.; Sumida, K.; Micklash, K. J.; Kaye, S. S.; Brown, C. M.; Long, J. R. Evaluation of Cation-exchanged Zeolite Adsorbents for Post-combustion Carbon Dioxide Capture. *Energy Environ. Sci.* **2013**, *6*, 128−138.
(21) Jiang, Y.; Ling, J.; Xiao, P.; He, Y.; Zhao, Q.; Chu, Z.; Liu, Y.; Li, P.; Webley, P. A. Simultaneous Biogas Purification and CO_2 capture by Vacuum Swing Adsorption using Zeolite NaUSY. *Chem. Eng. J.* **2018**, *334*, 2593−2602.
(22) Bower, J.; Barpaga, D.; Prodinger, S.; Krishna, R.; Schaef, H. T.; McGrail, B. P.; Derewinski, M. A.; Motkuri, R. K. Dynamic Adsorption of CO_2/N_2 on Cation-exchanged Chabazite SSZ-13: A Breakthrough Analysis. *ACS Appl. Mater. Interfaces* **2018**, *10*, 14287−14291.
(23) Yang, R. T. *Adsorbents: Fundamentals and Applications*. John Wiley & Sons, Inc.: Hoboken, New Jersey, 2003; pp. 1−410.
(24) Yang, J.; Shang, H.; Krishna, R.; Wang, Y.; Ouyang, K.; Li, J. Adjusting the Proportions of Extra-framework K^+ and Cs^+ cations to Construct a "Molecular Gate" on ZK-5 for CO_2 Removal. *Microporous Mesoporous Mater.* **2018**, *268*, 50−57.
(25) Prats, H.; Bahamon, D.; Giménez, X.; Gamallo, P.; Sayós, R. Computational simulation study of the influence of faujasite Si/Al ratio on CO_2 capture by temperature swing adsorption. *J. CO2 Util.* **2017**, *21*, 261−269.
(26) Prats, H.; Bahamon, D.; Alonso, G.; Giménez, X.; Gamallo, P.; Sayós, R. Optimal Faujasite structures for post combustion CO_2 capture and separation in different swing adsorption processes. *J. CO2 Util.* **2017**, *19*, 100−111.
(27) Koh, D.-Y.; Pimentel, B. R.; Babu, V. P.; Stephenson, N.; Chai, S. W.; Rosinski, A.; Lively, R. P. Sub-ambient air separation via Li^+ exchanged zeolite. *Microporous Mesoporous Mater.* **2018**, *256*, 140−146.
(28) Fu, Y.; Liu, Y.; Li, Z.; Zhang, Q.; Yang, X.; Zhao, C.; Zhang, C.; Wang, H.; Yang, R. T. Insights into adsorption separation of N_2/O_2 mixture on FAU zeolites under plateau special conditions: A molecular simulation study. *Sep. Purif. Technol.* **2020**, *251*, 117405.
(29) Arora, A.; Faruque Hasan, M. M. Flexible oxygen concentrators for medical applications. *Sci. Rep.* **2021**, *11*, 14317.
(30) Vemula, R. R.; Urich, M. D.; Kothare, M. V. Experimental design of a "Snap-on" and standalone single-bed oxygen concentrator for medical applications. *Adsorption* **2021**, *27*, 619−628.
(31) Ruthven, D. M.; Farooq, S.; Knaebel, K. S. *Pressure swing adsorption*. VCH Publishers: New York, 1994; pp. 1−352.
(32) Krishna, R. A Maxwell-Stefan-Glueckauf Description of Transient Mixture Uptake in Microporous Adsorbents. *Sep. Purif. Technol.* **2018**, *191*, 392−399.
(33) Krishna, R. Highlighting the Influence of Thermodynamic Coupling on Kinetic Separations with Microporous Crystalline Materials. *ACS Omega* **2019**, *4*, 3409−3419.
(34) Krishna, R. Maxwell-Stefan Modelling of Mixture Desorption Kinetics in Microporous Crystalline Materials. *Sep. Purif. Technol.* **2019**, *229*, 115790.
(35) Krishna, R. Metrics for Evaluation and Screening of Metal-Organic Frameworks for Applications in Mixture Separations. *ACS Omega* **2020**, *5*, 16987−17004.
(36) van Zandvoort, I.; Ras, E.-J.; de Graaf, R.; Krishna, R. Using Transient Breakthrough Experiments for Screening of Adsorbents for Separation of C_2H_4/CO_2 Mixtures. *Sep. Purif. Technol.* **2020**, *241*, 116706.
(37) Rangnekar, N.; Mittal, N.; Elyassi, B.; Caro, J.; Tsapatsis, M. Zeolite Membranes −A Review and Comparison with MOFs. *Chem. Soc. Rev.* **2015**, *44*, 7128−7154.
(38) Baker, R. W. *Membrane Technology and Applications*. 3rd Edition, John Wiley: New York, 2012.
(39) Krishna, R.; van Baten, J. M. Investigating the potential of MgMOF-74 membranes for CO_2 capture. *J. Membr. Sci.* **2011**, *377*, 249−260.
(40) Krishna, R.; van Baten, J. M. Maxwell-Stefan modeling of slowing-down effects in mixed gas permeation across porous membranes. *J. Membr. Sci.* **2011**, *383*, 289−300.
(41) Krishna, R.; van Baten, J. M. Using the Spreading Pressure to Inter-Relate the Characteristics of Unary, Binary and Ternary Mixture Permeation across Microporous Membranes. *J. Membr. Sci.* **2022**, *643*, 120049.
(42) Krishna, R. Using the Maxwell-Stefan formulation for Highlighting the Influence of Interspecies (1-2) Friction on Binary Mixture Permeation across Microporous and Polymeric Membranes. *J. Membr. Sci.* **2017**, *540*, 261−276.
(43) Algieri, C.; Drioli, E. Zeolite membranes: Synthesis and applications. *Sep. Purif. Technol.* **2021**, *278*, 119295.
(44) Ruthven, D. M. *Principles of Adsorption and Adsorption Processes*. John Wiley: New York, 1984; pp. 1−433.
(45) Myers, A. L.; Prausnitz, J. M. Thermodynamics of Mixed Gas Adsorption. *AIChE J.* **1965**, *11*, 121−130.
(46) Talu, O.; Myers, A. L. Rigorous Thermodynamic Treatment of Gas-Adsorption. *AIChE J.* **1988**, *34*, 1887−1893.
(47) Siperstein, F. R.; Myers, A. L. Mixed-Gas Adsorption. *AIChE J.* **2001**, *47*, 1141−1159.
(48) Krishna, R. Thermodynamic Insights into the Characteristics of Unary and Mixture Permeances in Microporous Membranes. *ACS Omega* **2019**, *4*, 9512−9521.
(49) Krishna, R.; Van Baten, J. M. Using Molecular Simulations to Unravel the Benefits of Characterizing Mixture Permeation in Microporous Membranes in Terms of the Spreading Pressure. *ACS Omega* **2020**, *5*, 32769−32780.
(50) Krishna, R. Thermodynamically Consistent Methodology for Estimation of Diffusivities of Mixtures of Guest Molecules in Microporous Materials. *ACS Omega* **2019**, *4*, 13520−13529.
(51) Krishna, R.; van Baten, J. M. Investigating the Relative Influences of Molecular Dimensions and Binding Energies on Diffusivities of Guest Species Inside Nanoporous Crystalline Materials. *J. Phys. Chem. C* **2012**, *116*, 23556−23568.
(52) Krishna, R.; van Baten, J. M. Influence of Adsorption Thermodynamics on Guest Diffusivities in Nanoporous Crystalline Materials. *Phys. Chem. Chem. Phys.* **2013**, *15*, 7994−8016.
(53) Robeson, L. M. The upper bound revisited. *J. Membr. Sci.* **2008**, *320*, 390−400.
(54) Himma, N. F.; Wardani, A. K.; Prasetya, N.; Aryanti, P. T. P.; Wenten, I. G. Recent progress and challenges in membrane based O_2/N_2 separation. *Rev. Chem. Eng.* **2019**, *35*, 591−625.

https://doi.org/10.1021/acsomega.2c00427
ACS Omega 2022, 7, 13050−13056

Supporting Information

Highlighting the Anti-Synergy between Adsorption and Diffusion in Cation-Exchanged Faujasite Zeolites

Rajamani Krishna* and Jasper M. van Baten

Van 't Hoff Institute for Molecular Sciences
University of Amsterdam
Science Park 904
1098 XH Amsterdam, The Netherlands
email: r.krishna@contact.uva.nl

Table of Contents

1 Preamble

The Supplementary Material accompanying our article *Highlighting the Anti-Synergy between Adsorption and Diffusion in Cation-Exchanged Faujasite Zeolites* provides: (a) CBMC and MD simulation methodologies, (b) Details of IAST calculations, (c) Maxwell-Stefan formulation for mixture diffusion, (d) CBMC data on unary isotherms and isotherm fits, (e) CBMC and MD data on adsorption, diffusion, and permeation of mixtures in various cation-exchanged FAU zeolites.

2 Separations with Cation-Exchanged Zeolites

Separation technologies such as distillation, absorption, and extraction are energy intensive because of vapor/liquid phase transformations in condensers, reboilers and solvent recovery sections. The energy consumption for distillation accounts for about 50% of the total energy consumption for all separations.[1] The largest opportunities for energy reduction are offered by replacing distillation with (a) low-energy demanding separation systems such as adsorption or membranes, or (b) hybrid systems that combine distillation with adsorption or membranes.[1] In many cases, the hybrid processing option is easier to implement technically because adsorption and membrane separations often cannot produce products with the purity levels that are achievable with distillation. The success of such replacement strategies is crucially dependent on development of suitable porous materials that can be used in fixed bed adsorption devices or as thin layers in membrane permeation units.

For gas separation applications, the most commonly used cation-exchanged zeolites are A, X, and Y; see Figure S1. Each unit cell of A, X, and Y contains 192 (Si, Al)O_4 tetrahedra.

Type A zeolites, also referred to as LTA (= Linde Type A), consist of cages of 743 $Å^3$ volume, separated by 4.1 Å × 4.47 Å 8-ring windows. Per unit cell, LTA-4A has 96 Si, 96 Al, 96 Na^+, with Si/Al=1. Per unit cell, LTA-5A has 96 Si, 96 Al, 32 Na^+, 32 Ca^{++} with Si/Al=1.

Zeolites X, and Y have the FAU (= Faujasite) topology consisting of cages of 786 $Å^3$ volume, separated by 7.25 Å 12-ring windows. The number of aluminum ions per unit cell of Type X zeolite varies from 96 to 77 (i.e., Si/Al = 1 to 1.5). For Type Y zeolites, the number of Al atoms per unit cell ranges from 76 to 48 (Si/Al = 1.5 to 3). NaX is commonly referred to by its trade name 13X.

We first summarize the various factors that govern the adsorption strength of a guest molecule; the treatment essentially follows that of Yang,[2] and Ruthven.[3]

2.1 Potential energies for adsorption

The total potential between the adsorbate molecules and the adsorbent is the sum of the adsorbate-adsorbate and adsorbate-adsorbent interaction potentials. Let us focus on the factors that govern the adsorbate-adsorbent interaction potential, ϕ. If we ignore π-complexation and chemical bonding,[2] the two contributions to the adsorbate-adsorbent interaction potential, ϕ, are dispersion interactions, $\phi_D + \phi_R$, and electrostatic interactions, $\phi_{Ind} + \phi_{F\mu} + \phi_{\dot{F}Q}$. The adsorbate-adsorbent interaction potential, ϕ, is the sum of various contributions

$$\phi = \phi_D + \phi_R + \phi_{Ind} + \phi_{F\mu} + \phi_{\dot{F}Q} \tag{S1}$$

In eq (S1), the dispersion interactions, $\phi_D + \phi_R$, are also termed London – van der Waals interactionsHere, $\phi_D = -\frac{A}{r^6}$ = dispersion (attraction) energy; $\phi_R = \frac{B}{r^{12}}$ = close-range repulsion energy, where r is the distance between the centers of the interacting pairs of atoms/molecules/

ϕ_{Ind} = induction energy (interaction between electric field and an induced dipole)

$\phi_{F\mu}$ = interaction between an electric field F and a permanent dipole μ

$\phi_{\dot{F}Q}$ = interaction between an electric field gradient $\dot{F}$ and a quadrupole (with quadrupole moment Q)

The dispersion and repulsion interactions form the Lennard-Jones potential

$$\phi_D + \phi_R = 4\varepsilon\left(\left(\frac{\sigma}{r}\right)^{12} - \left(\frac{\sigma}{r}\right)^{6}\right) \tag{S2}$$

At the equilibrium distance r_0 we have $\phi_D + \phi_R = 0$; $\frac{d\phi}{dr} = 0$ and $B = -\frac{Ar_0^6}{2}$.

The most commonly used expression for calculating A is the Kirkwood-Müller formula for interaction between atoms and molecules (denoted by subscripts i and j)

$$A = \frac{6mc^2\alpha_i\alpha_j}{\frac{\alpha_i}{\chi_i}+\frac{\alpha_j}{\chi_j}} \tag{S3}$$

The potential for interaction between electric field and an induced dipole is

$$\phi_{Ind} = -\frac{1}{2}\alpha F^2 = -\frac{1}{2}\alpha\frac{q^2}{r^4\left(4\pi\varepsilon_0\right)^2} \tag{S4}$$

The potential for interaction between electric field F (of an ion) and point dipole is

$$\phi_{F\mu} = -\mu F\cos\theta = -\mu\frac{q}{r^2\left(4\pi\varepsilon_0\right)}\cos\theta \tag{S5}$$

The potential for interaction between electric field gradient $\dot{F}$ and linear point quadrupole is

$$\phi_{\dot{F}Q} = \frac{1}{2}Q\dot{F} = -\frac{1}{2}Q\frac{q}{2r^3\left(4\pi\varepsilon_0\right)}\left(3\cos^2\theta - 1\right) \tag{S6}$$

where

m = mass of electron

c = speed of light

α = polarizability

χ = magnetic susceptibility

α = polarizability

F = electric field

q = electronic charge of ion on surface

ε_0 = permittivity of a vacuum

μ = permanent dipole moment

θ = angle between the direction of the field or field gradient and the axis of the dipole or linear quadrupole

Q = linear quadrupole moment (+ or -)

r = distance between the centers of the interacting pairs

For a given sorbent, the sorbate-sorbent interaction potential depends on the properties of the sorbate. Among the five different types of interactions, the first two contributions $\phi_D + \phi_R$ are non-specific, which are operative in all sorbate-sorbent systems; the non-specific interactions $\phi_D + \phi_R$ are non-electrostatic. The London – van der Waals dispersion interaction energies are largely dictated by the polarizabilities of the guest molecules and surfaces atoms of the adsorbent materials; see Figure S2. The polarizabilities of a wide variety of guest molecules are tabulated by Sircar and Myers.[4] Broadly speaking, the polarizabilites of molecules increase with increasing molar masses, as illustrated for noble gases He, Ne, Ar, Kr, and Xe in Figure S3, and for homologous series of hydrocarbons in Figure S4a,b. The value of α generally increases with the molecular weight because more electrons are available for polarization.

The last three contributions $\phi_{Ind} + \phi_{F\mu} + \phi_{FQ}$ arise from charges (which create electric fields) on the solid surface; see Figure S5. For activated carbon, the non-specific interactions dominate. On a surface without charges, such as graphite, ϕ_{Ind} = 0. For metal oxides, zeolites, and ionic solids, the electrostatic interactions often dominate, depending on the adsorbate. For adsorbate with a quadrupole, the net interaction between a uniform field and the quadrupole is zero. However, the quadrupole interacts strongly with the field gradient, thus the term ϕ_{FQ}.

Figure S6a,b compare the polarizabilities, dipole moments, and quadrupole moments of H_2, Ar, O_2, N_2, CO, CH_4, and CO_2. Of these sorbates, only CO has a permanent dipole moment. The four guest sorbates O_2, N_2, CO, and CO_2 all possess finite quadrupole moments, with the hierarchy of magnitudes $O_2 < N_2 < CO < CO_2$. Interestingly, the polarizability of CH_4 is higher than that of CO, but does not possess either dipole or significant quadrupole moments. Therefore, in a non-charged adsorbent such as activated the adsorption strength of CH_4 is higher than that of CO. However, in cation-exchanged zeolites, CO may have a higher adsorption strength than CH_4.

We also note that each of the three electrostatic contributions $\phi_{Ind}, \phi_{F\mu}, \phi_{\cdot FQ}$ are proportion to the ionic charges of the sorbent, q: $\phi_{Ind} \propto \alpha \frac{q^2}{r^4}$; $\phi_{F\mu} \propto \mu \frac{q}{r^2}$; $\phi_{\cdot FQ} \propto Q \frac{q}{r^3}$ Therefore Ca^{++} should be yield stronger interaction potential that Na^+, with say CO_2, on the basis of this consideration; note that these two cations have nearly the same ionic radius; see Figure S5. The electrostatic contributions are also inversely proportional to a power of the distance between the centers of the interacting pairs: $\phi_{Ind} \propto \alpha \frac{q^2}{r^4}$; $\phi_{F\mu} \propto \mu \frac{q}{r^2}$; $\phi_{\cdot FQ} \propto Q \frac{q}{r^3}$, we should expect the interaction potentials to be larger for Li^+ than for Na^+, because of the significantly smaller ionic radius of Li^+. This explains, albeit qualitatively, why LiLSX is the favored sorbent for selective adsorption of N_2 for O_2/N_2 mixtures.[2]

2.2 List of Figures for Separations with Cation-Exchanged Zeolites

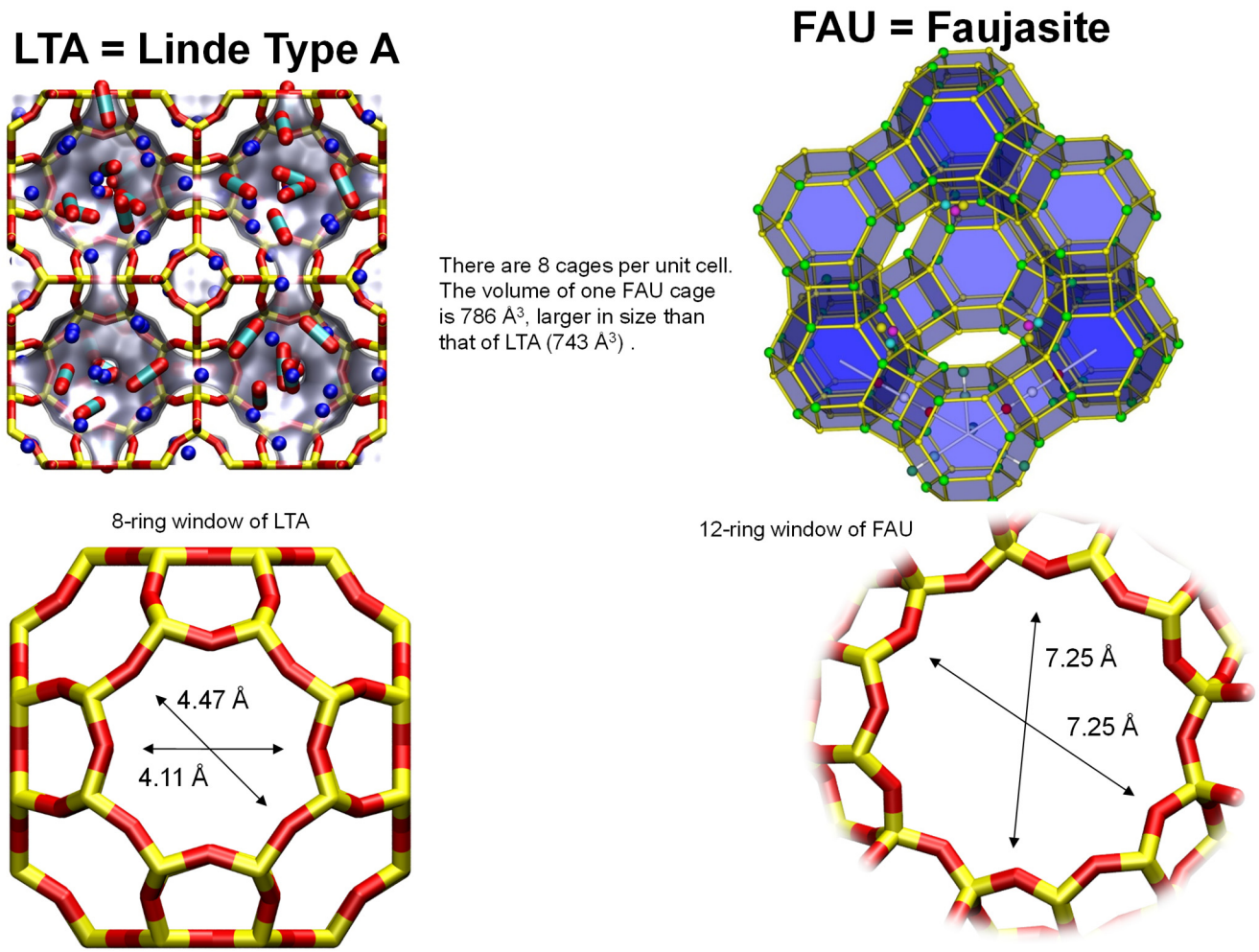

Figure S1. Pore topologies of LTA (= Linde Type A), and FAU (= Faujasite) zeolites.

London – van der Waals interactions

$$\text{London - van der Waals interactions} = \phi_D + \phi_R = \text{Attraction} + \text{Repulsion} = -\frac{A}{r^6} + \frac{B}{r^{12}}$$

These forces are proportional to polarizabilities of both
sorbate and sorbent atoms on surface, that increases with size of molecule

Figure S2. Dispersion interactions.

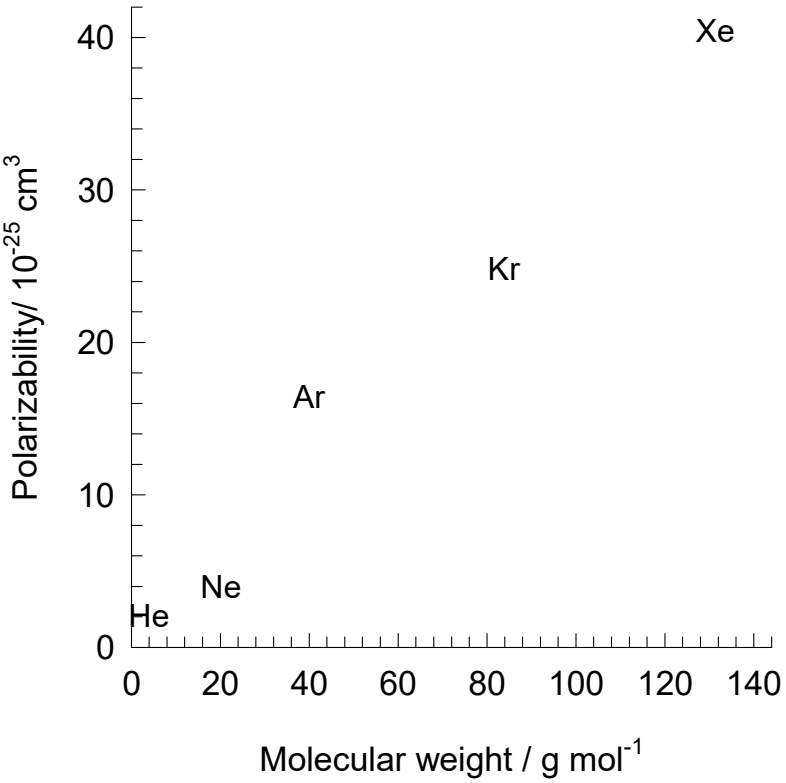

Figure S3. Polarizabilities and boiling points of noble gases. The data on polarizabilities are taken from Sircar and Myers.[4]

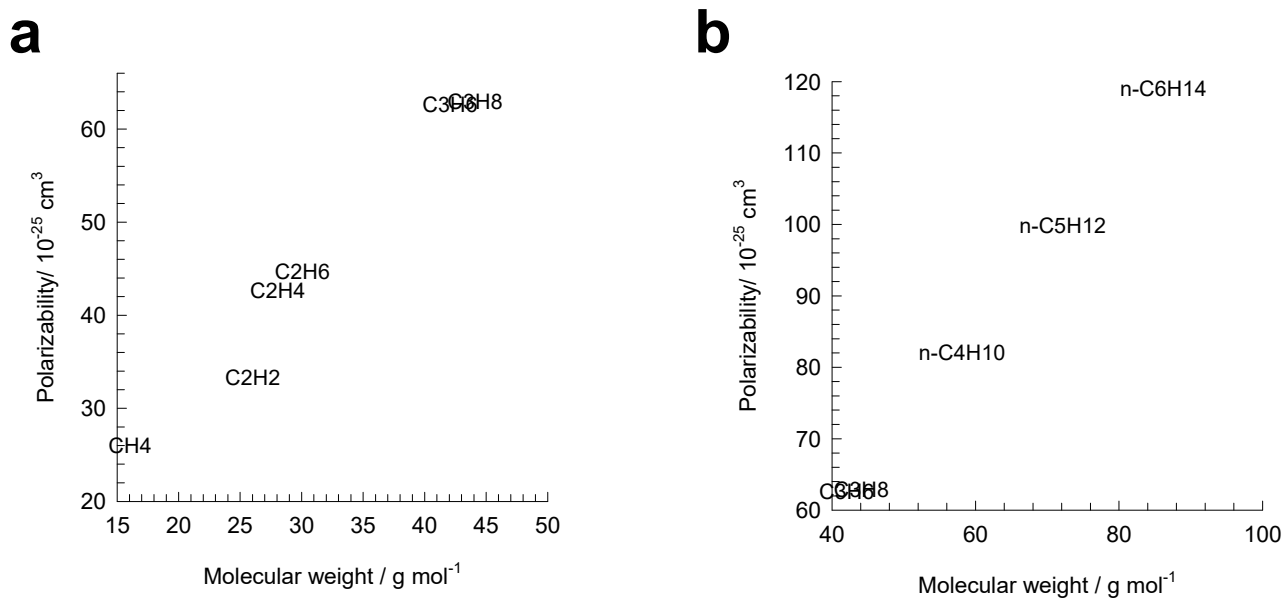

Figure S4. Polarizabilities of (a) light hydrocarbons, and (b) heavier hydrocarbons. The data on polarizabilities are taken from Sircar and Myers.[4]

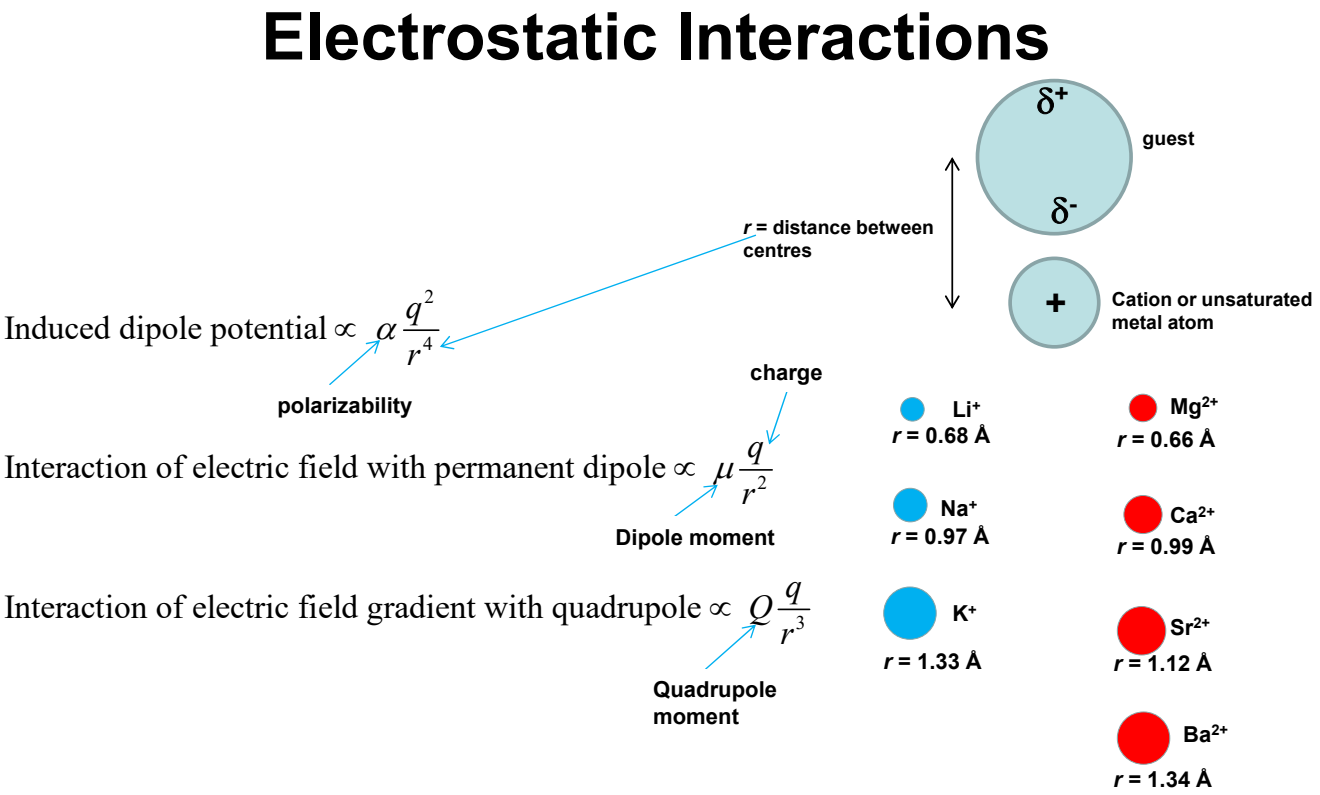

Larger electrostatic interactions with (a) smaller cations, (b) higher valency, (c) larger dipole, (d) larger quadrupole, (e) higher polarizability. Electric field gradients are strong in zeolites as cations are dispersed above the negatively charged O^{2-} in the framework

Figure S5. Electrostatic interactions. The cation sizes are culled from Yang.[2]

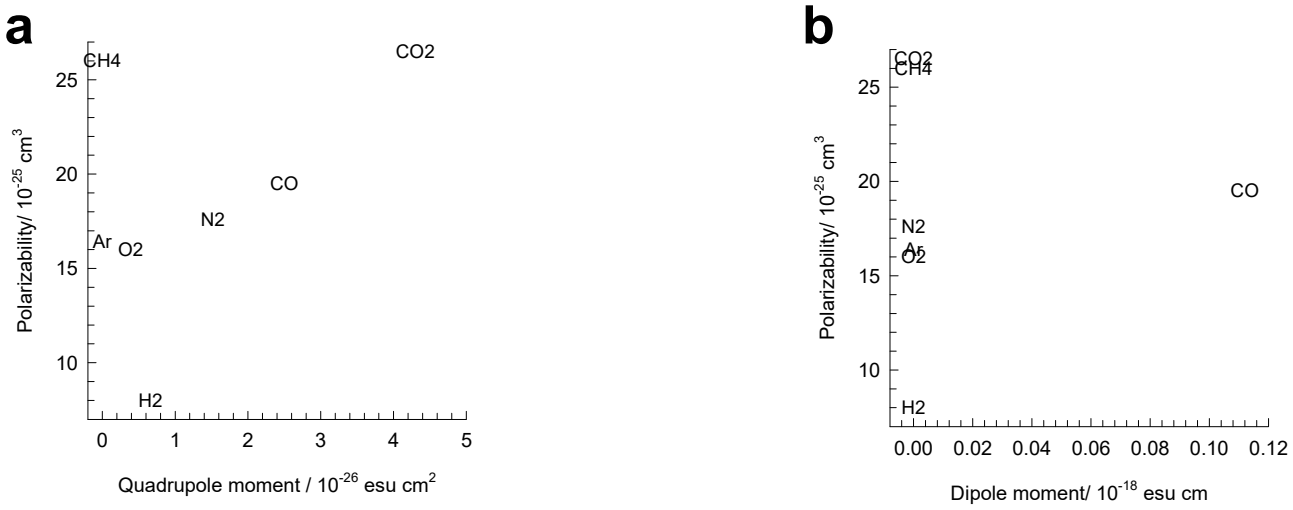

Figure S6. (a, b) Polarizabilities, dipole moments, and quadrupole moments of H_2, Ar, N_2, O_2, CO, CH_4, and CO_2. The data are taken from Sircar and Myers.[4]

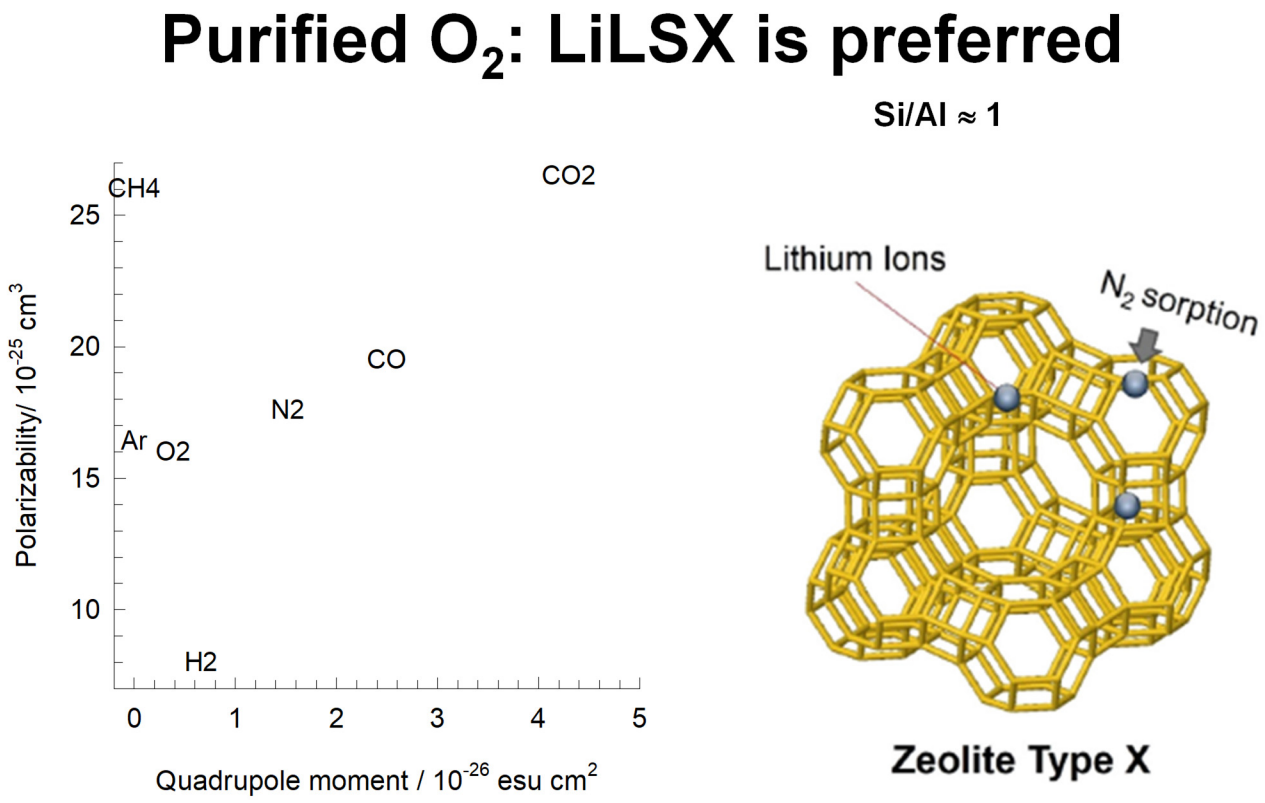

Figure S7. LiLSX is the favored sorbent for selective adsorption of N_2 for O_2/N_2 mixtures.[2]

3 Configurational-Bias Monte Carlo Simulation Methodology

The simulation methodologies and the force field information used are the same as detailed in the Supplementary Materials accompanying our earlier publications.[5-11] A short summary is provided hereunder.

3.1 Zeolites (all silica)

CH_4 molecules are described with a united atom model, in which each molecule is treated as a single interaction center.[12] The interaction between adsorbed molecules is described with Lennard-Jones terms; see Figure S8. The Lennard-Jones parameters for CH_4-zeolite interactions are taken from Dubbeldam et al.[13]. The force field for H_2 corresponds to that given by Kumar et al.[14] In implementing this force field, quantum effects for H_2 have been ignored because the work of Kumar et al.[14] has shown that quantum effects are of negligible importance for temperatures above 200 K; all our simulations were performed at 300 K. The Lennard-Jones parameters for CO_2-zeolite and N_2-zeolite are essentially those of Makrodimitris et al.[15]; see also García-Pérez et al.[16]. For simulations with linear alkanes with two or more C atoms, the beads in the chain are connected by harmonic bonding potentials. A harmonic cosine bending potential models the bond bending between three neighboring beads, a Ryckaert-Bellemans potential controls the torsion angle. The beads in a chain separated by more than three bonds interact with each other through a Lennard-Jones potential; see schematic in Figure S8. The force fields of Dubbeldam et al.[13] was used for the variety of potentials. The Lennard-Jones potentials are shifted and cut at 12 Å.

Following Kiselev and co-workers,[17] the zeolite is modeled as a rigid crystal. The interactions of the guest (pseudo) atoms with the host zeolite atoms are dominated by the dispersive interactions with the oxygen atoms, these interactions are described with a Lennard-Jones potential; see Table S1.

The Lorentz-Berthelot mixing rules were applied for calculating the Lennard-Jones parameters describing guest-host interactions

$$\sigma_{guest-host} = \frac{\left(\sigma_{guest} + \sigma_{host}\right)}{2}$$
$$\frac{\varepsilon_{guest-host}}{k_B} = \sqrt{\frac{\varepsilon_{guest}}{k_B} \times \frac{\varepsilon_{host}}{k_B}} \quad \text{(S7)}$$

The Lennard-Jones potentials are shifted and cut at 12 Å. Periodic boundary conditions were employed. The Configurational-Bias Monte Carlo (CBMC) simulation technique used is described in detail by Frenkel and Smit.[18]

3.2 Cation-exchanged zeolites

In this article, we carry out molecular simulations to investigate the adsorption and diffusion characteristics of:

all-silica FAU (192 Si, 0 Al, 0 Na^+, Si/Al=∞),

NaY (138 Si, 54 Al, 54 Na^+, Si/Al=2.56), and

NaX (106 Si, 86 Al, 86 Na^+, Si/Al=1.23) zeolites.

The force field information for the simulations with cations are taken from García-Sanchez et al.[19] In the MC simulations, the cations were allowed to move within the framework and both Lennard-Jones and Coulombic interactions are taken into consideration.

The presence of cations reduces the accessible pore volume. The location of the cations are pictured in Figure S10, and Figure S11.

We carried out CBMC and MD simulations for adsorption and diffusion of unary N_2, unary O_2, and N_2/O_2 mixtures in FAU zeolites with different Al contents per unit cell:

FAU all-silica = 0 Al

FAU48Al = 48 Al/uc, 48 Li^+/uc

FAU54Al = 54 Al/uc, 54 Li^+/uc

FAU86Al = 86 Al/uc, 86 Li^+/uc

FAU96Al = 96 Al/uc, 96 Li^+/uc

The Li force field is from Table 1 of Fu et al.[20] The remainder of the force field implementation is taken from Table 1 of Fu et al.[21]

In the CBMC simulations both Lennard-Jones and Coulombic interactions are taken into consideration; see schematic sketch in Figure S9.

3.3 Isosteric heats of adsorption

We determined the isosteric heats of adsorption, ΔQ_{st}, from CBMC simulations using the fluctuation formula

$$Q_{st} = RT - \frac{< U_i n_i > - < U_i >< n_i >}{\left\langle n_i^2 \right\rangle - \left\langle n_i \right\rangle^2} \qquad \text{(S8)}$$

where n_i represents the number of molecules in the simulation box and $\langle \ldots \rangle$ denotes ensemble averaging.

3.4 CBMC code

All simulations reported in this work were carried out using an in-house BIGMAC code, originally developed by T.J.H. Vlugt. This code was modified to handle rigid molecular structures and charges. The calculation of the accessible pore volume using the Widom insertion of He probe atoms is implemented within the BIGMAC code.

3.5 List of Tables for Configurational-Bias Monte Carlo Simulation Methodology

Table S1. Lennard-Jones parameters for host atoms in all-silica zeolites.

(pseudo-) atom	σ / Å	ε/k_B / K	charge
Si			2.05
O	3	93.53	-1.025

3.6 List of Figures for Configurational-Bias Monte Carlo Simulation Methodology

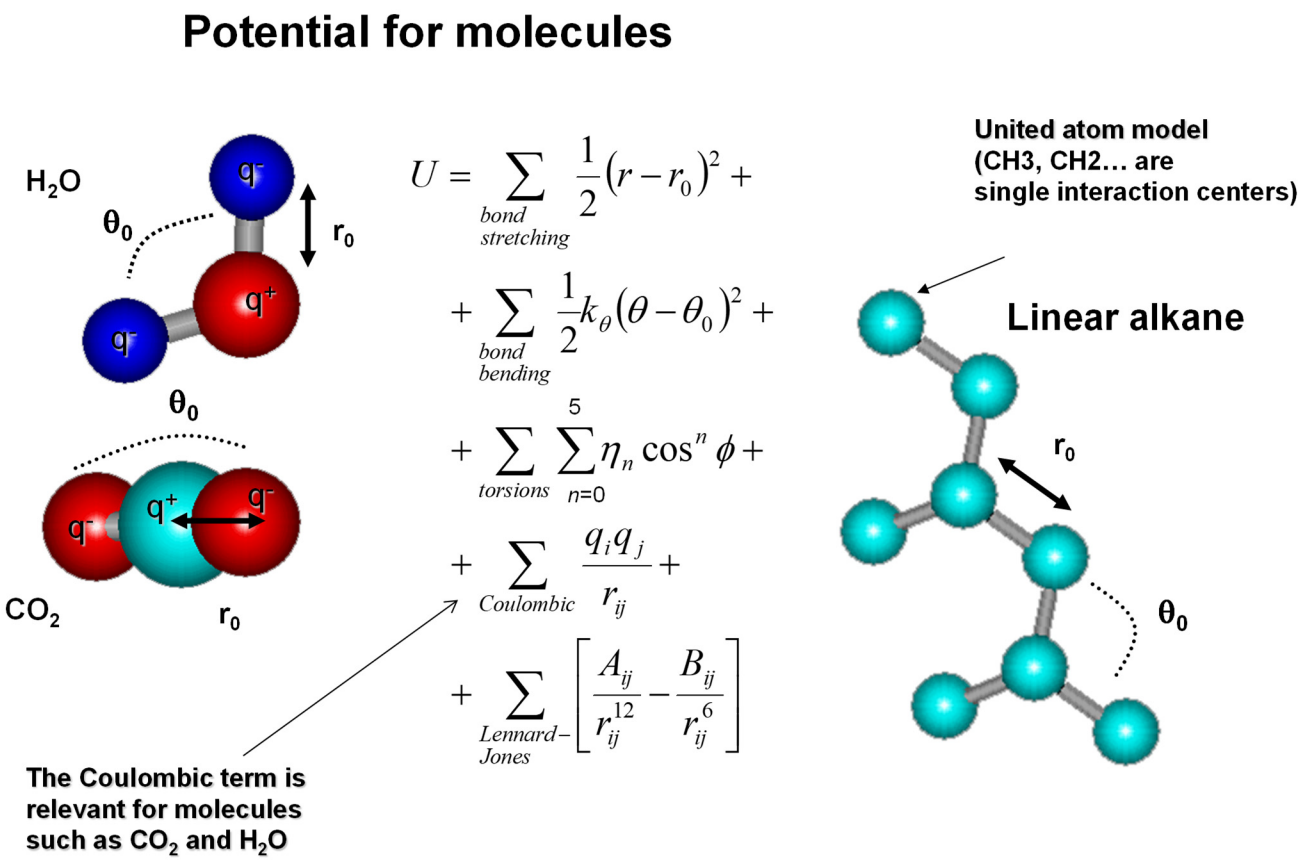

Figure S8. Potential for molecules.

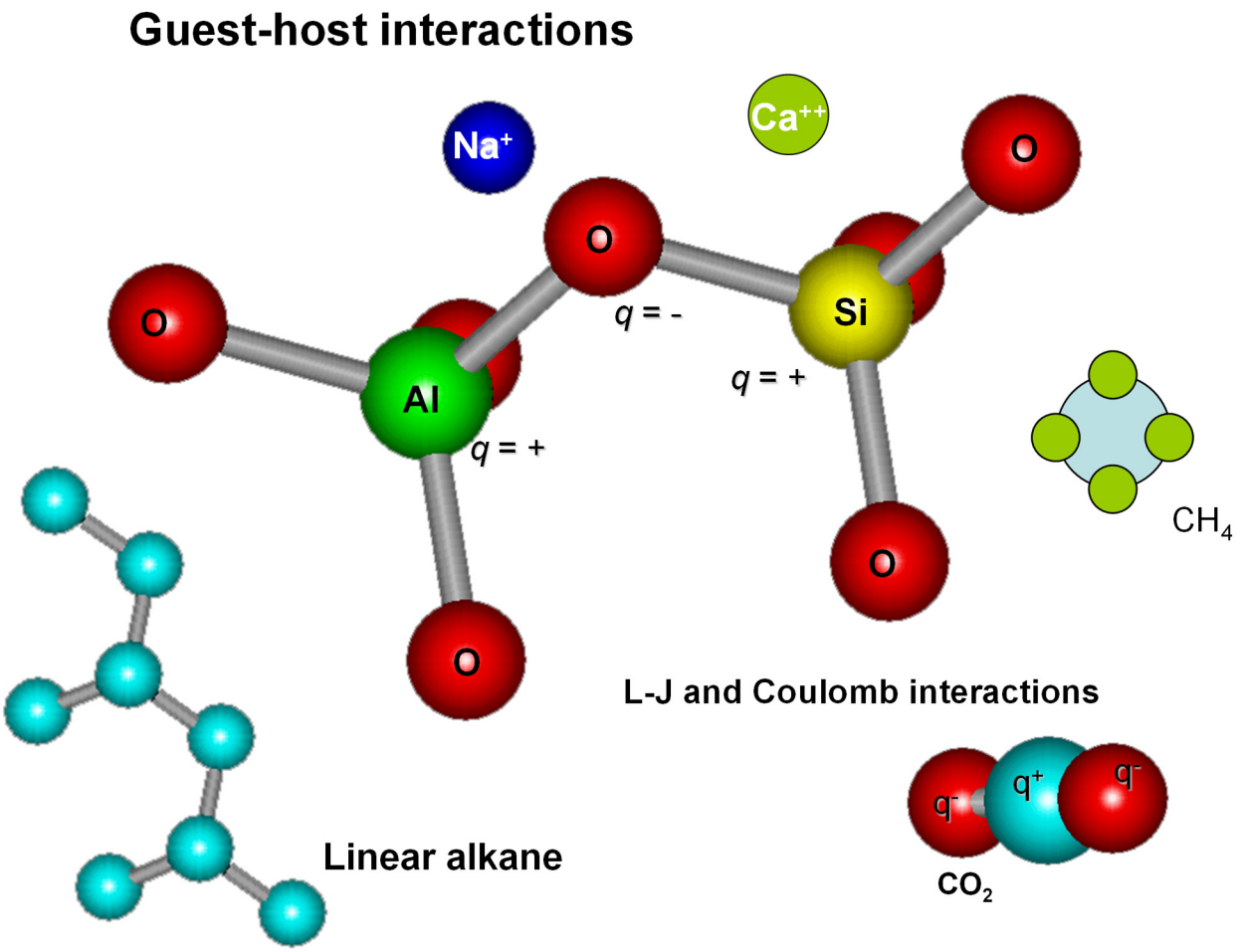

Figure S9. Guest-host interactions.

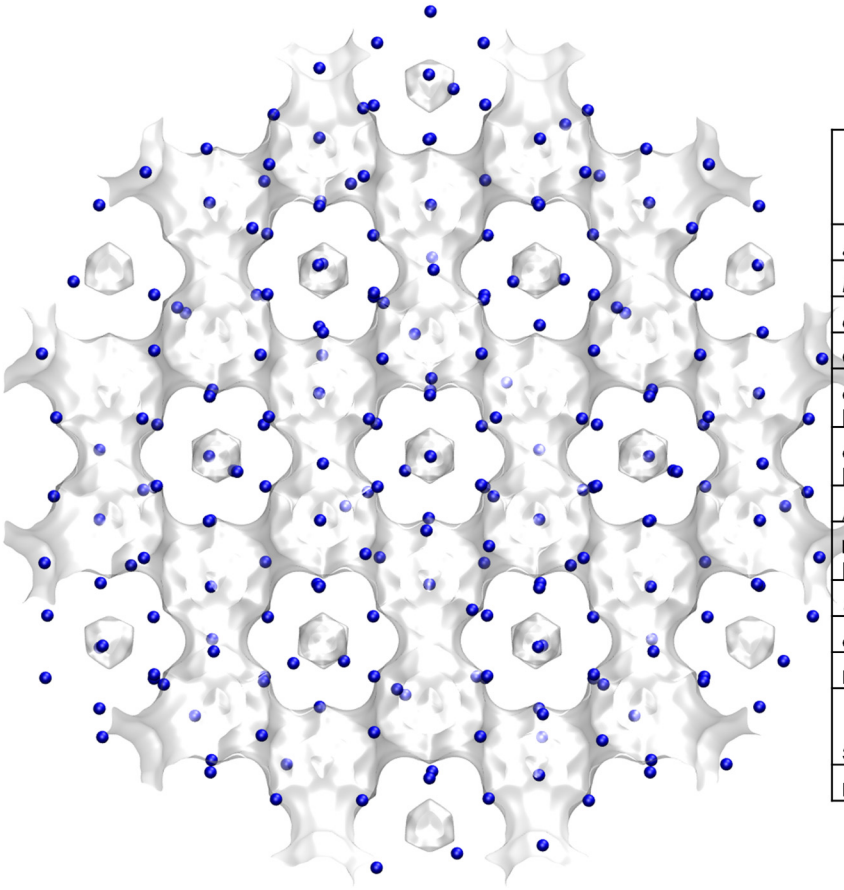

	FAU 86 Na/uc
a /Å	25.028
b /Å	25.028
c /Å	25.028
Cell volume / Å^3	15677.56
conversion factor for [molec/uc] to [mol per kg Framework]	0.0745
conversion factor for [molec/uc] to [kmol/m^3]	0.2658
ρ [kg/m3] (with cations)	1421.277
MW unit cell [g/mol(framework+cations)]	13418.42
ϕ, fractional pore volume	0.399
open space / Å^3/uc	6248.0
Pore volume / cm^3/g	0.280
Surface area /m^2/g	
DeLaunay diameter /Å	7.37

Figure S10. Location of cations for NaX zeolite (106 Si, 86 Al, 86 Na^+, Si/Al=1.23)

NaY (138 Si, 54 Al, 54 Na+, Si/Al=2.55)

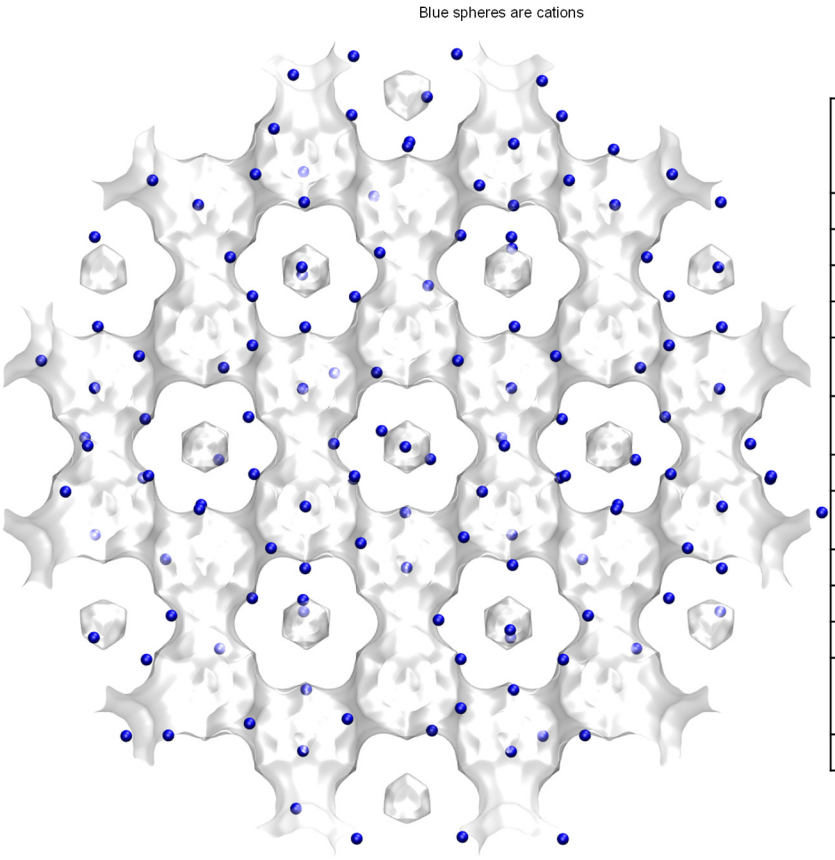

	FAU-54Al
a /Å	25.028
b /Å	25.028
c /Å	25.028
Cell volume / Å^3	15677.56
conversion factor for [molec/uc] to [mol per kg Framework]	0.0786
conversion factor for [molec/uc] to [kmol/m^3]	0.2596
ρ [kg/m3] (with cations)	1347.1
MW unit cell [g/mol(framework+cations)]	12718.08
ϕ, fractional pore volume	0.408
open space / Å^3/uc	6396.6
Pore volume / cm^3/g	0.303
Surface area /m^2/g	
DeLaunay diameter /Å	7.37

Figure S11. Location of cations for NaY zeolite (138 Si, 54 Al, 54 Na^+, Si/Al=2.55).

4 Thermodynamics of Mixture Adsorption in Micro-porous Materials

Within microporous crystalline materials, the guest molecules exist in the adsorbed phase, and the thermodynamics of mixture adsorption has an important bearing on the diffusion characteristics of guest molecules. For that reason, we provide below a brief summary of the Ideal Adsorbed Solution Theory (IAST) theory of Myers and Prausnitz.[22]

4.1 Brief outline of theory

The Gibbs adsorption equation[3] in differential form is

$$Ad\pi = \sum_{i=1}^{n} q_i d\mu_i \tag{S9}$$

The quantity A is the surface area per kg of framework, with units of m^2 per kg of the framework of the crystalline material; q_i is the molar loading of component i in the adsorbed phase with units moles per kg of framework; μ_i is the molar chemical potential of component i. The spreading pressure π has the same units as surface tension, i.e. N m^{-1}.

The chemical potential of any component in the adsorbed phase, μ_i, equals that in the bulk fluid phase. If the partial fugacities in the bulk fluid phase are f_i, we have

$$d\mu_i = RTd\ln f_i \tag{S10}$$

where R is the gas constant (= 8.314 J mol^{-1} K^{-1}).

Briefly, the basic equation of Ideal Adsorbed Solution Theory (IAST) theory of Myers and Prausnitz[22] is the analogue of Raoult's law for vapor-liquid equilibrium, i.e.

$$f_i = P_i^0 x_i; \quad i = 1, 2, ...n \tag{S11}$$

where x_i is the mole fraction in the adsorbed phase

$$x_i = \frac{q_i}{q_1 + q_2 + ...q_n} \tag{S12}$$

and P_i^0 is the pressure for sorption of every component *i*, which yields the same spreading pressure, π for each of the pure components, as that for the mixture:

$$\frac{\pi A}{RT} = \int_0^{P_1^0} \frac{q_1^0(f)}{f} df = \int_0^{P_2^0} \frac{q_2^0(f)}{f} df = \int_0^{P_3^0} \frac{q_3^0(f)}{f} df = ... \tag{S13}$$

where $q_i^0(f)$ is the *pure* component adsorption isotherm. The units of $\Phi \equiv \frac{\pi A}{RT}$, also called the surface potential, [23-27] are mol kg^{-1}.

The unary isotherm may be described by say the 1-site Langmuir isotherm

$$q^0(f) = q_{sat} \frac{bf}{1+bf}; \quad \theta = \frac{bf}{1+bf} \tag{S14}$$

where we define the fractional *occupancy* of the adsorbate molecules, $\theta = q^0(f)/q_{sat}$. The superscript 0 is used to emphasize that $q^0(f)$ relates the *pure component* loading to the bulk fluid fugacity. For all of the guest/host combinations considered in this article, the unary isotherms need to be described by the dual-Langmuir-Freundlich model

$$q^0(f) = q_{A,sat} \frac{b_A f^{\nu A}}{1+b_A f^{\nu A}} + q_{B,sat} \frac{b_B f^{\nu B}}{1+b_B f^{\nu B}} \tag{S15}$$

Each of the integrals in eq (S13) can be evaluated analytically. For the dual-site Langmuir-Freundlich isotherm, for example, the integration yields for component *i*,

$$\begin{aligned} \Phi \equiv \frac{\pi A}{RT} &= \int_{f=0}^{P_i^0} \frac{q_i^0(f)}{f} df = \frac{q_{A,sat}}{\nu_A} \ln\left(1 + b_A \left(P_i^0\right)^{\nu_A}\right) + \frac{q_{B,sat}}{\nu_B} \ln\left(1 + b_B \left(P_i^0\right)^{\nu_B}\right); \\ \Phi \equiv \frac{\pi A}{RT} &= \int_{f=0}^{P_i^0} \frac{q_i^0(f)}{f} df = \frac{q_{A,sat}}{\nu_A} \ln\left(1 + b_A \left(\frac{f_i}{x_i}\right)^{\nu_A}\right) + \frac{q_{B,sat}}{\nu_B} \ln\left(1 + b_B \left(\frac{f_i}{x_i}\right)^{\nu_B}\right) \end{aligned} \tag{S16}$$

The right hand side of eq (S16) is a function of P_i^0. For multicomponent mixture adsorption, each of the equalities on the right hand side of Eq (S13) must be satisfied. These constraints may be solved using

a suitable equation solver, to yield the set of values of P_1^0, P_2^0, P_3^0,.. P_n^0, each of which satisfy eq (S13). The corresponding values of the integrals using these as upper limits of integration must yield the same value of Φ for each component; this ensures that the obtained solution is the correct one.

The adsorbed phase mole fractions x_i are then determined from

$$x_i = \frac{f_i}{P_i^0}; \quad i = 1, 2, ...n \tag{S17}$$

The applicability of eqs (S11) and (S17) mandates that all of the adsorption sites within the microporous material are equally accessible to each of the guest molecules, implying a homogeneous distribution of guest adsorbates within the pore landscape, with no preferential locations of any guest species. The circumstances in which this mandate is not fulfilled are highlighted in recent works.[25, 26, 28]

A key assumption of the IAST is that the adsorption enthalpies and surface areas of the adsorbed molecules do not change upon mixing. If the total mixture loading is q_t, the area covered by the adsorbed mixture is $\frac{A}{q_t}$ with units of m^2 (mol mixture)$^{-1}$. Therefore, the assumption of no surface area change due to mixture adsorption translates as $\frac{A}{q_t} = \frac{Ax_1}{q_1^0\left(P_1^0\right)} + \frac{Ax_2}{q_2^0\left(P_2^0\right)} + \cdots \frac{Ax_n}{q_n^0\left(P_n^0\right)}$; the total mixture loading is q_t is calculated from

$$q_t = q_1 + q_2 ... + q_n = \frac{1}{\frac{x_1}{q_1^0(P_1^0)} + \frac{x_2}{q_2^0(P_2^0)} + ... + \frac{x_n}{q_n^0(P_n^0)}} \tag{S18}$$

in which $q_1^0(P_1^0)$, $q_2^0(P_2^0)$,… $q_n^0(P_n^0)$ are determined from the unary isotherm fits, using the sorption pressures for each component P_1^0, P_2^0, P_3^0,.. P_n^0 that are available from the solutions to equations Eqs (S13), and (S16).

The occurrence of molecular clustering and hydrogen bonding should be expected to applicability of eq (S18) because the surface area occupied by a molecular cluster is different from that of each of the un-clustered guest molecules in the adsorbed phase.

The entire set of eqs (S11) to (S18) need to be solved numerically to obtain the loadings, q_i of the individual components in the mixture.

For the interpretation and analysis of the MD simulations for binary mixture diffusion in microporous host materials, the IAST calculation procedure has to be performed differently because in the MD simulations, the molar loadings q_1, and q_2 in the mixture are specified, and the partial fugacities in the bulk fluid mixture are not known *a priori*. Also in this case, the equalities in eq (S16) must be satisfied in conjunction with eq (S18). The entire set of eqs (S11) to (S18) need to be solved numerically to obtain the partial fugacities, f_i of the individual components in the mixture, that yield the same loadings as chosen in the MD simulations. In all of the calculations presented in this article, the set of equations were solved using an Excel macro that was developed for this specific purpose.

4.2 Selectivity for mixture adsorption

For *n*-component mixture adsorption, the selectivity of guest constituent *i* with respect to another guest constituent *j*, in that mixture, $S_{ads,ij}$, is defined by

$$S_{ads,ij} = \frac{q_i/q_j}{f_i/f_j} = \frac{x_i/f_i}{x_j/f_j} \tag{S19}$$

where q_i, q_j are the molar loadings of the constituents *i* and *j*, in the adsorbed phase in equilibrium with a bulk fluid phase mixture with partial fugacities f_i, f_j, and mole fractions $y_i = f_i/f_t$; $f_t = \left(\sum_{k=1}^{n} f_k\right)$. In view of eqs (S17), and (S18), we may re-write eq (S19) as the ratio of the sorption pressures

$$S_{ads,ij} = \frac{P_j^0}{P_i^0} \tag{S20}$$

Applying the restriction specified by eq (S13), it follows that $S_{ads,ij}$ is uniquely determined by the surface potential Φ. It is important to note that eq (S20) is valid irrespective of the total number of components in the mixture. Put another way, the presence of component 3 in the ternary mixture has no

influence of the adsorption selectivity $S_{ads,12} = \frac{P_2^0}{P_1^0}$ for the 1-2 pair, except insofar as the presence of component 3 alters the value of the surface potential Φ for the 1-2-3 mixture. Therefore, for an ideal adsorbed phase mixture, the presence of additional guest constituents, say species 3, 4, 5, etc. do not influence the selectivity of the 1-2 pair.

4.3 IAST model: 1-site Langmuir isotherms

The IAST procedure will be applied for binary mixture adsorption in which the unary isotherms are described by the 1-site Langmuir model in which the saturation capacities of components 1 and 2 are identical to each other, i.e. $q_{1,sat} = q_{2,sat} = q_{sat}$:

$$q_i^0\left(f\right) = q_{sat}\frac{b_i f}{1+b_i f} \tag{S21}$$

For unary adsorption, the surface potential for a 1-site Langmuir isotherm can be calculated analytically

$$\Phi \equiv \frac{\pi A}{RT} = q_{sat}\ln\left(1+bP^0\right) \tag{S22}$$

The objective is to determine the molar loadings, q_1, and q_2, in the adsorbed phase.

Performing the integration of eq (S13) results in an expression relating the sorption pressures P_i^0 of the two species

$$\begin{aligned}\Phi &\equiv \frac{\pi A}{RT} = q_{sat}\ln\left(1+b_1P_1^0\right) = q_{sat}\ln\left(1+b_2P_2^0\right)\\ b_1P_1^0 &= b_2P_2^0 = \exp\left(\frac{\pi A}{q_{sat}RT}\right)-1\end{aligned} \tag{S23}$$

The adsorbed phase mole fractions of component 1, and component 2 are given by eq (S17)

$$x_1 = \frac{f_1}{P_1^0};\quad x_2 = 1-x_1 = \frac{f_2}{P_2^0} \tag{S24}$$

Combining eqs (S23), and (S24):

$$\exp\left(\frac{\pi A}{q_{sat}RT}\right)-1 = b_1\frac{f_1}{x_1} = b_2\frac{f_2}{1-x_1} \tag{S25}$$

The adsorbed phase mole fractions can be determined

$$\frac{x_1}{x_2}=\frac{q_1}{q_2}=\frac{b_1f_1}{b_2f_2};\quad x_1=\frac{q_1}{q_t}=\frac{b_1f_1}{b_1f_1+b_2f_2};\quad x_2=\frac{q_2}{q_t}=\frac{b_2f_2}{b_1f_1+b_2f_2} \tag{S26}$$

Once x_1, and $x_2=1-x_1$ are determined, the sorption pressures can be calculated:

$$P_1^0=\frac{f_1}{x_1};\quad P_2^0=\frac{f_2}{x_2}=\frac{f_2}{1-x_1} \tag{S27}$$

From eqs (S23), and (S27) we get

$$\begin{aligned} b_iP_1^0&=\frac{b_1f_1}{x_1}=b_2P_2^0=\frac{b_2f_2}{x_2}=b_1f_1+b_2f_2\\ 1+b_iP_1^0&=1+b_2P_2^0=1+b_1f_1+b_2f_2\end{aligned} \tag{S28}$$

Combining eqs (S23), and (S28) we obtain the following explicit expression for the surface potential

$$\Phi=q_{sat}\ln\left(1+b_1f_1+b_2f_2\right) \tag{S29}$$

The total amount adsorbed, $q_t=q_1+q_2$ can be calculated from Eq (S18)

$$q_t=q_1+q_2=q_{sat}\frac{b_1P_1^0}{1+b_1P_1^0}=q_{sat}\frac{b_2P_2^0}{1+b_2P_2^0}=q_{sat}\frac{b_1f_1+b_2f_2}{1+b_1f_1+b_2f_2} \tag{S30}$$

Combining eqs (S26), and (S30) we obtain the following explicit expressions for the component loadings, and fractional occupancies

$$\theta_1=\frac{q_1}{q_{sat}}=\frac{b_1f_1}{1+b_1f_1+b_2f_2};\quad \theta_2=\frac{q_2}{q_{sat}}=\frac{b_2f_2}{1+b_1f_1+b_2f_2} \tag{S31}$$

Eq (S31) is commonly referred to as the mixed-gas Langmuir model.

From eqs (S23), (S30), and (S31) we derive the following expression for the total occupancy of the mixture

$$\theta=\theta_1+\theta_2=\frac{q_t}{q_{sat}}=1-\exp\left(-\frac{\Phi}{q_{sat}}\right)=\frac{b_1f_1+b_2f_2}{1+b_1f_1+b_2f_2} \tag{S32}$$

For *unary* adsorption of component *i*, say, $f_i = P_i^0$, the occupancy of component 1 is

$$\theta_i = 1 - \exp\left(-\frac{\Phi}{q_{i,sat}}\right) = \frac{b_i f_i}{1 + b_i f_i}; \quad \text{unary adsorption of species i} \tag{S33}$$

From eqs (S32), and (S33) we may also conclude the *occupancy* may be considered to be the appropriate *proxy* for the spreading pressure. The conclusion that we draw from the foregoing analysis is that the equalities of spreading pressures for unary adsorption of component 1, unary adsorption of component 2, and binary 1-2 mixture adsorption also implies the corresponding equalities of the corresponding *occupancies* for unary adsorption of component 1, unary adsorption of component 2, and binary 1-2 mixture adsorption.

For *n*-component mixtures, eq (S29) may be generalized to

$$\Phi = q_{sat} \ln\left(1 + \sum_{i=1}^{n} b_i f_i\right) \tag{S34}$$

4.4 Generalized expression for fractional occupancy

From knowledge of the surface potential, Φ, the fractional occupancy for *n*-component mixture adsorption is then calculated using

$$\theta = 1 - \exp\left(-\frac{\pi A}{q_{sat,mix} RT}\right) = 1 - \exp\left(-\frac{\Phi}{q_{sat,mix}}\right) \tag{S35}$$

For an *n*-component mixture, the saturation capacity $q_{sat,mix}$ is calculated from the saturation capacities of the constituent guests

$$q_{sat,mix} = \frac{1}{\frac{x_1}{q_{1,sat}} + \frac{x_2}{q_{2,sat}} + \ldots \frac{x_n}{q_{n,sat}}}; \quad q_{i,sat} = q_{i,A,sat} + q_{i,B,sat}; \quad i = 1,2 \ldots n \tag{S36}$$

where

$$x_i = \frac{q_i}{q_1 + q_2 + \ldots q_n}; \quad i = 1,2,\ldots n \tag{S37}$$

are the mole fractions in the adsorbed mixture. For binary mixtures, eq (S35) simplifies to yield

$$q_{sat,mix} = \frac{1}{\frac{x_1}{q_{1,sat}} + \frac{x_2}{q_{2,sat}}}.$$

The fundamental justification of Eq (S36) is provided by invoking eq (S18).

Eq (S35) is the appropriate generalization of Eq (S32), derived in the following section for the mixed-gas Langmuir model. It is also to be noted that eq (15) of our earlier publication[29] has a typographical error in the calculation of $q_{sat,mix}$; the correct form is given by eq (S36).

5 Molecular Dynamics (MD) Simulation Methodology

Diffusion is simulated using Newton's equations of motion until the system properties, on average, no longer change in time. The Verlet algorithm is used for time integration. A time step of 1 fs was used in all simulations. For each simulation, *initializing* CBMC moves are used to place the molecules in the domain, minimizing the energy. Next, follows an *equilibration* stage. These are essentially the same as the production cycles, only the statistics are not yet taken into account. This removes any initial large disturbances in the system that do not affect statistics on molecular displacements. After a fixed number of initialization and equilibrium steps, the MD simulation *production* cycles start. For every cycle, the statistics for determining the mean square displacements (MSDs) are updated. The MSDs are determined for time intervals ranging from 2 fs to 1 ns. In order to do this, an order-*N* algorithm, as detailed in Chapter 4 of Frenkel and Smit[18] is implemented. The Nosé-Hoover thermostat is applied to all the diffusing particles. In the MD simulations the cations were allowed to move within the framework and both Lennard-Jones and Coulombic interactions are taken into consideration; see schematic sketch in Figure S9.

For all the MD simulation results presented in this article, the DLPOLY code[30] was used along with the force field implementation as described in the previous section. DL_POLY is a molecular dynamics simulation package written by W. Smith, T.R. Forester and I.T. Todorov and has been obtained from CCLRCs Daresbury Laboratory via the website.[30]

The MD simulations were carried out for a variety of loadings within the various structures. All simulations were carried out on the LISA clusters of PCs equipped with Intel Xeon processors running at 3.4 GHz on the Linux operating system.[31] Each MD simulation, for a specified loading, was run for a time duration that is sufficiently long to obtain reliable statistics for determination of the diffusivities. In several cases the campaigns were replicated and the results averaged.

Molecular Dynamics (MD) Simulation Methodology

The self-diffusivities $D_{i,self}$ are computed from MD simulations by analyzing the mean square displacement of each species i for each coordinate direction

$$D_{i,self} = \frac{1}{2n_i} \lim_{\Delta t \to \infty} \frac{1}{\Delta t} \left\langle \left(\sum_{l=1}^{n_i} \left(\mathbf{r}_{l,i}(t + \Delta t) - \mathbf{r}_{l,i}(t) \right)^2 \right) \right\rangle \tag{S38}$$

In this expression n_i represents the number of molecules of species i, and $\mathbf{r}_{l,i}(t)$ is the position of molecule l of species i at any time t.

For three-dimensional pore networks (e.g. FAU, NaY, NaX) the arithmetic average of the diffusivities in the three coordinate directions were used in further analysis and reported.

MD simulations were performed to determine the self-diffusivities $D_{i,self}$ in a variety of equimolar $(q_1 = q_2)$ binary and ternary $(q_1 = q_2 = q_3)$ mixtures. In a few cases, the MD simulations were performed for mixtures in which the total loading $q_t = q_1 + q_2$ was held constant and the mole fraction of the adsorbed phase mixture, $x_1 = \frac{q_1}{q_1 + q_2}$ was varied from 0 to 1. All MD simulations reported in this work were conducted at a temperature T = 300 K.

For the interpretation and analysis of the MD simulations for mixture diffusion in microporous host materials, the IAST calculation procedure needs to be performed differently because in the MD simulations, the molar loadings q_i in the mixture are specified, and the partial fugacities in the bulk fluid mixture are not known *a priori*. Also, in this case, the equalities in eq (S13) must be satisfied in conjunction with eq (S16). The entire set of eqs (S11) to (S18) need to be solved numerically to obtain the partial fugacities, f_i of the individual components in the mixture, that yield the same loadings as chosen in the MD simulations. The IAST calculations also determine the surface potential Φ. In all of the calculations presented in this article, the set of equations were solved using an Excel macro that was developed for this specific purpose.

6 Diffusion in Microporous Crystalline Materials

6.1 The Maxwell-Stefan (M-S) description of diffusion

Within micro-porous crystalline materials, such as zeolites, metal-organic frameworks (MOFs), and zeolitic imidazolate frameworks (ZIFs), the guest molecules exist in the adsorbed phase. The Maxwell-Stefan (M-S) equations for *n*-component diffusion in porous materials is applied in the following manner[10, 11, 32-37]

$$-\rho \frac{q_i}{RT}\frac{\partial \mu_i}{\partial r} = \sum_{\substack{j=1 \\ j\neq i}}^{n} \frac{x_j N_i - x_i N_j}{Đ_{ij}} + \frac{N_i}{Đ_i}; \qquad i = 1, 2, ..n \tag{S39}$$

where ρ is the framework density with units of kg m^{-3}, q_i is the molar loading of adsorbate, and the adsorbed phase mole fractions are $x_i = q_i / q_t$ where q_t is the *total* mixture loading $q_t = \sum_{i=1}^{n} q_i$. The fluxes N_i in equations (S39) are defined in terms of the moles transported per m^2 of the *total surface of crystalline material*.

An important, persuasive, argument for the use of the M-S formulation for mixture diffusion is that the M-S diffusivity $Đ_i$ in mixtures can be estimated using information on the loading dependence of the corresponding unary diffusivity values, provided the comparison is made at the same value of the adsorption potential, calculated from IAST using eq (S13), or its proxy the occupancy, θ, calculated using eqs (S35), (S36), (S37). Essentially this implies that the M-S diffusivity $Đ_i$ can be estimated from experimental data on *unary* diffusion in the porous material.

The *exchange coefficients* $Đ_{ij}$, defined by the first right member of eq (S39), are introduced to quantify the coupling between species diffusion. At the molecular level, the $Đ_{ij}$ reflect how the facility for transport of species *i correlates* with that of species *j*.

The Maxwell-Stefan diffusion formulation is consistent with the theory of irreversible thermodynamics. The Onsager Reciprocal Relations imply that the M-S pair diffusivities are symmetric

$$Đ_{ij} = Đ_{ji} \tag{S40}$$

6.2 Thermodynamic correction factors

At thermodynamic equilibrium, the chemical potential of component *i* in the bulk fluid mixture equals the chemical potential of that component in the adsorbed phase. For the bulk fluid phase mixture we have

$$\frac{1}{RT}\frac{\partial \mu_i}{\partial r} = \frac{\partial \ln f_i}{\partial r} = \frac{1}{f_i}\frac{\partial f_i}{\partial r}; \qquad i = 1, 2, ..n \tag{S41}$$

The chemical potential gradients $\partial \mu_i / \partial r$ can be related to the gradients of the molar loadings, q_i, by defining thermodynamic correction factors Γ_{ij}

$$\frac{q_i}{RT}\frac{\partial \mu_i}{\partial r} = \sum_{j=1}^{n} \Gamma_{ij}\frac{\partial q_j}{\partial r}; \quad \Gamma_{ij} = \frac{q_i}{f_i}\frac{\partial f_i}{\partial q_j}; \qquad i, j = 1, ...n \tag{S42}$$

The thermodynamic correction factors Γ_{ij} can be calculated by differentiation of the model describing mixture adsorption equilibrium. Generally speaking, the Ideal Adsorbed Solution Theory (IAST) of Myers and Prausnitz[22] is the preferred method for estimation of mixture adsorption equilibrium. In the special case in which the unary isotherms are described for every component with the 1-site Langmuir model with equal saturation capacities, the mixed-gas Langmuir model

$$\frac{q_i}{q_{sat}} = \theta_i = \frac{b_i f_i}{1 + \sum_{i=1}^{n} b_i f_i}; \quad i = 1, 2, ...n \tag{S43}$$

Is derivable from the IAST. Analytic differentiation of eq (S43) yields

$$\Gamma_{ij} = \delta_{ij} + \left(\frac{\theta_i}{\theta_V}\right); \qquad i, j = 1, 2 \ldots n \tag{S44}$$

where the fractional vacancy θ_V is defined as

$$\theta_V = 1 - \theta_t = 1 - \sum_{i=1}^{n} \theta_i \tag{S45}$$

The elements of the matrix of thermodynamic factors Γ_{ij} can be calculated explicitly from information on the component loadings q_i in the adsorbed phase; this is the persuasive advantage of the use of the

mixed-gas Langmuir model. By contrast, the IAST does not allow the calculation of Γ_{ij} explicitly from knowledge on the component loadings q_i in the adsorbed phase; a numerical procedure is required.

6.3 M-S formulation for binary mixture diffusion

For binary mixture diffusion inside microporous crystalline materials the Maxwell-Stefan equations (S39) are written

$$\begin{aligned} -\rho\frac{q_1}{RT}\frac{\partial\mu_1}{\partial r} &= \frac{x_2N_1 - x_1N_2}{Đ_{12}} + \frac{N_1}{Đ_1} \\ -\rho\frac{q_2}{RT}\frac{\partial\mu_2}{\partial r} &= \frac{x_1N_2 - x_2N_1}{Đ_{12}} + \frac{N_2}{Đ_2} \end{aligned} \tag{S46}$$

The first members on the right hand side of eq (S46) are required to quantify slowing-down effects that characterize binary mixture diffusion.[10, 11, 38] There is no experimental technique for direct determination of the exchange coefficients $Đ_{12}$, that quantify molecule-molecule interactions; the $Đ_{12}$ are accessible from MD simulations.

In two-dimensional matrix notation, eq (S42) take the form

$$-\begin{pmatrix} \frac{q_1}{RT}\frac{\partial\mu_1}{\partial r} \\ \frac{q_2}{RT}\frac{\partial\mu_2}{\partial r} \end{pmatrix} = [\Gamma]\begin{pmatrix} \frac{\partial q_1}{\partial r} \\ \frac{\partial q_2}{\partial r} \end{pmatrix} \tag{S47}$$

For the mixed-gas Langmuir model, eq (S43), we can derive simple analytic expressions for the four elements of the matrix of thermodynamic factors:[39]

$$\begin{bmatrix} \Gamma_{11} & \Gamma_{12} \\ \Gamma_{21} & \Gamma_{22} \end{bmatrix} = \frac{1}{1-\theta_1-\theta_2}\begin{bmatrix} 1-\theta_2 & \theta_1 \\ \theta_2 & 1-\theta_1 \end{bmatrix} \tag{S48}$$

where the fractional occupancies, θ_i, are defined by eq (S43).

Let us define the square matrix [B]

$$[B] = \begin{bmatrix} \frac{1}{Đ_1} + \frac{x_2}{Đ_{12}} & -\frac{x_1}{Đ_{12}} \\ -\frac{x_2}{Đ_{12}} & \frac{1}{Đ_2} + \frac{x_1}{Đ_{12}} \end{bmatrix}; \quad [B]^{-1} = \frac{1}{1 + \frac{x_1Đ_2}{Đ_{12}} + \frac{x_2Đ_1}{Đ_{12}}}\begin{bmatrix} Đ_1\left(1 + \frac{x_1Đ_2}{Đ_{12}}\right) & \frac{x_1Đ_1Đ_2}{Đ_{12}} \\ \frac{x_2Đ_1Đ_2}{Đ_{12}} & Đ_2\left(1 + \frac{x_2Đ_1}{Đ_{12}}\right) \end{bmatrix} \tag{S49}$$

In proceeding further, it is convenient to define a 2×2 dimensional square matrix $[\Lambda]$:

$$[\Lambda]=\begin{bmatrix} \frac{1}{Đ_1}+\frac{x_2}{Đ_{12}} & -\frac{x_1}{Đ_{12}} \\ -\frac{x_2}{Đ_{12}} & \frac{1}{Đ_2}+\frac{x_1}{Đ_{12}} \end{bmatrix}^{-1} = \frac{1}{1+\frac{x_1 Đ_2}{Đ_{12}}+\frac{x_2 Đ_1}{Đ_{12}}} \begin{bmatrix} Đ_1\left(1+\frac{x_1 Đ_2}{Đ_{12}}\right) & \frac{x_1 Đ_1 Đ_2}{Đ_{12}} \\ \frac{x_2 Đ_1 Đ_2}{Đ_{12}} & Đ_2\left(1+\frac{x_2 Đ_1}{Đ_{12}}\right) \end{bmatrix} \tag{S50}$$

The elements of the Maxwell-Stefan matrix Λ_{ij} are accessible from MD simulations [7, 10, 29, 34, 37, 40] by monitoring the individual molecular displacements

$$\Lambda_{ij} = \frac{1}{2}\lim_{\Delta t\to\infty}\frac{1}{n_j}\frac{1}{\Delta t}\left\langle\left(\sum_{l=1}^{n_i}\left(\mathbf{r}_{l,i}(t+\Delta t)-\mathbf{r}_{l,i}(t)\right)\right)\bullet\left(\sum_{k=1}^{n_j}\left(\mathbf{r}_{k,j}(t+\Delta t)-\mathbf{r}_{k,j}(t)\right)\right)\right\rangle \tag{S51}$$

In this expression n_i and n_j represent the number of molecules of species *i* and *j* respectively, and $\mathbf{r}_{l,i}(t)$ is the position of molecule *l* of species *i* at any time *t*. In this context we note a typographical error in equation (S51) as printed in earlier publications[8, 41, 42] wherein the denominator in the right member had n_i instead of n_j. The simulation results presented in these publications are, however, correct as the proper formula given in equation (S51) was used.

Compliance with the Onsager Reciprocal Relations demands

$$n_j\Lambda_{ij} = n_i\Lambda_{ji}; \quad i,j=1,2,....n \tag{S52}$$

Eq (S46) can be re-cast into 2-dimensional matrix notation

$$(N) = -\rho[\Lambda][\Gamma]\frac{\partial(q)}{\partial r};$$

$$\begin{pmatrix} N_1 \\ N_2 \end{pmatrix} = -\frac{\rho}{1+\frac{x_1 Đ_2}{Đ_{12}}+\frac{x_2 Đ_1}{Đ_{12}}} \begin{bmatrix} Đ_1\left(1+\frac{x_1 Đ_2}{Đ_{12}}\right) & \frac{x_1 Đ_1 Đ_2}{Đ_{12}} \\ \frac{x_2 Đ_1 Đ_2}{Đ_{12}} & Đ_2\left(1+\frac{x_2 Đ_1}{Đ_{12}}\right) \end{bmatrix} \begin{bmatrix} \Gamma_{11} & \Gamma_{12} \\ \Gamma_{21} & \Gamma_{22} \end{bmatrix} \begin{pmatrix} \frac{\partial q_1}{\partial r} \\ \frac{\partial q_2}{\partial r} \end{pmatrix} \tag{S53}$$

The elements of $[B]$ can be obtained by inverting the matrix $[\Lambda]$:

$$\begin{bmatrix} B_{11} & B_{12} \\ B_{21} & B_{22} \end{bmatrix} = \begin{bmatrix} \frac{1}{Đ_1} + \frac{x_2}{Đ_{12}} & -\frac{x_1}{Đ_{12}} \\ -\frac{x_2}{Đ_{12}} & \frac{1}{Đ_2} + \frac{x_1}{Đ_{12}} \end{bmatrix} = [\Lambda]^{-1} \quad \text{(S54)}$$

The three M-S diffusivities can be backed-out from the four elements $\begin{bmatrix} B_{11} & B_{12} \\ B_{21} & B_{22} \end{bmatrix}$ using

$$Đ_{12} = -\frac{x_1}{B_{12}} = -\frac{x_2}{B_{21}}; \quad Đ_1 = \frac{1}{B_{11} + B_{21}}; \quad Đ_2 = \frac{1}{B_{22} + B_{12}} \quad \text{(S55)}$$

Figure S12a,b,c,d present MD simulated values of the M-S diffusivities, $Đ_1, Đ_2$, self-diffusivities, $D_{1,self}, D_{2,self}$, and $\Lambda_{11}, \Lambda_{12}, \Lambda_{21}, \Lambda_{22}$ for binary Ne(1)/Ar(2) mixtures in all-silica FAU zeolite at 300 K. Also plotted in Figure S12a are the diffusivities in the constituent unaries, as function of the molar loadings. Two different MD campaigns were conducted: (i) equimolar $q_1 = q_2$ mixtures, and (ii) mixtures for which $\Theta_t = \Theta_1 + \Theta_2$ = 100 uc^{-1}. We note that the $\Lambda_{11}, \Lambda_{12}, \Lambda_{21}, \Lambda_{22}$, along with the M-S diffusivities, $Đ_1, Đ_2$ are strongly dependent on the total mixture loadings. Also, at constant mixture loading $\Theta_t = \Theta_1 + \Theta_2$ = 100 uc^{-1}, the diffusivities are strongly dependent on the mole fraction of component 1 in the mixture, $x_1 = \frac{\Theta_1}{\Theta_t}$. In Figure S12e the M-S diffusivities, $Đ_1, Đ_2$ are plotted as function of the pore occupancy θ, calculated using eq (S35). The fractional occupancy is a proxy for the surface potential, Φ. We note that the constituent M-S diffusivities, $Đ_1, Đ_2$ have practically the same values as the corresponding unary diffusivities, when compared at the same occupancy irrespective of the total mixture loading and the mixture composition; further evidence is provided in our earlier publications.[29, 40] From Figure S12f we note the component self-diffusivities $D_{1,self}, D_{2,self}$ for binary Ne(1)/Ar(2) mixtures in all-silica FAU zeolite have practically the same values as the corresponding unary diffusivities, when compared at the same occupancy θ.

Precisely analogous results are realized for binary CO_2(1)/Ar(2) mixtures in all-silica FAU zeolite; see Figure S13, The data show that component M-S diffusivities, $Đ_1, Đ_2$ and self-diffusivities $D_{1,self}, D_{2,self}$

in binary mixtures have practically the same values as the corresponding unary diffusivities, when compared at the same occupancy, θ, irrespective of the total mixture loading and the mixture composition.

The above findings regarding the unique θ-dependence of component M-S diffusivities, $Đ_1, Đ_2$ and self-diffusivities $D_{1,self}, D_{2,self}$ in binary mixtures and in the constituent unaries are confirmed for other guest/host combinations. As illustration, we present data for:

CO_2(1)/Ne(2) mixtures in FAU (all-silica); see Figure S14,

CO_2(1)/CH_4(2) mixtures in FAU (all-silica); see Figure S15.

CO_2(1)/N_2(2) mixtures in FAU (all-silica); see Figure S16.

CH_4(1)/C_2H_6(2) mixtures in FAU (all-silica) zeolite; see Figure S17.

CH_4(1)/C_3H_8(2) mixtures in FAU (all-silica) zeolite; see Figure S18.

CH_4(1)/Ar(2) mixtures in FAU (all-silica) zeolite; see Figure S19.

CH_4(1)/C_2H_6(2) mixtures in NaY zeolite, see Figure S20.

CH_4(1)/C_3H_8(2) mixtures in NaY zeolite, see Figure S21.

CO_2(1)/CH_4(2) mixtures in NaY; see Figure S22.

CO_2(1)/N_2(2) mixtures in NaY; see Figure S23.

CH_4(1)/C_2H_6(2) mixtures in NaX (106 Si, 86 Al, 86 Na^+, Si/Al=1.23) zeolite, see Figure S24.

CH_4(1)/C_3H_8(2) mixtures in NaX (106 Si, 86 Al, 86 Na^+, Si/Al=1.23) zeolite, see Figure S25.

CO_2(1)/CH_4(2) mixtures in NaX; see Figure S26.

CO_2(1)/N_2(2) mixtures in NaX; see Figure S27.

For CO_2(1)/H_2(2) and CH_4(1)/H_2(2) mixture diffusion, the correlation effects are very strong and the self-diffusivities in mixtures are lowered below the values of the unary diffusivities for hydrogen:

CO_2(1)/H_2(2) mixtures in all-silica FAU zeolite; see Figure S28

CH_4(1)/H_2(2) mixtures in all-silica FAU zeolite; see Figure S29

CO_2(1)/H_2(2) mixtures in NaY zeolite; see Figure S30

$CH_4(1)/H_2(2)$ mixtures in NaY zeolite; see Figure S31

$CO_2(1)/H_2(2)$ mixtures in NaX zeolite; see Figure S32

$CH_4(1)/H_2(2)$ mixtures in NaX zeolite; see Figure S33

In this article, we exploit the uniqueness of the dependence of component self-diffusivities as functions of the occupancy θ, that serves as a proxy for the surface potential, Φ.

6.4 Analytic expressions for self-diffusivities

Applying eqs (S46) to a binary mixture of two components that are identical; one is tagged and the other is untagged, we derive the following expressions for the self-diffusivities[11]

$$\frac{1}{D_{1,self}} = \frac{1}{Đ_1} + \frac{x_1}{Đ_{11}} + \frac{x_2}{Đ_{12}}; \quad \frac{1}{D_{2,self}} = \frac{1}{Đ_2} + \frac{x_2}{Đ_{22}} + \frac{x_1}{Đ_{12}} \tag{S56}$$

6.5 Correlation effects for M-S diffusivities

Of the four all-silica zeolites investigated in this work, correlation effects are of importance in MFI and FAU. For values of $Đ_1/Đ_{12} \to 0$, and $Đ_2/Đ_{12} \to 0$, the contribution of the first right member of M-S Eq (S46) can be ignored and correlations can be considered to be of negligible importance; we derive

$$\frac{Đ_1}{Đ_{12}} \to 0; \quad \frac{Đ_2}{Đ_{12}} \to 0; \quad \begin{bmatrix} \Lambda_{11} & \Lambda_{12} \\ \Lambda_{21} & \Lambda_{22} \end{bmatrix} \to \begin{bmatrix} Đ_1 & 0 \\ 0 & Đ_2 \end{bmatrix}$$
$$\begin{pmatrix} N_1 \\ N_2 \end{pmatrix} = -\rho \begin{bmatrix} Đ_1 & 0 \\ 0 & Đ_2 \end{bmatrix} \begin{bmatrix} \Gamma_{11} & \Gamma_{12} \\ \Gamma_{21} & \Gamma_{22} \end{bmatrix} \begin{pmatrix} \frac{\partial q_1}{\partial r} \\ \frac{\partial q_2}{\partial r} \end{pmatrix} \tag{S57}$$

Eq (S57) is valid, as a first approximation, for diffusion in cage-type zeolites with 8-ring windows (CHA, DDR, LTA, ERI) and ZIF-8.[7-9, 34, 43-46] When correlation effects are negligible, the diffusional coupling effects are solely traceable to mixture adsorption thermodynamics, embodied in the matrix $[\Gamma]$. When correlations are negligible, we obtain the self-diffusivities can be identified with the Maxwell-Stefan diffusivities.

$$Đ_1/Đ_{12} \to 0; \quad Đ_2/Đ_{12} \to 0; \quad D_{1,self} = Đ_1; \quad D_{2,self} = Đ_2 \tag{S58}$$

6.6 Membrane permeabilities and permeation selectivities

For any given application, the separation performance of a microporous membrane is characterized by two metrics: permeability and permeation selectivity. The permeability of component *i* is defined as

$$\Pi_i = \frac{N_i}{\Delta f_i/\delta} \tag{S59}$$

where N_i is the permeation flux and $\Delta f_i = f_i - f_{i\delta}$ is the difference in the partial fugacities between the upstream (f_i) and downstream $(f_{i\delta})$ faces of the membrane layer of thickness δ. If the gas mixtures may be considered to be thermodynamically ideal, the partial fugacities may be replaced by the corresponding partial pressures p_i. Often, the component permeances, defined by $N_i/\Delta f_i \equiv \Pi_i/\delta$, are more easily accessible from experiments because of uncertainties in the precise values of the membrane thickness, δ. If the downstream compartments of the membrane are evacuated we may approximate the concentration differences as follows

$$\frac{\Delta q_1}{\delta} \approx \frac{q_1}{\delta}; \quad \frac{\Delta q_2}{\delta} \approx \frac{q_2}{\delta} \tag{S60}$$

where q_i are the molar loadings in equilibrium with the partial fugacities q_i in the upstream face of the membrane. The permeability can be determined from MD simulations by using the following expression[6]

$$\Pi_i = \frac{\rho D_{i,self} q_i}{f_i} \tag{S61}$$

where ρ is the crystal framework density. In SI units, the permeability has the units mol m m^{-2} s^{-1} Pa^{-1}. The more commonly used engineering unit for permeability is the Barrer expressed in cm^3 (STP) cm cm^{-2} s^{-1} $(cm\ Hg)^{-1}$. To convert to the commonly used engineering units of Barrers we divide the value in mol m m^{-2} s^{-1} Pa^{-1} by 3.348×10^{-16}.

Let us further assume that the M-S diffusivities vary with the fractional occupancies according to

$$Đ_i = Đ_i(0)(1-\theta) \tag{S62}$$

where $Đ_i(0)$ are the zero-loading diffusivities. For multicomponent Langmuir isotherm, the M-S equations for binary mixtures can be integrated analytically to obtain [47]

$$\begin{aligned} N_1 &= \rho\Lambda_{11}\frac{q_1}{\delta} + \rho\Lambda_{12}\frac{q_2}{\delta} \\ N_2 &= \rho\Lambda_{21}\frac{q_1}{\delta} + \rho\Lambda_{22}\frac{q_2}{\delta} \end{aligned} \tag{S63}$$

where the elements of the matrix $[\Lambda]$ are evaluated at the upstream loadings. It is convenient to define the effective diffusivities, $D_{i,eff}$,

$$\begin{aligned} D_{1,eff} &= \Lambda_{11} + \Lambda_{12}\frac{q_2}{q_1} \\ D_{2,eff} &= \Lambda_{22} + \Lambda_{21}\frac{q_1}{q_2} \end{aligned} \tag{S64}$$

From eqs (S60), (S62), (S63), (S64) we derive the following explicit expressions

$$\begin{aligned} D_{1,eff} &= \Lambda_{11} + \Lambda_{12}\frac{q_2}{q_1} = \frac{Đ_1\left(1+\frac{x_1Đ_2}{Đ_{12}}\right)}{1+\frac{x_1Đ_2}{Đ_{12}}+\frac{x_2Đ_1}{Đ_{12}}} + \frac{Đ_1\frac{x_1Đ_2}{Đ_{12}}}{1+\frac{x_1Đ_2}{Đ_{12}}+\frac{x_2Đ_1}{Đ_{12}}}\frac{q_2}{q_1} = \frac{Đ_1\left(1+\frac{Đ_2}{Đ_{12}}\right)}{1+\frac{x_1Đ_2}{Đ_{12}}+\frac{x_2Đ_1}{Đ_{12}}} \\ D_{2,eff} &= \Lambda_{22} + \Lambda_{21}\frac{q_1}{q_2} = \frac{Đ_2\left(1+\frac{x_2Đ_1}{Đ_{12}}\right)}{1+\frac{x_1Đ_2}{Đ_{12}}+\frac{x_2Đ_1}{Đ_{12}}} + \frac{Đ_2\frac{x_2Đ_1}{Đ_{12}}}{1+\frac{x_1Đ_2}{Đ_{12}}+\frac{x_2Đ_1}{Đ_{12}}}\frac{q_1}{q_2} = \frac{Đ_2\left(1+\frac{Đ_1}{Đ_{12}}\right)}{1+\frac{x_1Đ_2}{Đ_{12}}+\frac{x_2Đ_1}{Đ_{12}}} \end{aligned} \tag{S65}$$

For separation of a binary mixture, the permeation selectivity is

$$S_{perm} = \frac{N_1/f_1}{N_2/f_2} \tag{S66}$$

In view of eqs (S63), (S64), and (S65) the permeation selectivity can be expressed as

$$S_{perm} = \frac{N_1/f_1}{N_2/f_2} = \frac{D_{1,eff}}{D_{2,eff}}\frac{q_1/f_1}{q_2/f_2} \tag{S67}$$

For separation of a binary mixture, the diffusion selectivity can be defined as follows

$$S_{diff} = \frac{D_{1,eff}}{D_{2,eff}} \tag{S68}$$

From eqs (S65) and (S68) we get

$$\frac{D_{1,eff}}{D_{2,eff}} = \frac{\left(\frac{1}{Đ_2}+\frac{1}{Đ_{12}}\right)}{\left(\frac{1}{Đ_1}+\frac{1}{Đ_{12}}\right)} = \frac{Đ_1}{Đ_2}\frac{\left(1+\frac{Đ_2}{Đ_{12}}\right)}{\left(1+\frac{Đ_1}{Đ_{12}}\right)} \tag{S69}$$

We now show that S_{diff} can be approximated by the ratio of self-diffusivities. From eqs (S56) the ratio of self-diffusivities can be written as follows

$$\frac{D_{1,self}}{D_{2,self}} = \frac{\frac{1}{Đ_2}+\frac{x_2}{Đ_{22}}+\frac{x_1}{Đ_{12}}}{\frac{1}{Đ_1}+\frac{x_1}{Đ_{11}}+\frac{x_2}{Đ_{12}}} = \frac{Đ_1}{Đ_2}\frac{1+\frac{x_2 Đ_2}{Đ_{22}}+\frac{x_1 Đ_2}{Đ_{12}}}{1+\frac{x_1 Đ_1}{Đ_{11}}+\frac{x_2 Đ_1}{Đ_{12}}} \tag{S70}$$

In view of the Vignes interpolation formula [10]

$$Đ_{12} = \left(Đ_{11}\right)^{x_1}\left(Đ_{22}\right)^{x_2} \tag{S71}$$

we conclude that the ratio of the self-diffusivities is a good approximation for the diffusion selectivities

$$\frac{D_{1,self}}{D_{2,self}} \approx \frac{Đ_1}{Đ_2}\frac{1+\frac{Đ_2}{Đ_{12}}}{1+\frac{Đ_1}{Đ_{12}}} = \frac{D_{1,eff}}{D_{2,eff}} = S_{diff} \tag{S72}$$

As conformation of the accuracy of eq (S72), Figure S34 presents MD simulation data for (a) CO_2/CH_4, (b) CO_2/N_2, and (c) CH_4/C_2H_6 diffusion selectivities, S_{diff}, for mixtures determined from equimolar binary $\left(q_1 = q_2\right)$ mixtures in all-silica FAU zeolite at 300 K, plotted as function of the surface potential Φ. The diffusion selectivities calculated from $\frac{D_{1,self}}{D_{2,self}}$ agree reasonably well with those calculated from $\frac{D_{1,eff}}{D_{2,eff}}$.

In view of eq (S19), the adsorption selectivity for the binary 1-2 mixture is

$$S_{ads} = \frac{q_1/q_2}{f_1/f_2} = \frac{x_1/f_1}{x_2/f_2} = \frac{P_2^0\gamma_2}{P_1^0\gamma_1} \tag{S73}$$

Therefore, the permeation selectivity is the product of the adsorption selectivity and the diffusion selectivity

$$S_{perm} = S_{ads} \times S_{diff} \tag{S74}$$

6.7 List of Figures for Diffusion in Microporous Crystalline Materials

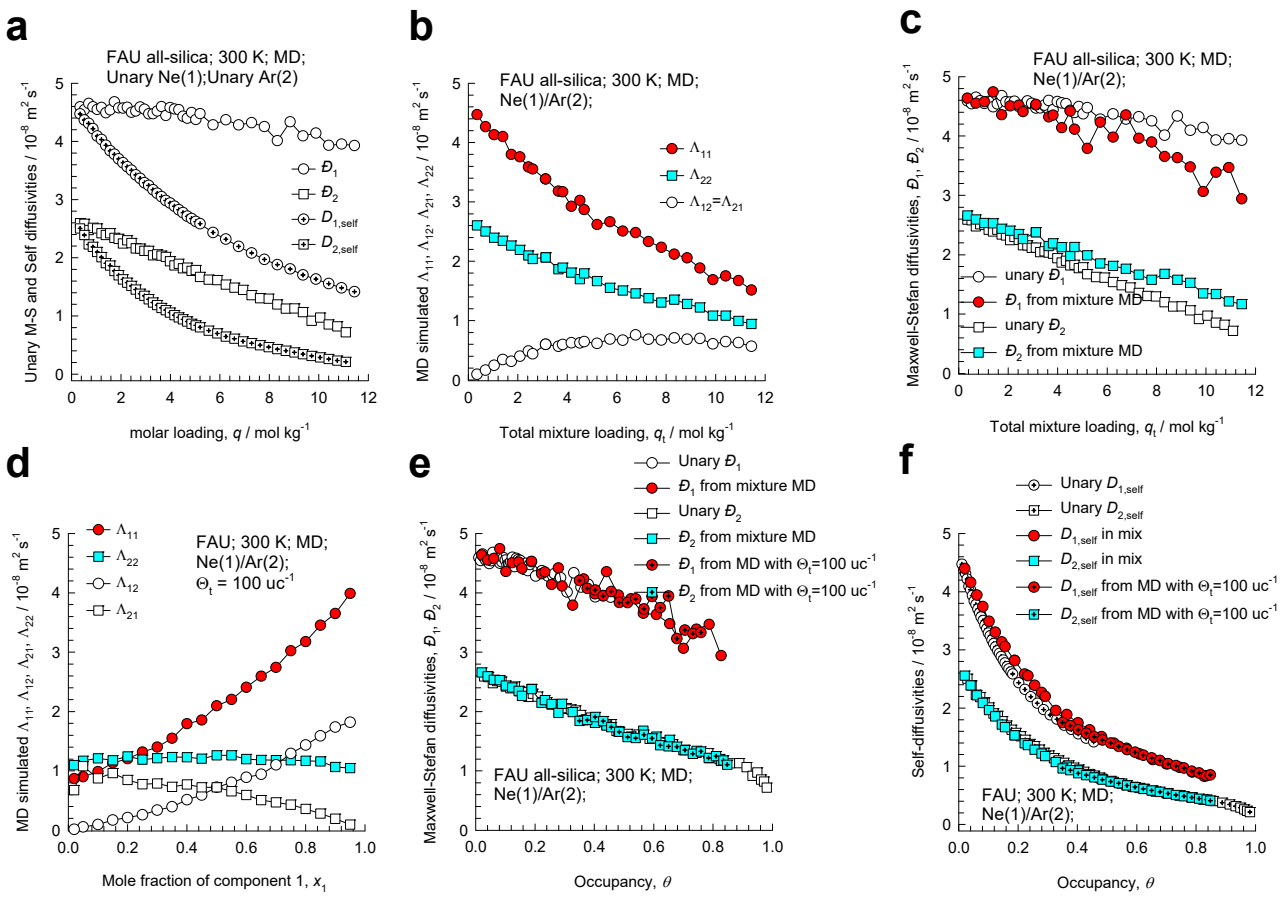

Figure S12. (a, b, c, d) MD simulated values of the M-S diffusivities, $Đ_1, Đ_2$, self-diffusivities, $D_{1,self}, D_{2,self}$, and $\Lambda_{11}, \Lambda_{12}, \Lambda_{21}, \Lambda_{22}$ for binary Ne(1)/Ar(2) mixtures in FAU zeolite at 300 K. Two different MD campaigns were conducted: (i) equimolar $q_1 = q_2$ mixtures, and (ii) mixtures for which $\Theta_t = \Theta_1 + \Theta_2 = 100$ uc^{-1}. In (e, f) the M-S diffusivities, $Đ_1, Đ_2$, and self-diffusivities, $D_{1,self}, D_{2,self}$, are plotted as a function of the occupancy θ.

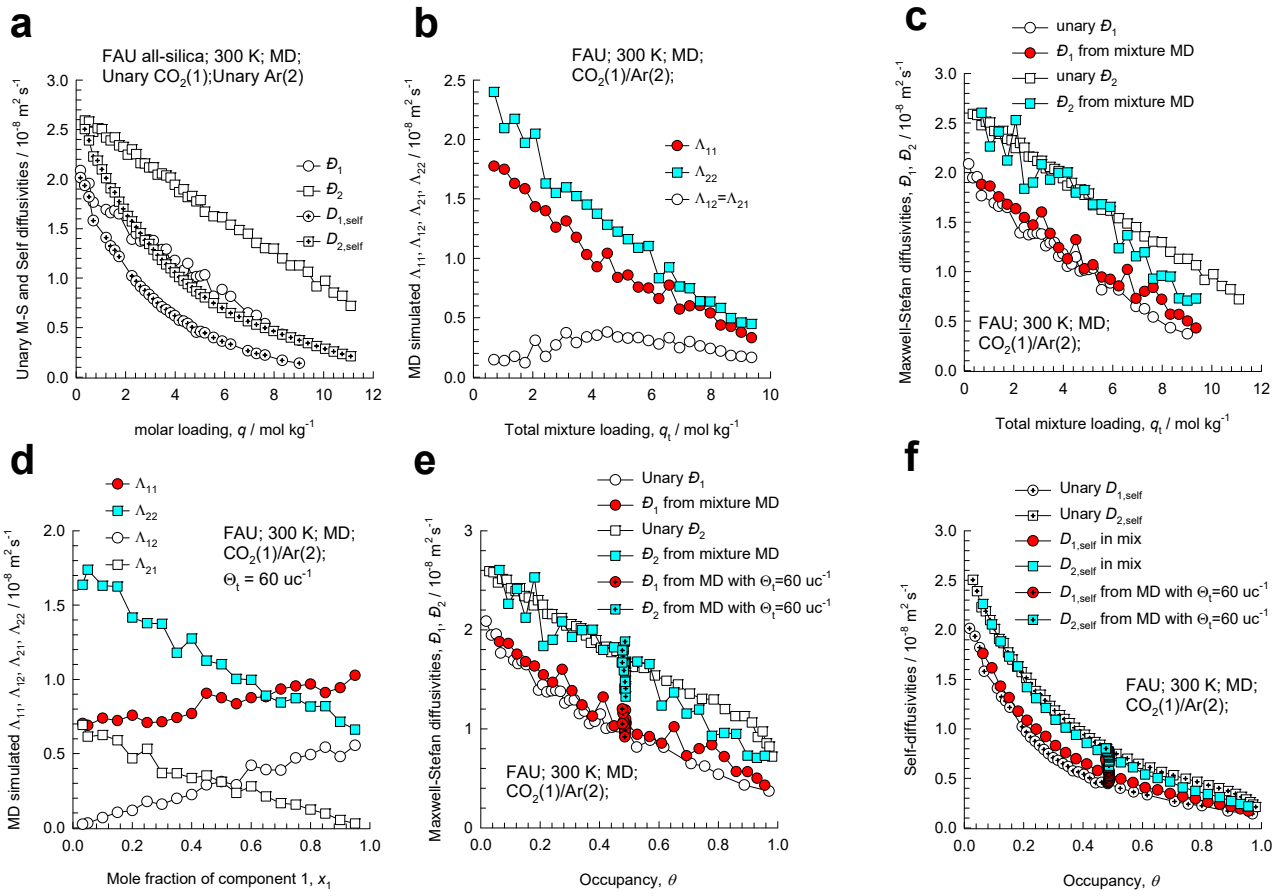

Figure S13. (a, b, c, d) MD simulated values of the M-S diffusivities, $Đ_1, Đ_2$, self-diffusivities, $D_{1,self}, D_{2,self}$, and $\Lambda_{11}, \Lambda_{12}, \Lambda_{21}, \Lambda_{22}$ for binary CO2(1)/Ar(2) mixtures in FAU zeolite at 300 K. Two different MD campaigns were conducted: (i) equimolar $q_1 = q_2$ mixtures, and (ii) mixtures for which $\Theta_t = \Theta_1 + \Theta_2 = 60$ uc^{-1}. In (e, f) the M-S diffusivities, $Đ_1, Đ_2$, and self-diffusivities, $D_{1,self}, D_{2,self}$, are plotted as a function of the occupancy θ.

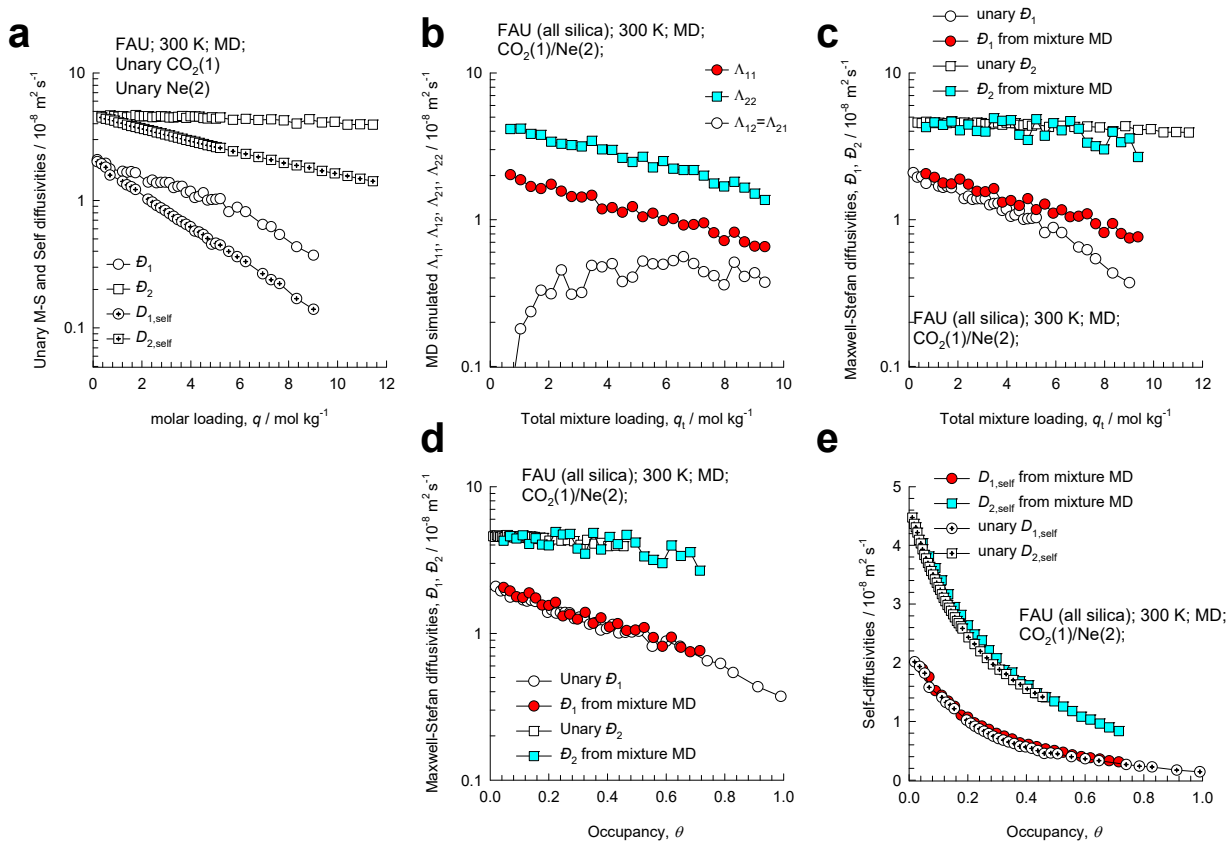

Figure S14. (a, b, c) MD simulated values of the M-S diffusivities, $Đ_1, Đ_2$, self-diffusivities, $D_{1,self}, D_{2,self}$, and $\Lambda_{11}, \Lambda_{12} = \Lambda_{21}, \Lambda_{22}$ for equimolar binary $q_1 = q_2$ CO2(1)/Ne(2) mixtures in all-silica FAU zeolite at 300 K. In (d, e) the M-S diffusivities, $Đ_1, Đ_2$, and self-diffusivities, $D_{1,self}, D_{2,self}$, are plotted as a function of the occupancy θ.

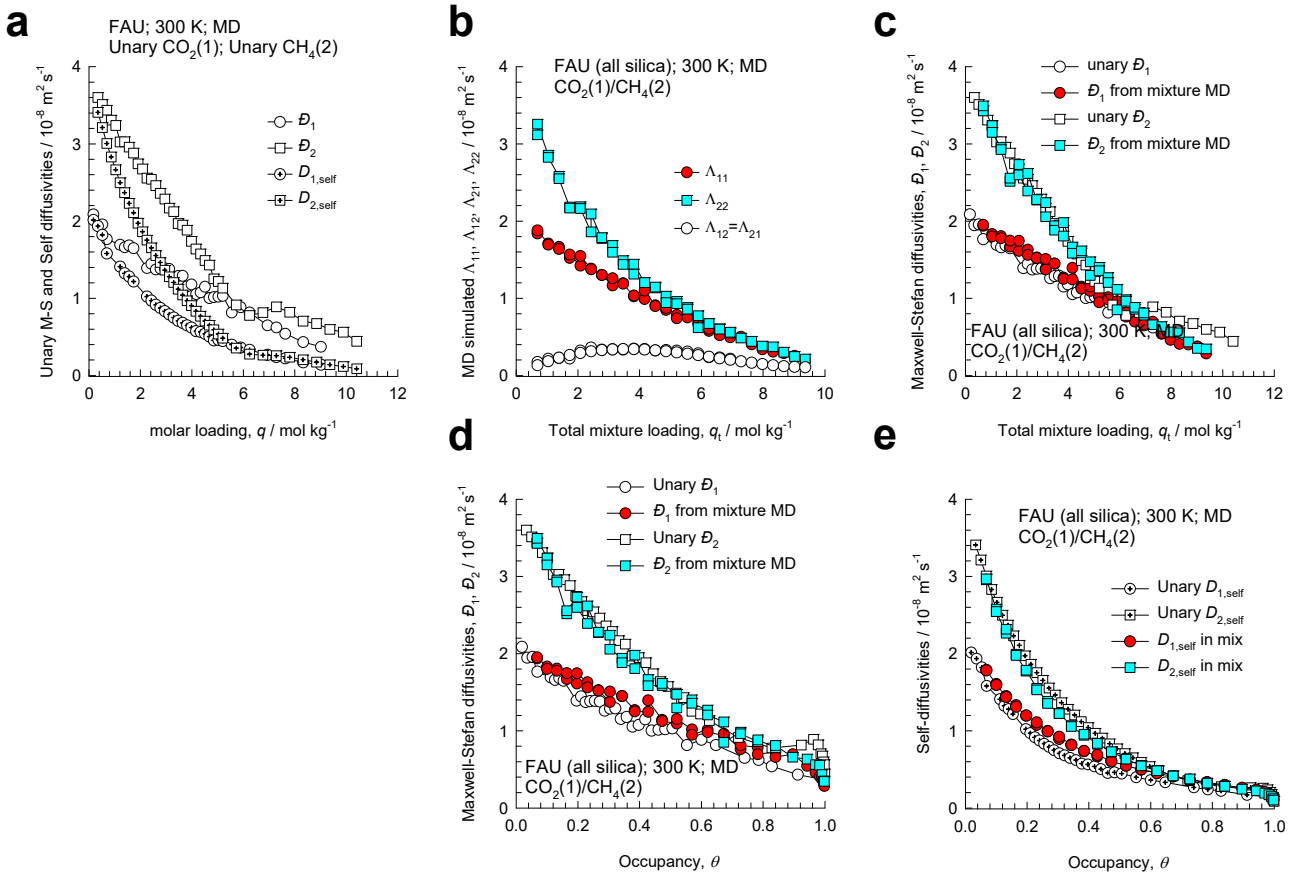

Figure S15. (a, b, c) MD simulated values of the M-S diffusivities, $Đ_1, Đ_2$, self-diffusivities, $D_{1,self}, D_{2,self}$, and $\Lambda_{11}, \Lambda_{12} = \Lambda_{21}, \Lambda_{22}$ for equimolar binary $q_1 = q_2$ CO2(1)/CH4(2) mixtures in all-silica FAU zeolite at 300 K. In (d, e) the M-S diffusivities, $Đ_1, Đ_2$, and self-diffusivities, $D_{1,self}, D_{2,self}$, are plotted as a function of the occupancy θ.

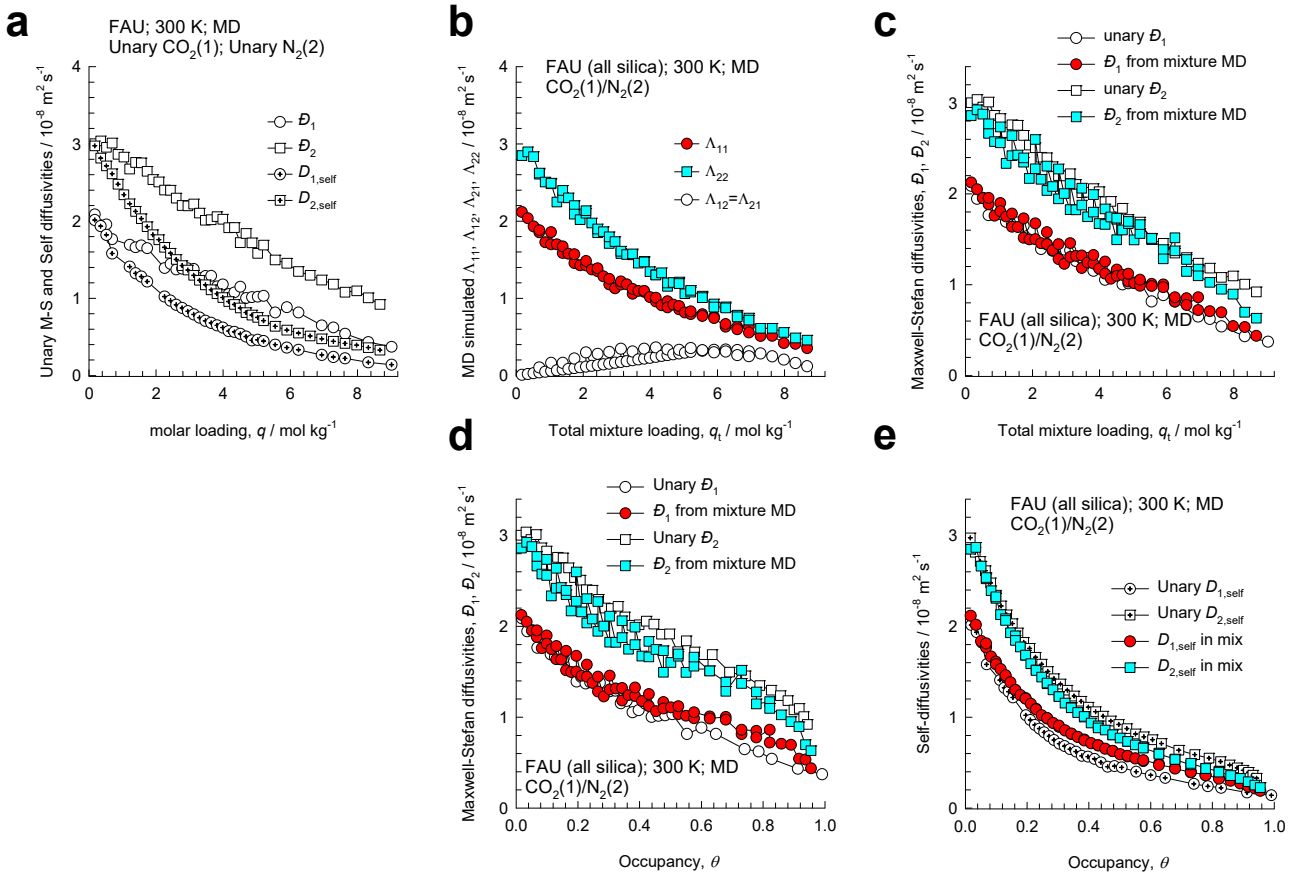

Figure S16. (a, b, c) MD simulated values of the M-S diffusivities, $Đ_1, Đ_2$, self-diffusivities, $D_{1,self}, D_{2,self}$, and $\Lambda_{11}, \Lambda_{12} = \Lambda_{21}, \Lambda_{22}$ for equimolar binary $q_1 = q_2$ $CO_2(1)/N_2(2)$ mixtures in all-silica FAU zeolite at 300 K. In (d, e) the M-S diffusivities, $Đ_1, Đ_2$, and self-diffusivities, $D_{1,self}, D_{2,self}$, are plotted as a function of the occupancy θ.

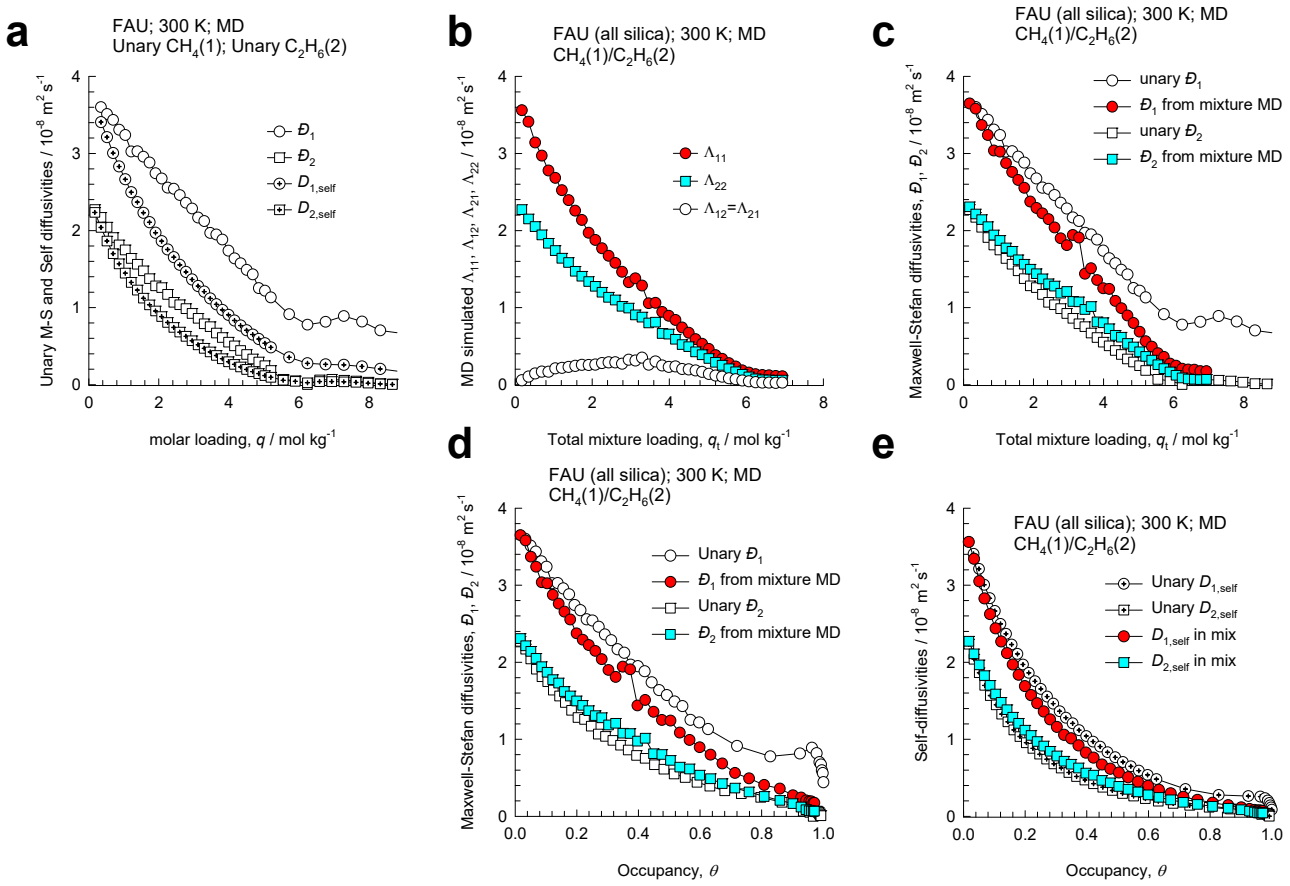

Figure S17. (a, b, c) MD simulated values of the M-S diffusivities, $Đ_1, Đ_2$, self-diffusivities, $D_{1,self}, D_{2,self}$, and $\Lambda_{11}, \Lambda_{12} = \Lambda_{21}, \Lambda_{22}$ for equimolar binary $q_1 = q_2$ CH4(1)/C2H6(2) mixtures in all-silica FAU zeolite at 300 K. In (d, e) the M-S diffusivities, $Đ_1, Đ_2$, and self-diffusivities, $D_{1,self}, D_{2,self}$, are plotted as a function of the occupancy θ.

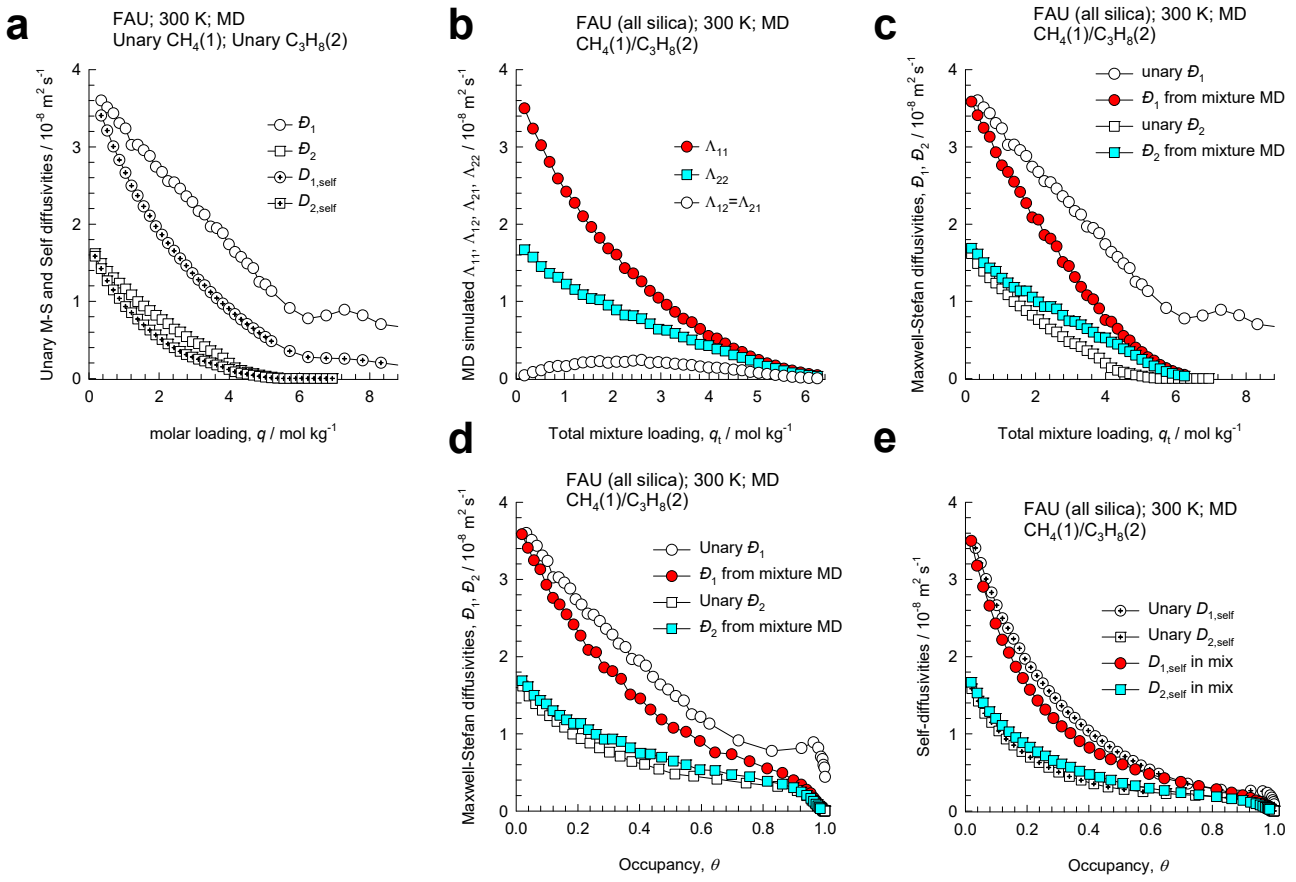

Figure S18. (a, b, c) MD simulated values of the M-S diffusivities, $Đ_1, Đ_2$, self-diffusivities, $D_{1,self}, D_{2,self}$, and $\Lambda_{11}, \Lambda_{12} = \Lambda_{21}, \Lambda_{22}$ for equimolar binary $q_1 = q_2$ CH4(1)/C3H8(2) mixtures in all-silica FAU zeolite at 300 K. In (d, e) the M-S diffusivities, $Đ_1, Đ_2$, and self-diffusivities, $D_{1,self}, D_{2,self}$, are plotted as a function of the occupancy θ.

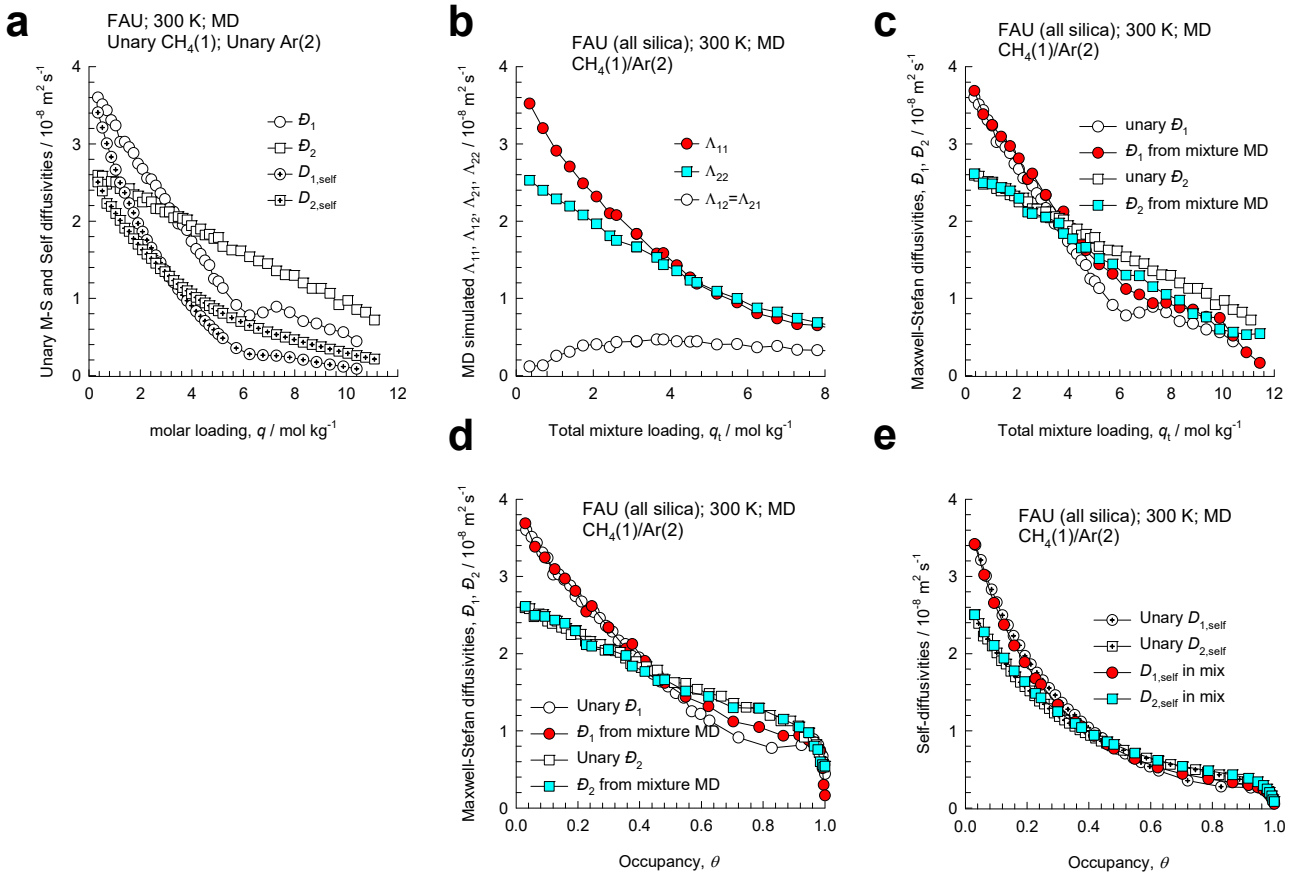

Figure S19. (a, b, c) MD simulated values of the M-S diffusivities, $Đ_1, Đ_2$, self-diffusivities, $D_{1,self}, D_{2,self}$, and $\Lambda_{11}, \Lambda_{12} = \Lambda_{21}, \Lambda_{22}$ for equimolar binary $q_1 = q_2$ CH4(1)/Ar(2) mixtures in all-silica FAU zeolite at 300 K. In (d, e) the M-S diffusivities, $Đ_1, Đ_2$, and self-diffusivities, $D_{1,self}, D_{2,self}$, are plotted as a function of the occupancy θ.

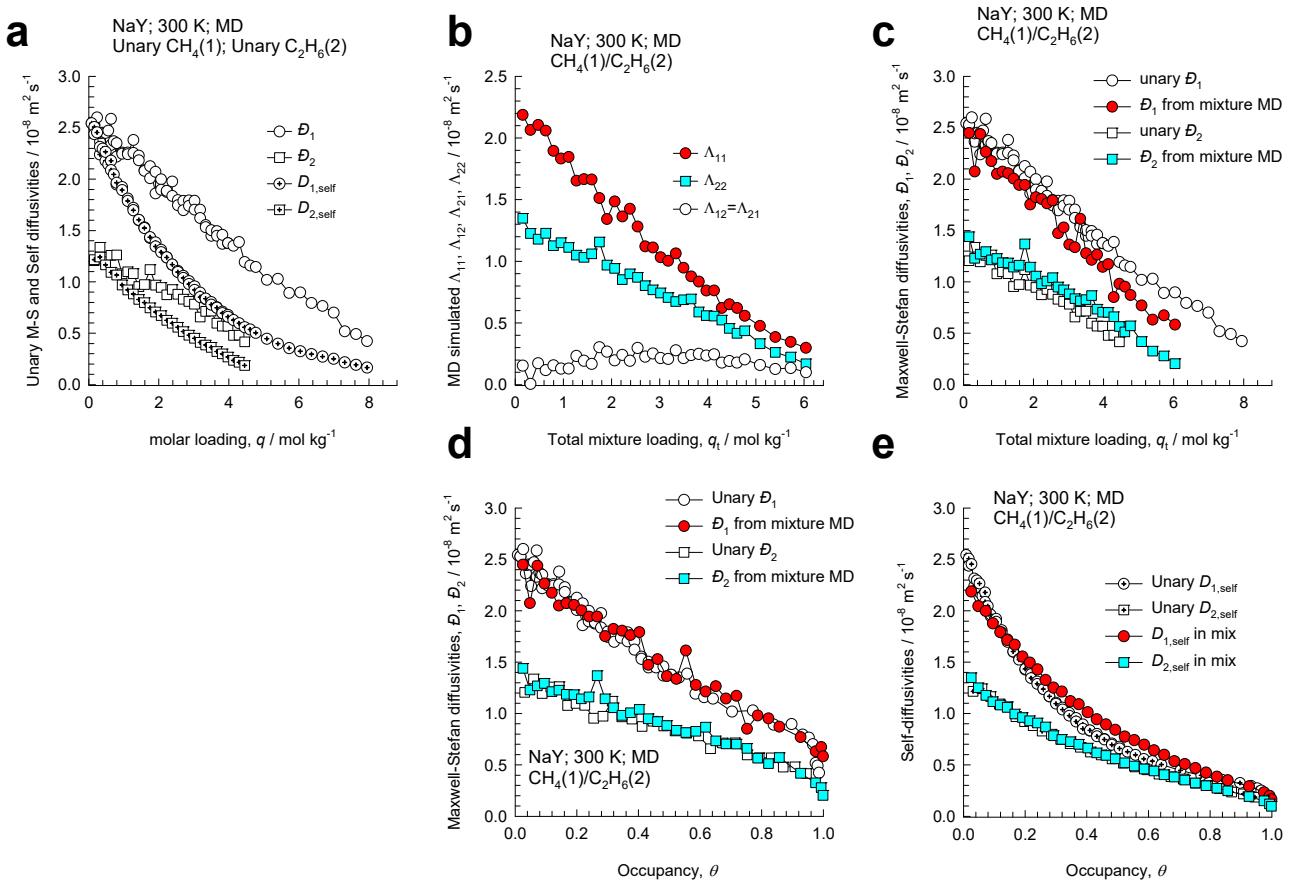

Figure S20. (a, b, c) MD simulated values of the M-S diffusivities, $Đ_1, Đ_2$, self-diffusivities, $D_{1,self}, D_{2,self}$, and $\Lambda_{11}, \Lambda_{12} = \Lambda_{21}, \Lambda_{22}$ for equimolar binary $q_1 = q_2$ CH4(1)/C2H6(2) mixtures in NaY zeolite at 300 K. In (d, e) the M-S diffusivities, $Đ_1, Đ_2$, and self-diffusivities, $D_{1,self}, D_{2,self}$, are plotted as a function of the occupancy θ.

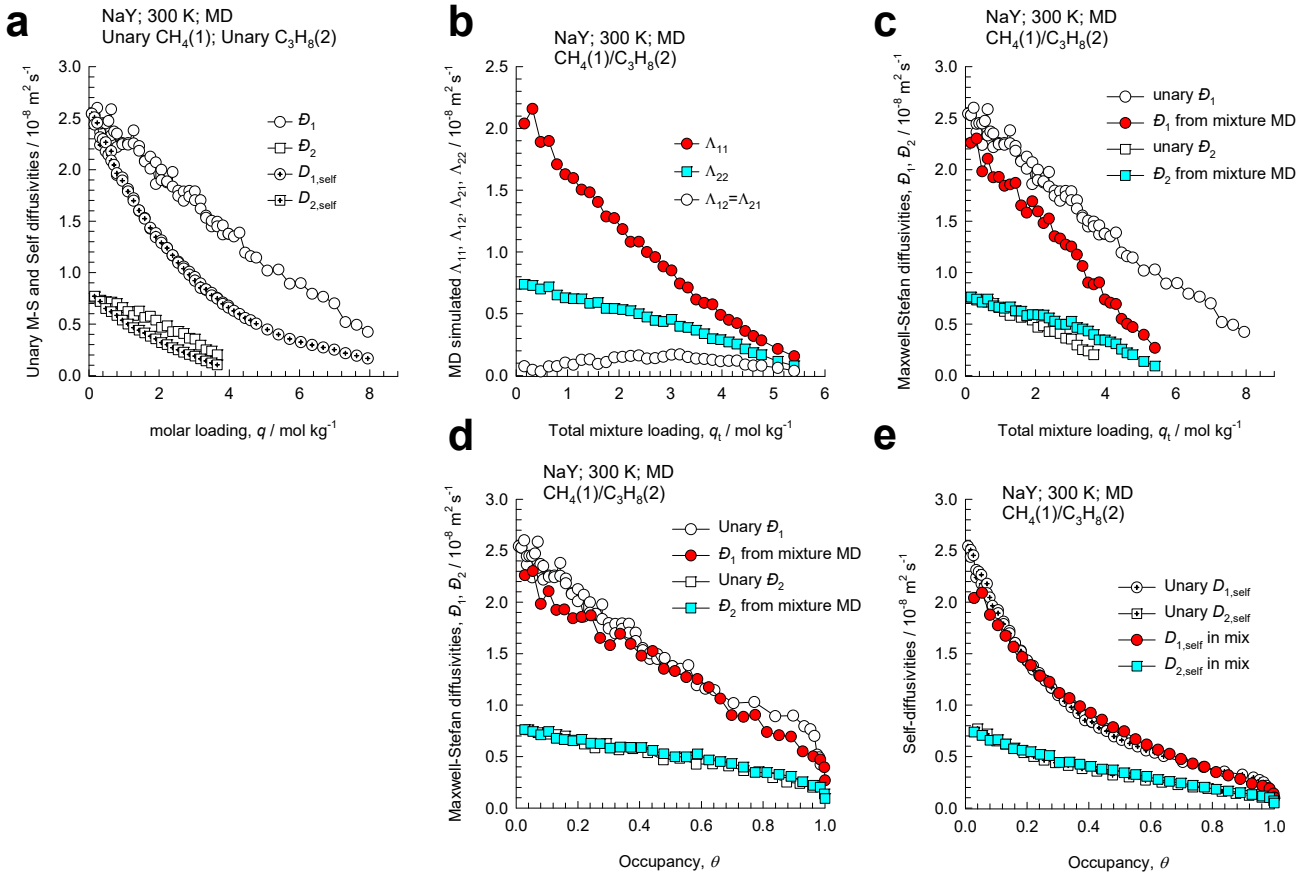

Figure S21. (a, b, c) MD simulated values of the M-S diffusivities, $Đ_1, Đ_2$, self-diffusivities, $D_{1,self}, D_{2,self}$, and $\Lambda_{11}, \Lambda_{12} = \Lambda_{21}, \Lambda_{22}$ for equimolar binary $q_1 = q_2$ CH4(1)/C3H8(2) mixtures in NaY zeolite at 300 K. In (d, e) the M-S diffusivities, $Đ_1, Đ_2$, and self-diffusivities, $D_{1,self}, D_{2,self}$, are plotted as a function of the occupancy θ.

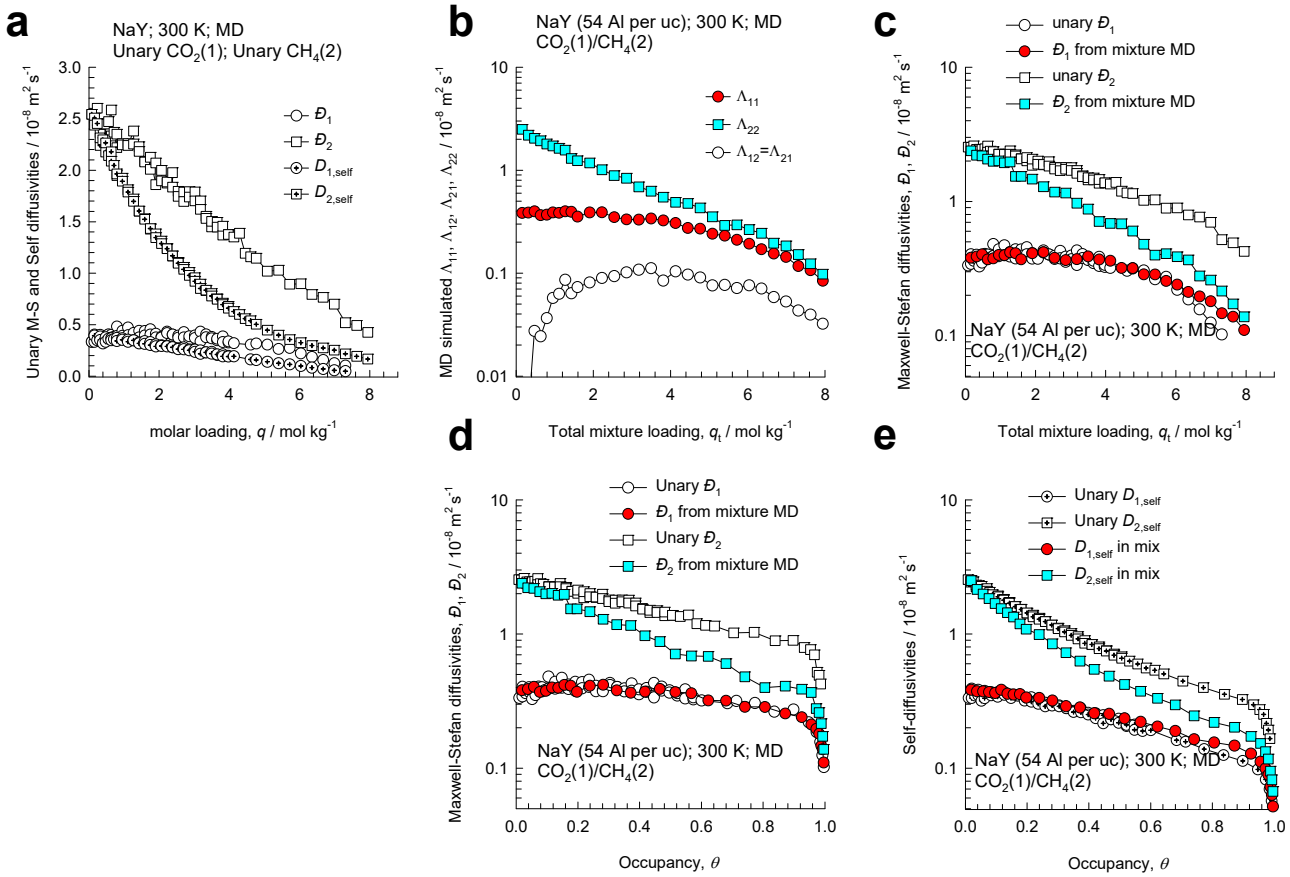

Figure S22. (a, b, c) MD simulated values of the M-S diffusivities, $Đ_1, Đ_2$, self-diffusivities, $D_{1,self}, D_{2,self}$, and $\Lambda_{11}, \Lambda_{12} = \Lambda_{21}, \Lambda_{22}$ for equimolar binary $q_1 = q_2$ $CO_2(1)/CH_4(2)$ mixtures in NaY zeolite at 300 K. In (d, e) the M-S diffusivities, $Đ_1, Đ_2$, and self-diffusivities, $D_{1,self}, D_{2,self}$, are plotted as a function of the occupancy θ.

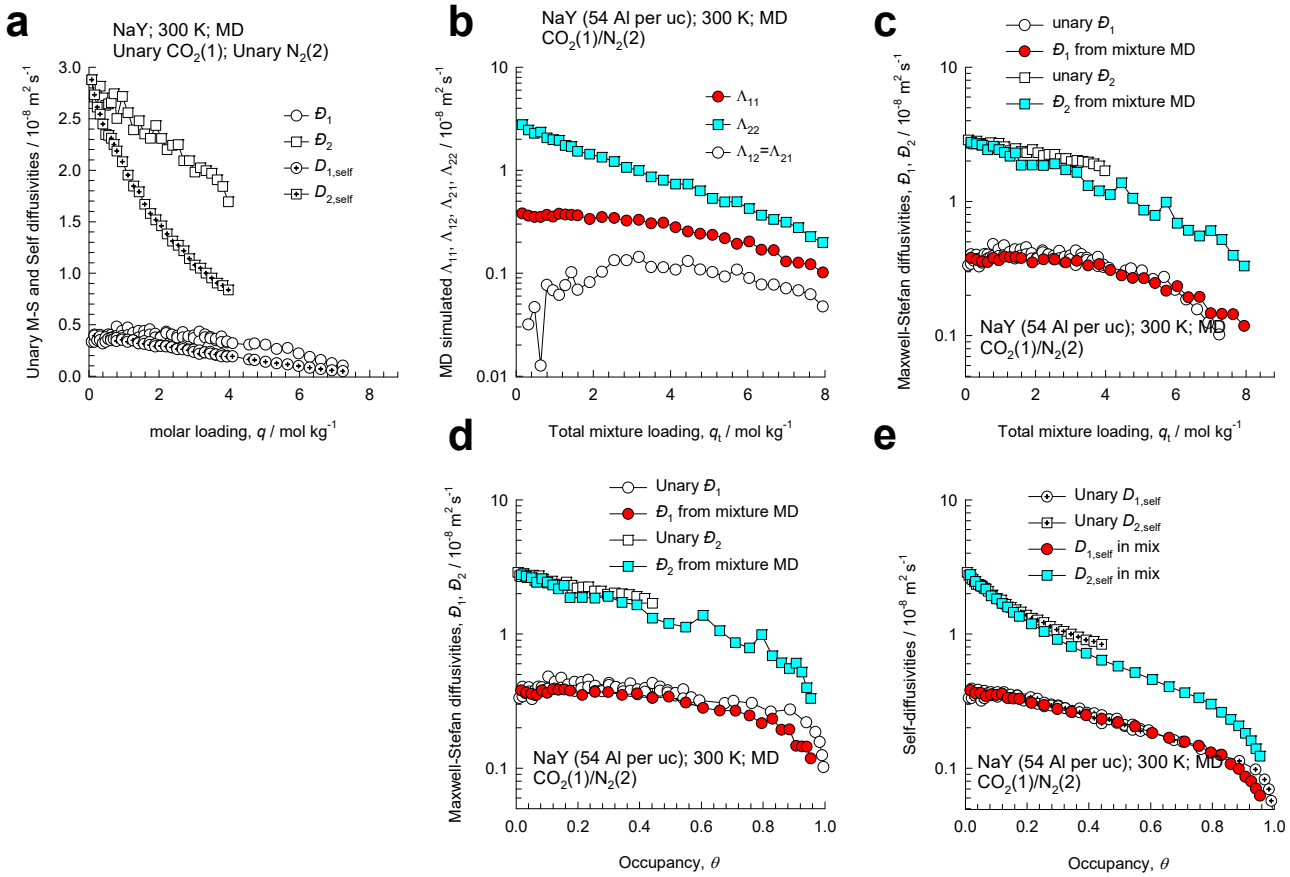

Figure S23. (a, b, c) MD simulated values of the M-S diffusivities, $Đ_1, Đ_2$, self-diffusivities, $D_{1,self}, D_{2,self}$, and $\Lambda_{11}, \Lambda_{12} = \Lambda_{21}, \Lambda_{22}$ for equimolar binary $q_1 = q_2$ CO2(1)/N2(2) mixtures in NaY zeolite at 300 K. In (d, e) the M-S diffusivities, $Đ_1, Đ_2$, and self-diffusivities, $D_{1,self}, D_{2,self}$, are plotted as a function of the occupancy θ.

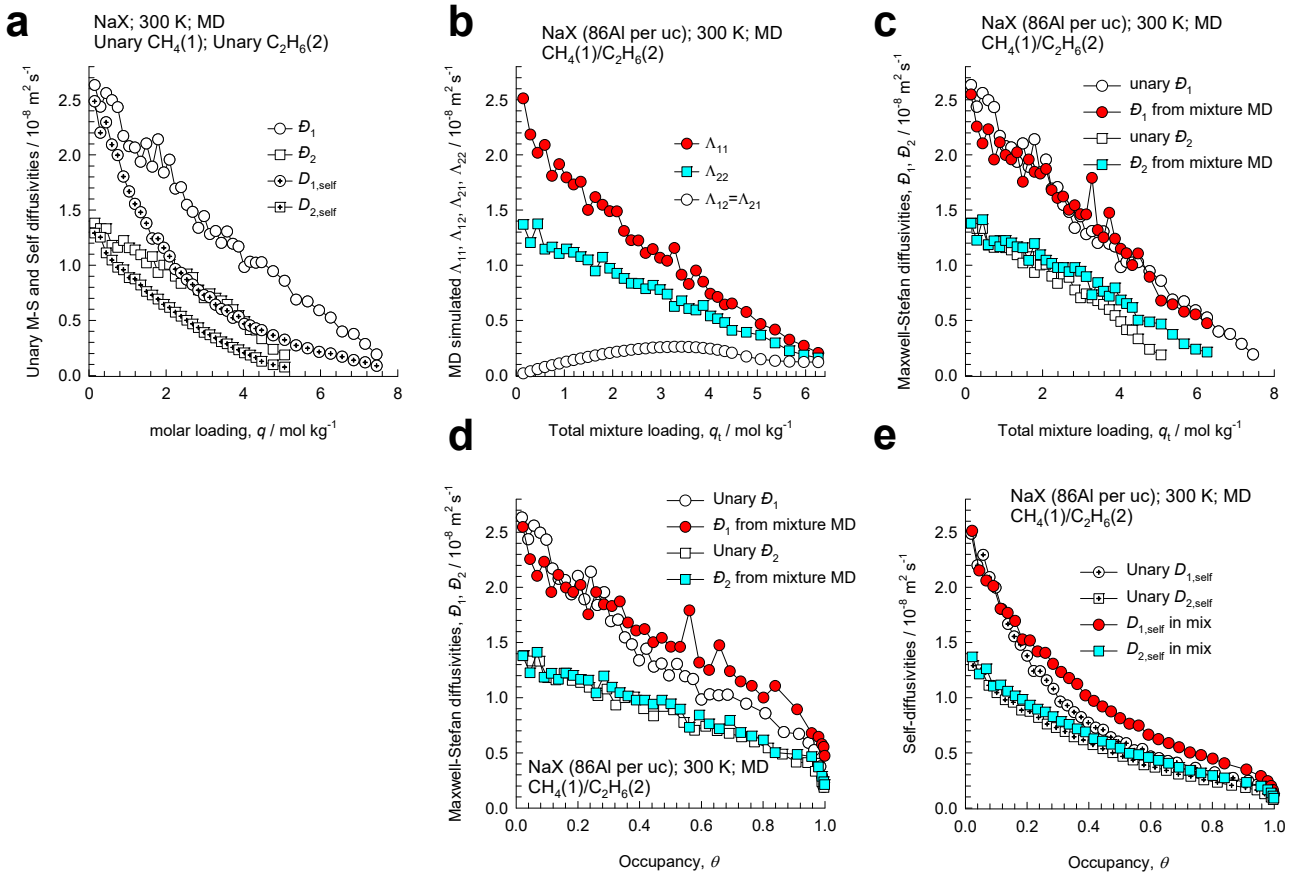

Figure S24. (a, b, c) MD simulated values of the M-S diffusivities, $Đ_1, Đ_2$, self-diffusivities, $D_{1,self}, D_{2,self}$, and $\Lambda_{11}, \Lambda_{12} = \Lambda_{21}, \Lambda_{22}$ for equimolar binary $q_1 = q_2$ $CH_4(1)/C_2H_6(2)$ mixtures in NaX zeolite at 300 K. In (d, e) the M-S diffusivities, $Đ_1, Đ_2$, and self-diffusivities, $D_{1,self}, D_{2,self}$, are plotted as a function of the occupancy θ.

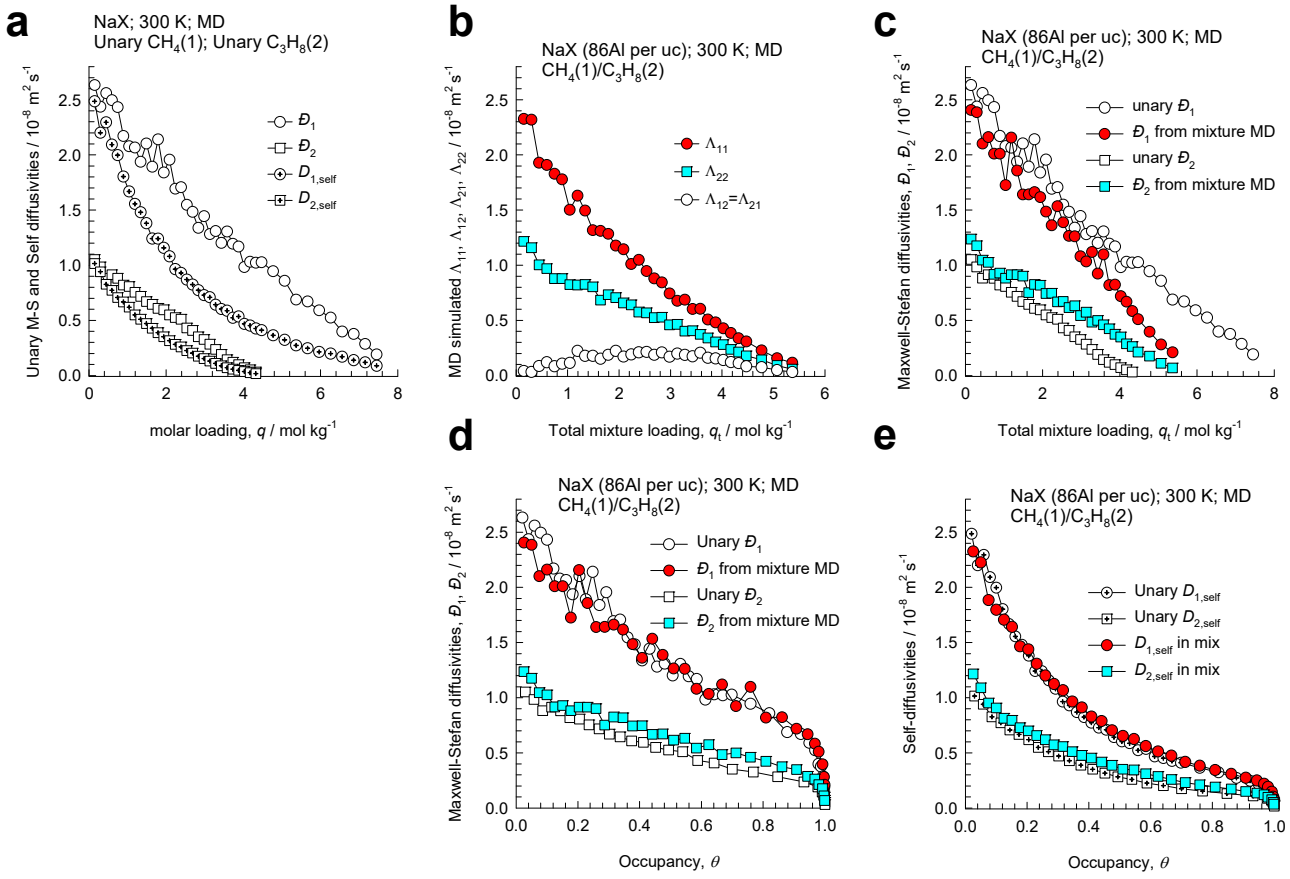

Figure S25. (a, b, c) MD simulated values of the M-S diffusivities, $Đ_1, Đ_2$, self-diffusivities, $D_{1,self}, D_{2,self}$, and $\Lambda_{11}, \Lambda_{12} = \Lambda_{21}, \Lambda_{22}$ for equimolar binary $q_1 = q_2$ CH4(1)/C3H8(2) mixtures in NaX zeolite at 300 K. In (d, e) the M-S diffusivities, $Đ_1, Đ_2$, and self-diffusivities, $D_{1,self}, D_{2,self}$, are plotted as a function of the occupancy θ.

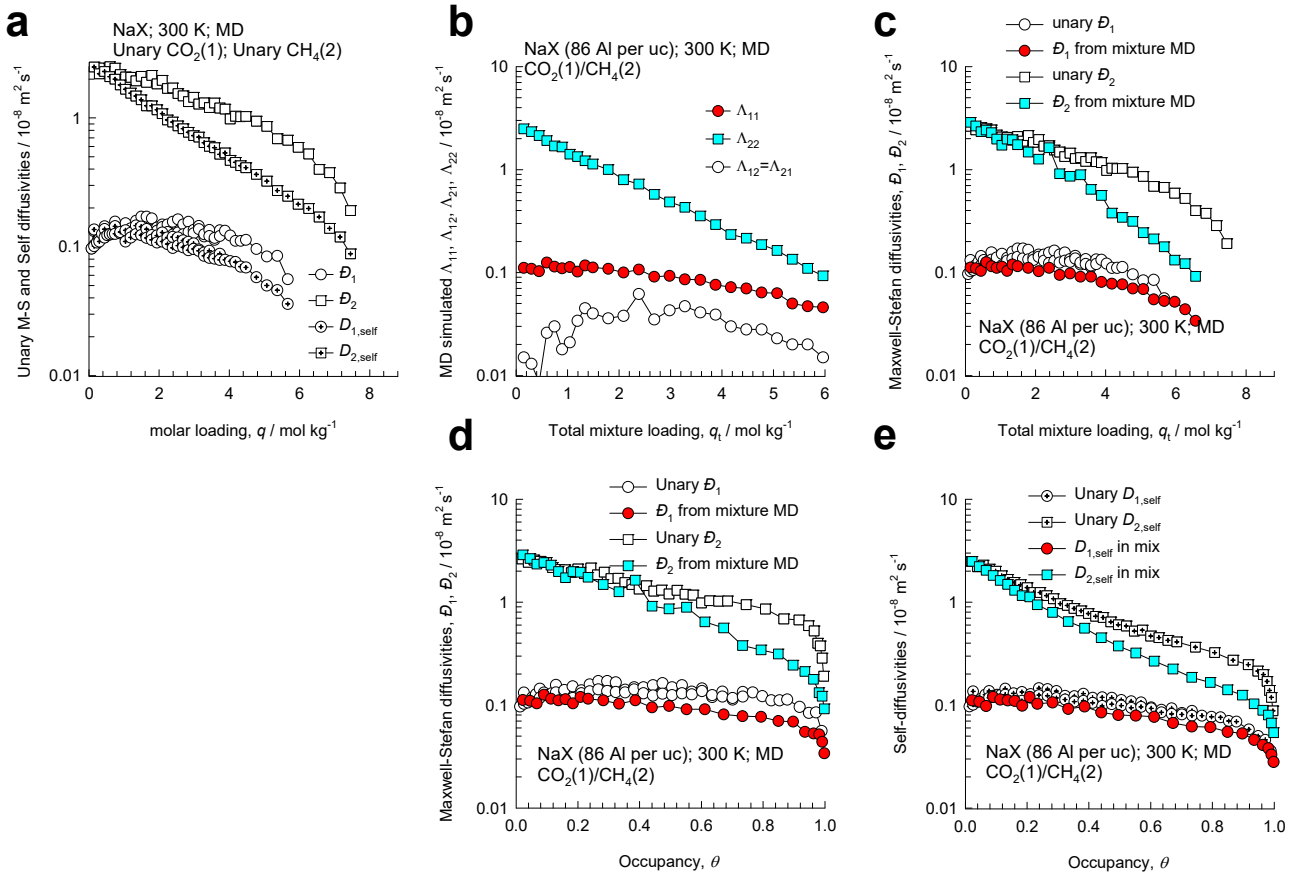

Figure S26. (a, b, c) MD simulated values of the M-S diffusivities, $Đ_1, Đ_2$, self-diffusivities, $D_{1,self}, D_{2,self}$, and $\Lambda_{11}, \Lambda_{12} = \Lambda_{21}, \Lambda_{22}$ for equimolar binary $q_1 = q_2$ CO2(1)/CH4(2) mixtures in NaX zeolite at 300 K. In (d, e) the M-S diffusivities, $Đ_1, Đ_2$, and self-diffusivities, $D_{1,self}, D_{2,self}$, are plotted as a function of the occupancy θ.

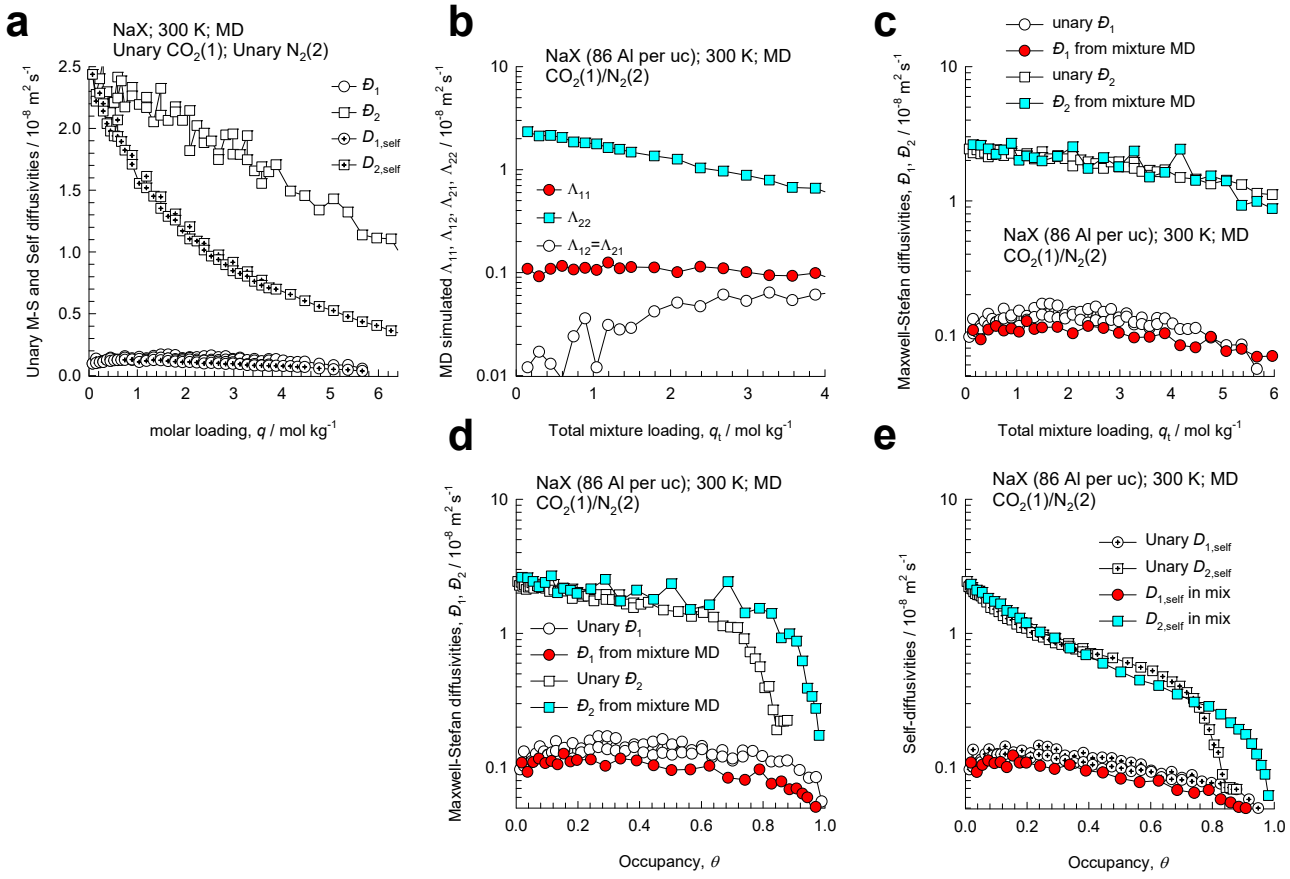

Figure S27. (a, b, c) MD simulated values of the M-S diffusivities, $Đ_1, Đ_2$, self-diffusivities, $D_{1,self}, D_{2,self}$, and $\Lambda_{11}, \Lambda_{12} = \Lambda_{21}, \Lambda_{22}$ for equimolar binary $q_1 = q_2$ CO2(1)/N2(2) mixtures in NaX zeolite at 300 K. In (d, e) the M-S diffusivities, $Đ_1, Đ_2$, and self-diffusivities, $D_{1,self}, D_{2,self}$, are plotted as a function of the occupancy θ.

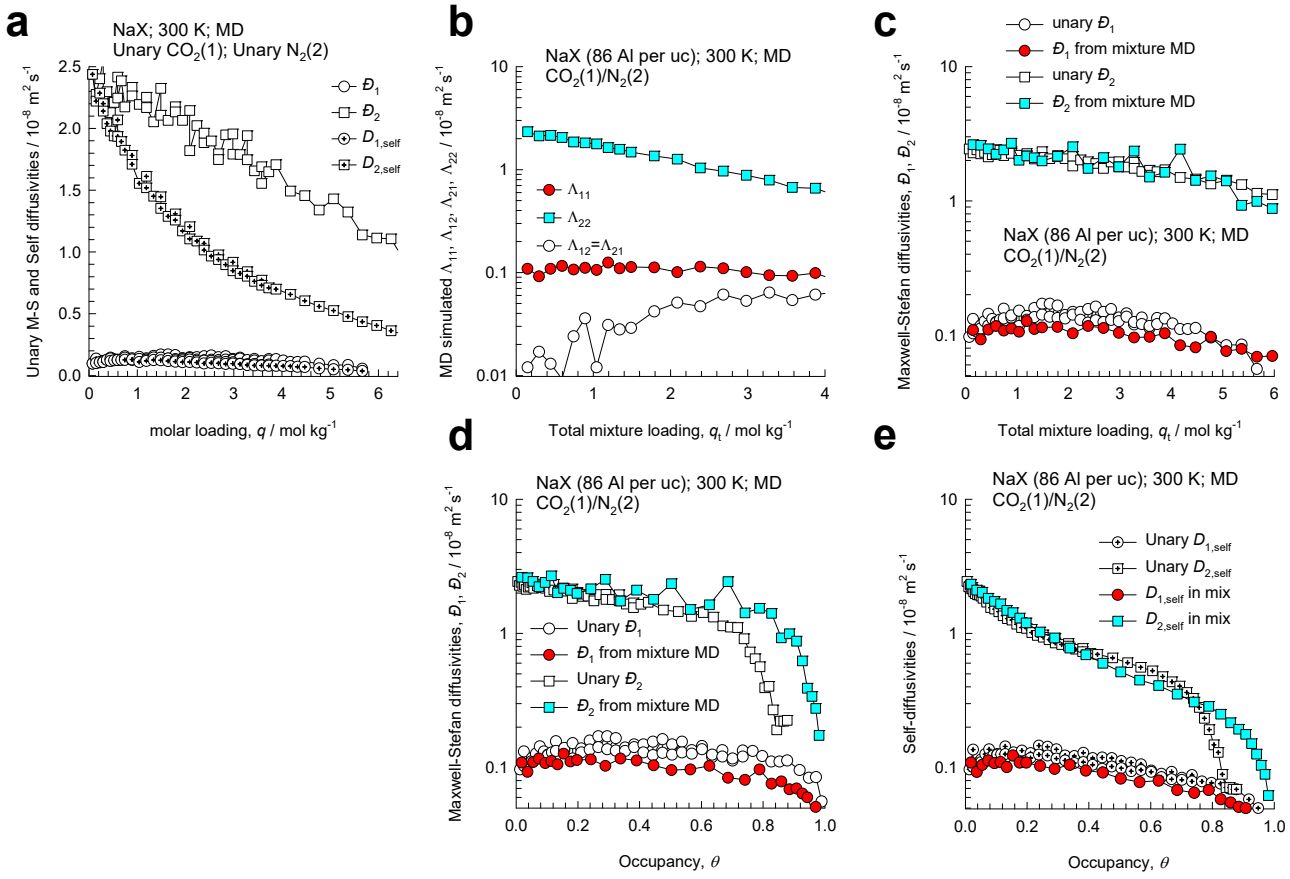

Figure S28. (a, b, c) MD simulated values of the M-S diffusivities, $Đ_1, Đ_2$, self-diffusivities, $D_{1,self}, D_{2,self}$, and $\Lambda_{11}, \Lambda_{12} = \Lambda_{21}, \Lambda_{22}$ for equimolar binary $q_1 = q_2$ CO2(1)/H2(2) mixtures in all-silica FAU zeolite at 300 K. In (d, e) the M-S diffusivities, $Đ_1, Đ_2$, and self-diffusivities, $D_{1,self}, D_{2,self}$, are plotted as a function of the occupancy θ.

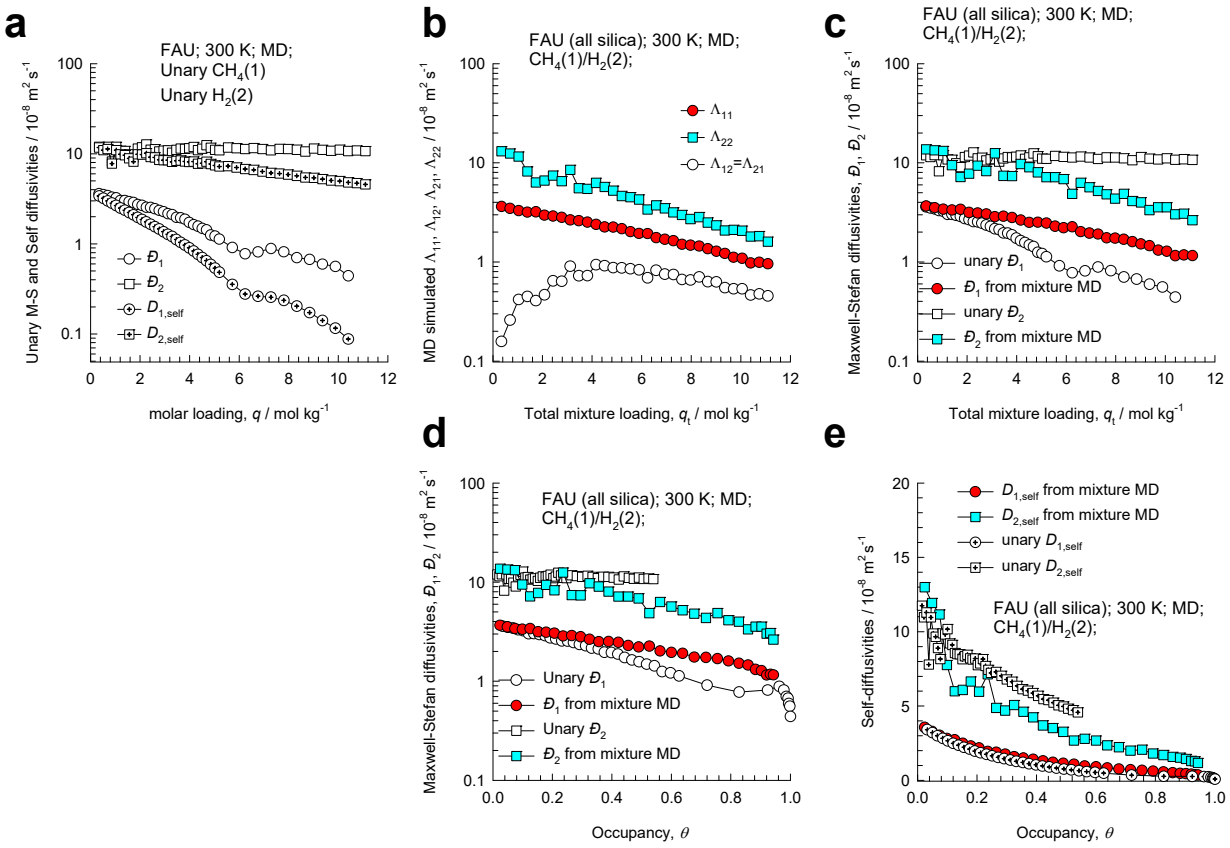

Figure S29. (a, b, c) MD simulated values of the M-S diffusivities, $Đ_1, Đ_2$, self-diffusivities, $D_{1,self}, D_{2,self}$, and $\Lambda_{11}, \Lambda_{12} = \Lambda_{21}, \Lambda_{22}$ for equimolar binary $q_1 = q_2$ CH4(1)/H2(2) mixtures in all-silica FAU zeolite at 300 K. In (d, e) the M-S diffusivities, $Đ_1, Đ_2$, and self-diffusivities, $D_{1,self}, D_{2,self}$, are plotted as a function of the occupancy θ.

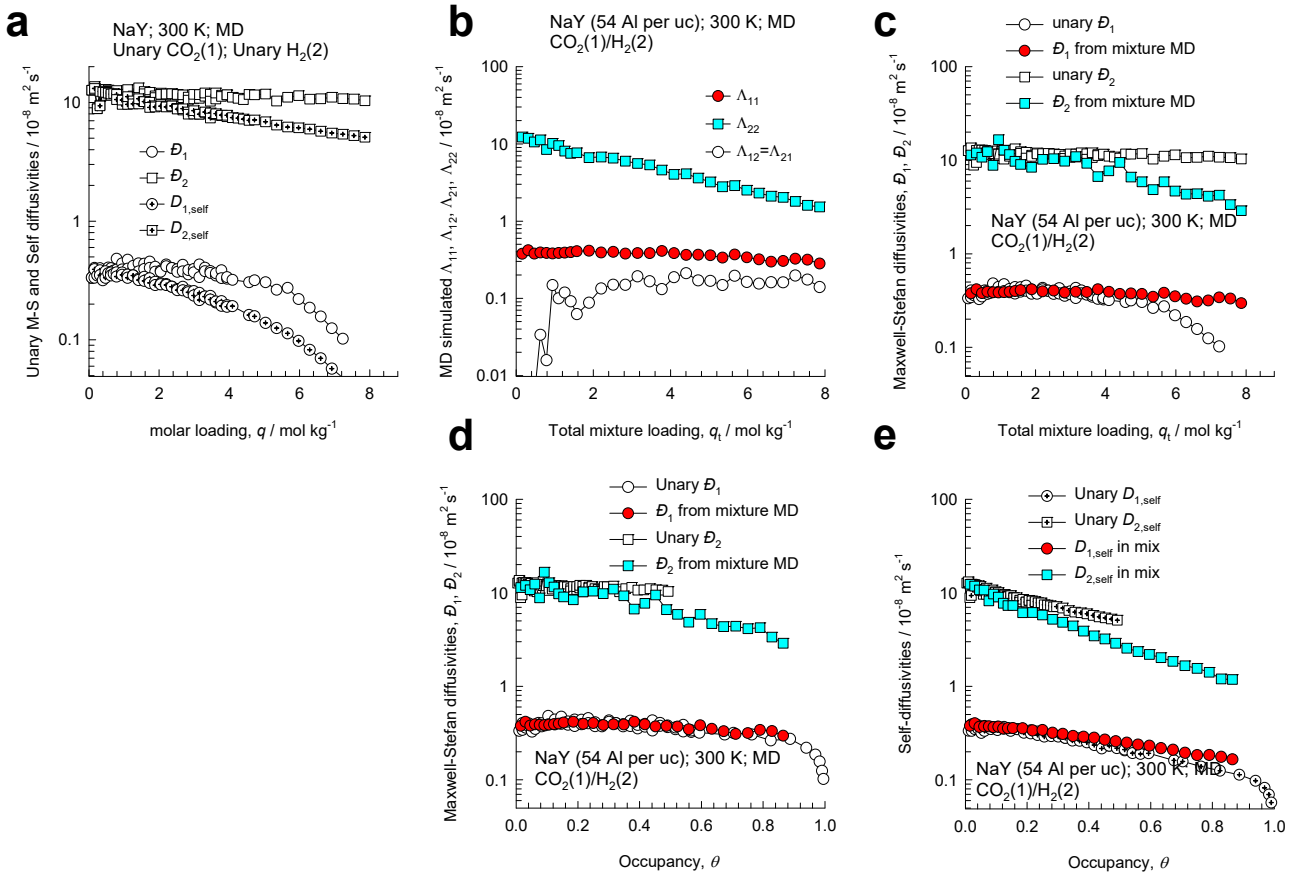

Figure S30. (a, b, c) MD simulated values of the M-S diffusivities, $Đ_1, Đ_2$, self-diffusivities, $D_{1,self}, D_{2,self}$, and $\Lambda_{11}, \Lambda_{12} = \Lambda_{21}, \Lambda_{22}$ for equimolar binary $q_1 = q_2$ CO2(1)/H2(2) mixtures in NaY zeolite at 300 K. In (d, e) the M-S diffusivities, $Đ_1, Đ_2$, and self-diffusivities, $D_{1,self}, D_{2,self}$, are plotted as a function of the occupancy θ.

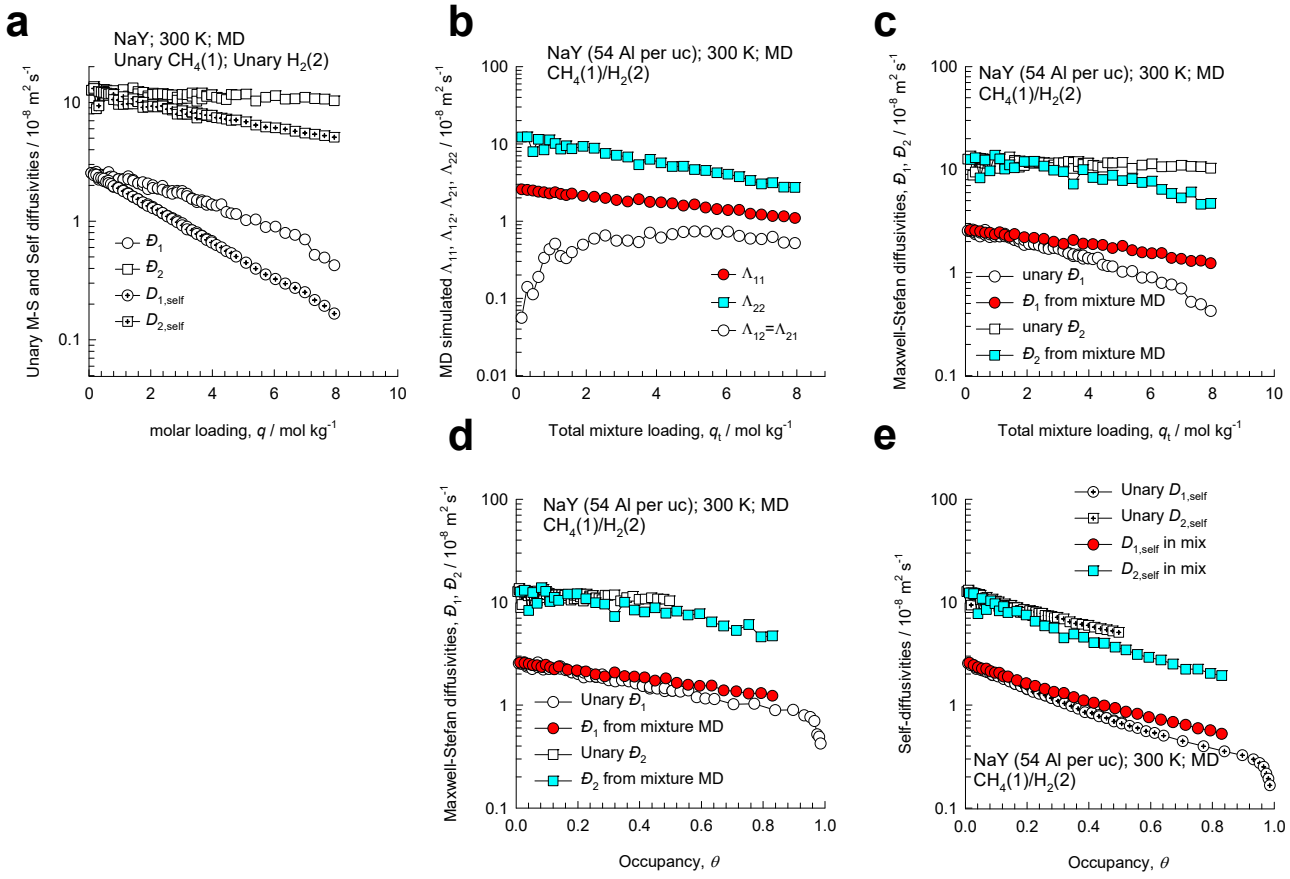

Figure S31. (a, b, c) MD simulated values of the M-S diffusivities, $Đ_1, Đ_2$, self-diffusivities, $D_{1,self}, D_{2,self}$, and $\Lambda_{11}, \Lambda_{12} = \Lambda_{21}, \Lambda_{22}$ for equimolar binary $q_1 = q_2$ CH4(1)/H2(2) mixtures in NaY zeolite at 300 K. In (d, e) the M-S diffusivities, $Đ_1, Đ_2$, and self-diffusivities, $D_{1,self}, D_{2,self}$, are plotted as a function of the occupancy θ.

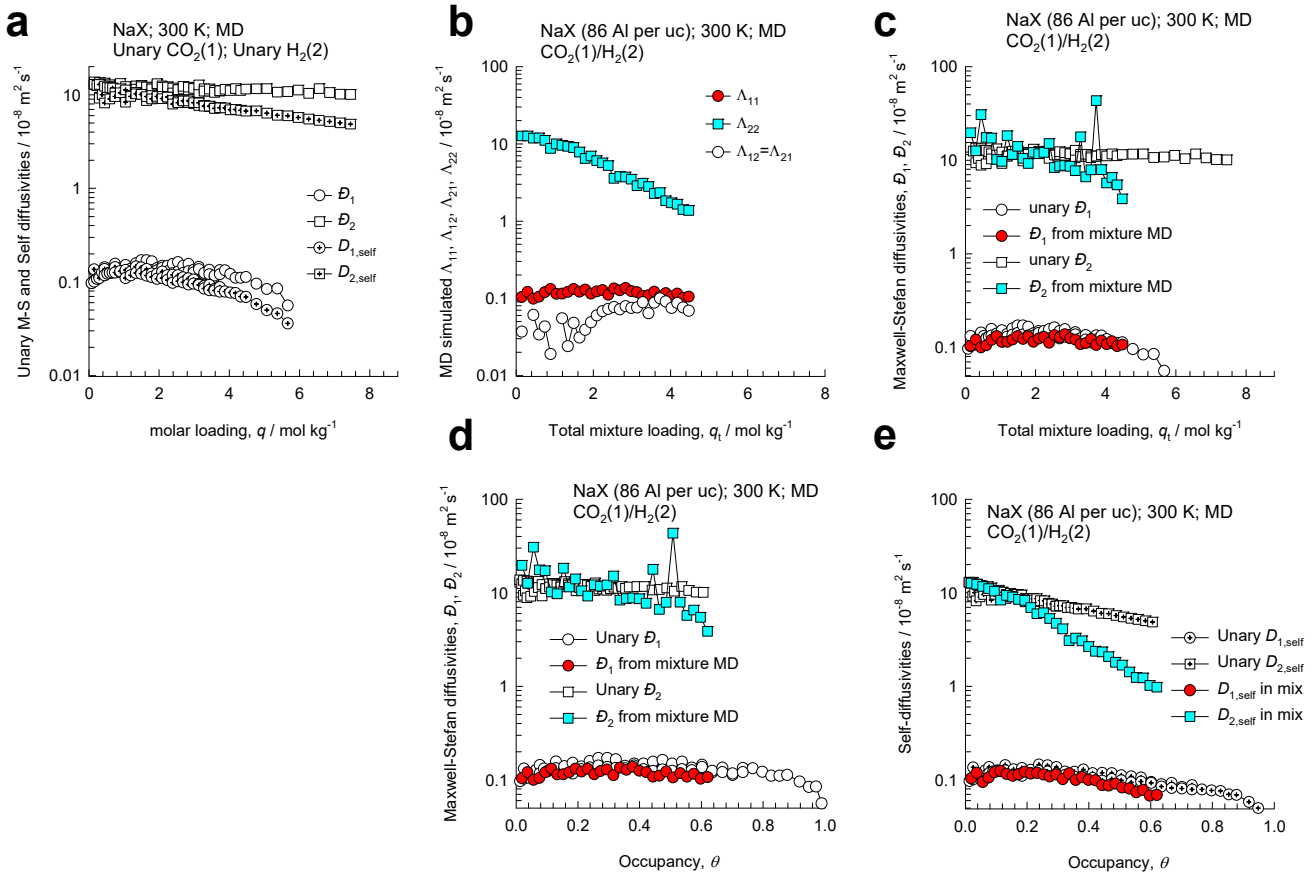

Figure S32. (a, b, c) MD simulated values of the M-S diffusivities, $Đ_1, Đ_2$, self-diffusivities, $D_{1,self}, D_{2,self}$, and $\Lambda_{11}, \Lambda_{12} = \Lambda_{21}, \Lambda_{22}$ for equimolar binary $q_1 = q_2$ $CO_2(1)/H_2(2)$ mixtures in NaX zeolite at 300 K. In (d, e) the M-S diffusivities, $Đ_1, Đ_2$, and self-diffusivities, $D_{1,self}, D_{2,self}$, are plotted as a function of the occupancy θ.

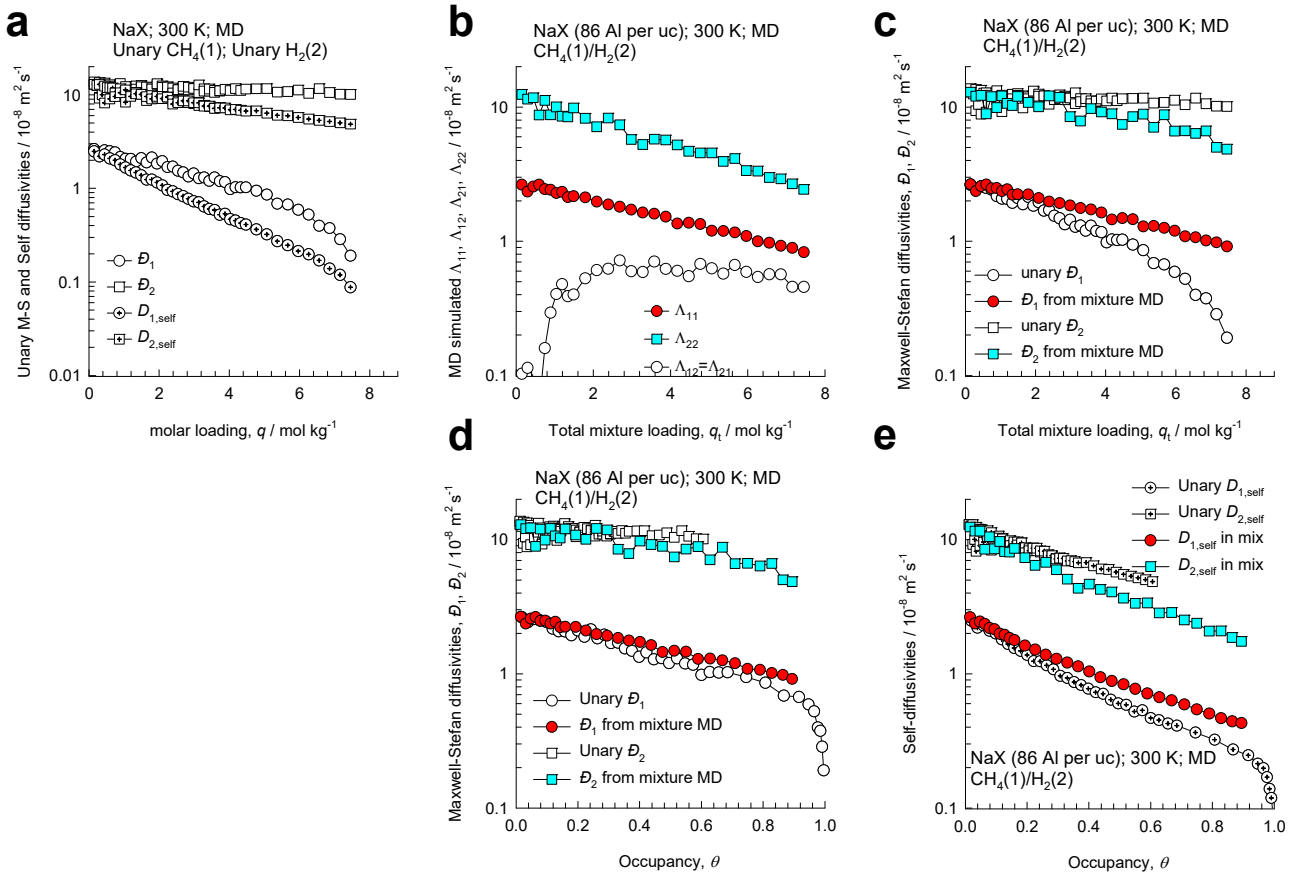

Figure S33. (a, b, c) MD simulated values of the M-S diffusivities, $Đ_1, Đ_2$, self-diffusivities, $D_{1,self}, D_{2,self}$, and $\Lambda_{11}, \Lambda_{12} = \Lambda_{21}, \Lambda_{22}$ for equimolar binary $q_1 = q_2$ CH4(1)/H2(2) mixtures in NaX zeolite at 300 K. In (d, e) the M-S diffusivities, $Đ_1, Đ_2$, and self-diffusivities, $D_{1,self}, D_{2,self}$, are plotted as a function of the occupancy θ.

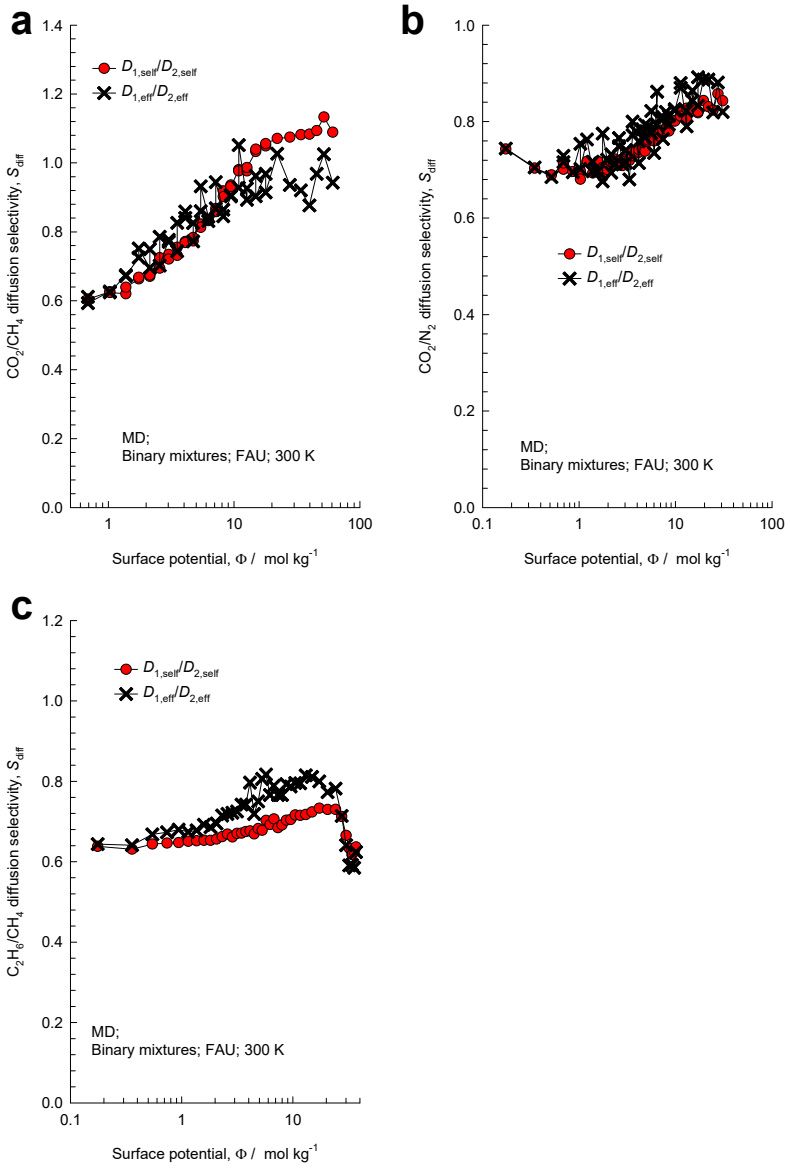

Figure S34. MD simulations of (a) CO_2/CH_4, (b) CO_2/N_2, and (c) CH_4/C_2H_6 diffusion selectivities determined from equimolar binary $(q_1 = q_2)$ mixtures in FAU zeolite at 300 K, plotted as function of the surface potential Φ.

7 Adsorption, Diffusion, Permeation in FAU zeolite

Figure S35 presents the structural details of FAU (all-silica) zeolite. It has cages of 786 Å^3 volume, separated by 7.4 Å 12-ring windows.

CBMC simulations of the unary isotherms in all-silica FAU were fitted with the dual-site Langmuir-Freundlich model, eq (S15); the fit parameters for each guest molecule (with sites A, and B) are tabulated for each guest in Table S2.

7.1 Adsorption of mixtures in all-silica FAU zeolite

In Figure S36, CBMC simulation data for (a) CO_2/CH_4, (b) CO_2/N_2, (c) CH_4/N_2, (d) CO_2/H_2, and (e) CH_4/H_2 adsorption selectivities, S_{ads} , determined from binary mixture are compared with the values of the corresponding binary pairs in 20/40/40 $CO_2/CH_4/N_2$ and quaternary 1/1/1/1 $CO_2/CH_4/N_2/H_2$ mixtures. The IAST estimations (dashed lines) are in good agreement with the CBMC simulated values of S_{ads}. Each of the pair selectivities shows a unique dependence on Φ, as prescribed by eq (S20). Put another way, the presence of component 3 and/or component 4 in the ternary mixture has no influence of the adsorption selectivity for the 1-2 pair other than via the sorption pressures and surface potential.

7.2 Diffusion and permeation selectivities of binary pairs

MD simulations of the self-diffusivities $D_{i,self}$ for equimolar $q_1 = q_2$; $x_1 = 1 - x_2 = 0.5$ binary CO_2/CH_4, CO_2/N_2, CO_2/H_2, CH_4/N_2, CH_4/H_2, CH_4/C_2H_6, and CH_4/C_3H_8 mixtures and equimolar $\left(q_1 = q_2 = q_3\right)$ ternary $CO_2/CH_4/N_2$, $CO_2/CH_4/H_2$, $CO_2/N_2/H_2$, and $CH_4/C_2H_6/C_3H_8$ mixtures in all-silica FAU zeolite were also performed. For ternary $CH_4/C_2H_6/C_3H_8$ mixtures, additional MD campaigns were conducted in which the total mixture loading was maintained constant at the value $\left(\Theta_1 + \Theta_2 + \Theta_3\right) = 48$ molecules uc^{-1}, the loading of propane was held constant at the value of $\Theta_3 = 12$ molecules uc^{-1}, and the proportions of

the methane and ethane components were varied in the mixtures, holding the total loading $\left(\Theta_1 + \Theta_2\right) = 36$ molecules uc^{-1}.

Figure S37a shows MD simulations of the CO_2/CH_4 diffusion selectivities, S_{diff}, determined from both equimolar binary $\left(q_1 = q_2\right)$ mixtures and equimolar $\left(q_1 = q_2 = q_3\right)$ ternary ($CO_2/CH_4/N_2$, and $CO_2/CH_4/H_2$) mixtures in all-silica FAU zeolite at 300 K, plotted as function of the surface potential Φ. Also plotted are MD data for binary mixtures in which the total molar loading $\Theta_t = \Theta_2 + \Theta_2 = 10$ molecules uc^{-1}, with varying mole fractions $x_1 = \Theta_1 / \left(\Theta_2 + \Theta_2\right)$. All three MD data sets follow a unique dependence on the surface potential Φ. In view of the fact that IAST also shows that the adsorption selectivity S_{ads} is also uniquely dependent on Φ, we should expect the permeation selectivity $S_{perm} = \dfrac{D_{1,self} q_1 / f_1}{D_{2,self} q_2 / f_2} = S_{ads} \times S_{diff}$ to be also uniquely dependent on Φ. This is confirmed by the data presented in Figure S37b for the CO_2/CH_4 permeation selectivities, S_{perm}.

Figure S38, Figure S39, Figure S40, Figure S41, Figure S42, and Figure S43 present analogous sets of data on S_{diff} and S_{perm} for CO_2/N_2, CO_2/H_2, CH_4/N_2, and CH_4/H_2, CH_4/C_2H_6, and CH_4/C_3H_8 pairs. In all cases the S_{diff} and S_{perm} for binary and ternary mixtures is uniquely dependent on Φ.

7.3 Component self-diffusivities and permeabilities

Figure S44 presents MD simulation data on the self-diffusivities, $D_{i,self}$, of (a) CO_2, (b) CH_4, (c) N_2, (d) C_2H_6, and (e) H_2 in equimolar $q_1 = q_2$; $x_1 = 1 - x_2 = 0.5$ binary CO_2/CH_4, CO_2/N_2, CO_2/H_2, CH_4/N_2, CH_4/H_2, CH_4/C_2H_6, and CH_4/C_3H_8 mixtures and equimolar $\left(q_1 = q_2 = q_3\right)$ ternary $CO_2/CH_4/N_2$, $CO_2/CH_4/H_2$, $CO_2/N_2/H_2$, and $CH_4/C_2H_6/C_3H_8$ mixtures, plotted as a function of the surface potential Φ. The data demonstrate that the component self-diffusivities in binary and ternary mixtures are nearly the same, independent of the partner(s) in the mixtures. Also plotted are the corresponding values of the unary self-diffusivities. Except for H_2, the self-diffusivities in the binary and ternary mixtures are also nearly

the same as the unary self-diffusivities. The unary self-diffusivity for H_2, is larger in value for those in mixtures. The lowering of the H_2 self-diffusivity in mixtures is attributable to correlation effects, that slows-down the more mobile H_2.

Figure S45 presents data on the permeabilities, Π_i, of a) CO_2, (b) CH_4, (c) N_2, (d) C_2H_6, and (e) H_2 in equimolar $q_1 = q_2;\quad x_1 = 1 - x_2 = 0.5$ binary CO_2/CH_4, CO_2/N_2, CO_2/H_2, CH_4/N_2, CH_4/H_2, CH_4/C_2H_6, CH_4/C_3H_8, and C_2H_6/C_3H_8 mixtures and equimolar $\left(q_1 = q_2 = q_3\right)$ ternary $CO_2/CH_4/N_2$, $CO_2/CH_4/H_2$, $CO_2/N_2/H_2$, and $CH_4/C_2H_6/C_3H_8$ mixtures, plotted as a function of the surface potential Φ. The data demonstrate that the component permeabilities in binary and ternary mixtures are nearly the same, independent of the partner(s) in the mixtures. Also plotted are the corresponding values of the unary permeabilities. Except for H_2, the permeabilities in the binary and ternary mixtures are also nearly the same as the unary permeabilities. The unary permeability for H_2, appears to be larger in value for those in mixtures. The lowering of the H_2 permeabilities in mixtures is attributable to correlation effects, that slows-down the more mobile H_2.

7.4 List of Tables for Adsorption, Diffusion, Permeation in FAU zeolite

Table S2. Dual-site Langmuir-Freundlich parameters for pure components CO_2, CH_4, N_2, C_2H_6, and C_3H_8 at 300K in all-silica FAU. The fit parameters are based on the CBMC simulations of pure component isotherms presented in earlier works.[5, 48, 49]

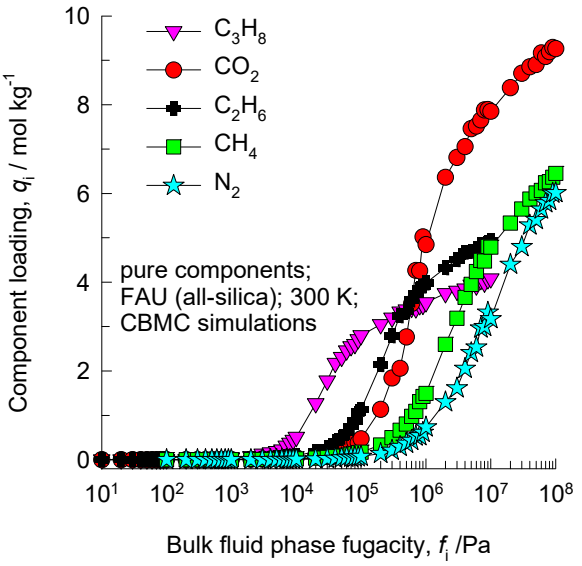

	Site A			Site B		
	$q_{A,sat}$ mol kg^{-1}	b_A Pa$^{-\nu_A}$	ν_A dimensionless	$q_{B,sat}$ mol kg^{-1}	b_B Pa$^{-\nu_B}$	ν_B dimensionless
CO_2	2.4	2.52×10^{-14}	2.4	6.7	6.74×10^{-7}	1
CH_4	4	7×10^{-9}	0.86	6.5	2.75×10^{-7}	1
N_2	5.2	1.55×10^{-9}	1	5.8	1.32×10^{-7}	1
C_2H_6	5.201	2.872E-06	1	5.201	1.000E-09	1
C_3H_8	3.467	1.338E-05	0.6	3.467	1.718E-06	1.27

7.5 List of Figures for Adsorption, Diffusion, Permeation in FAU zeolite

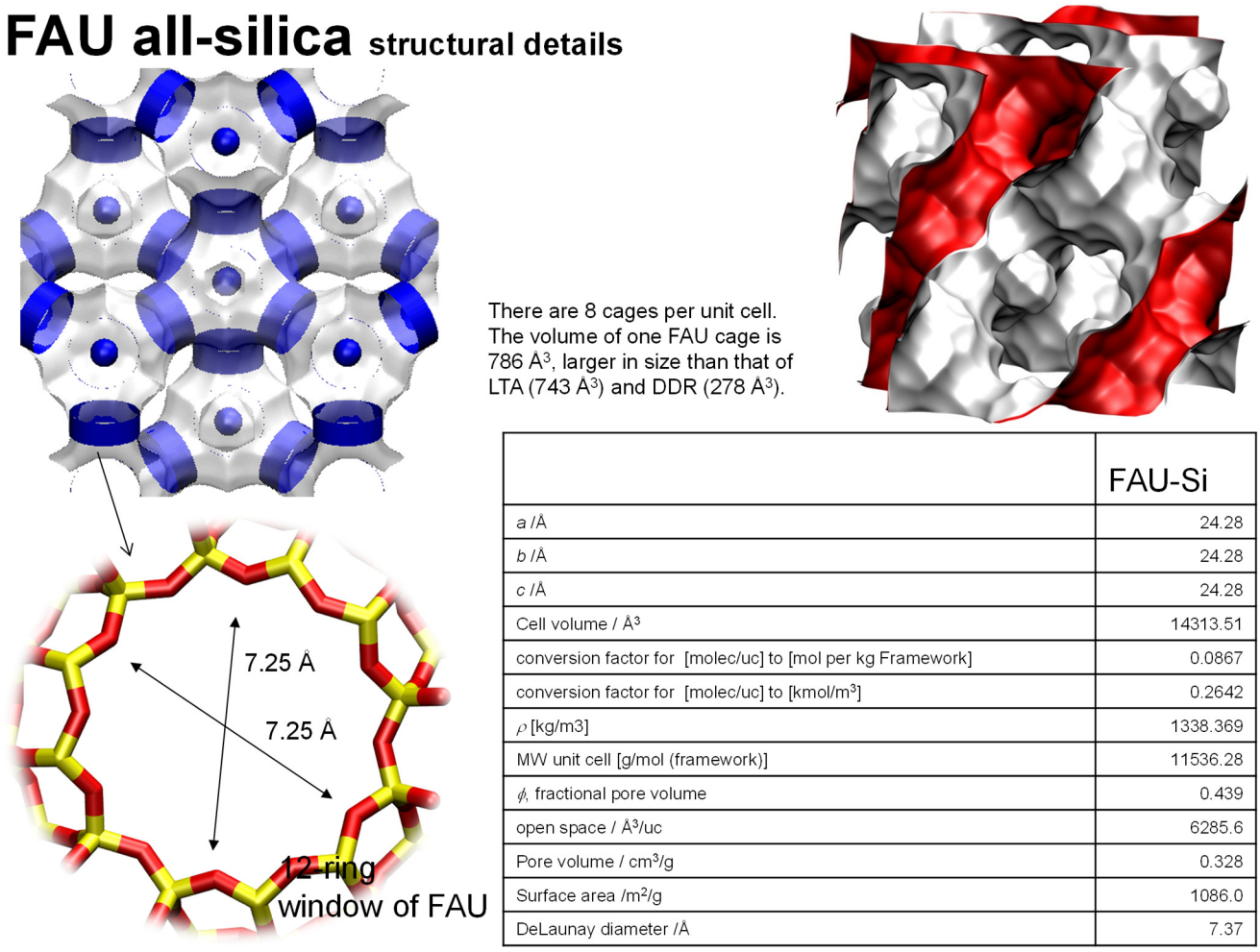

	FAU-Si
a /Å	24.28
b /Å	24.28
c /Å	24.28
Cell volume / Å^3	14313.51
conversion factor for [molec/uc] to [mol per kg Framework]	0.0867
conversion factor for [molec/uc] to [kmol/m^3]	0.2642
ρ [kg/m3]	1338.369
MW unit cell [g/mol (framework)]	11536.28
ϕ, fractional pore volume	0.439
open space / Å^3/uc	6285.6
Pore volume / cm^3/g	0.328
Surface area /m^2/g	1086.0
DeLaunay diameter /Å	7.37

Figure S35. Pore landscape for all-silica FAU zeolite.

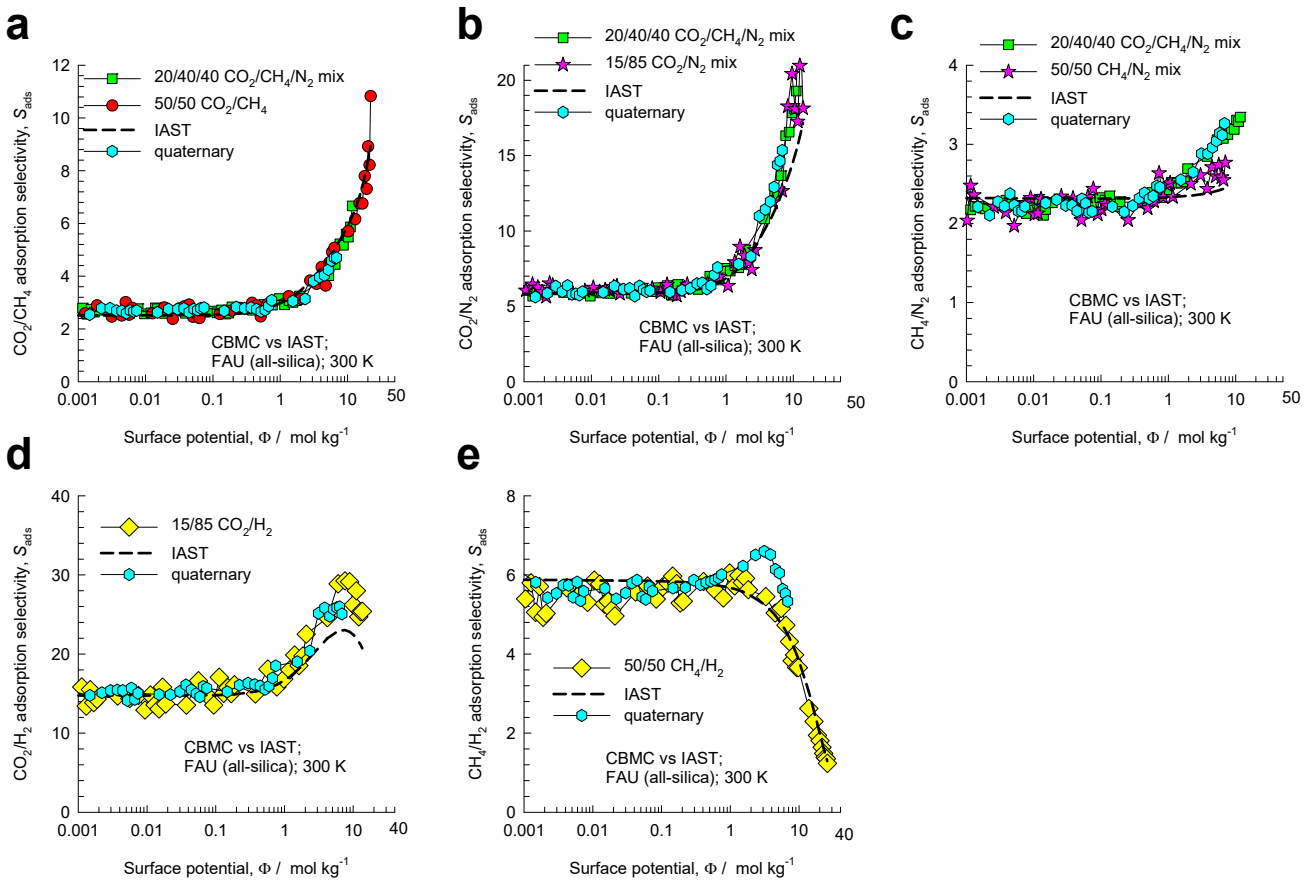

Figure S36. CBMC simulations of (a) CO_2/CH_4, (b) CO_2/N_2, (c) CH_4/N_2, (d) CO_2/H_2, and (e) CH_4/H_2, adsorption selectivities, S_{ads} , determined from binary, ternary, and quaternary mixture adsorption in all-silica FAU zeolite at 300 K, plotted as function of the surface potential, Φ .

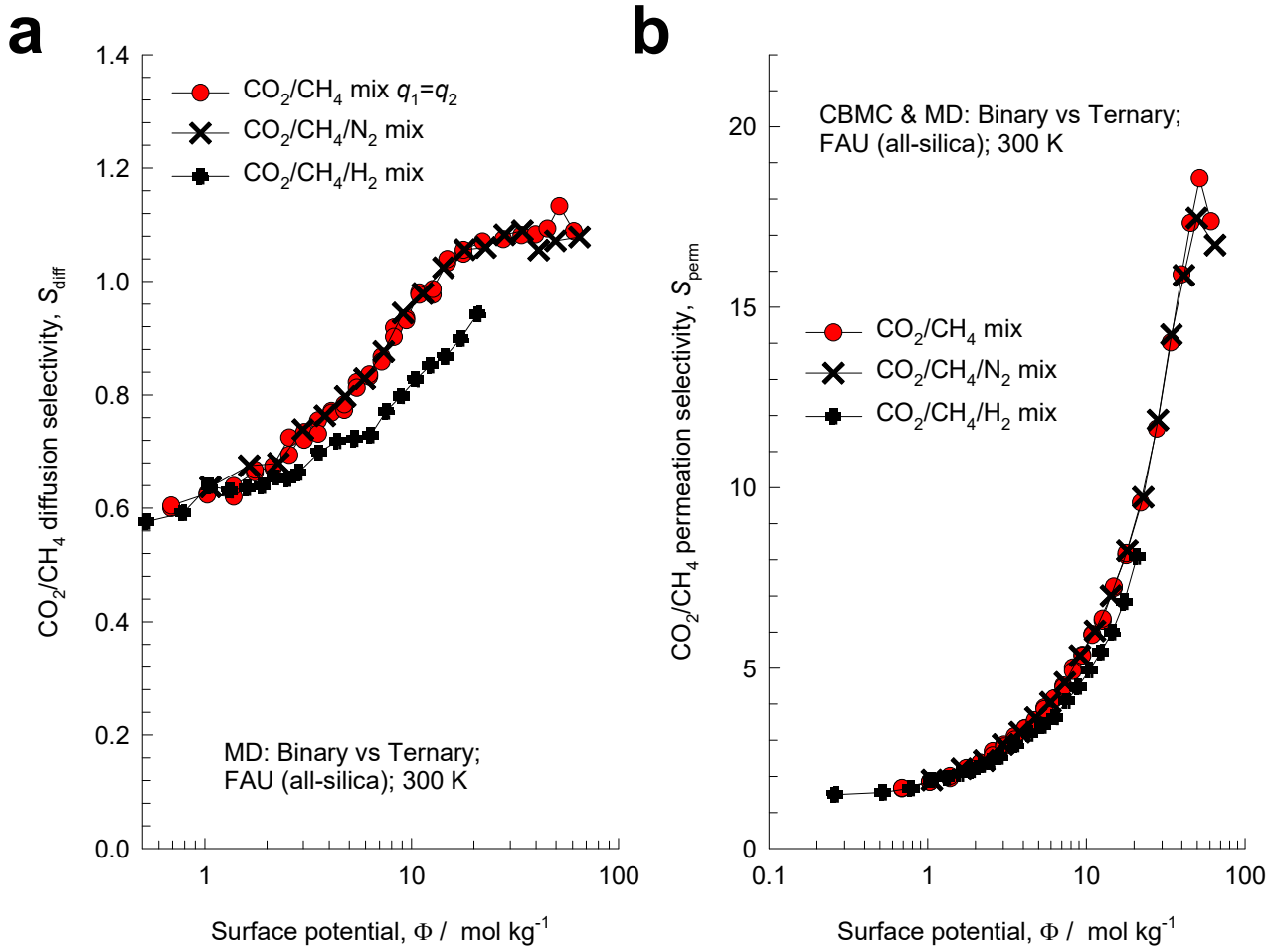

Figure S37. (a) MD simulations of the CO_2/CH_4 diffusion selectivities, S_{diff}, determined from both equimolar $(q_1 = q_2)$ binary mixtures and equimolar $(q_1 = q_2 = q_3)$ ternary ($CO_2/CH_4/N_2$, and $CO_2/CH_4/H_2$) mixtures in all-silica FAU zeolite at 300 K, plotted as function of the surface potential Φ. (b) Plot of the CO_2/CH_4 permeation selectivity S_{perm} as function of the surface potential Φ, determined from binary and ternary ($CO_2/CH_4/N_2$, and $CO_2/CH_4/H_2$) MD campaigns.

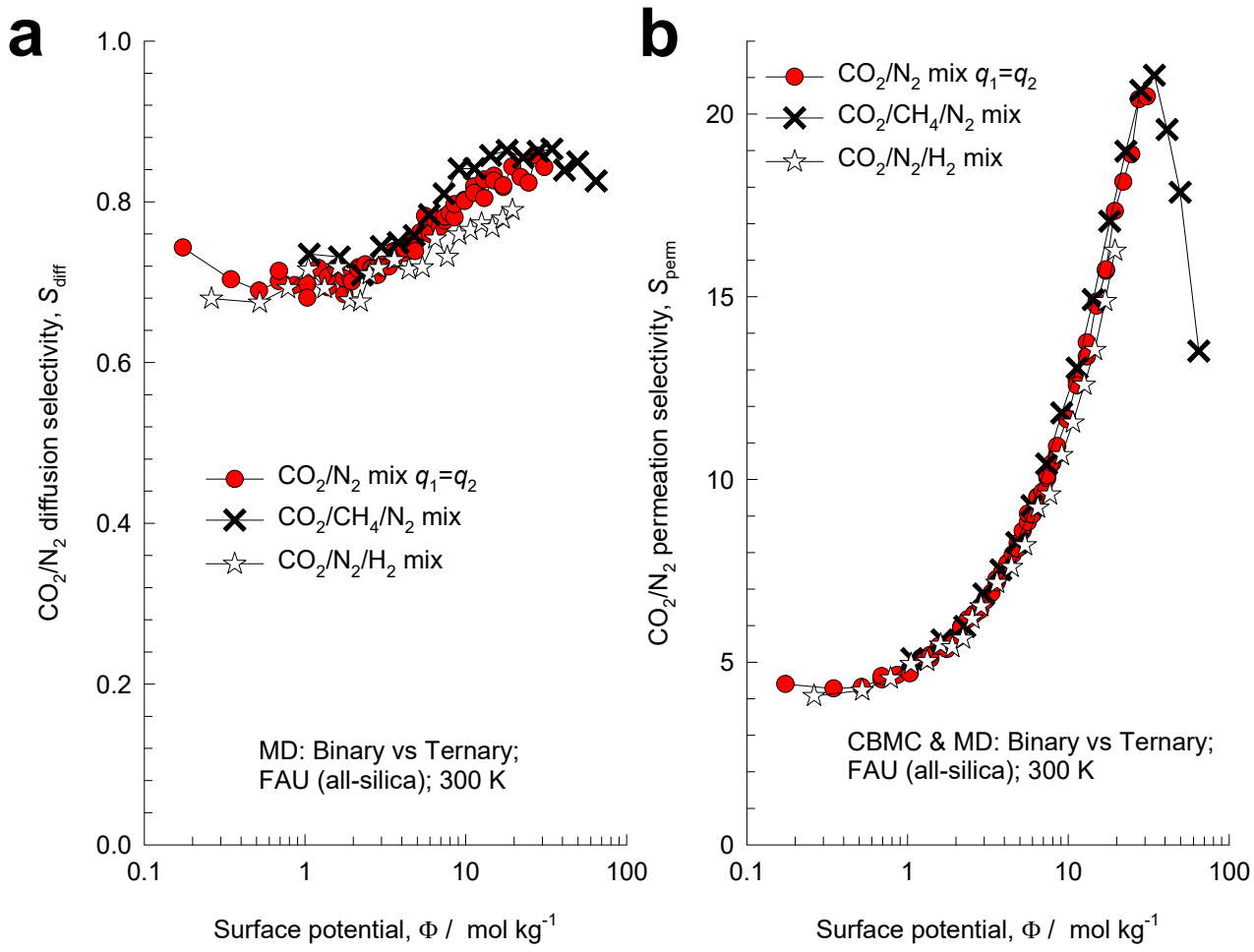

Figure S38. (a) MD simulations of the CO_2/N_2 diffusion selectivities, S_{diff}, determined from both equimolar $(q_1 = q_2)$ binary and equimolar $(q_1 = q_2 = q_3)$ ternary ($CO_2/CH_4/N_2$, and $CO_2/N_2/H_2$) mixtures in all-silica FAU zeolite at 300 K, plotted as function of the surface potential Φ. (b) Plot of the CO_2/N_2 permeation selectivity S_{perm} as function of the surface potential Φ, determined from binary and ternary ($CO_2/CH_4/N_2$, and $CO_2/N_2/H_2$) mixtures MD campaigns.

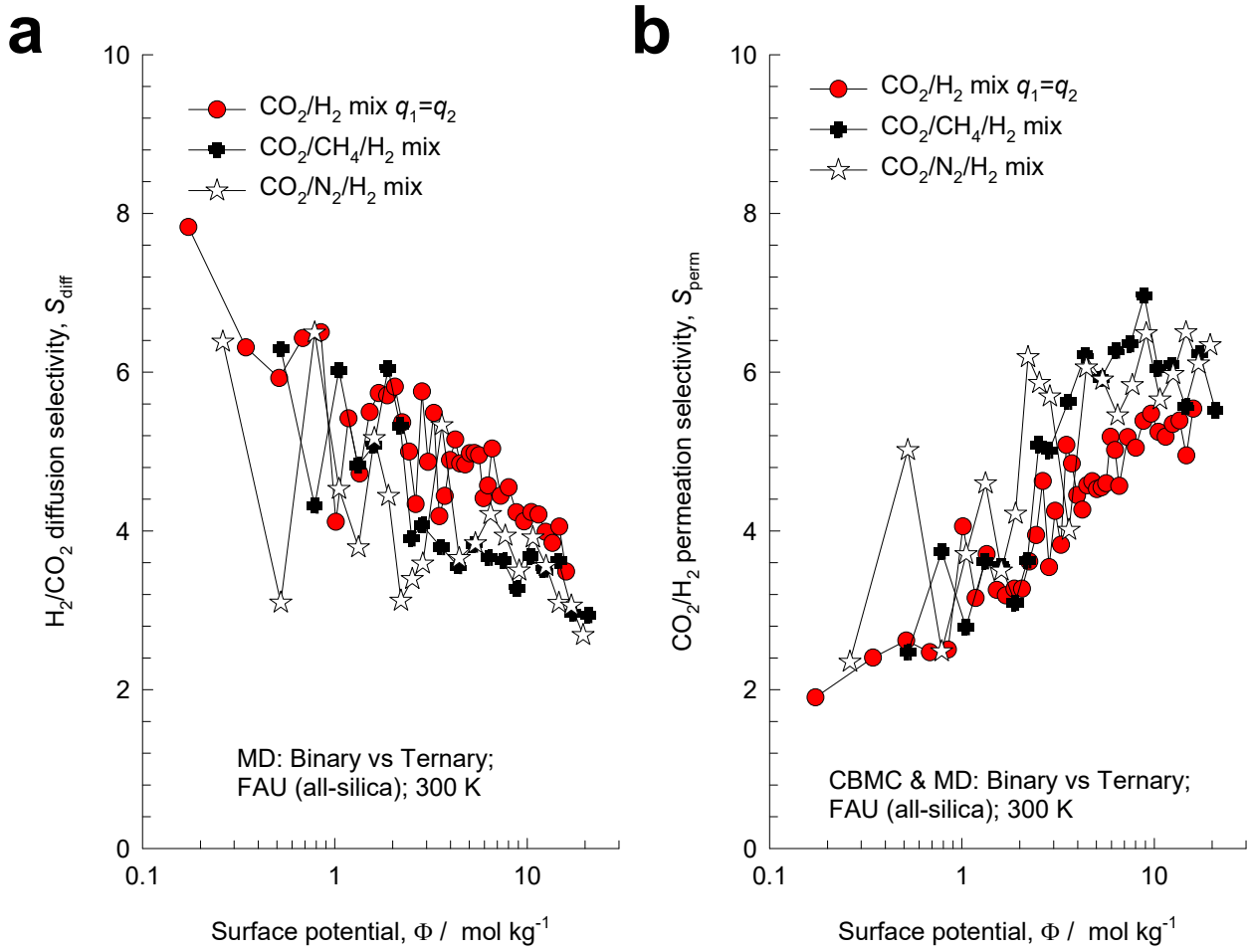

Figure S39. (a) MD simulations of the H_2/CO_2 diffusion selectivities, S_{diff}, determined from both equimolar $(q_1 = q_2)$ binary and equimolar $(q_1 = q_2 = q_3)$ ternary ($CO_2/N_2/H_2$, and $CO_2/CH_4/H_2$) mixtures in all-silica FAU zeolite at 300 K, plotted as function of the surface potential Φ. (b) Plot of the CO_2/H_2 permeation selectivity S_{perm} as function of the surface potential Φ, determined from binary and ternary ($CO_2/N_2/H_2$, and $CO_2/CH_4/H_2$) MD campaigns.

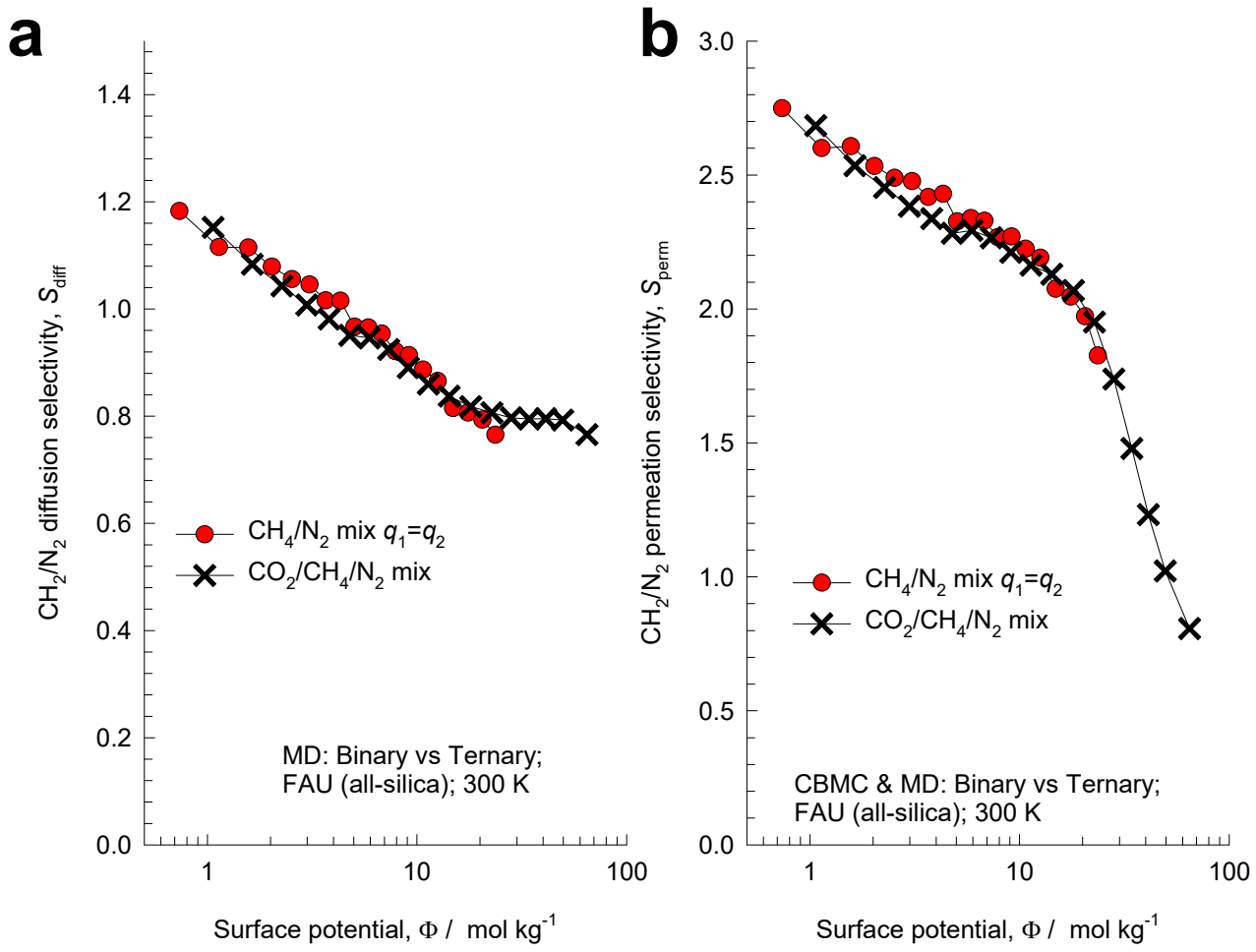

Figure S40. (a) MD simulations of the CH4/N2 diffusion selectivities, S_{diff}, determined from both equimolar $(q_1 = q_2)$ binary and equimolar $(q_1 = q_2 = q_3)$ ternary (CO2/CH4/N2) mixtures in all-silica FAU zeolite at 300 K, plotted as function of the surface potential Φ. (b) Plot of the CH4/N2 permeation selectivity S_{perm} as function of the surface potential Φ, determined from binary and ternary (CO2/CH4/N2) MD campaigns.

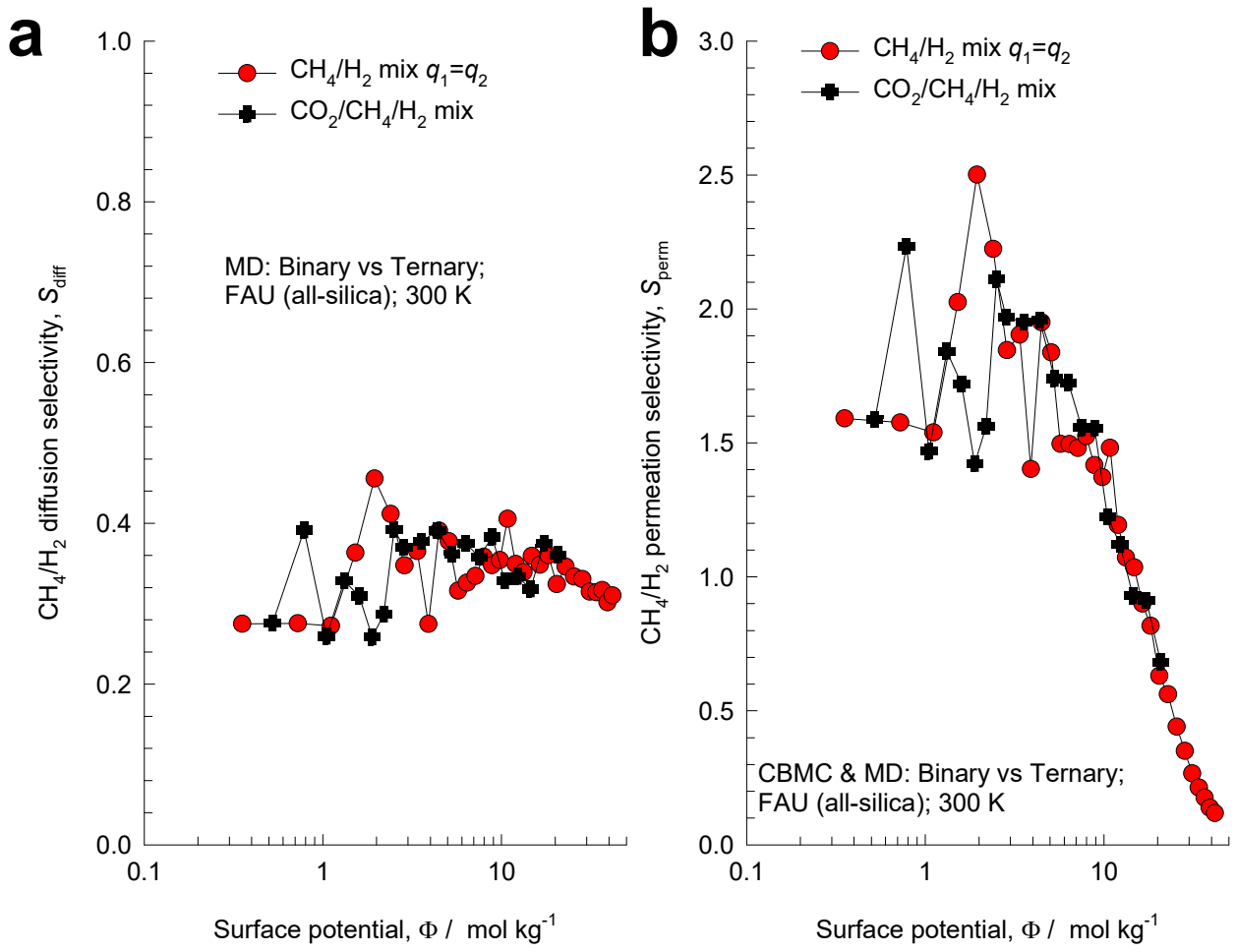

Figure S41. (a) MD simulations of the CH4/H2 diffusion selectivities, S_{diff}, determined from both equimolar $(q_1 = q_2)$ binary and equimolar $(q_1 = q_2 = q_3)$ ternary (CO2/CH4/H2) mixtures in all-silica FAU zeolite at 300 K, plotted as function of the surface potential Φ. (b) Plot of the CH4/H2 permeation selectivity S_{perm} as function of the surface potential Φ, determined from binary and ternary (CO2/CH4/H2) MD campaigns.

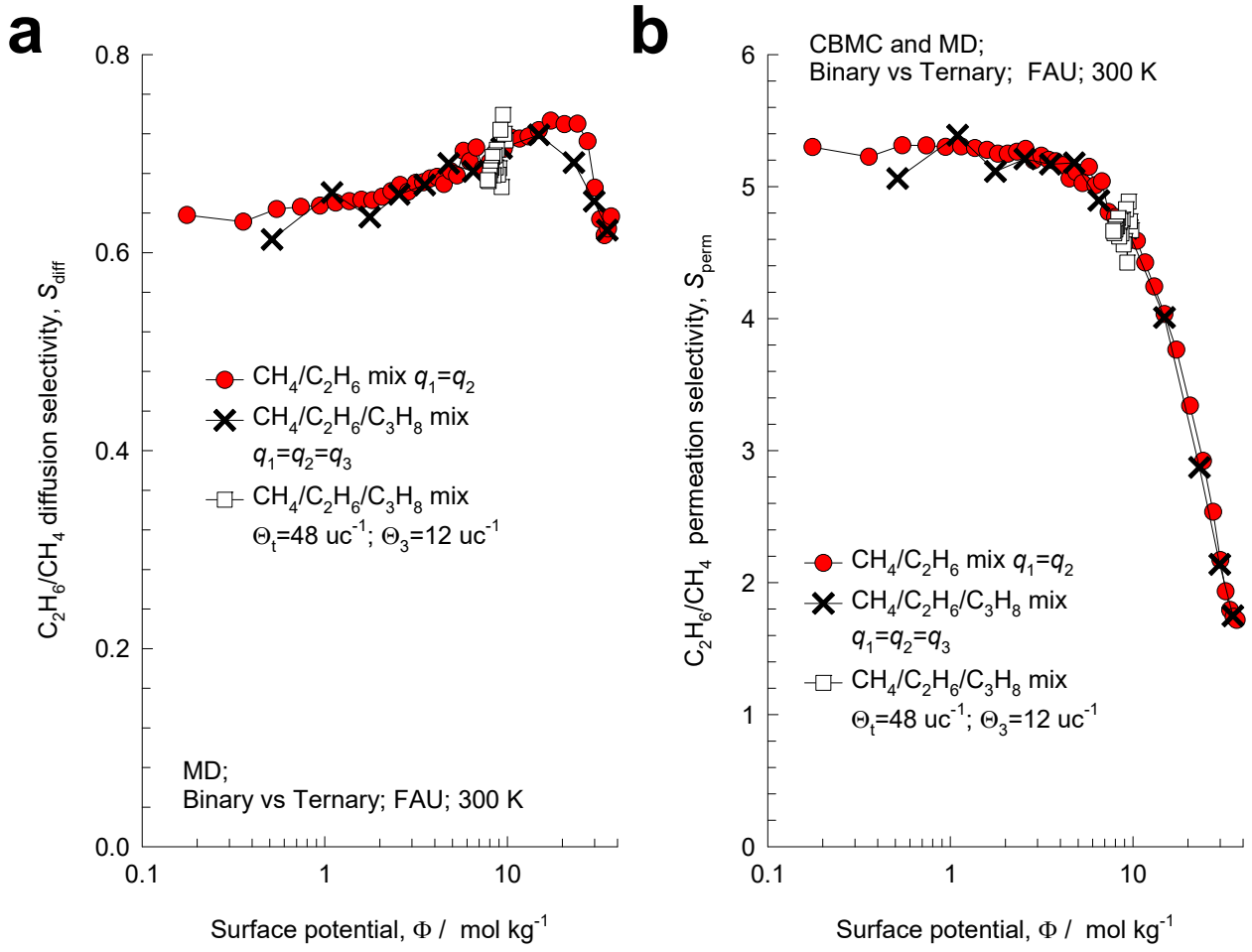

Figure S42. (a) MD simulations of the C_2H_6/CH_4 diffusion selectivities, S_{diff}, determined from both equimolar $(q_1 = q_2)$ binary and equimolar $(q_1 = q_2 = q_3)$ ternary ($CH_4/C_2H_6/C_3H_8$) mixtures in all-silica FAU zeolite at 300 K, plotted as function of the surface potential Φ. (b) Plot of the C_2H_6/CH_4 permeation selectivity S_{perm} as function of the surface potential Φ, determined from binary and ternary ($CH_4/C_2H_6/C_3H_8$) MD campaigns.

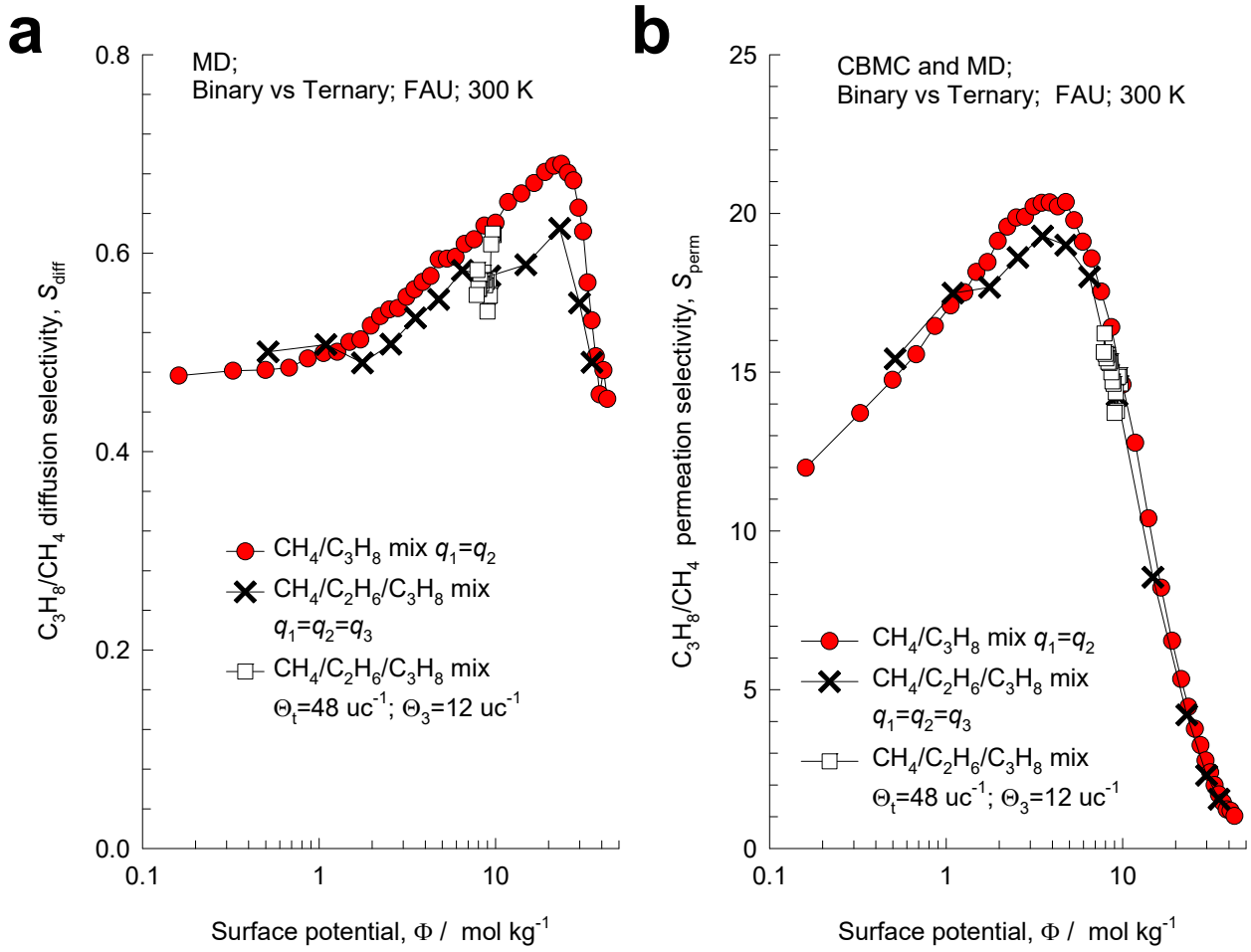

Figure S43. (a) MD simulations of the C_3H_8/CH_4 diffusion selectivities, S_{diff}, determined from both equimolar $(q_1 = q_2)$ binary and equimolar $(q_1 = q_2 = q_3)$ ternary ($CH_4/C_2H_6/C_3H_8$) mixtures in all-silica FAU zeolite at 300 K, plotted as function of the surface potential Φ. (b) Plot of the C_3H_8/CH_4 permeation selectivity S_{perm} as function of the surface potential Φ, determined from binary and ternary ($CH_4/C_2H_6/C_3H_8$) MD campaigns.

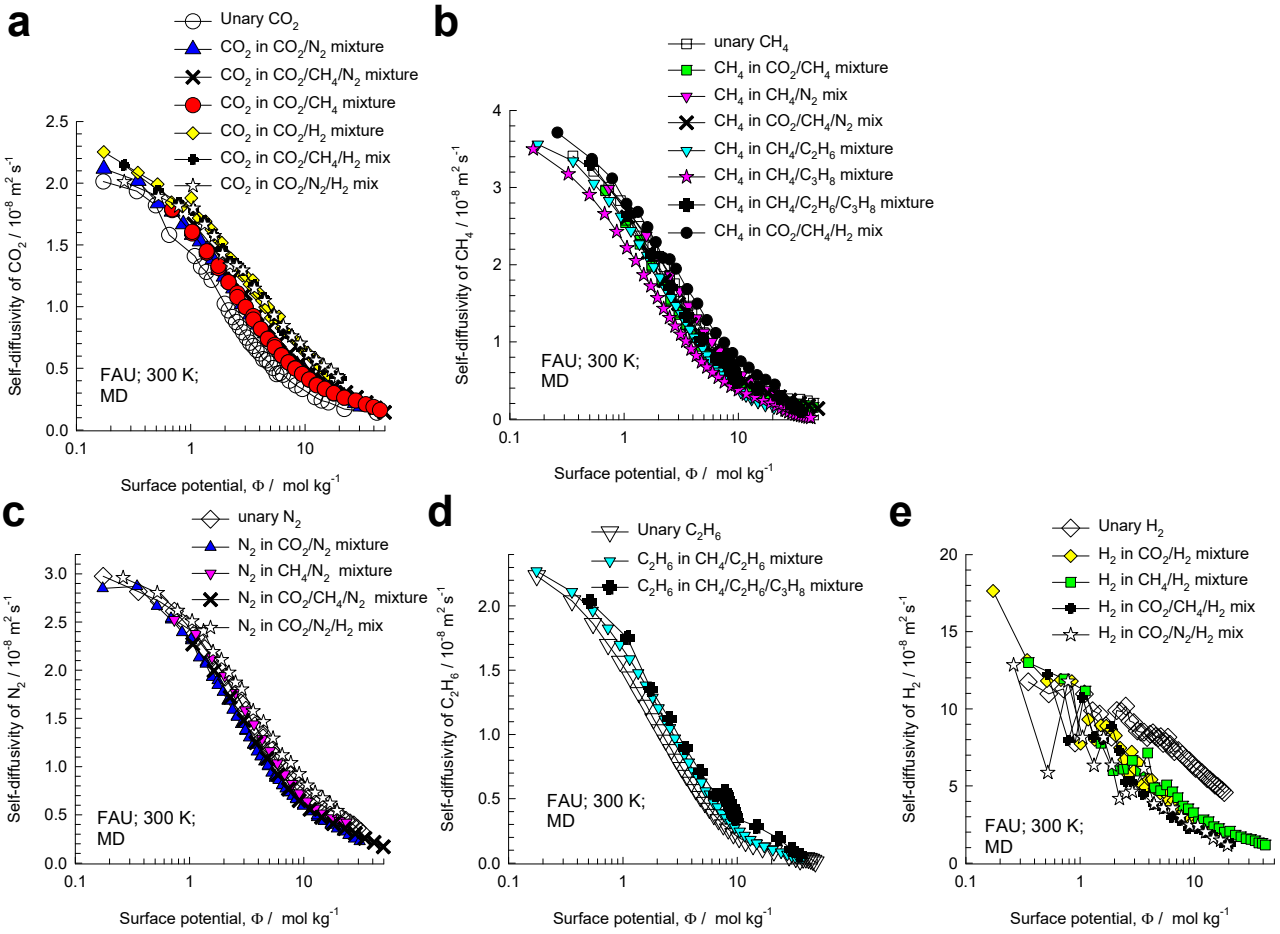

Figure S44. MD simulation data on the self-diffusivities, $D_{i,self}$, of (a) CO_2, (b) CH_4, (c) N_2, (d) C_2H_6, and (e) H_2 in equimolar $q_1 = q_2$; $x_1 = 1 - x_2 = 0.5$ binary CO_2/CH_4, CO_2/N_2, CO_2/H_2, CH_4/N_2, CH_4/H_2, CH_4/C_2H_6, CH_4/C_3H_8, and C_2H_6/C_3H_8 mixtures and equimolar $(q_1 = q_2 = q_3)$ ternary $CO_2/CH_4/N_2$, $CO_2/CH_4/H_2$, $CO_2/N_2/H_2$, and $CH_4/C_2H_6/C_3H_8$ mixtures in FAU zeolite at 300 K, plotted as a function of the surface potential Φ. Also plotted are the corresponding values of the unary self-diffusivities.

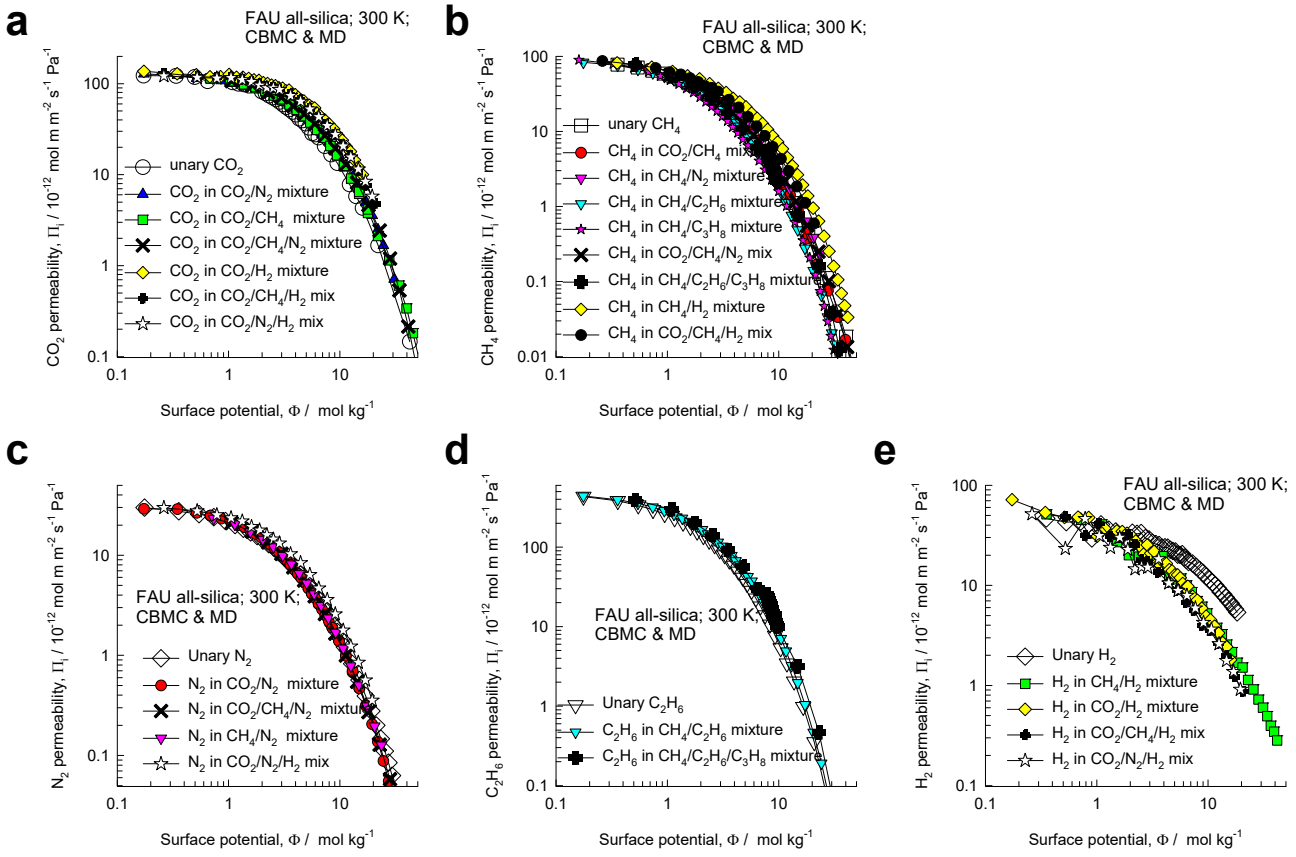

Figure S45. CBMC/MD simulations of the permeabilities, Π_i, of (a) CO_2, (b) CH_4, (c) N_2, (d) C_2H_6, and (e) H_2 in equimolar $q_1 = q_2$; $x_1 = 1 - x_2 = 0.5$ binary CO_2/CH_4, CO_2/N_2, CO_2/H_2, CH_4/N_2, CH_4/H_2, CH_4/C_2H_6, CH_4/C_3H_8, and C_2H_6/C_3H_8 mixtures and equimolar $(q_1 = q_2 = q_3)$ ternary $CO_2/CH_4/N_2$, $CO_2/CH_4/H_2$, $CO_2/N_2/H_2$, and $CH_4/C_2H_6/C_3H_8$ mixtures in FAU zeolite at 300 K, plotted as a function of the surface potential Φ. Also plotted are the corresponding values of the unary permeabilities.

8 Adsorption, Diffusion, Permeation in NaX, and NaY zeolites

8.1 Mixture adsorption in cation-exchanged NaX (=13X) zeolite

Figure S46a shows CBMC simulation data of the adsorption selectivity, S_{ads}, for CO_2(1)/CH_4(2) mixtures in NaX zeolite at 300 K, determined from five different campaigns:

(i) the bulk gas phase mole fractions are maintained at y_1 =0.05, and the total mixture fugacity $f_t = f_1 + f_2$ is varied up to $f_t = 10$ MPa at which pore saturation conditions are approached,

(ii) the bulk gas phase mole fractions are maintained at $y_1 = 0.10$, and the total mixture fugacity $f_t = f_1 + f_2$ is varied up to $f_t = 10$ MPa at which pore saturation conditions are approached,

(iii) the bulk gas phase mole fractions are maintained at y_1 =0.20, and the total mixture fugacity $f_t = f_1 + f_2$ is varied up to $f_t = 10$ MPa at which pore saturation conditions are approached,

(iv) the bulk gas phase mole fractions are maintained at y_1 =0.50, and the total mixture fugacity $f_t = f_1 + f_2$ is varied up to $f_t = 10$ MPa at which pore saturation conditions are approached,

(v) the total bulk gas mixture fugacity is held constant, $f_t = f_1 + f_2 = 10^5$ Pa, and the mole fraction of the bulk gas mixture of CO_2(1), y_1, is varied from 0 to 1

For all five CBMC data sets, the CBMC simulated values of the adsorption selectivity, S_{ads}, follows a near-unique dependence on the surface potential Φ, see Figure S46a. CBMC simulations were also performed for 20/40/40 CO_2/CH_4/N_2 and 5/25/70 CO_2/CH_4/N_2 mixtures in NaX zeolite at 300 K, in which the bulk gas phase mole fractions are maintained constant and the total mixture fugacity $f_t = f_1 + f_2 + f_3$ is varied up to $f_t = 10$ MPa. The values of the CO_2/CH_4 adsorption selectivity in the ternary mixture are

also plotted in Figure S46a. The ternary CBMC data follows the same unique dependence on Φ. Put another way, the presence of component 3 in the ternary mixture has no influence of the adsorption selectivity for the 1-2 pair.

The IAST calculations (indicated by dashed lines in Figure S46a) of the adsorption selectivity show large deviations from the CBMC simulated data due to congregation of the CO_2 molecules around the Na^+ cations; detailed explanations are provided in our earlier works. [26, 28, 44, 50, 51] With the introduction of activity coefficients, the expression for the adsorption selectivity for the $CO_2(1)/CH_4(2)$ pair in binary and ternary mixtures is

$$S_{ads,12} = \frac{q_1/q_2}{f_1/f_2} = \frac{x_1/f_1}{x_2/f_2} = \frac{P_2^0\gamma_2}{P_1^0\gamma_1} \tag{S75}$$

Using the CBMC data for binary and ternary mixture adsorption, the activity coefficients of $CO_2(1)$ and $CH_4(2)$ were determined for both binary and ternary mixtures. Figure S46b plots the ratio of the activity coefficient of $CO_2(1)$ to that of $CH_4(2)$, $\frac{\gamma_1}{\gamma_2}$, as a function of Φ. We note that $\frac{\gamma_1}{\gamma_2}$ for both binary and ternary mixtures are of comparable magnitudes when plotted as a function of Φ. For this reason, the CO_2/CH_4 adsorption selectivity shows a unique dependence on Φ, despite the significant deviations from IAST estimates.

Figure S47a,b plot data obtained from CBMC simulations of the CO_2/N_2 and CH_4/N_2 adsorption selectivities in binary and ternary $CO_2/CH_4/N_2$ in NaX zeolite at 300 K. The CO_2/N_2 and CH_4/N_2 adsorption selectivities for binary and ternary mixtures display unique dependence on Φ, despite the fact that the IAST estimates are not in perfect agreement with CBMC data.

Figure S48ab plot data obtained from CBMC simulations of the CO_2/C_3H_8 and C_3H_8/CH_4 adsorption selectivities in binary mixtures and ternary $CO_2/CH_4/C_3H_8$ mixtures in NaX zeolite at 300 K. The CO_2/C_3H_8 and C_3H_8/CH_4 adsorption selectivities for binary and ternary mixtures display unique dependence on Φ, in line with the IAST precepts.

8.2 Component self-diffusivities and permeabilities in NaX, and NaY zeolites

Figure S49 presents MD simulation data on the self-diffusivities, $D_{i,self}$, of (a) CO_2, (b) CH_4, (c) N_2, and (d) H_2 in equimolar $q_1 = q_2$; $x_1 = 1 - x_2 = 0.5$ binary CO_2/CH_4, CO_2/N_2, CO_2/H_2, CH_4/H_2, CH_4/C_2H_6, and CH_4/C_3H_8 mixtures in NaX zeolite, plotted as a function of the surface potential Φ. Also plotted are the corresponding values of the unary self-diffusivities. Except for H_2, the self-diffusivities in the binary mixtures are also nearly the same as the unary self-diffusivities. The unary self-diffusivity for H_2, is larger in value for those in mixtures. The lowering of the H_2 self-diffusivity in mixtures is attributable to correlation effects, that slows-down the more mobile H_2.

Figure S50 presents data on the permeabilities, Π_i, of a) CO_2, (b) CH_4, (c) N_2, and (d) H_2 in equimolar $q_1 = q_2$; $x_1 = 1 - x_2 = 0.5$ binary CO_2/CH_4, CO_2/N_2, CO_2/H_2, CH_4/H_2, CH_4/C_2H_6, an CH_4/C_3H_8 mixtures in NaX zeolite, plotted as a function of the surface potential Φ. Also plotted are the corresponding values of the unary permeabilities. Except for H_2, the permeabilities in the binary mixtures are nearly the same as the unary permeabilities. The unary permeability for H_2, appears to be larger in value for those in mixtures. The lowering of the H_2 permeabilities in mixtures is attributable to correlation effects, that slows-down the more mobile H_2.

Figure S51 presents MD simulation data on the self-diffusivities, $D_{i,self}$, of (a) CO_2, (b) CH_4, (c) N_2, and (d) H_2 in equimolar $q_1 = q_2$; $x_1 = 1 - x_2 = 0.5$ binary CO_2/CH_4, CO_2/N_2, CO_2/H_2, CH_4/H_2, CH_4/C_2H_6, and CH_4/C_3H_8 mixtures in NaY zeolite, plotted as a function of the surface potential Φ. Also plotted are the corresponding values of the unary self-diffusivities. Except for H_2, the self-diffusivities in the binary mixtures are also nearly the same as the unary self-diffusivities. The unary self-diffusivity for H_2, is larger in value for those in mixtures. The lowering of the H_2 self-diffusivity in mixtures is attributable to correlation effects, that slows-down the more mobile H_2.

Figure S52 presents data on the permeabilities, Π_i, of a) CO_2, (b) CH_4, (c) N_2, and (d) H_2 in equimolar $q_1 = q_2$; $x_1 = 1 - x_2 = 0.5$ binary CO_2/CH_4, CO_2/N_2, CO_2/H_2, CH_4/H_2, CH_4/C_2H_6, an CH_4/C_3H_8 mixtures

in NaY zeolite, plotted as a function of the surface potential Φ . Also plotted are the corresponding values of the unary permeabilities. Except for H_2, the permeabilities in the binary mixtures are nearly the same as the unary permeabilities. The unary permeability for H_2, appears to be larger in value for those in mixtures. The lowering of the H_2 permeabilities in mixtures is attributable to correlation effects, that slows-down the more mobile H_2.

8.3 List of Tables for Adsorption, Diffusion, Permeation in NaX, and NaY zeolites

Table S3. Dual-site Langmuir-Freundlich parameters for pure components at 300 K in NaX zeolite containing 86 Na^+/uc with Si/Al=1.23. The fit parameters are based on the CBMC simulations of pure component isotherms.

	Site A			Site B		
	$q_{A,sat}$ mol kg^{-1}	b_A Pa$^{-\nu_A}$	ν_A dimensionless	$q_{B,sat}$ mol kg^{-1}	b_B Pa$^{-\nu_B}$	ν_B dimensionless
CO_2	1.7	1.390E-05	1	4.2	0.000478244	1
CH_4	2.3	1.24E-08	1	5.5	0.00000217	1
N_2	9.8	2.136E-09	0.96	4.2	1.224E-07	1
H_2	10.5	8.38E-09	1	2.2	3.14856E-08	1
C_2H_6	4.173	1.23E-05	1.1	1.267	9.24E-06	0.72
C_3H_8	2.2	1.194E-04	1.46	1.6	1.15E-03	0.66

Table S4. Dual-site Langmuir-Freundlich parameters for pure components at 300 K in NaY zeolite containing 54 Na^+/uc. The fit parameters are based on the CBMC simulations of pure component isotherms.

	Site A			Site B		
	$q_{A,sat}$ mol kg^{-1}	b_A $Pa^{-\nu_A}$	ν_A dimensionless	$q_{B,sat}$ mol kg^{-1}	b_B $Pa^{-\nu_B}$	ν_B dimensionless
CO_2	1.8	2.002E-05	0.7	5.9	4.15803E-05	1
CH_4	3.4	6.53E-09	1	5.9	1.134E-06	1
N_2	9.8	1.33E-09	1	4.2	1.472E-07	1
H_2	14	9.552E-09	1	2.4	3.0667E-08	1
C_2H_6	1.43	6.76E-09	1.8	3.257	1.08E-05	1
C_3H_8	1.033	5.68E-09	2.48	2.78	1.20E-04	1

8.4 List of Figures for Adsorption, Diffusion, Permeation in NaX, and NaY zeolites

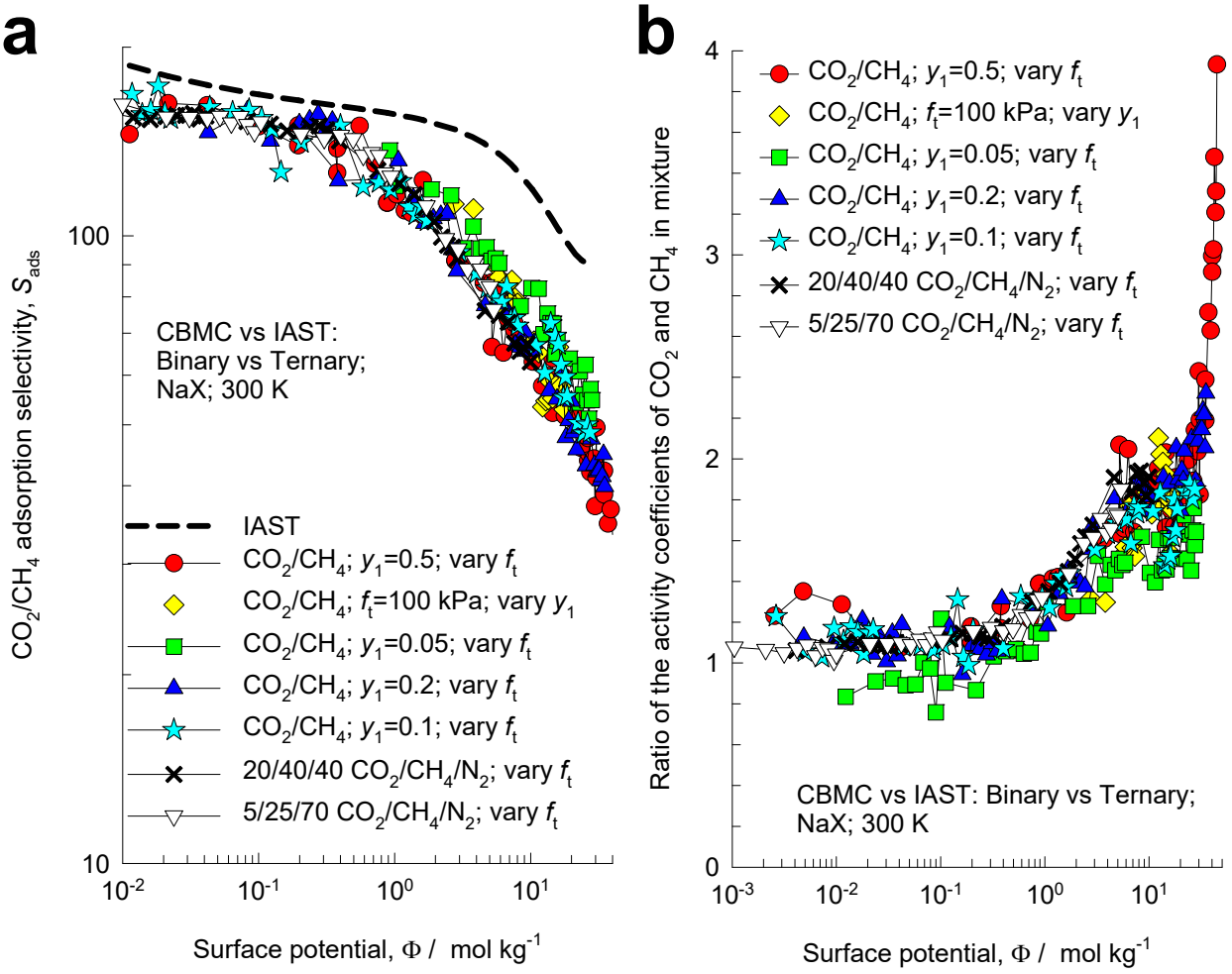

Figure S46. (a) CBMC simulations of the CO_2/CH_4 adsorption selectivity, S_{ads}, for binary and ternary mixture adsorption in NaX zeolite at 300 K. The adsorption selectivities are plotted as function of the surface potential Φ. The dashed lines are the IAST calculations; the unary isotherm fit parameters are provided in Table S3. (b) CBMC simulations of the ratio of activity coefficients of CO_2, and CH_4 plotted as function of the surface potential Φ.

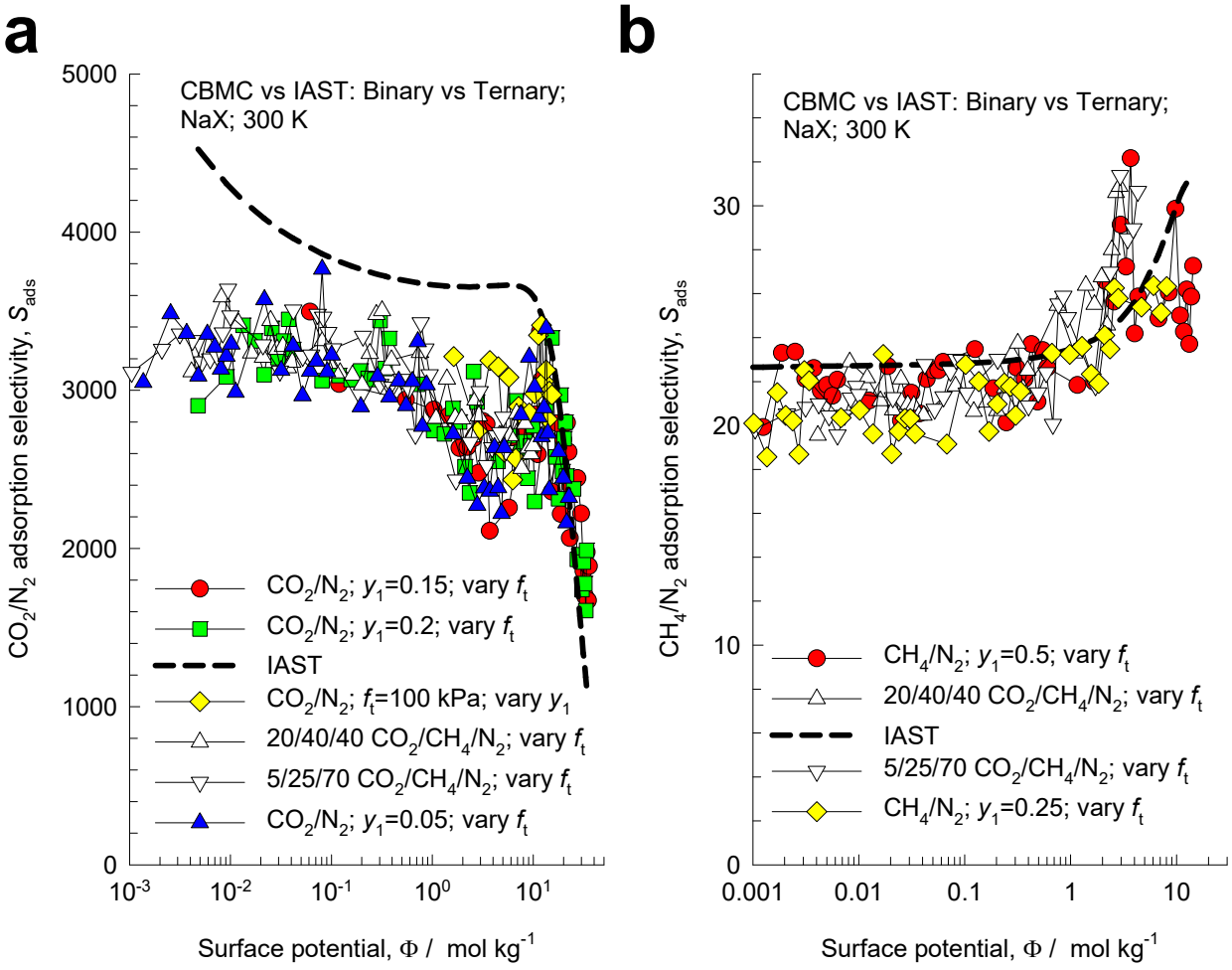

Figure S47. (a) CBMC simulations of the CO_2/N_2 adsorption selectivity, S_{ads}, for binary and ternary mixture adsorption in NaX zeolite at 300 K. (b) CBMC simulations of the CH_4/N_2 adsorption selectivities in binary and ternary mixtures in NaX zeolite at 300 K. The selectivities are plotted as function of the surface potential Φ. The dashed lines are the IAST calculations; the unary isotherm fit parameters are provided in Table S3.

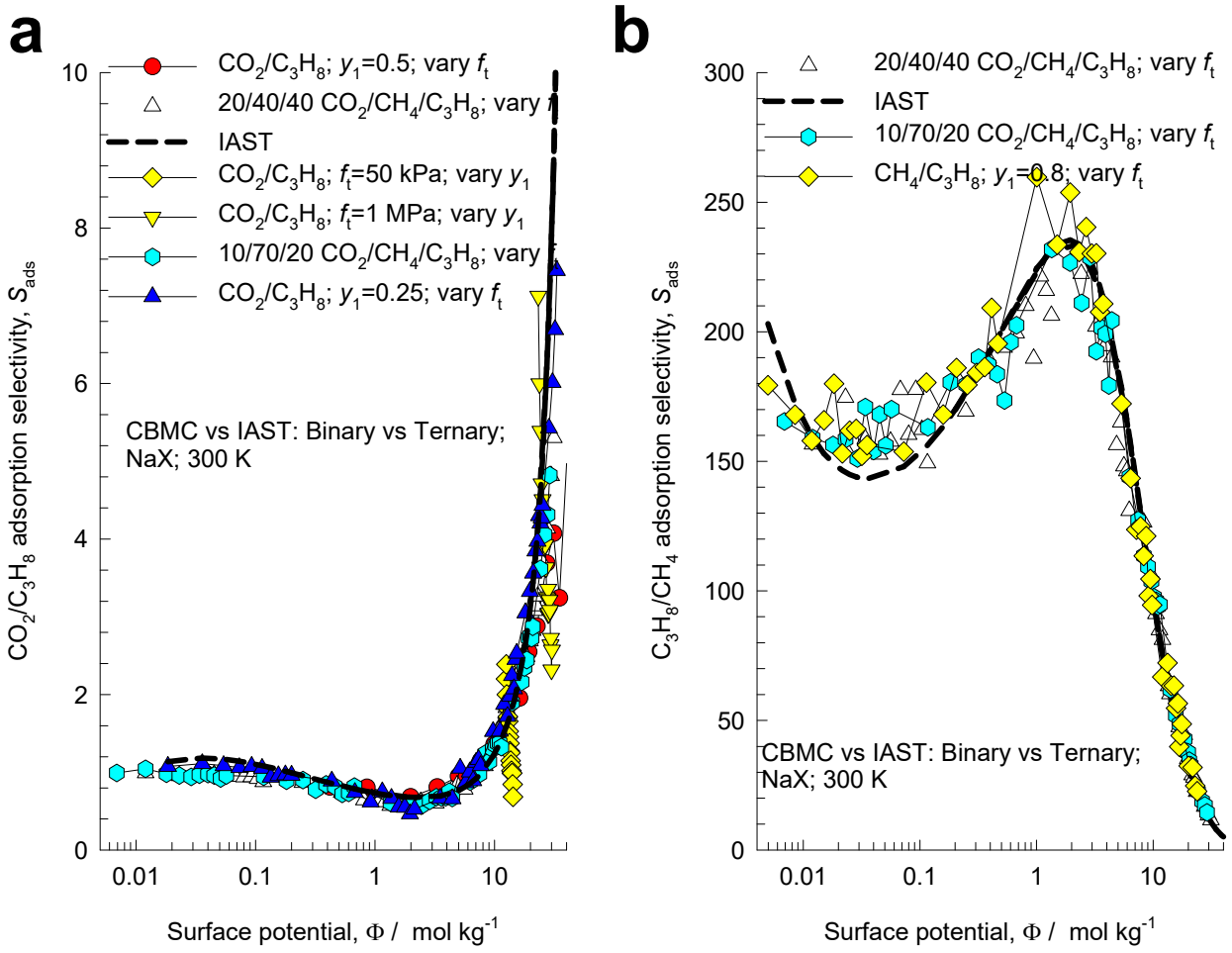

Figure S48. (a) CBMC simulations of the CO_2/C_3H_8 adsorption selectivity, S_{ads}, for binary and ternary mixture adsorption in NaX zeolite at 300 K. (b) CBMC simulations of the C_3H_8/CH_4 adsorption selectivities in binary and ternary mixtures in NaX zeolite at 300 K. The selectivities are plotted as function of the surface potential Φ. The dashed lines are the IAST calculations; the unary isotherm fit parameters are provided in Table S3.

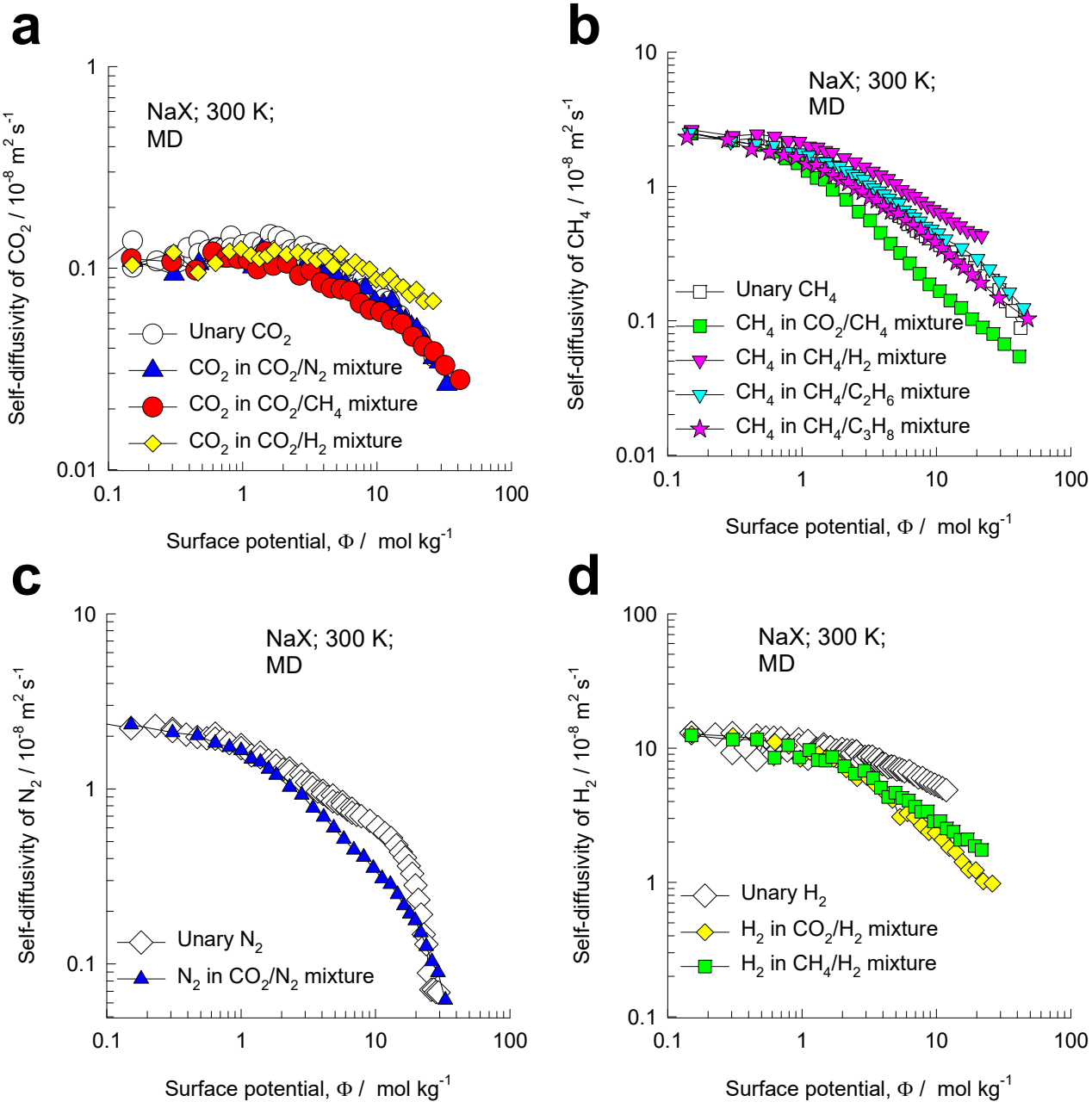

Figure S49. MD simulation data on the self-diffusivities, $D_{i,self}$, of (a) CO_2, (b) CH_4, (c) N_2, and (d) H_2 in binary CO_2/CH_4, CO_2/N_2, CO_2/H_2, CH_4/H_2, CH_4/C_2H_6, and CH_4/C_3H_8 mixtures in NaX zeolite at 300 K, plotted as a function of the surface potential Φ. Also plotted are the corresponding values of the unary self-diffusivities.

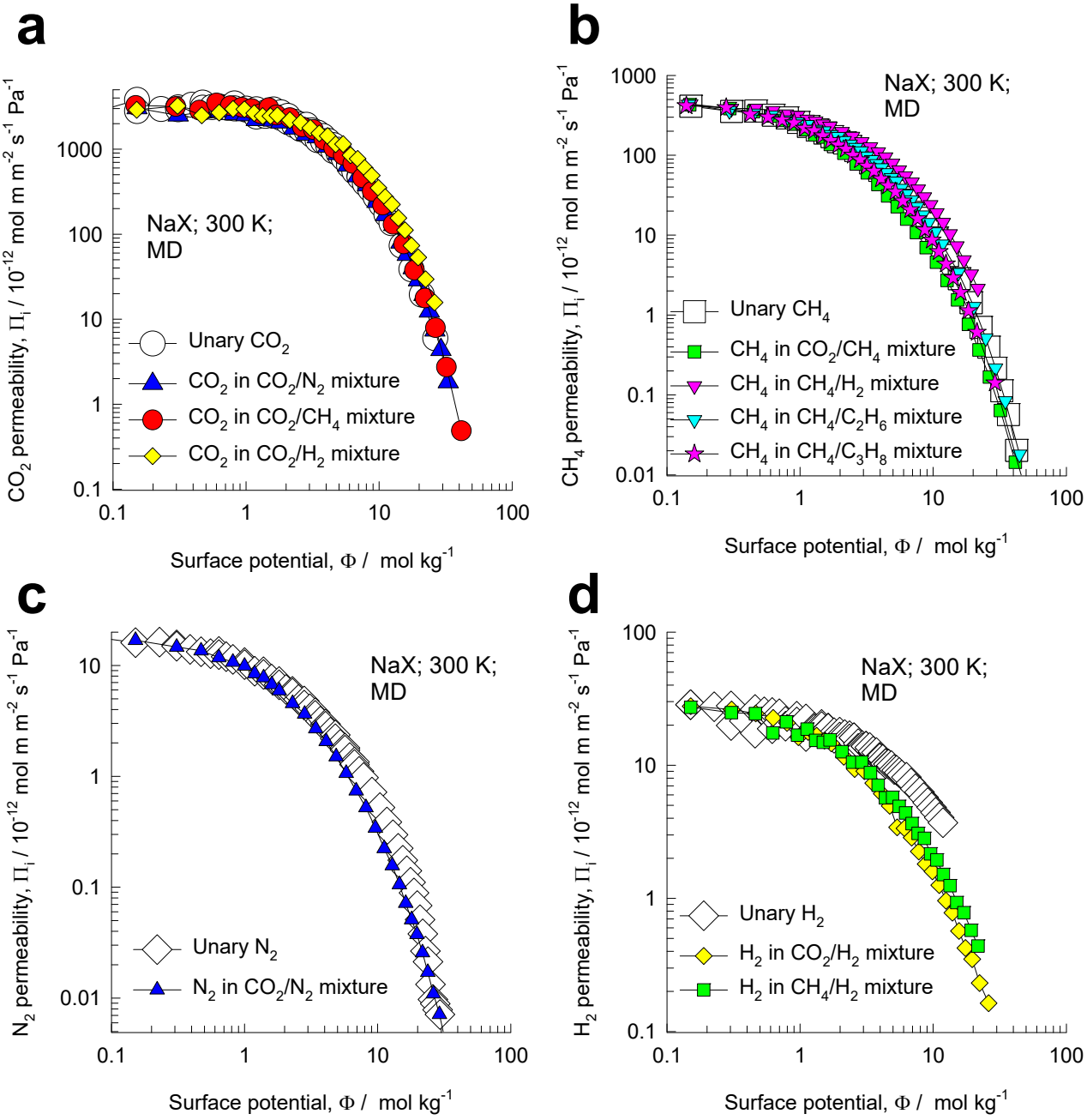

Figure S50. CBMC/MD simulations of the permeabilities, Π_i, of (a) CO_2, (b) CH_4, (c) N_2, and (d) H_2 in binary CO_2/CH_4, CO_2/N_2, CO_2/H_2, CH_4/H_2, CH_4/C_2H_6, and CH_4/C_3H_8 mixtures in NaX zeolite at 300 K, plotted as a function of the surface potential Φ. Also plotted are the corresponding values of the unary permeabilities.

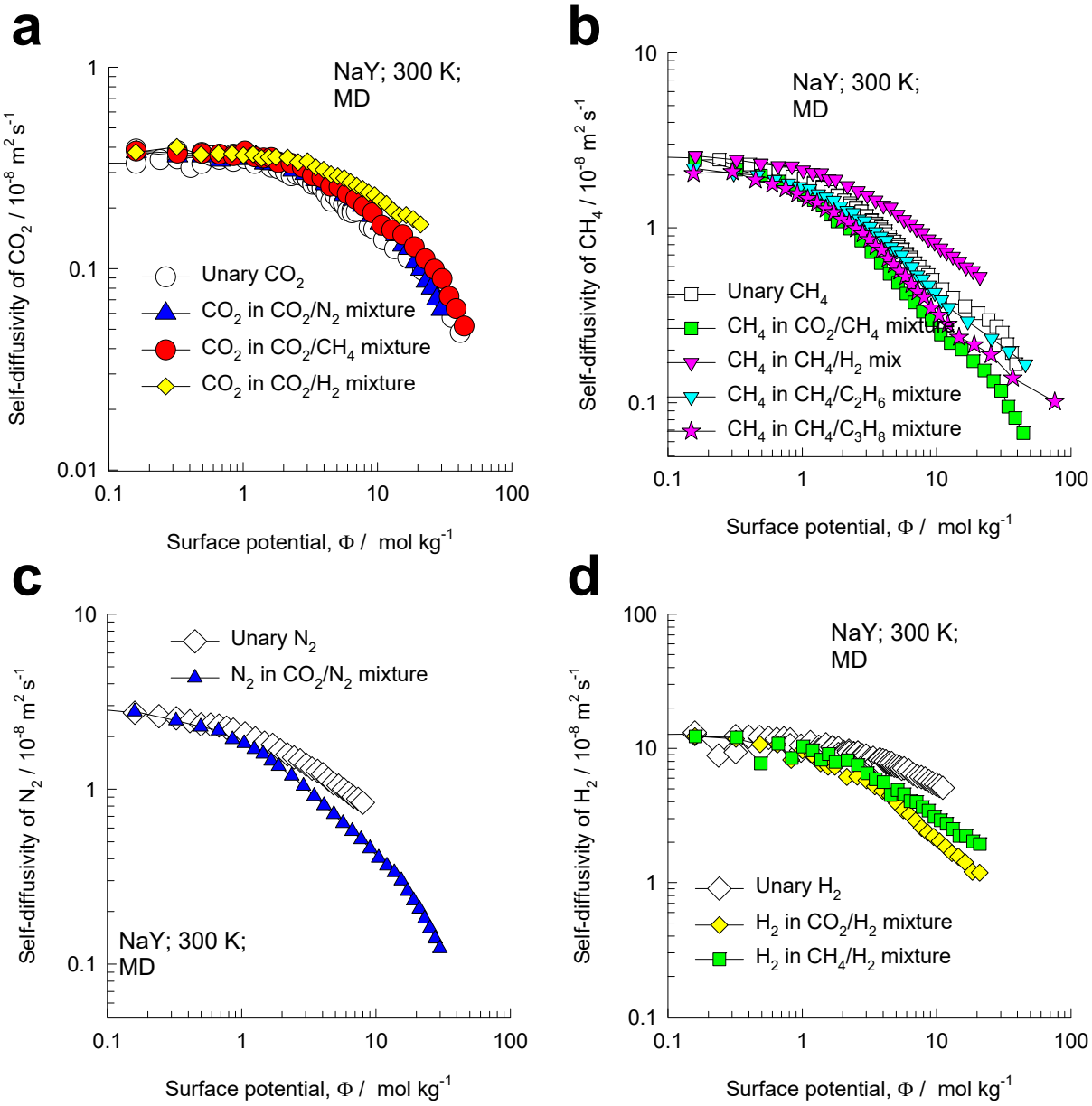

Figure S51. MD simulation data on the self-diffusivities, $D_{i,self}$, of (a) CO_2, (b) CH_4, (c) N_2, and (d) H_2 in binary CO_2/CH_4, CO_2/N_2, CO_2/H_2, CH_4/H_2, CH_4/C_2H_6, and CH_4/C_3H_8 mixtures in NaY zeolite at 300 K, plotted as a function of the surface potential Φ. Also plotted are the corresponding values of the unary self-diffusivities.

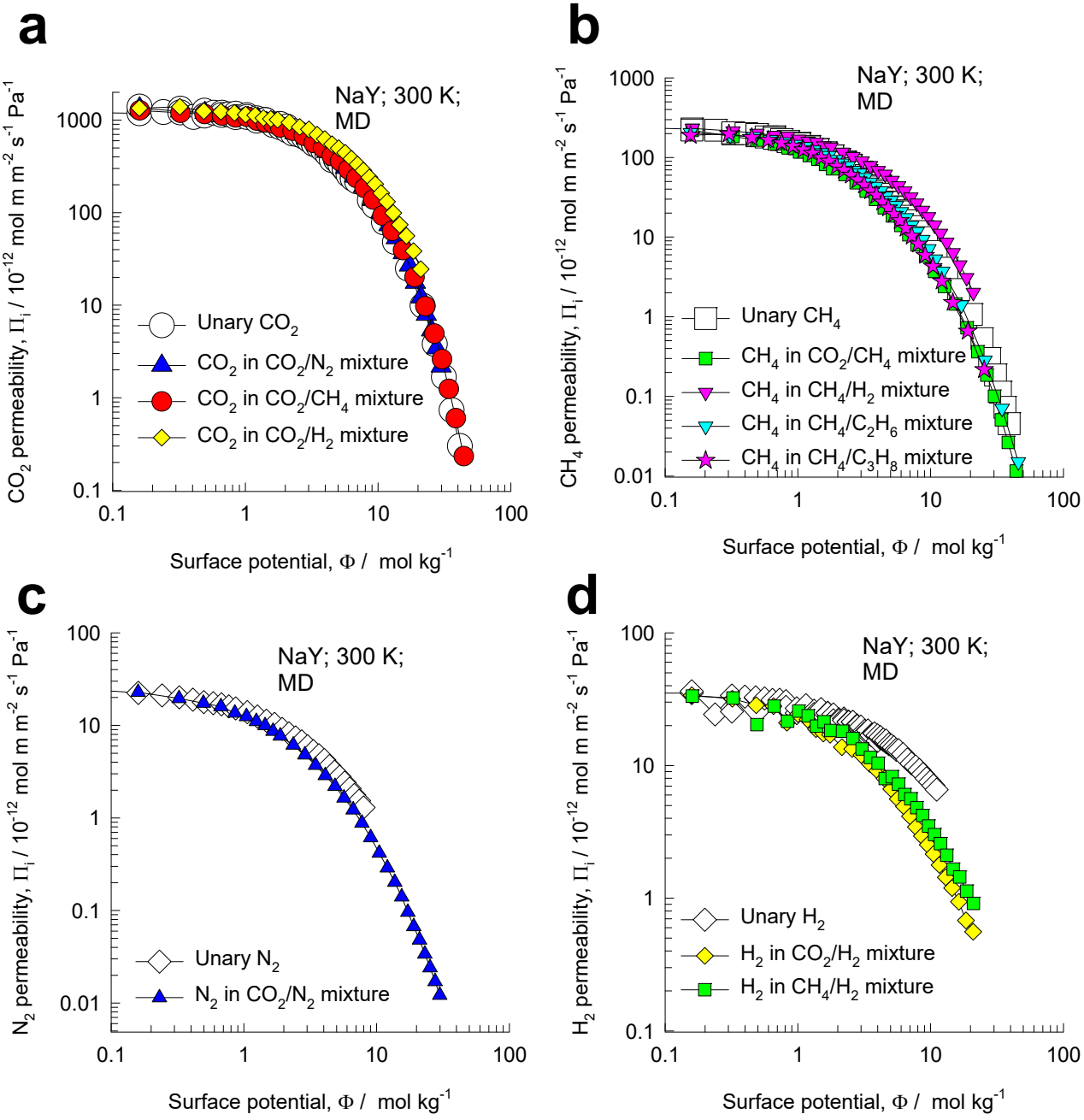

Figure S52. CBMC/MD simulations of the permeabilities, Π_i, of (a) CO_2, (b) CH_4, (c) N_2, and (d) H_2 in binary CO_2/CH_4, CO_2/N_2, CO_2/H_2, CH_4/H_2, CH_4/C_2H_6, and CH_4/C_3H_8 mixtures in NaY zeolite at 300 K, plotted as a function of the surface potential Φ. Also plotted are the corresponding values of the unary permeabilities

9 Comparing FAU (all-silica) with NaY and NaX zeolites

Figure S53 compares the CBMC simulations of the unary isotherms for (a) CO_2, and (b) CH_4 in FAU (all-silica), NaY, and NaX zeolites, determined at 300 K. For CO_2, the molar loadings, q, increases with increasing number of extra-framework cations. At a bulk gas fugacity f = 1 kPa, the molar loadings of CO_2 in FAU, NaY, and NaX zeolites are, respectively, 0.044, 0.25, and 1.26 mol kg^{-1}. This implies that a significantly larger amount of CO_2 may be captured by increasing the number of extra-framework Na^+ cations from 0 to 86 per unit cell.

There is a disadvantage in increasing the number of extra-framework Na^+ cations. In the desorption phase, if the molar loadings are to be reduced to say 0.01 mol kg^{-1}, the required pressure needs to be as low as 2000 Pa, 300 Pa, and 5 Pa, respectively. In other words, significantly deeper vacuum is required for operating with NaY, and NaX zeolites.

The isosteric heats of adsorption, Q_{st}, reflect the binding energy of guest molecules. The stronger the degree of binding, the higher is the value of Q_{st}. We should therefore expect Q_{st} to increase with the number of extra-framework cations. Figure S54, and Figure S55 present CBMC simulations of the isosteric heats of adsorption, Q_{st}, of CO_2, CH_4, N_2, and H_2 in FAU (all-silica), NaY, and NaX zeolites, plotted as functions of both the surface potential Φ. For CO_2, the Q_{st} increases with increasing number of extra-framework cations. For CH_4, the Q_{st} also increases with increasing number of extra-framework cations, but the increase is far less significant; the same holds for N_2, and H_2.

A different way of interpreting Q_{st} is to consider this quantity to represent the "stickiness" of the guest molecule. We should expect the intra-crystalline diffusivities to decrease as the stickiness of the guest increases. Figure S56 compares MD simulations of the self-diffusivities, $D_{i,self}$, of (a) CO_2, and (b) CH_4

in FAU (all-silica), NaY, and NaX zeolites Indeed, we note that the self-diffusivities of CO_2 are significantly reduced with increasing number of framework cations. The corresponding influence on the self-diffusivities of CH_4 is much lower, nearly negligible. In Figure S57, the self-diffusivities, $D_{i,self}$, of (a) CO_2, and (b) CH_4 in FAU (all-silica), NaY, and NaX zeolites are plotted as functions of both the surface potential Φ, and the isosteric heats of adsorption, Q_{st}. The diffusivities decrease with increasing binding strength, quantified by Q_{st}. The diffusivities also decrease with increasing pore occupancy, reflected by the surface potential Φ.

Figure S58 presents the comparison of the Maxwell-Stefan diffusivities, $Đ_i$, of (a) CO_2, and (b) CH_4 in FAU (all-silica), NaY, and NaX zeolites. The same conclusions hold for $Đ_i$. The higher the Q_{st}, the lower is the value of $D_{i,self}$ and $Đ_i$.

Figure S59 presents a comparison of CBMC and MD simulations of (a) adsorption selectivities, S_{ads}, (b) diffusion selectivities, S_{diff}, and (c) permeation selectivities, S_{perm}, of $CO_2(1)/CH_4(2)$ mixtures in FAU, NaY, and NaX zeolites at 300 K. The selectivities are plotted as function of the surface potential Φ. Also plotted using dashed lines in Figure S59a are the IAST estimates of the adsorption selectivity S_{ads}. While the IAST estimates are of excellent accuracy for all-silica FAU, the IAST tends to over-estimate the adsorption selectivity of NaY and NaX zeolites. The elucidation of the reasons for reduced accuracy of the IAST is provided in our earlier works.[25, 26, 28, 50, 51] We note that the adsorption selectivity follows the hierarchy NaX >> NaY >> FAU (all-silica). The diffusion selectivity $S_{diff} = \frac{D_{1,self}}{D_{2,self}}$ follows the hierarchy NaX < NaY < FAU (all-silica). Due to the stronger binding of CO_2, the self-diffusivity of CO_2 is significantly lowered with increasing number of cations, while the self-diffusivity of $CH_4(2)$ is less strongly influenced. From Figure S59a,b we conclude that adsorption and diffusion selectivities do not proceed hand-in-hand. If the host materials were used in membrane constructs, the permeation selectivity S_{perm} is a product of the adsorption and diffusion selectivities, i.e. $S_{perm} = S_{ads} \times S_{diff}$. Figure S59c

compares the permeation selectivities of FAU, NaY and NaX. We note that the permeation selectivities follow the hierarchy NaX > NaY > FAU (all-silica), and reflect the counter-acting influences of mixture adsorption and mixture diffusion. In Figure S59d, the membrane permeability of CO_2 is plotted as a function of the surface potential Φ. For the specific choice of upstream operating conditions, $f_t = f_1 + f_2 = 10^6$ Pa, Figure S59e shows the Robeson[52] plot of S_{perm} vs Π_1 for the three host structures. We note that the performances of both NaY and NaX, lie above the line representing the Robeson upper bound.[52] Since both S_{perm} and Π_1 are important metrics governing the choice of the appropriate membrane material, there is room of optimization of the Si/Al ratio depending on the relative weightage to be assigned to permeation selectivity and permeability.

Figure S60, Figure S61, Figure S62, Figure S63, and Figure S64 summarize the CBMC/MD data on adsorption selectivities, S_{ads}, diffusion selectivities, S_{diff}, permeation selectivities, S_{perm}, and permeabilities for CO_2/N_2, CO_2/H_2, CH_4/H_2, CH_4/C_2H_6, and CH_4/C_3H_8 mixtures.

9.1 List of Figures for Comparing FAU (all-silica) with NaY and NaX zeolites

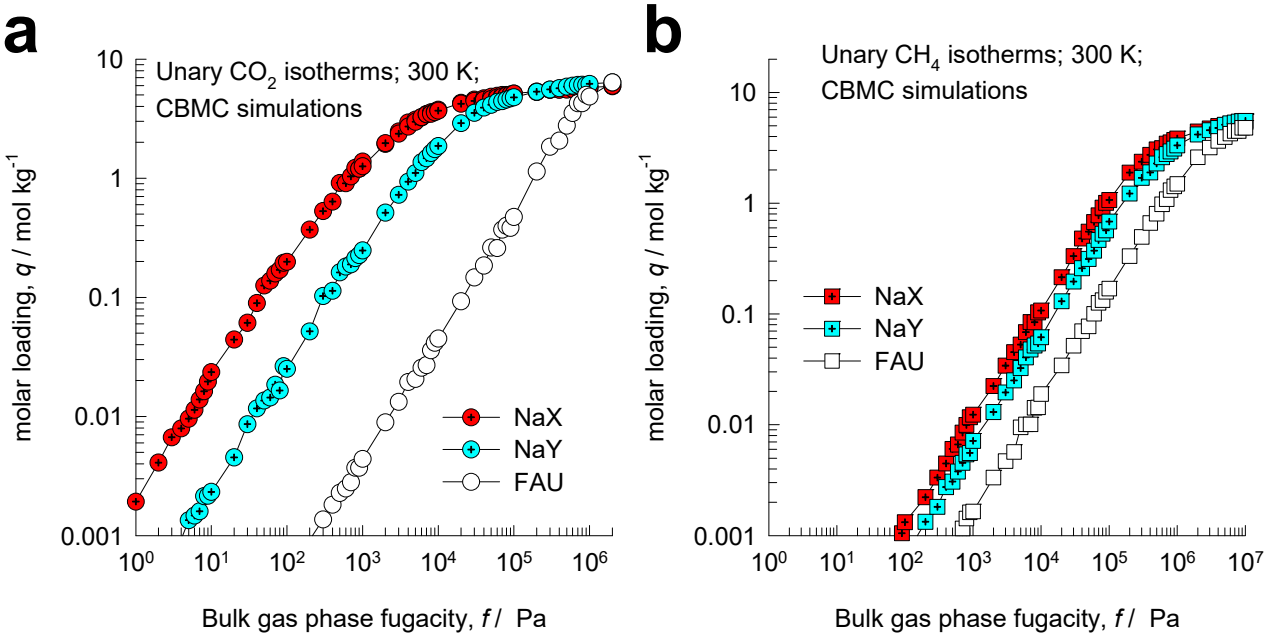

Figure S53. CBMC simulations of the molar loadings of (a) CO_2, and (b) CH_4 in FAU (all-silica), NaY, and NaX zeolites, determined at 300 K, plotted as function of the bulk gas fugacity f.

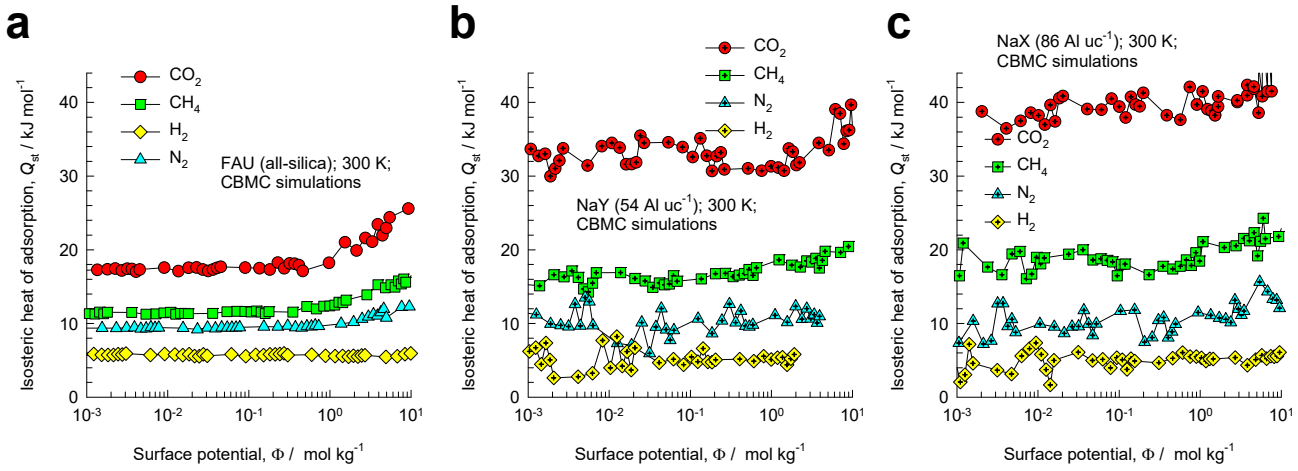

Figure S54. CBMC simulations of the isosteric heats of adsorption, Q_{st}, of CO_2, CH_4, N_2, and H_2 in (a) FAU (all-silica), (b) NaY, and (c) NaX zeolites, determined at 300 K, plotted as function of the surface potential Φ.

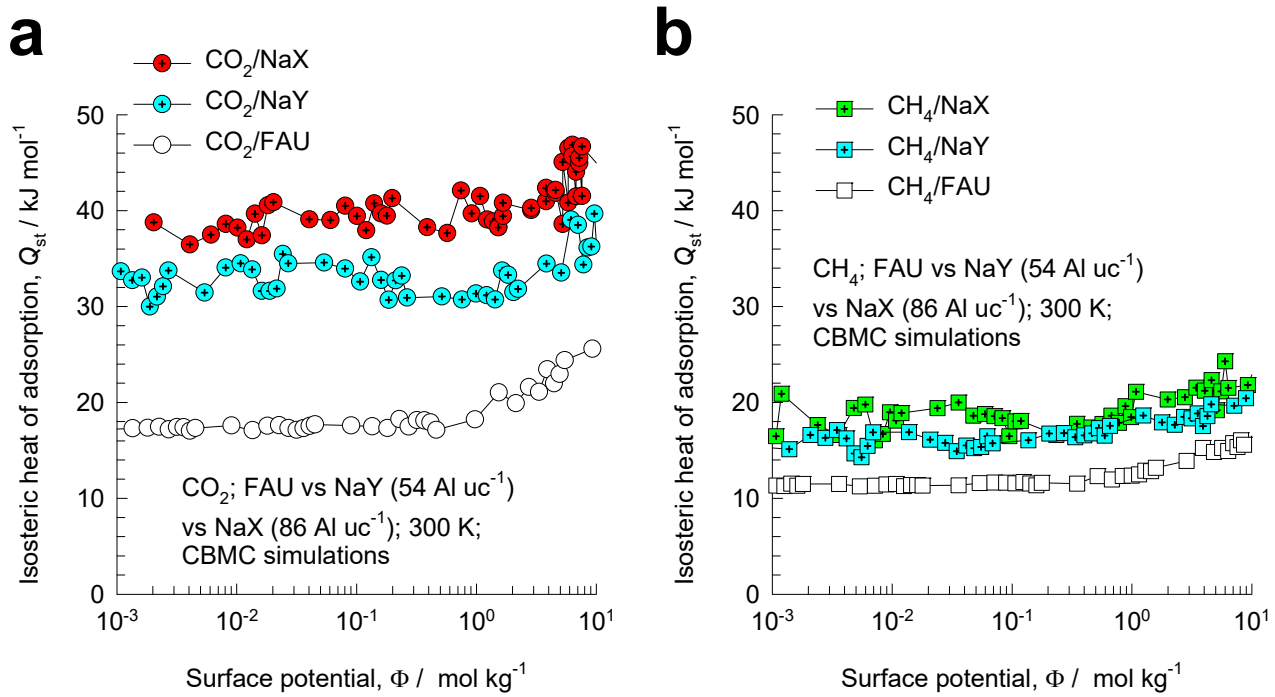

Figure S55. CBMC simulations of the isosteric heats of adsorption of (a) CO_2, and (b) CH_4 in FAU (all-silica), NaY, and NaX zeolites, determined at 300 K, plotted as function of the surface potential Φ.

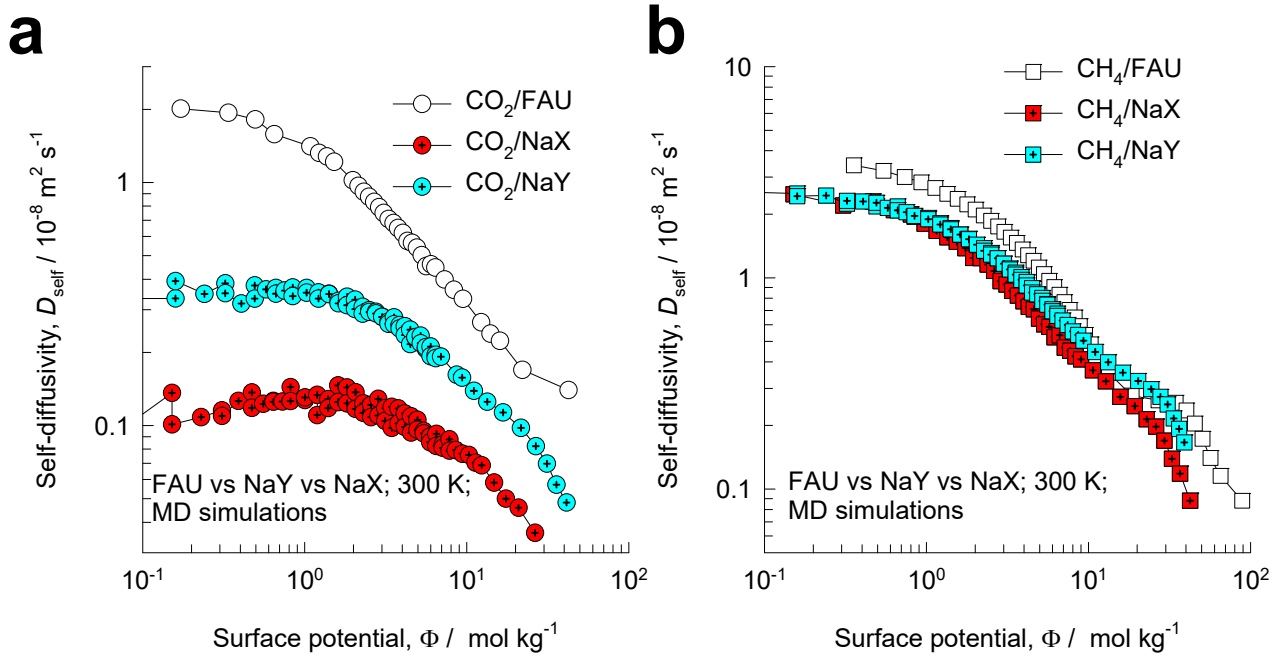

Figure S56. MD simulations of the self-diffusivities, $D_{i,self}$, of (a) CO_2, and (b) CH_4 in FAU (all-silica), NaY, and NaX zeolites, determined at 300 K, plotted as function of the surface potential Φ.

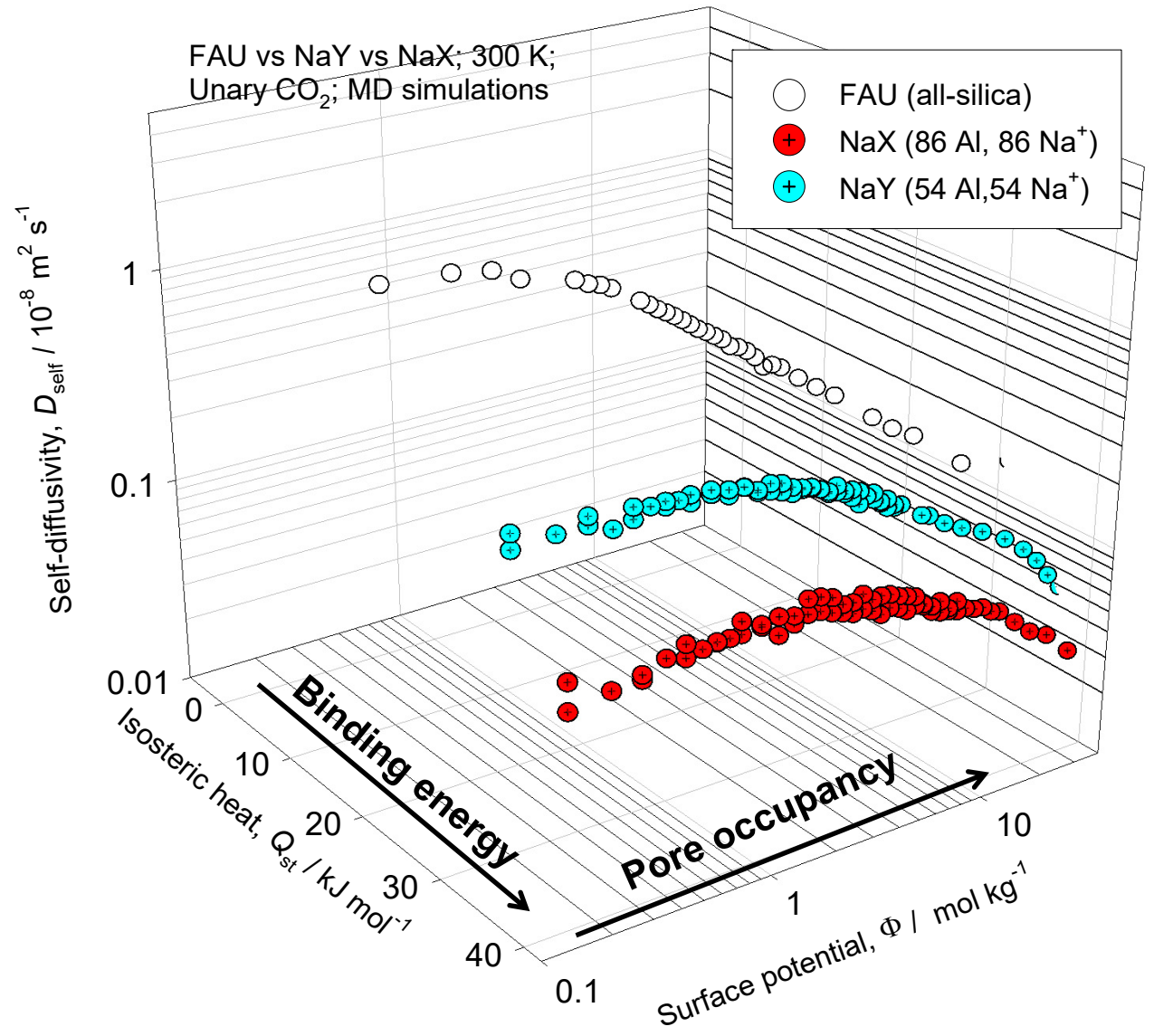

Figure S57. MD simulations of the self-diffusivities, $D_{i,self}$, of CO_2 in FAU (all-silica), NaY, and NaX zeolites, determined at 300 K, plotted as function of the surface potential Φ and the isosteric heat of adsorption, Φ.

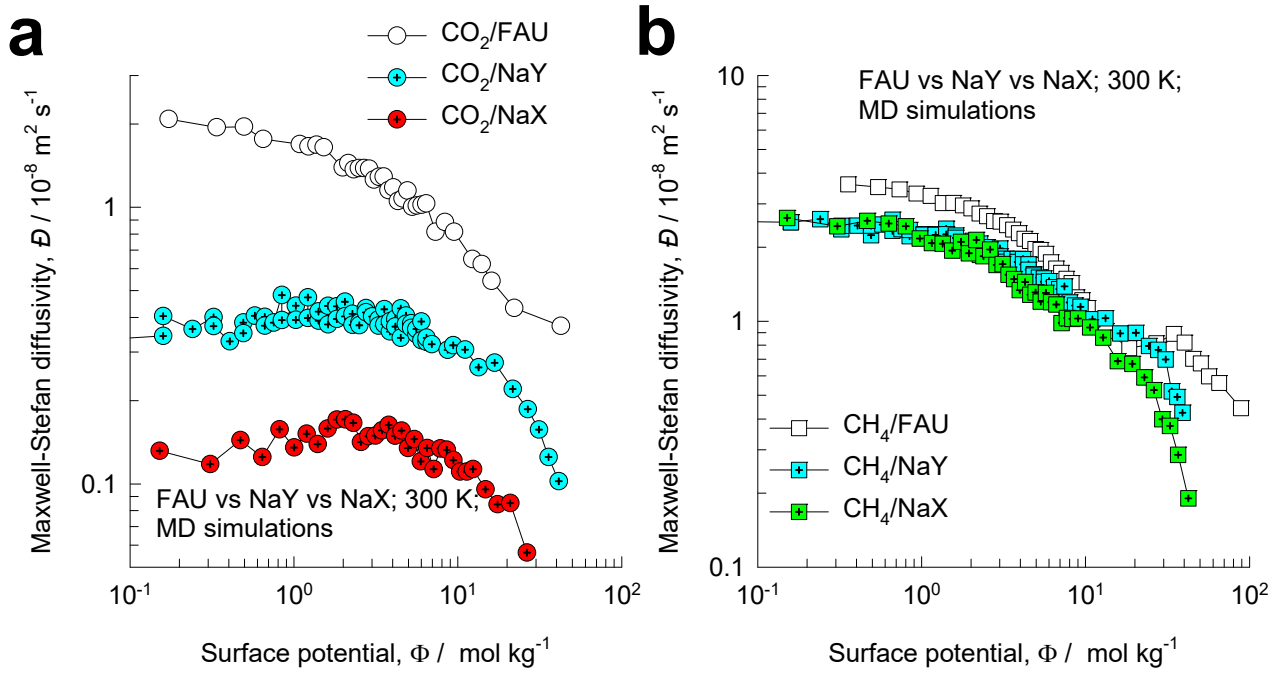

Figure S58. MD simulations of the Maxwell-Stefan diffusivities, $Đ_i$, of (a) CO_2, and (b) CH_4 in FAU (all-silica), NaY, and NaX zeolites, determined at 300 K, plotted as function of the surface potential Φ.

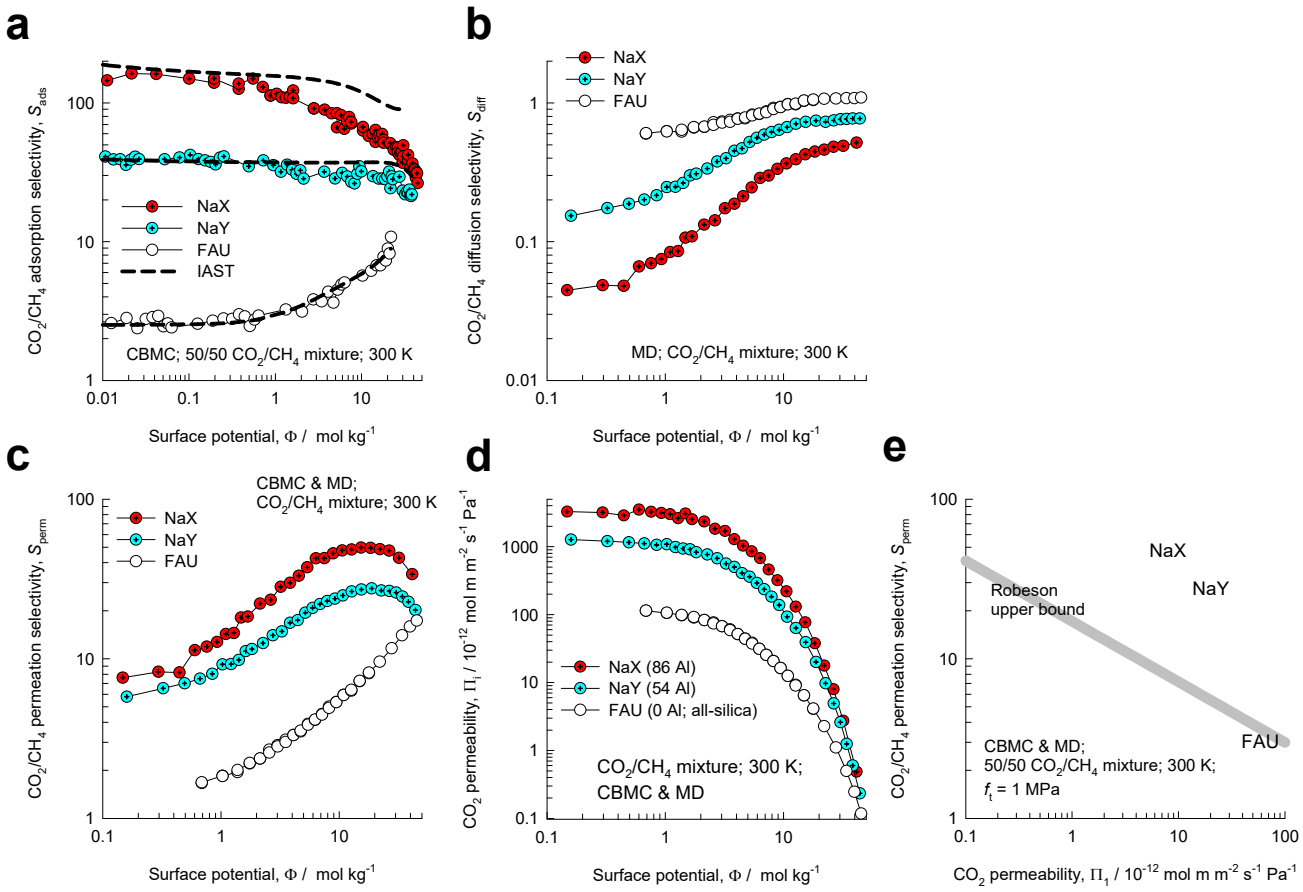

Figure S59. Comparison of CBMC and MD simulations of (a) adsorption selectivities, S_{ads}, (b) diffusion selectivities, S_{diff}, (c) permeation selectivities, S_{perm}, and (d) CO_2 permeabilities for CO_2/CH_4 mixtures in FAU, NaY, and NaX zeolites at 300 K. (e) Robeson plot of S_{perm} vs Π_1 data at $f_t = f_1 + f_2 = 10^6$ Pa and 300 K.

Comparing FAU (all-silica) with NaY and NaX zeolites

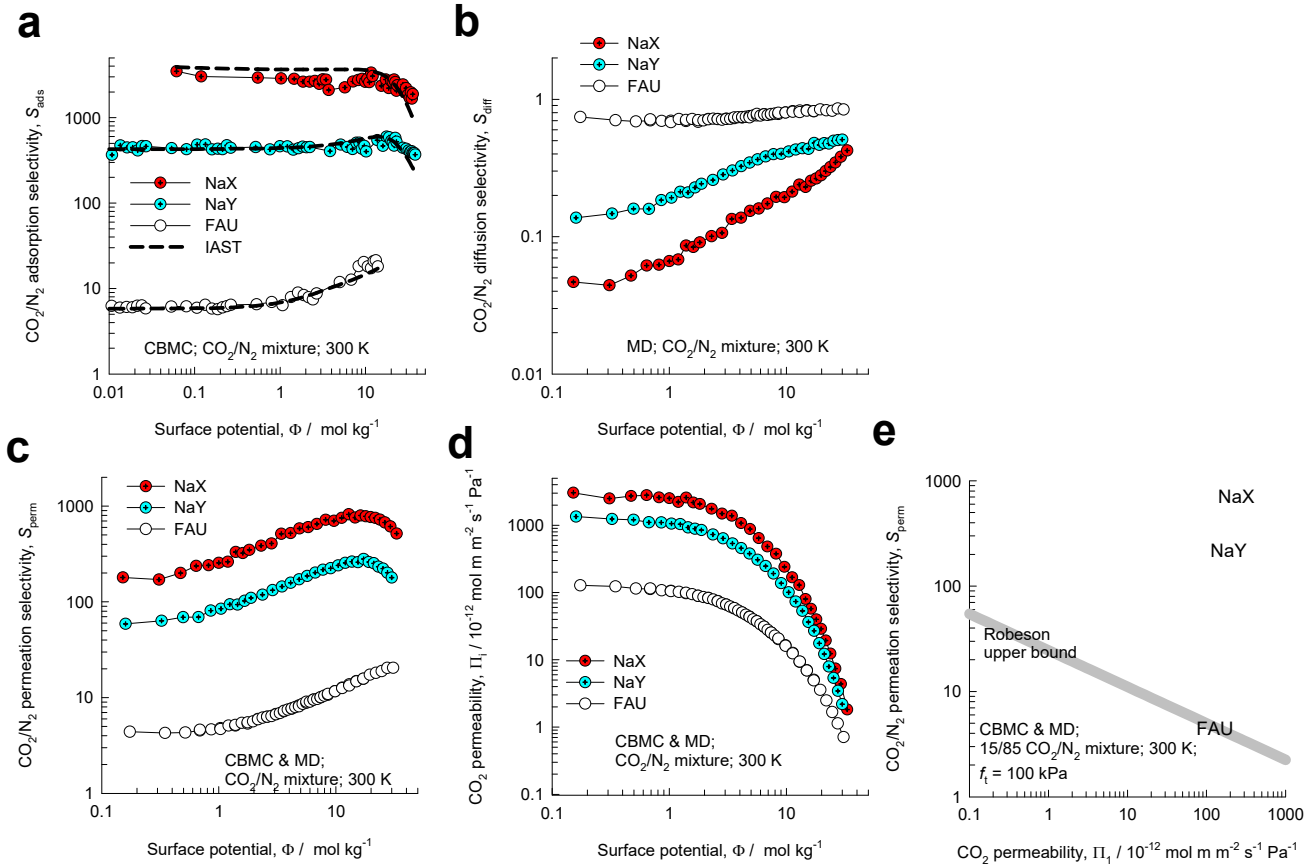

Figure S60. Comparison of CBMC and MD simulations of (a) adsorption selectivities, S_{ads}, (b) diffusion selectivities, S_{diff}, (c) permeation selectivities, S_{perm}, and (d) CO_2 permeabilities for CO_2/N_2 mixtures in FAU, NaY, and NaX zeolites at 300 K. (e) Robeson plot of S_{perm} vs Π_1 data at $f_t = f_1 + f_2 = 10^5$ Pa and 300 K.

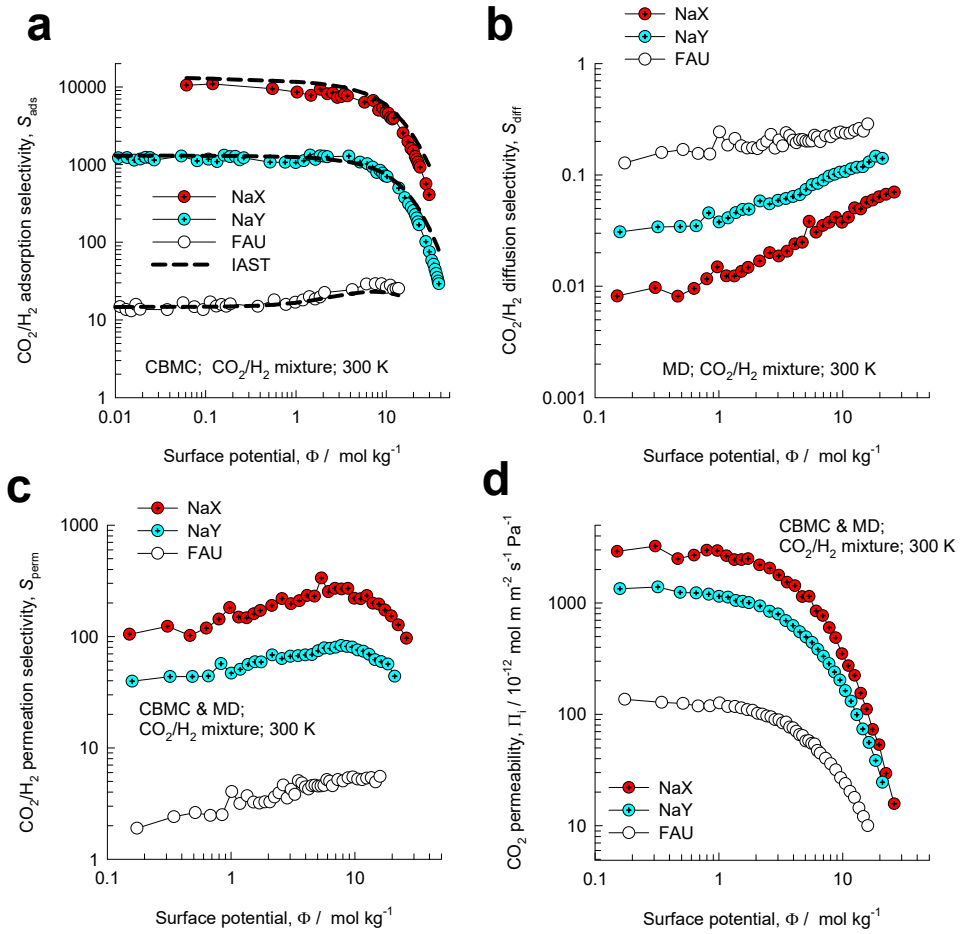

Figure S61. Comparison of CBMC and MD simulations of (a) adsorption selectivities, S_{ads}, (b) diffusion selectivities, S_{diff}, (c) permeation selectivities, S_{perm}, and (d) CO_2 permeabilities for CO_2/N_2 mixtures in FAU, NaY, and NaX zeolites at 300 K.

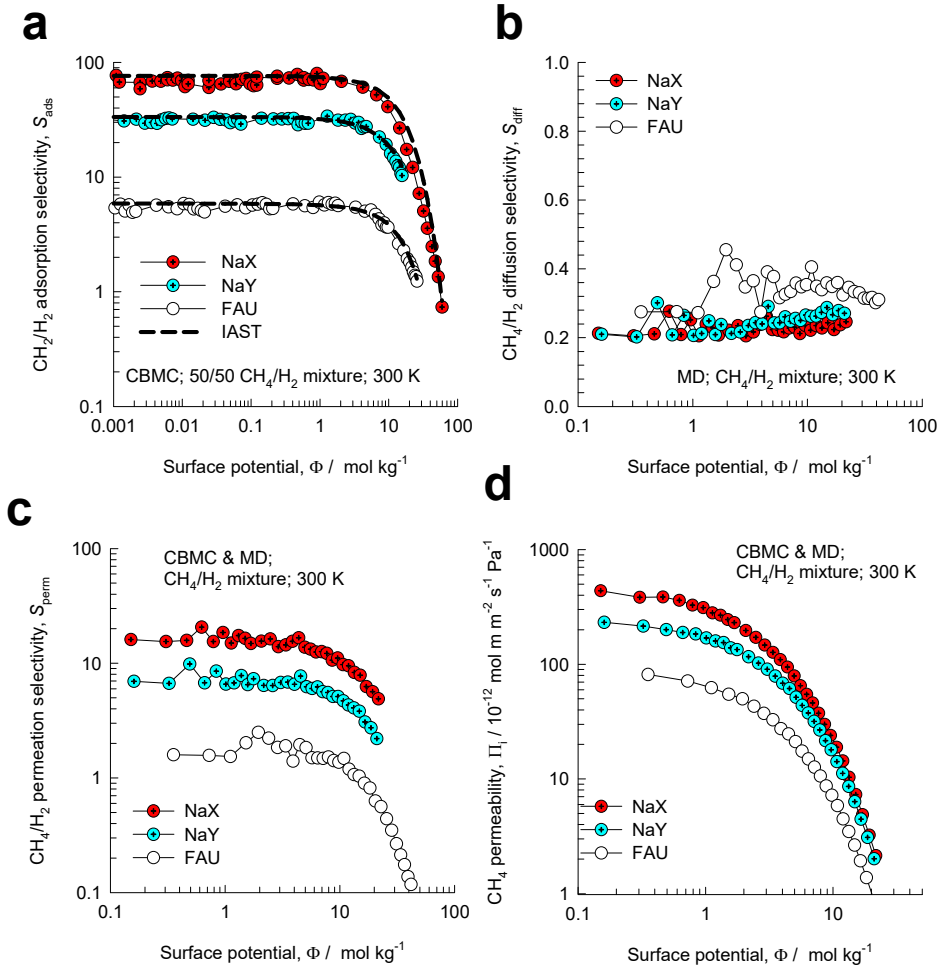

Figure S62. Comparison of CBMC and MD simulations of (a) adsorption selectivities, S_{ads}, (b) diffusion selectivities, S_{diff}, (c) permeation selectivities, S_{perm}, and (d) CH_4 permeabilities for CH_4/H_2 mixtures in FAU, NaY, and NaX zeolites at 300 K.

Comparing FAU (all-silica) with NaY and NaX zeolites

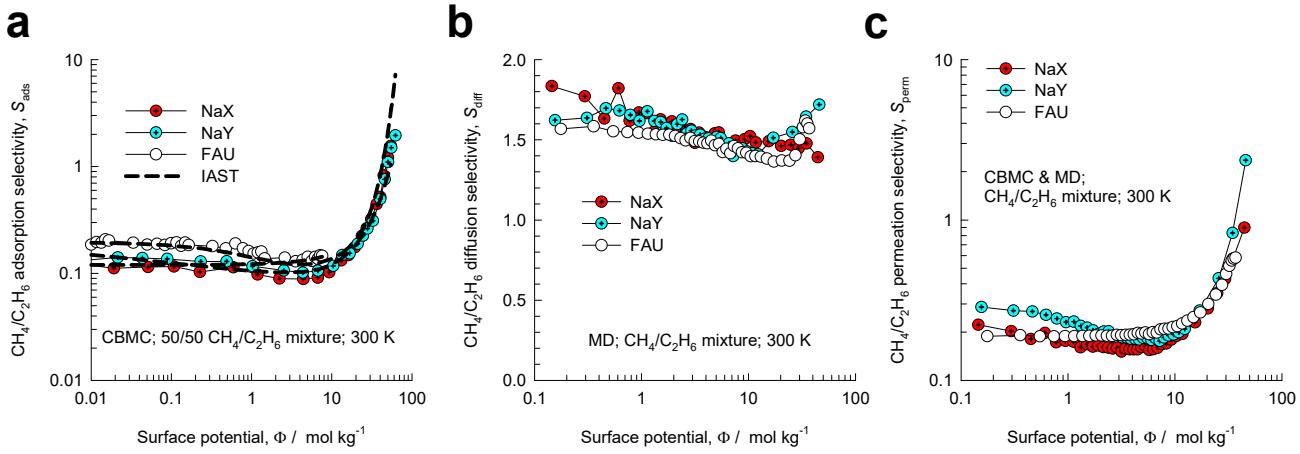

Figure S63. Comparison of CBMC and MD simulations of (a) adsorption selectivities, S_{ads}, (b) diffusion selectivities, S_{diff}, and (c) permeation selectivities, S_{perm}, of CH4/C2H6 mixtures in FAU, NaY, and NaX zeolites at 300 K. The selectivities are plotted as function of the surface potential Φ.

Comparing FAU (all-silica) with NaY and NaX zeolites

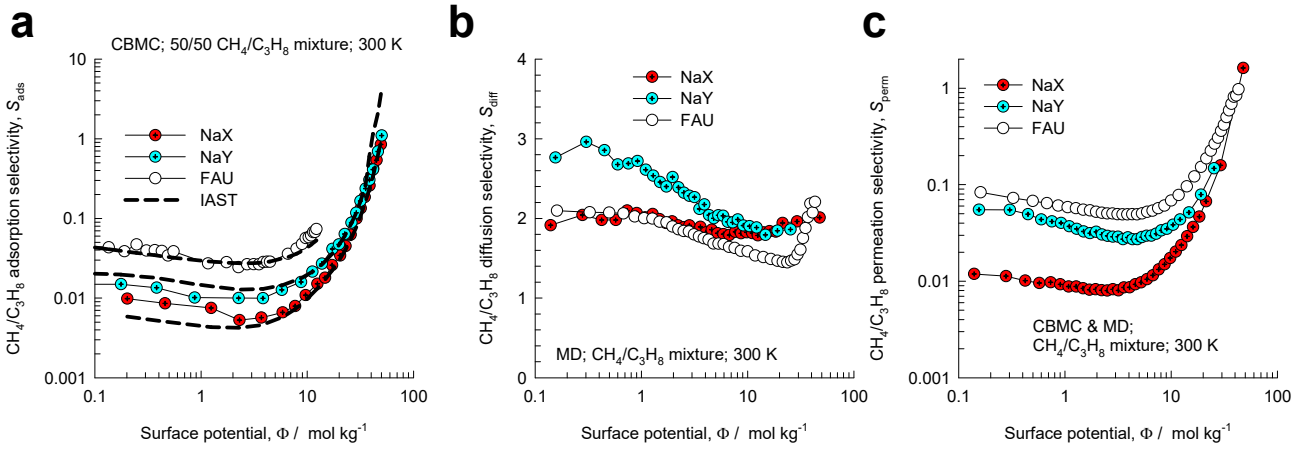

Figure S64. Comparison of CBMC and MD simulations of (a) adsorption selectivities, S_{ads}, (b) diffusion selectivities, S_{diff}, and (c) permeation selectivities, S_{perm}, of CH4/C3H8 mixtures in FAU, NaY, and NaX zeolites at 300 K. The selectivities are plotted as function of the surface potential Φ.

10 N_2/O_2 separations in Li-exchanged FAU zeolites

The separation of air to produce N_2 and O_2 of high purities is one of the most important industrial processes that uses pressure swing adsorption technology.[53, 54] The process technologies are geared to either production of purified O_2 or purified N_2. Cryogenic distillation has been the common technologies for this separation, but adsorptive separations offer energy efficient alternatives. Purified O_2 is required for a wide variety of applications that include portable adsorption units for medical applications and in space vehicles. Nitrogen is required in applications where it is desired or necessary to exclude oxygen. Typical industrial applications include preservation of fruit and produce during trucking, the blanketing of fuel tanks of fighter aircraft, the inerting of reactors in a number of pharmaceutical processes, laser cutting. N_2 is required for use in laboratory analytical equipment such as GC, LC, LCMS, FTIR, ICP, and in glove boxes.

For production of purified O_2, cation-exchanged zeolites LTA-5A (also called 5A or NaCaA zeolite containing 96 Si, 96 Al, 32 Na^+, 32 Ca^{++} per unit cell; Si/Al=1), NaX (also called 13 X zeolite, containing 106 Si, 86 Al, 86 Na^+ per unit cell; Si/Al=1.23), CaX, LiX, and LiLSX (= low silica LiX zeolite) and can be used as selective adsorbents.[4, 54-57] The larger permanent quadrupole of N_2 compared to that of O_2 is responsible for the stronger adsorption strength of N_2 on these zeolites.[4] Both O_2, and N_2 have similar polarizabilities and magnetic susceptibilities. However, the quadrupole moment of N_2 is about 4 times that of O_2; see Figure S6.

We carried out CBMC and MD simulations for adsorption and diffusion of unary N_2, unary O_2, and N_2/O_2 mixtures in Li-exchanged FAU zeolites with different Al contents per unit cell:

FAU all-silica = 0 Al

FAU48Al = 48 Al/uc, 48 Li^+/uc

FAU54Al = 54 Al/uc, 54 Li^+/uc

FAU86Al = 86 Al/uc, 86 Li^+/uc

FAU96Al = 96 Al/uc, 96 Li^+/uc

The force field is from Table 1 of Fu et al.[20] The Li^+ force field implementation is taken from Table 1 of Fu et al.[21]

10.1 Unary and mixture adsorption in Li-exchanged FAU zeolites

Figure S65a,b present CBMC simulations of the unary isotherms for (a) N_2, and (b) O_2 at 300 K in Li-exchanged FAU zeolites, with different Al contents per unit cell: 0, 48, 54, 86, and 96. The unary isotherm fit parameters are provided in Table S5, and Table S6. With increasing amounts of Li^+/uc, the component loadings of N_2 increase, due to the strong electrostatic interactions engendered by the quadrupole moment. The influence on the component loadings of O_2 is minimal, because of the significantly lower electrostatic interactions. The increase in the electrostatic interactions is also reflected in the increase in the isosteric heat of adsorption, Q_{st}, also determined from CBMC simulations. For N_2, the addition of cations to all-silica FAU, increases Q_{st} but the corresponding influence for O_2, is negligible; see Figure S65c.

CBMC simulations were performed to determine the adsorption selectivity, S_{ads}, for 80/20 N_2(1)/O_2(2) mixtures in Li-exchanged zeolites at 300 K; see Figure S66a,b. The adsorption selectivities are plotted as function of the surface potential Φ. The dashed lines in Figure S66b are the IAST calculations; the unary isotherm fit parameters are provided in Table S5, and Table S6. The IAST calculations are in good agreement with the CBMC simulations and thermodynamic non-idealities are of negligible importance.

For mixture adsorption at a total fugacity = 100 kPa, Figure S66c plots S_{ads} as a function of the Al content per unit cell. We note that the S_{ads} increases with increasing Al content, and this rationalizes the use of LiLSX (LS = low silica) in industrial practice. [58, 59]

10.2 Self-diffusivities, and diffusion selectivities

Figure S67a,b present MD simulations of the unary self-diffusivities $D_{i,self}$ for (a) N_2, and (b) O_2 at 300 K in Li-exchanged FAU zeolites, with different Al contents per unit cell: 0, 48, 54, 86, and 96, plotted as function of the surface potential Φ. We note that the self-diffusivity of N_2 decreases with increasing amounts of Li^+/uc. The stronger the binding, the lower is the mobility of the guest molecule. On the other hand, the self-diffusivity of O_2 is almost independent of the amounts of Li^+/uc because the binding strengths, Q_{st} are practically uninfluenced by the addition of extra-framework cations. The values of the diffusivities at zero loadings, correlate reasonably well with the values of the corresponding isosteric heat of adsorption, Q_{st}; see Figure S67c. The stronger the binding, the lower is the mobility of the guest molecule.

In Figure S68 the self-diffusivities are plotted as functions of both the surface potential Φ, and the isosteric heats of adsorption, Q_{st}. For N_2, the diffusivities decrease with increasing binding strength, quantified by Q_{st}. The diffusivities also decrease with increasing pore occupancy, reflected by the surface potential Φ. On the other hand, the self-diffusivity of O_2 is almost independent of the amounts of Li^+/uc because the binding strengths, Q_{st} are practically uninfluenced by the addition of extra-framework cations.

In Figure S69a,b,c,d,e the MD data on the self-diffusivities of N_2, and O_2 determined for equimolar $\left(q_1 = q_2\right)$ N_2/O_2 mixtures are compared to the corresponding values of the unary diffusivities; the comparison is made on the basis of the surface potential Φ. For a chosen guest structure, we note that self-diffusivities of N_2, and O_2 in binary mixtures have practically the value as the corresponding unary self-diffusivities at the same value of Φ.

Figure S70a,b compare the plots of the adsorption selectivity, S_{ads}, and N_2/O_2 diffusion selectivity, S_{diff}. These plots demonstrate the anti-synergy between adsorption and diffusion. The higher the adsorption selectivity, the lower is the corresponding diffusion selectivity.

The N_2/O_2 permeation selectivity, $S_{perm} = S_{ads} \times S_{diff}$ are plotted in Figure S70c. Due to the anti-synergy between adsorption and diffusion, the permeation selectivity is lower than the adsorption selectivity for each of the five host structures.

10.3 Membrane permeabilities and permeation selectivities

The component membrane permeabilities can be determined using eq (S61), $\Pi_i = \frac{\rho D_{i,self} q_i}{f_i}$. In Figure S71a,b,c,d,e the component permeabilities of N_2, and O_2 determined for equimolar $\left(q_1 = q_2\right)$ N_2/O_2 mixtures are compared to the corresponding values of the unary diffusivities; the comparison is made on the basis of the surface potential Φ. For a chosen guest structure, we note that permeabilities of N_2, and O_2 in binary mixtures have practically the same value as the corresponding unary permeabilities at the same value of Φ.

In Figure S72a, CBMC/MD simulations of S_{ads}, S_{diff}, and S_{perm} for binary 80/20 N_2/O_2 mixture permeation at a upstream total pressure of 100 kPa across Li-exchanged FAU zeolite membranes are plot as a function of the Al contents per unit cell: 0, 48, 54, 86, and 96. Figure S72b is a Robeson plot of S_{perm} vs component permeabilities of N_2 for binary 80/20 N_2/O_2 mixture permeation across Li-exchanged FAU zeolite membrane. The best membrane performance is realized with 96Al.

10.4 List of Tables for N2/O2 separations in Li-exchanged FAU zeolites

Table S5. Dual-site Langmuir parameters for pure N_2 at 300 K in Li-exchanged FAU zeolites

	Site A		Site B	
	$q_{A,sat}$ mol kg^{-1}	b_A Pa^{-1}	$q_{B,sat}$ mol kg^{-1}	b_B Pa^{-1}
0Al = FAU	2.2	3.314E-08	5.7	5.199E-07
48Al	4.8	1.372E-07	4.4	2.832E-06
54Al	5.2	7.277E-08	5.3	2.420E-06
86Al	3.4	3.142E-07	5.5	4.287E-06
96Al	3.3	2.108E-07	6.05	4.865E-06

Table S6. Dual-site Langmuir parameters for pure O_2 at 300 K in Li-exchanged FAU zeolites

	Site A		Site B	
	$q_{A,sat}$ mol kg^{-1}	b_A Pa^{-1}	$q_{B,sat}$ mol kg^{-1}	b_B Pa^{-1}
0Al = FAU	7.7	3.782E-07		
48Al	4.8	4.344E-07	3.4	4.344E-07
54Al	4.9	4.099E-07	3.5	4.595E-07
86Al	5.4	5.820E-07	2.8	5.822E-07
96Al	2.6	2.091E-08	7.7	6.740E-07

10.5 List of Figures for N2/O2 separations in Li-exchanged FAU zeolites

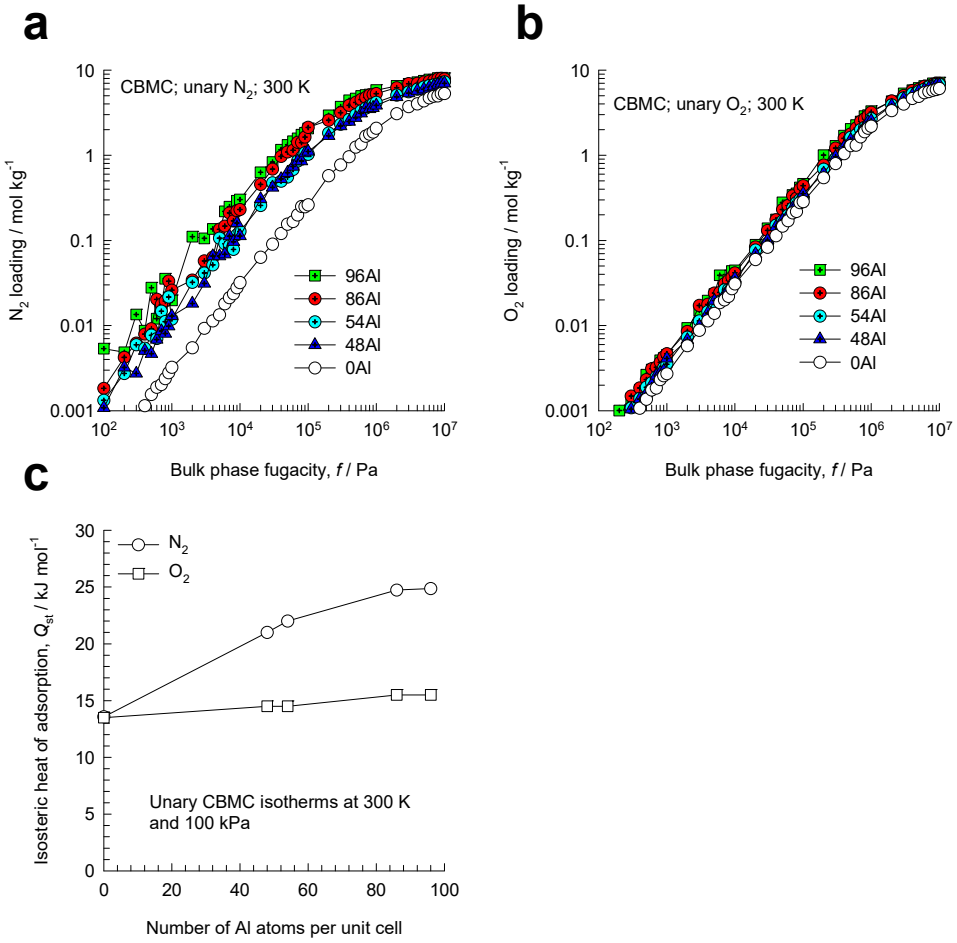

Figure S65. (a, b) CBMC simulations of the unary isotherms for N_2, and O_2 at 300 K in Li-exchanged FAU zeolites, with different Al contents per unit cell: 0, 48, 54, 86, and 96. The unary isotherm fit parameters are provided in Table S5, and Table S6. (c) CBMC simulations of the isosteric heats of adsorption, Q_{st}, for N_2, and O_2, plotted as function of the surface potential Φ.

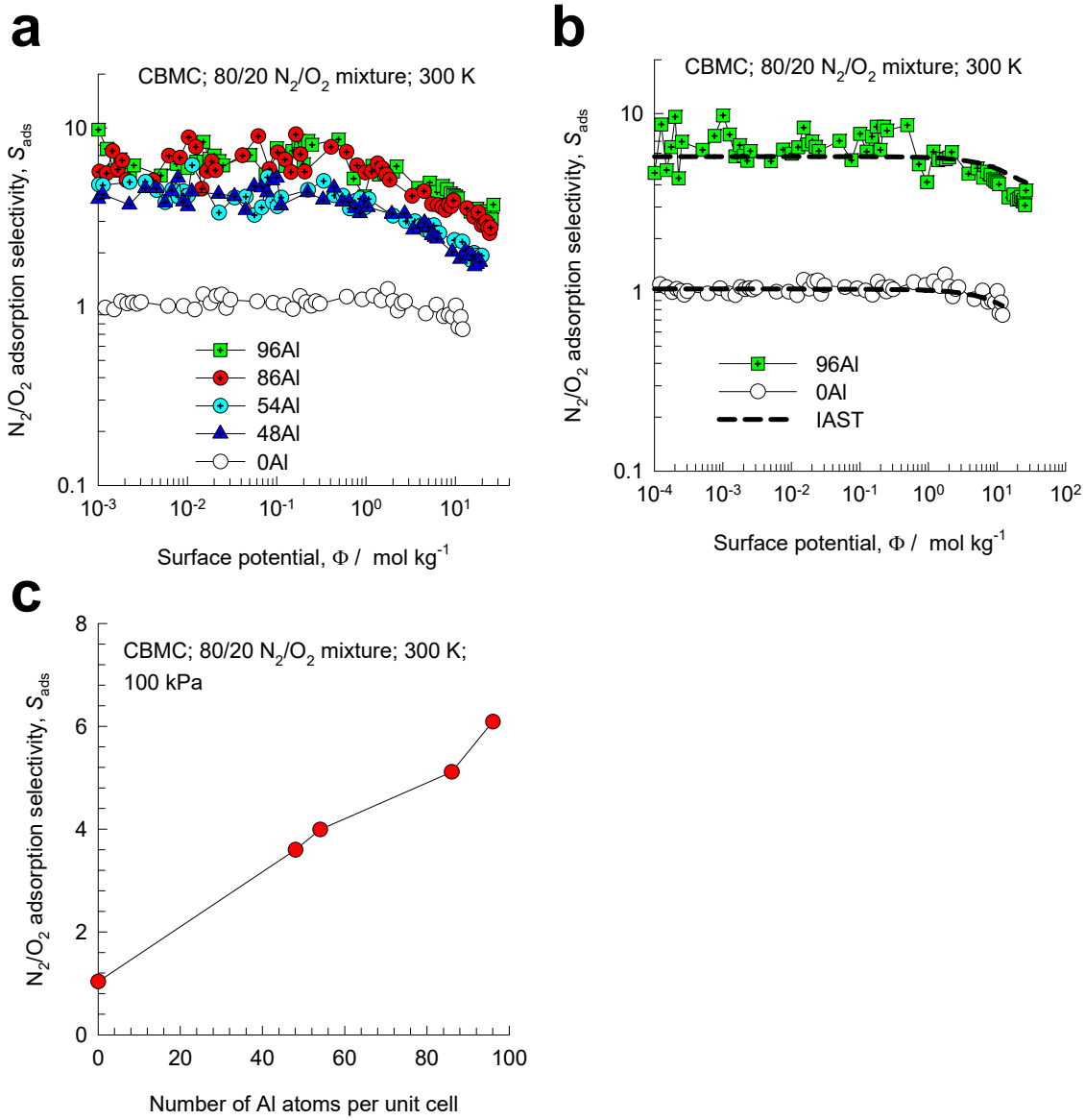

Figure S66. (a, b) CBMC simulations of the adsorption selectivity, S_{ads}, for binary 80/20 N_2/O_2 mixture adsorption in Li-exchanged FAU zeolites at 300 K. The adsorption selectivities are plotted as function of the surface potential Φ. The dashed lines in (b) are the IAST calculations; the unary isotherm fit parameters are provided in Table S5, and Table S6. (c) CBMC simulations of the adsorption selectivity, S_{ads}, for 80/20 N_2/O_2 mixture adsorption in Li-exchanged FAU zeolites at a total fugacity = 100 kPa, plotted as a function of the Al content per unit cell.

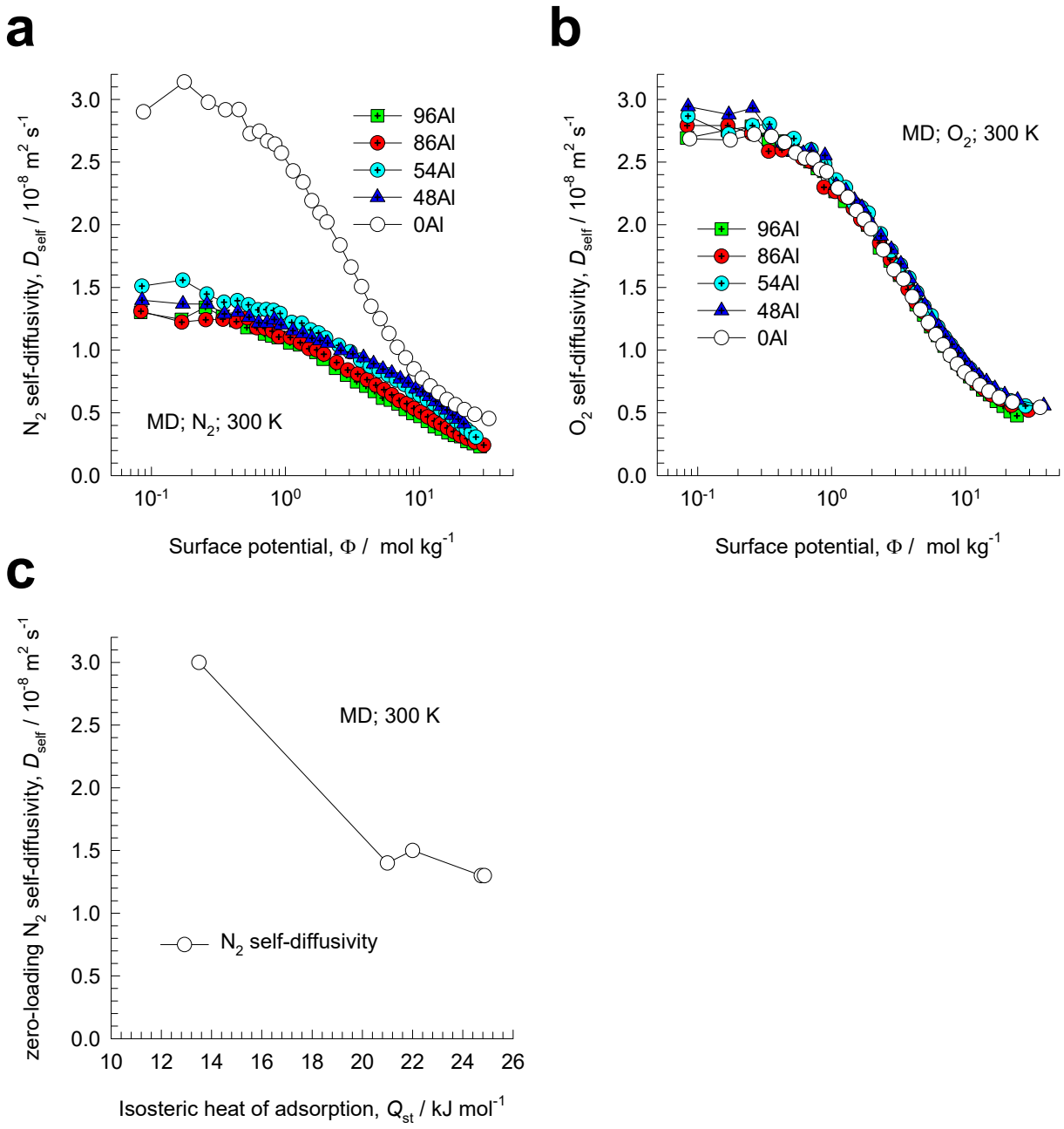

Figure S67. (a, b) MD simulations of the unary self-diffusivities for N_2, and O_2 at 300 K in Li-exchanged FAU zeolites, with different Al contents per unit cell: 0, 48, 54, 86, and 96, plotted as function of the surface potential Φ. (c) The values of the N_2 diffusivities at zero loadings, plotted as function of the isosteric heat of adsorption, Q_{st}.

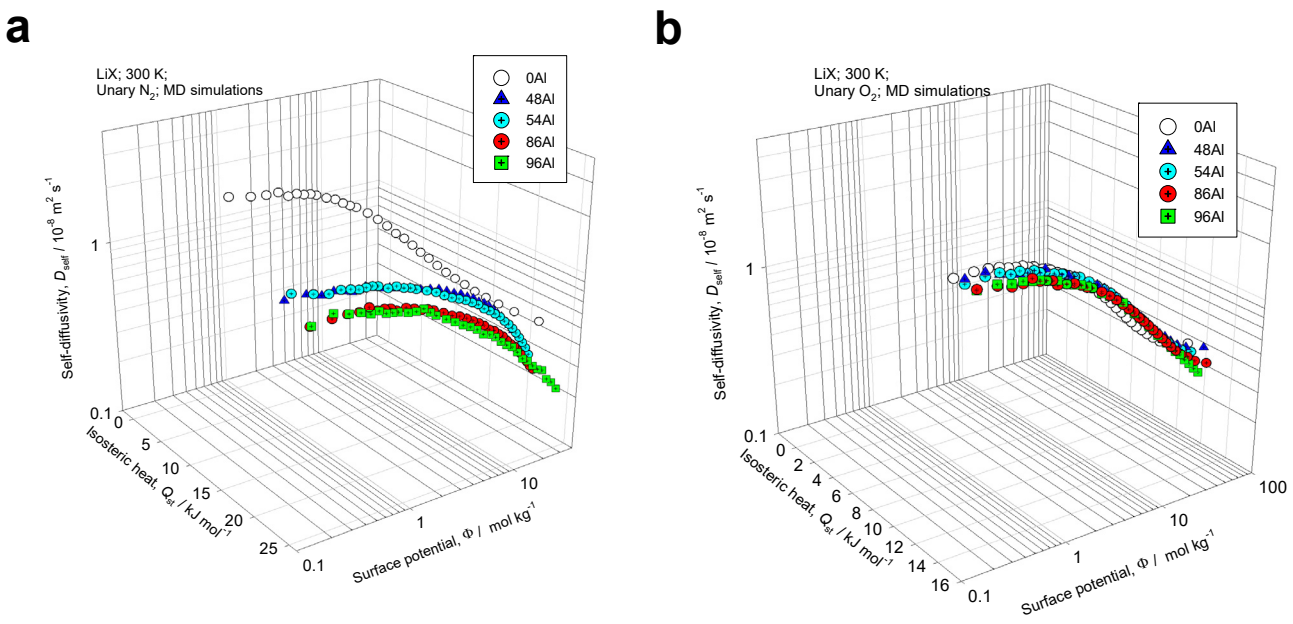

Figure S68. (a, b) MD simulations of the unary self-diffusivities for N_2, and O_2 at 300 K in Li-exchanged FAU zeolites, with different Al contents per unit cell: 0, 48, 54, 86, and 96, plotted as function of the surface potential Φ, and the isosteric heats of adsorption Φ.

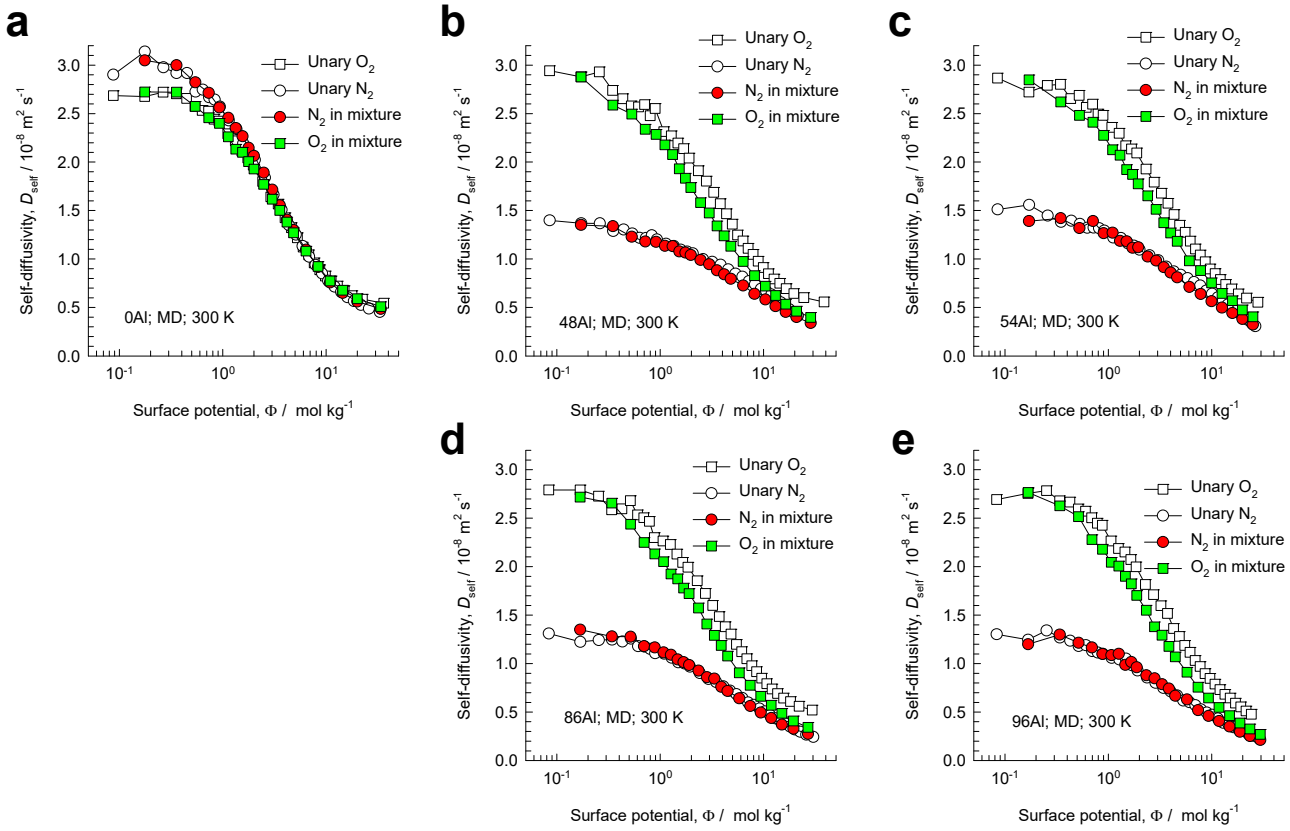

Figure S69. MD simulations of the self-diffusivities of N_2, and O_2 at 300 K in Li-exchanged FAU zeolites, with different Al contents per unit cell: (a) 0, (b) 48, (c) 54, (d) 86, and (e) 96, plotted as function of the surface potential Φ. The filled symbols represent the self-diffusivities in equimolar $(q_1 = q_2)$ N_2/O_2 mixtures. The open symbols represent the unary diffusivities.

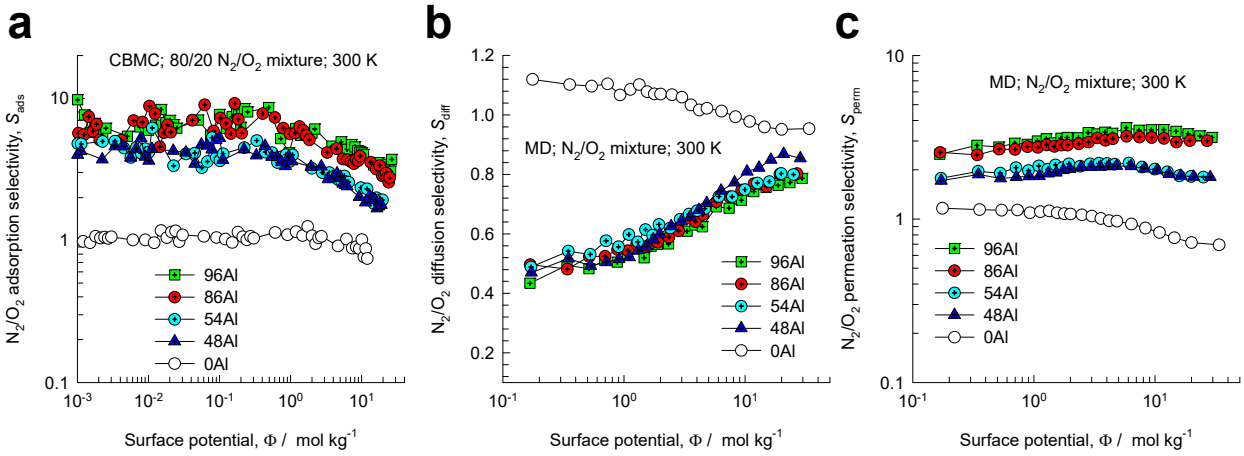

Figure S70. (a) CBMC simulations of the adsorption selectivity, S_{ads}, for binary 80/20 N_2/O_2 mixture adsorption in Li-exchanged FAU zeolites, with different Al contents per unit cell: 0, 48, 54, 86, and 96. (b) MD simulations of the N_2/O_2 diffusion selectivity, S_{diff}, at 300 K in Li-exchanged FAU zeolites. (c) CBMC/MD simulations of the N_2/O_2 permeation selectivity, S_{perm}, at 300 K in Li-exchanged FAU zeolites. In (a, b, c), the selectivities are plotted as function of the surface potential Φ.

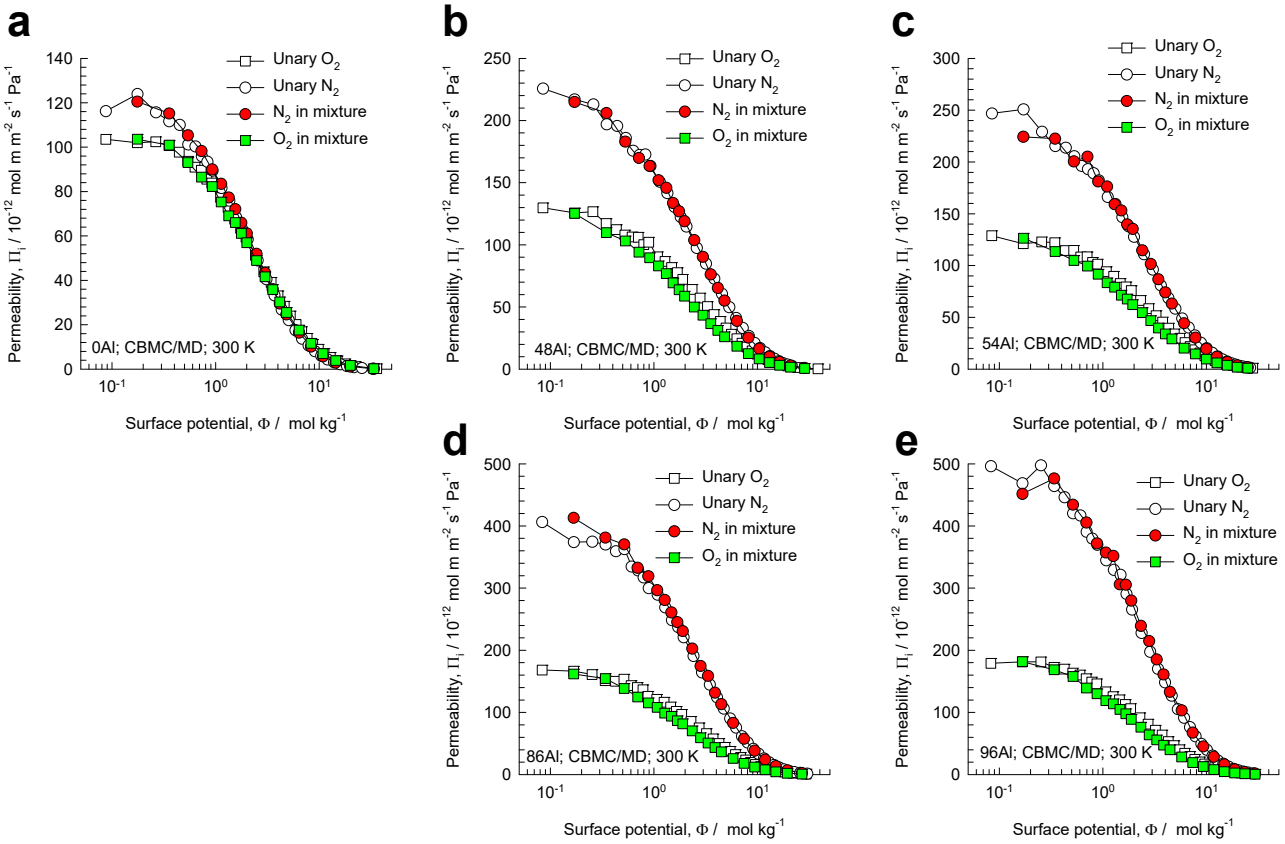

Figure S71. Component permeabilities of N_2, and O_2 at 300 K in Li-exchanged FAU zeolites, with different Al contents per unit cell: (a) 0, (b) 48, (c) 54, (d) 86, and (e) 96, plotted as function of the surface potential Φ. The filled symbols represent the permeabilities in equimolar $(q_1 = q_2)$ N_2/O_2 mixtures. The open symbols represent the unary permeabilities.

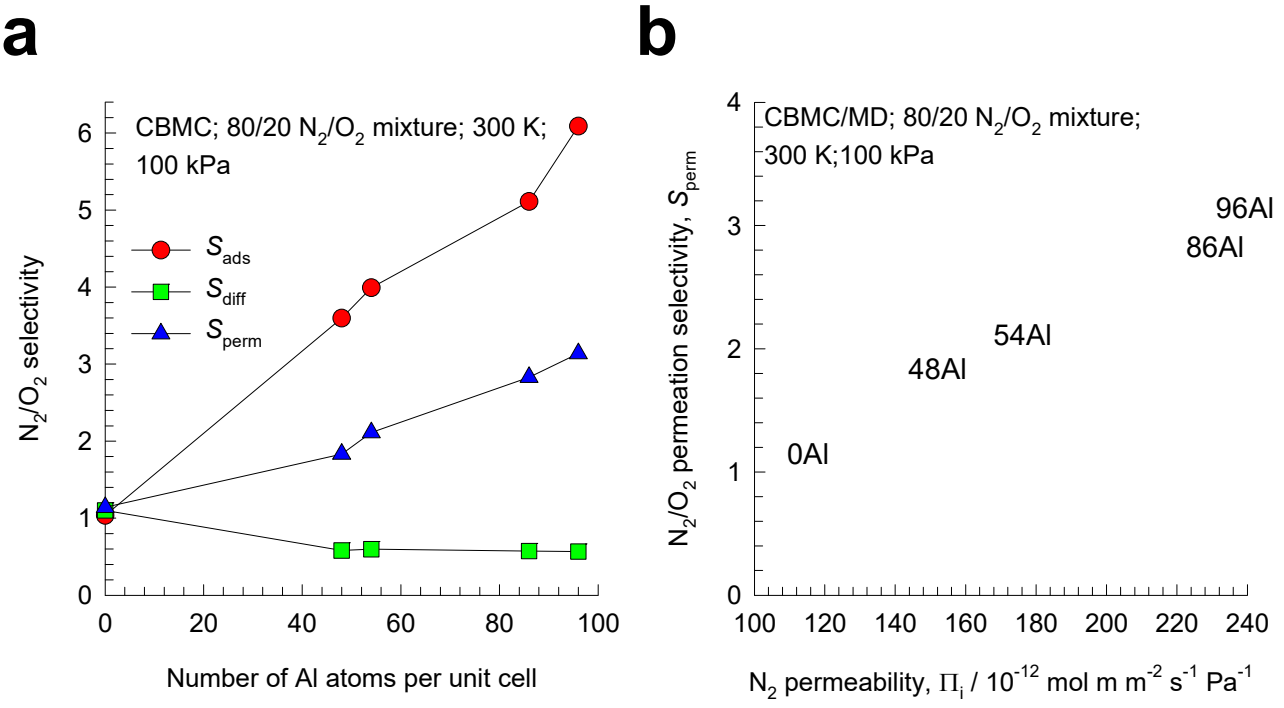

Figure S72. (a) CBMC/MD simulations of S_{ads}, S_{diff}, and S_{perm} for binary 80/20 N_2/O_2 mixture permeation across Li-exchanged FAU zeolite membrane, with different Al contents per unit cell: 0, 48, 54, 86, and 96. The upstream total pressure is 100 kPa. (b) Robeson plot of S_{perm} vs component permeabilities of N_2 for binary 80/20 N_2/O_2 mixture permeation across Li-exchanged FAU zeolite membrane, with different Al contents per unit cell: 0, 48, 54, 86, and 96.

11 N_2/O_2 separations in Na-exchanged FAU zeolites

We carried out CBMC and MD simulations for adsorption and diffusion of unary N_2, unary O_2, and N_2/O_2 mixtures in Na-exchanged FAU zeolites with different Al contents per unit cell:

FAU all-silica = 0 Al

FAU48Al = 48 Al/uc, 48 Li^+/uc

FAU54Al = 54 Al/uc, 54 Li^+/uc

FAU86Al = 86 Al/uc, 86 Li^+/uc

FAU96Al = 96 Al/uc, 96 Li^+/uc

The force field implementation is from Table 1 of Fu et al.[20]

11.1 Unary and mixture adsorption in Na-exchanged FAU zeolites

Figure S73a,b present CBMC simulations of the unary isotherms for (a) N_2, and (b) O_2 at 300 K in Na-exchanged FAU zeolites, with different Al contents per unit cell: 0, 48, 54, 86, and 96. The unary isotherm fit parameters are provided in Table S7, and Table S8. With increasing amounts of Na^+/uc, the component loadings of N_2 increase, due to the strong electrostatic interactions engendered by the quadrupole moment. The influence on the component loadings of O_2 is significantly lower, because of the significantly lower electrostatic interactions. The increase in the electrostatic interactions is also reflected in the increase in the isosteric heat of adsorption, Q_{st}, also determined from CBMC simulations. For N_2, the addition of cations to all-silica FAU, increases Q_{st} but the corresponding influence for O_2, is less strong; see Figure S73c.

CBMC simulations were performed to determine the adsorption selectivity, S_{ads}, for 80/20 $N_2(1)/O_2(2)$ mixtures in Na-exchanged zeolites at 300 K; see Figure S74a,b. The adsorption selectivities are plotted

as function of the surface potential Φ. The dashed lines Figure S74b are the IAST calculations; the unary isotherm fit parameters are provided in Table S7, and Table S8. The IAST calculations are in good agreement with the CBMC simulations and thermodynamic non-idealities are of negligible importance.

For mixture adsorption at a total fugacity = 100 kPa, Figure S74c plots S_{ads} as a function of the Al content per unit cell. We note that the S_{ads} increases with increasing Al content.

11.2 Self-diffusivities, and diffusion selectivities

Figure S75a,b present MD simulations of the unary self-diffusivities $D_{i,self}$ for (a) N_2, and (b) O_2 at 300 K in Na-exchanged FAU zeolites, with different Al contents per unit cell: 0, 48, 54, 86, and 96, plotted as function of the surface potential Φ. We note that the self-diffusivity of N_2 decreases with increasing amounts of Na^+/uc. The self-diffusivity of O_2 is also lowered with increasing amounts of Na^+/uc but the influence is less strong as compared to that for N_2. The values of the diffusivities at zero loadings, correlate reasonably well with the values of the corresponding isosteric heat of adsorption, Q_{st}; see Figure S75c. The stronger the binding, the lower is the mobility of the guest molecule.

In Figure S76 the self-diffusivities are plotted as functions of both the surface potential Φ, and the isosteric heats of adsorption, Q_{st}. For both N_2, and O_2 the self- diffusivities decrease with increasing binding strength, quantified by Q_{st}. The diffusivities also decrease with increasing pore occupancy, reflected by the surface potential Φ.

In Figure S77a,b,c,d,e the MD data on the self-diffusivities of N_2, and O_2 determined for equimolar $\left(q_1 = q_2\right)$ N_2/O_2 mixtures are compared to the corresponding values of the unary diffusivities; the comparison is made on the basis of the surface potential Φ. For a chosen guest structure, we note that self-diffusivities of N_2, and O_2 in binary mixtures have practically the value as the corresponding unary self-diffusivities at the same value of Φ.

Figure S78a,b compare the plots of the adsorption selectivity, S_{ads}, and N_2/O_2 diffusion selectivity, S_{diff}. These plots demonstrate the anti-synergy between adsorption and diffusion. The higher the adsorption

selectivity, the lower is the corresponding diffusion selectivity. The N_2/O_2 permeation selectivity, $S_{perm} = S_{ads} \times S_{diff}$ are plotted in Figure S78c. Due to the anti-synergy between adsorption and diffusion, the permeation selectivity is lower than the adsorption selectivity for each of the five host structures.

11.3 Membrane permeabilities and permeation selectivities

The component membrane permeabilities can be determined using eq (S61), $\Pi_i = \frac{\rho D_{i,self} q_i}{f_i}$. In Figure S79a,b,c,d,e the component permeabilities of N_2, and O_2 determined for equimolar $(q_1 = q_2)$ N_2/O_2 mixtures are compared to the corresponding values of the unary diffusivities; the comparison is made on the basis of the surface potential Φ. For a chosen guest structure, we note that permeabilities of N_2, and O_2 in binary mixtures have practically the same value as the corresponding unary permeabilities at the same value of Φ.

In Figure S80a, CBMC/MD simulations of S_{ads}, S_{diff}, and S_{perm} for binary 80/20 N_2/O_2 mixture permeation at a upstream total pressure of 100 kPa across Na-exchanged FAU zeolite membranes are plot as a function of the Al contents per unit cell: 0, 48, 54, 86, and 96. Figure S80b is a Robeson plot of S_{perm} vs component permeabilities of N_2 for binary 80/20 N_2/O_2 mixture permeation across Na-exchanged FAU zeolite membrane. The best membrane performance is realized with 96Al.

11.4 Comparing Li-FAU and Na-FAU zeolites for N_2/O_2 separations.

Figure S81 presents a comparison of the (a) isosteric heats of adsorption, (b) adsorption selectivity, (c) diffusion selectivity, (d) permeation selectivity, and (e) nitrogen permeabilities for N_2/O_2 separations using either Li-exchanged or Na-exchange FAU zeolites, with different Al contents per unit cell: 0, 48, 54, 86, and 96. It is evident that Li-exchanged FAU is more effective for N_2/O_2 separations; this is because the electrostatic interactions for interactions of N_2 with Li^+ are stronger than with Na^+, due to the smaller ionic radius of Li^+.

11.5 Comparing RDFs for Li-FAU and Na-FAU zeolites

The interaction potential, engendered by quadrupole moment, is inversely proportional to the cube of the center-to-center distance between nitrogen molecules and the extra-framework cations; see Figure S5. By sampling a total of 10^7 simulation steps, the radial distribution of the separation distances between the molecular pairs N_2-Li^+, and N_2-Na^+ were determined for binary 80/20 N_2/O_2 mixture adsorption at a total pressure of 100 kPa. The samples were taken up to a radial distance of 12 Å, but the *x*-axis has been truncated at 8 Å because only the first peaks are of interest. Due to the smaller ionic radius of Li^+, compared to Na^+, the N_2-Li^+ distances are smaller than the N_2-Na^+ distances; this is confirmed by radial distribution functions for N_2-Li^+ and the N_2-Na^+ pairs for 80/20 N_2/O_2 mixture adsorption in Li-FAU(96Al) and Na-FAU(96Al); see Figure S82.

11.6 List of Tables for N2/O2 separations in Na-exchanged FAU zeolites

Table S7. Dual-site Langmuir parameters for pure N_2 at 300 K in Na-exchanged FAU zeolites

	Site A		Site B	
	$q_{A,sat}$ mol kg^{-1}	b_A Pa^{-1}	$q_{B,sat}$ mol kg^{-1}	b_B Pa^{-1}
0Al = FAU	2.2	3.314E-08	5.7	5.199E-07
48Al	2.5	1.981E-07	4.9	1.925E-06
54Al	2.8	8.468E-08	5.4	2.008E-06
86Al	2.7	1.060E-07	5.5	4.481E-06
96Al	3	7.51562E-08	5.7	5.04093E-06

Table S8. Dual-site Langmuir parameters for pure O_2 at 300 K in Na-exchanged FAU zeolites

	Site A		Site B	
	$q_{A,sat}$ mol kg^{-1}	b_A Pa^{-1}	$q_{B,sat}$ mol kg^{-1}	b_B Pa^{-1}
0Al = FAU	7.7	3.782E-07		
48Al	2.7	4.005E-08	6.6	7.177E-07
54Al	4	1.126E-08	7	7.382E-07
86Al	6.6	1.251E-06	6.2	8.723E-09
96Al	5.7	1.896E-08	6.2	1.529E-06

11.7 List of Figures for N2/O2 separations in Na-exchanged FAU zeolites

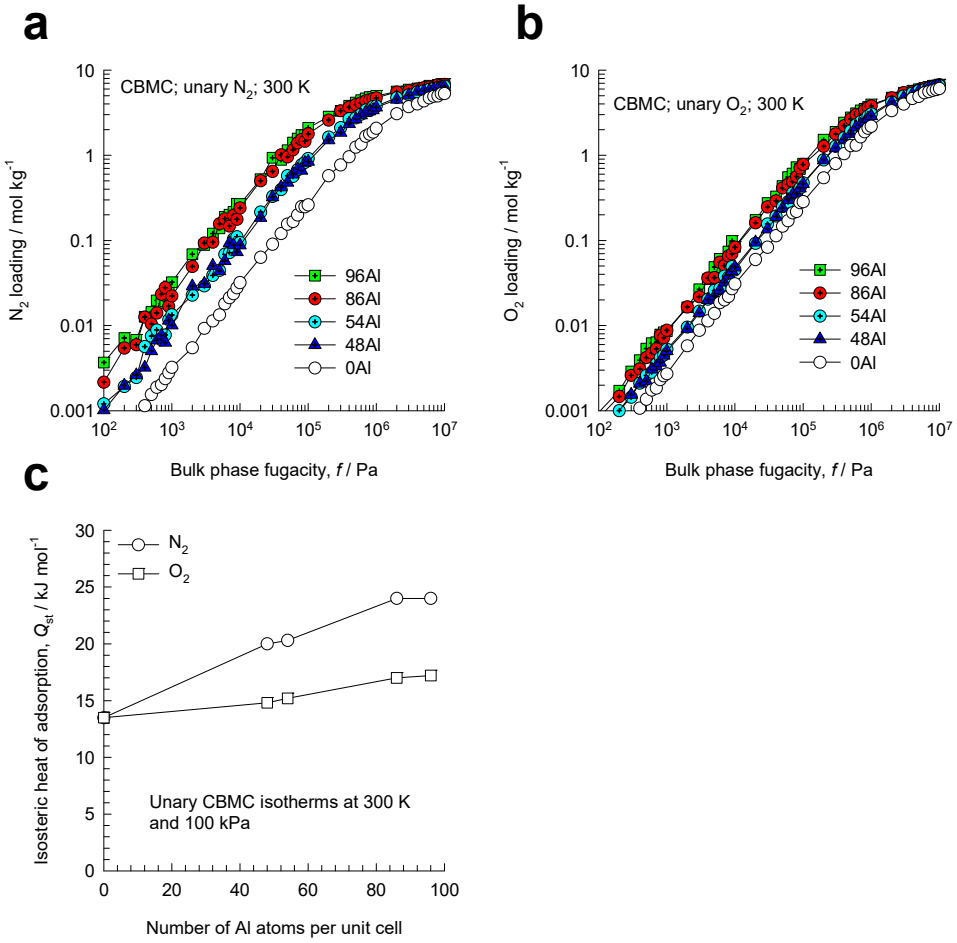

Figure S73. (a, b) CBMC simulations of the unary isotherms for N_2, and O_2 at 300 K in Na-exchanged FAU zeolites, with different Al contents per unit cell: 0, 48, 54, 86, and 96. The unary isotherm fit parameters are provided in Table S7, and Table S8. (c) CBMC simulations of the isosteric heats of adsorption, Q_{st}, for N_2, and O_2, plotted as function of the surface potential Φ.

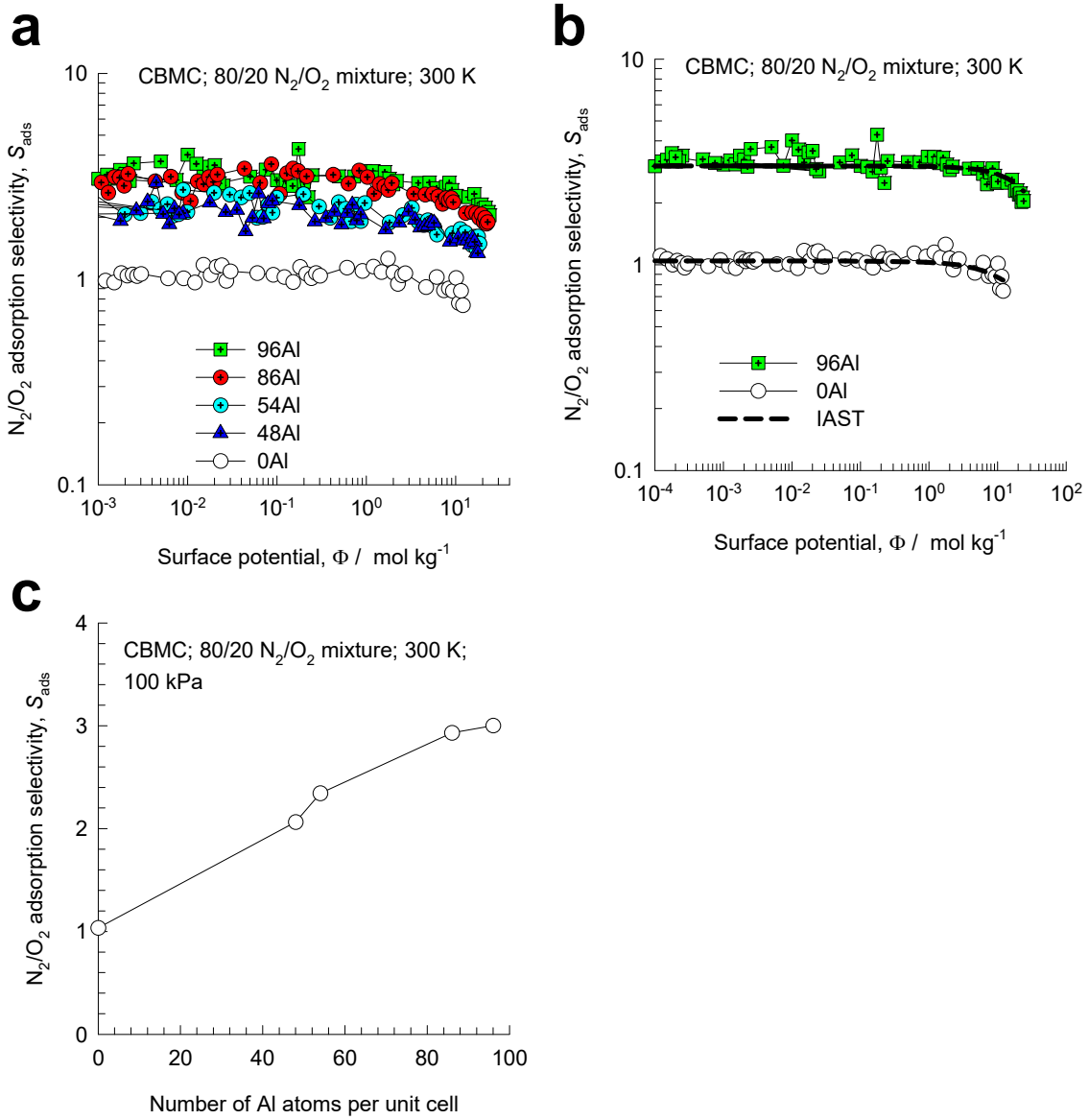

Figure S74. (a, b) CBMC simulations of the adsorption selectivity, S_{ads}, for binary 80/20 N_2/O_2 mixture adsorption in Na-exchanged FAU zeolites at 300 K. The adsorption selectivities are plotted as function of the surface potential Φ. The dashed lines in (b) are the IAST calculations; the unary isotherm fit parameters are provided in Table S7, and Table S8. (c) CBMC simulations of the adsorption selectivity, S_{ads}, for 80/20 N_2/O_2 mixture adsorption in Li-exchanged FAU zeolites at a total fugacity = 100 kPa, plotted as a function of the Al content per unit cell.

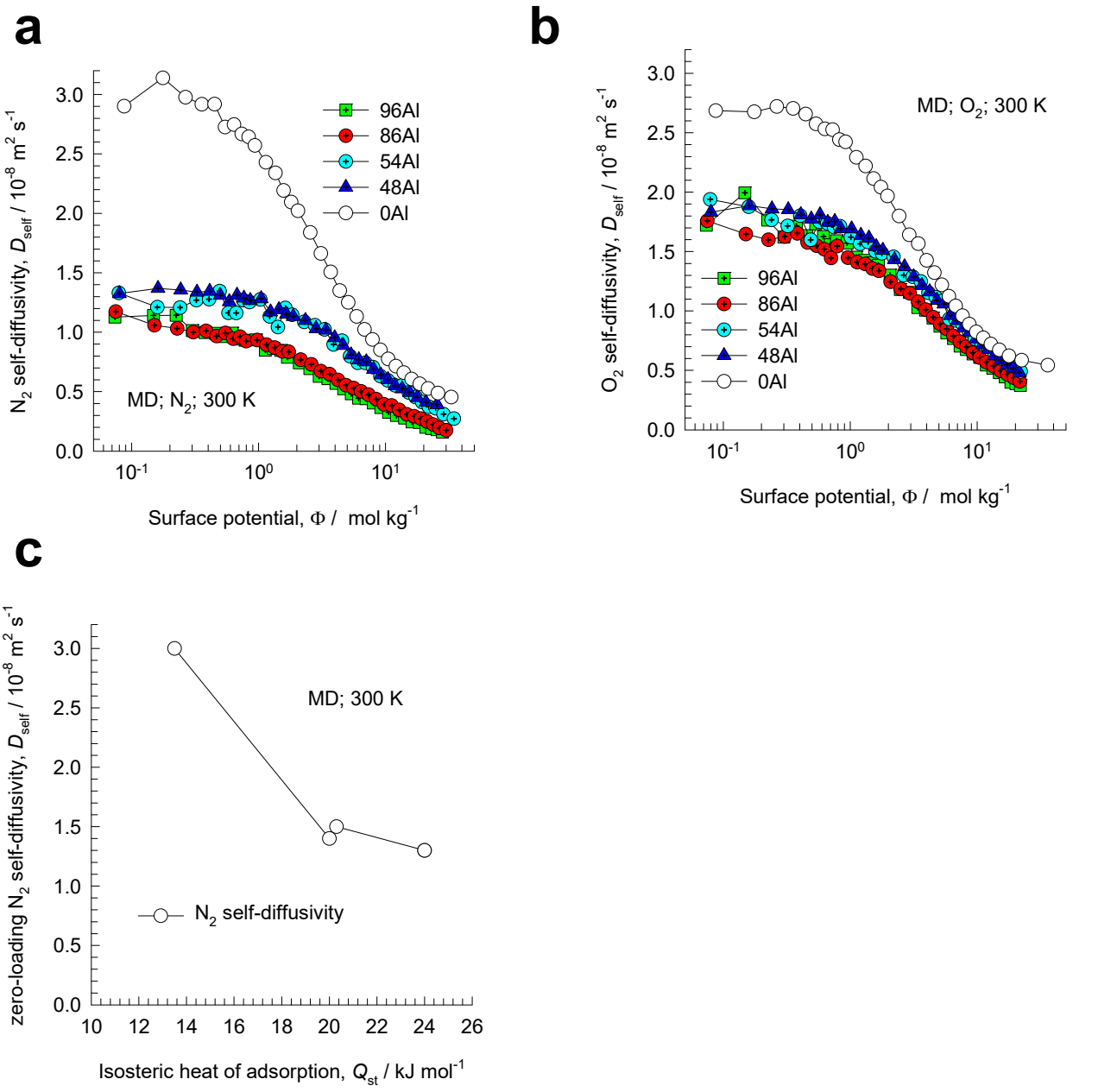

Figure S75. (a, b) MD simulations of the unary self-diffusivities for N_2, and O_2 at 300 K in Na-exchanged FAU zeolites, with different Al contents per unit cell: 0, 48, 54, 86, and 96, plotted as function of the surface potential Φ. (c) The values of the N_2 diffusivities at zero loadings, plotted as function of the isosteric heat of adsorption, Q_{st}.

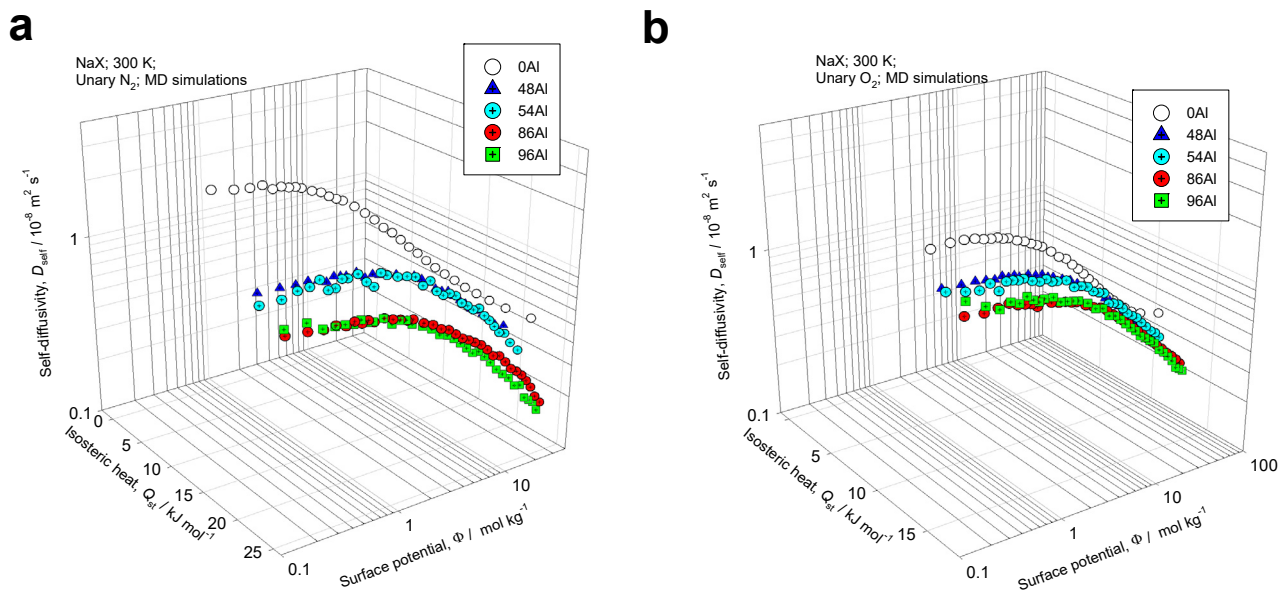

Figure S76. (a, b) MD simulations of the unary self-diffusivities for (a) N_2, and (b) O_2 at 300 K in Na-exchanged FAU zeolites, with different Al contents per unit cell: 0, 48, 54, 86, and 96, plotted as function of the surface potential Φ, and the isosteric heats of adsorption Φ.

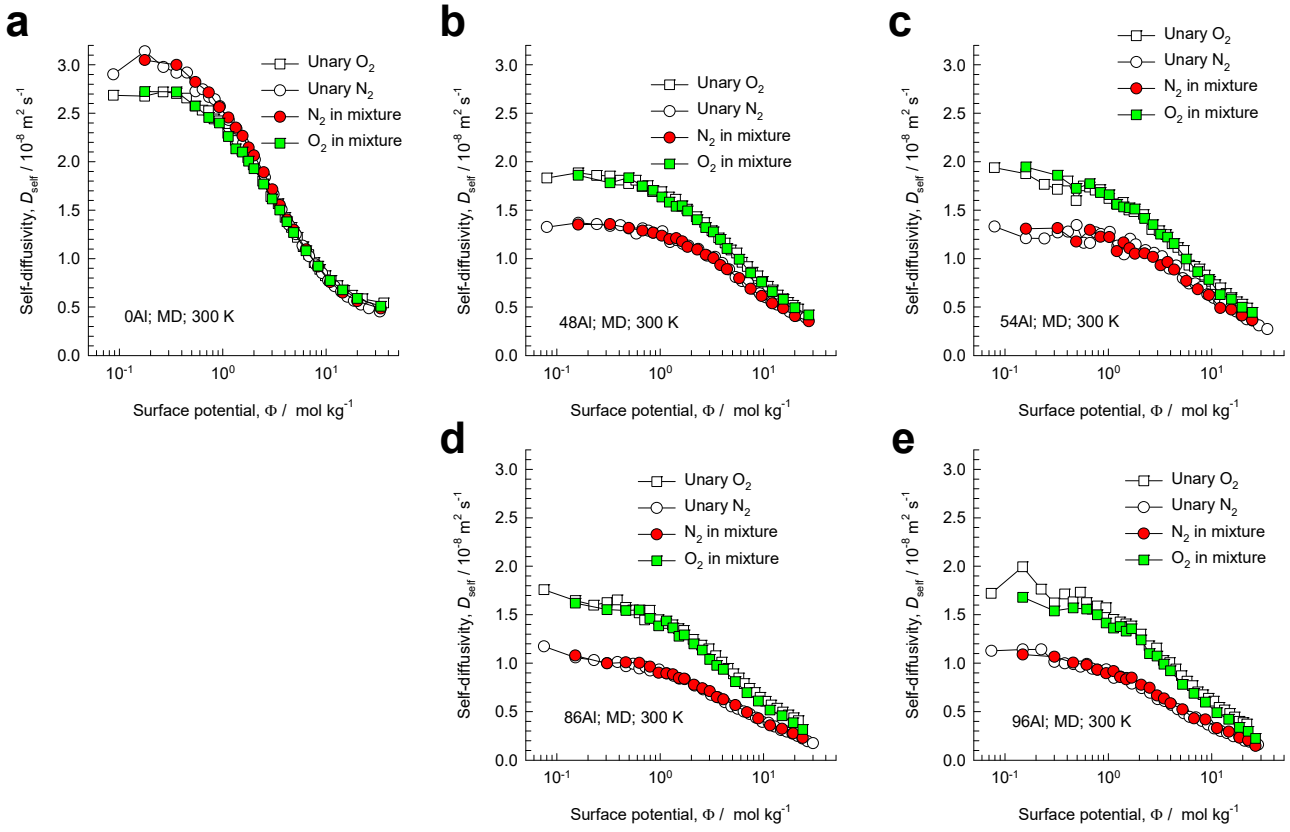

Figure S77. MD simulations of the self-diffusivities of N_2, and O_2 at 300 K in Na-exchanged FAU zeolites, with different Al contents per unit cell: (a) 0, (b) 48, (c) 54, (d) 86, and (e) 96, plotted as function of the surface potential Φ. The filled symbols represent the self-diffusivities in equimolar $\left(q_1 = q_2\right)$ N_2/O_2 mixtures. The open symbols represent the unary diffusivities.

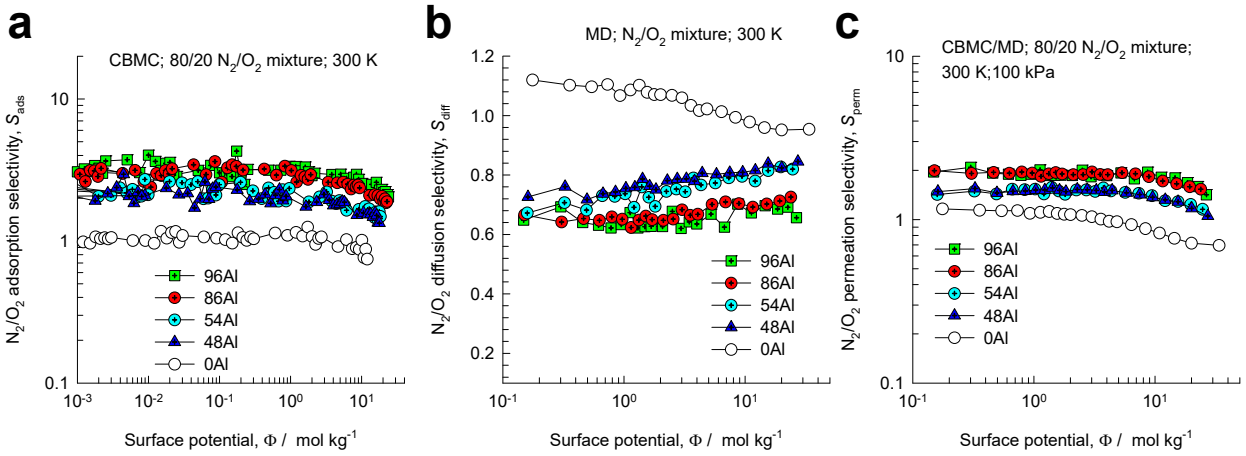

Figure S78. (a) CBMC simulations of the adsorption selectivity, S_{ads}, for binary 80/20 N_2/O_2 mixture adsorption in Na-exchanged FAU zeolites, with different Al contents per unit cell: 0, 48, 54, 86, and 96. (b) MD simulations of the N_2/O_2 diffusion selectivity, S_{diff}, at 300 K in Li-exchanged FAU zeolites. (c) CBMC/MD simulations of the N_2/O_2 permeation selectivity, S_{perm}, at 300 K in Na-exchanged FAU zeolites. In (a, b, c), the selectivities are plotted as function of the surface potential Φ.

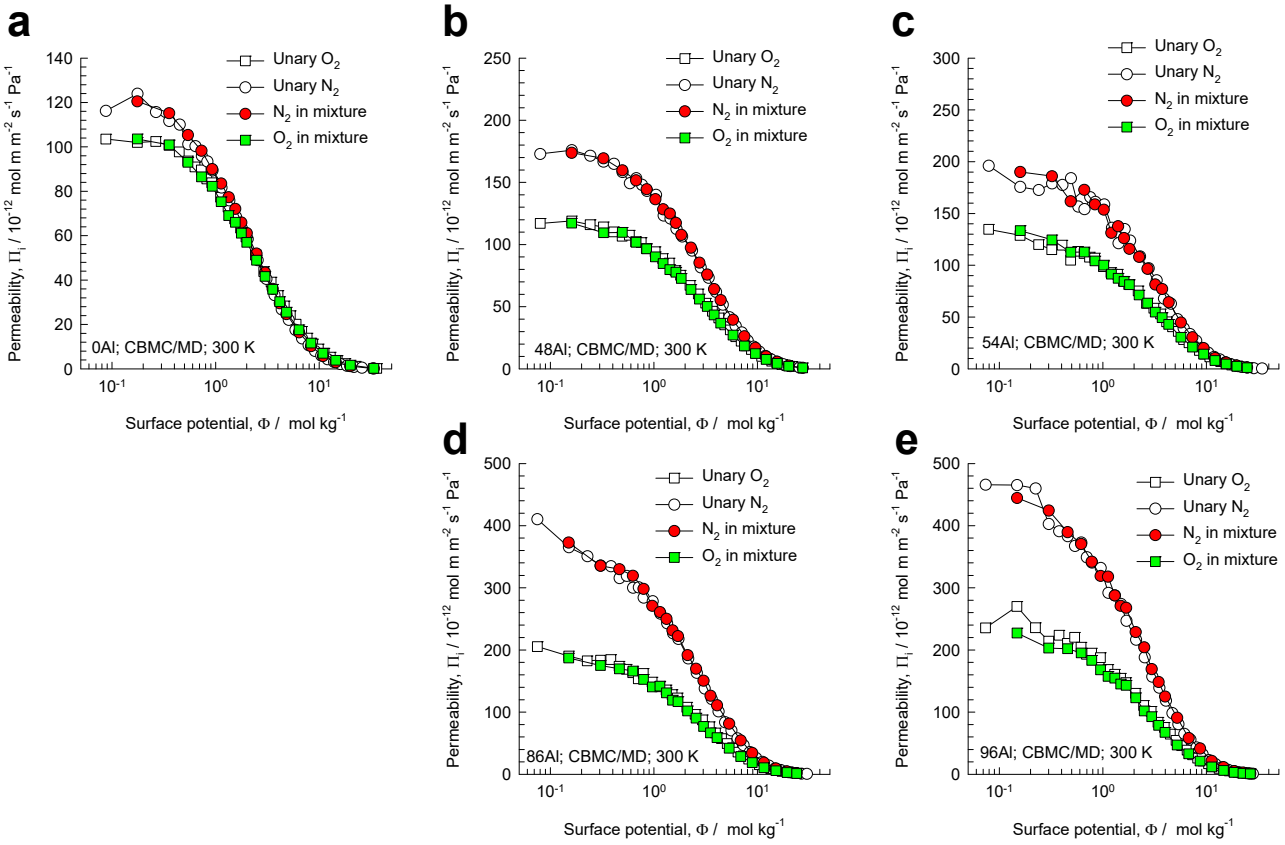

Figure S79. Component permeabilities of N_2, and O_2 at 300 K in Na-exchanged FAU zeolites, with different Al contents per unit cell: (a) 0, (b) 48, (c) 54, (d) 86, and (e) 96, plotted as function of the surface potential Φ. The filled symbols represent the permeabilities in equimolar $(q_1 = q_2)$ N_2/O_2 mixtures. The open symbols represent the unary permeabilities.

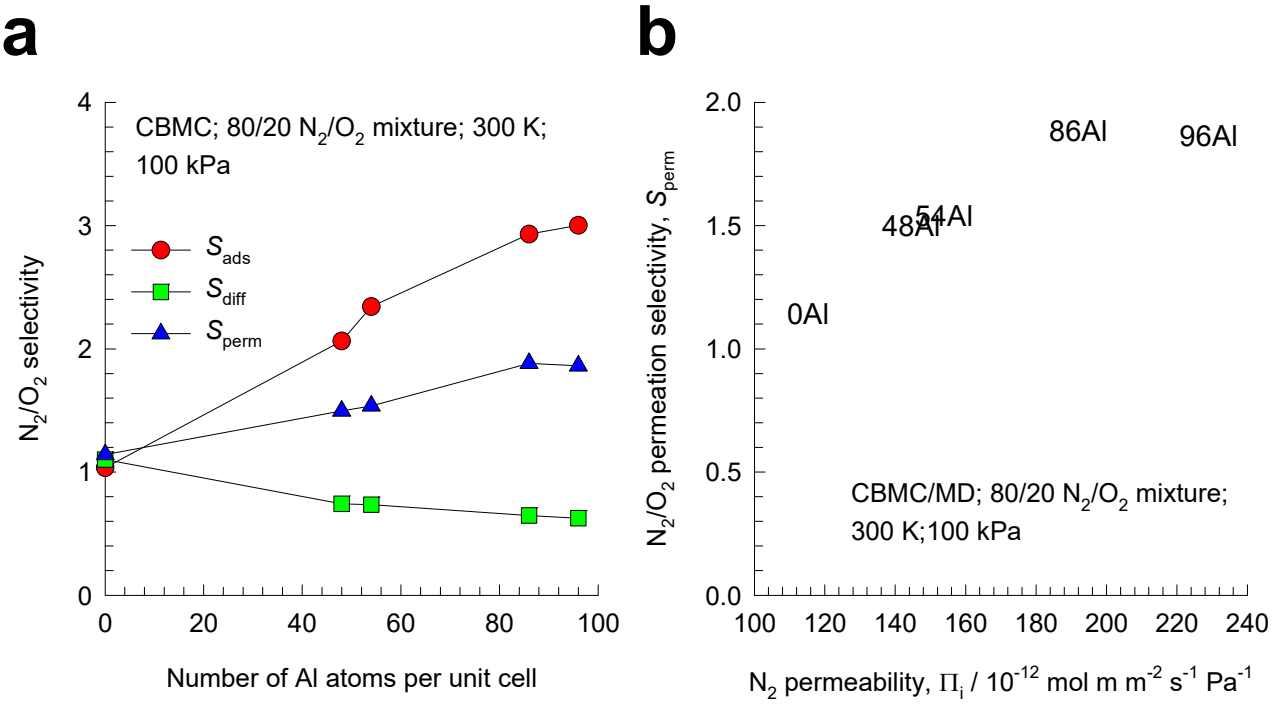

Figure S80. (a) CBMC/MD simulations of S_{ads}, S_{diff}, and S_{perm} for binary 80/20 N_2/O_2 mixture permeation across Na-exchanged FAU zeolite membrane, with different Al contents per unit cell: 0, 48, 54, 86, and 96. The upstream total pressure is 100 kPa (b) Robeson plot of S_{perm} vs component permeabilities of N_2 for binary 80/20 N_2/O_2 mixture permeation across Na-exchanged FAU zeolite membrane, with different Al contents per unit cell: 0, 48, 54, 86, and 96.

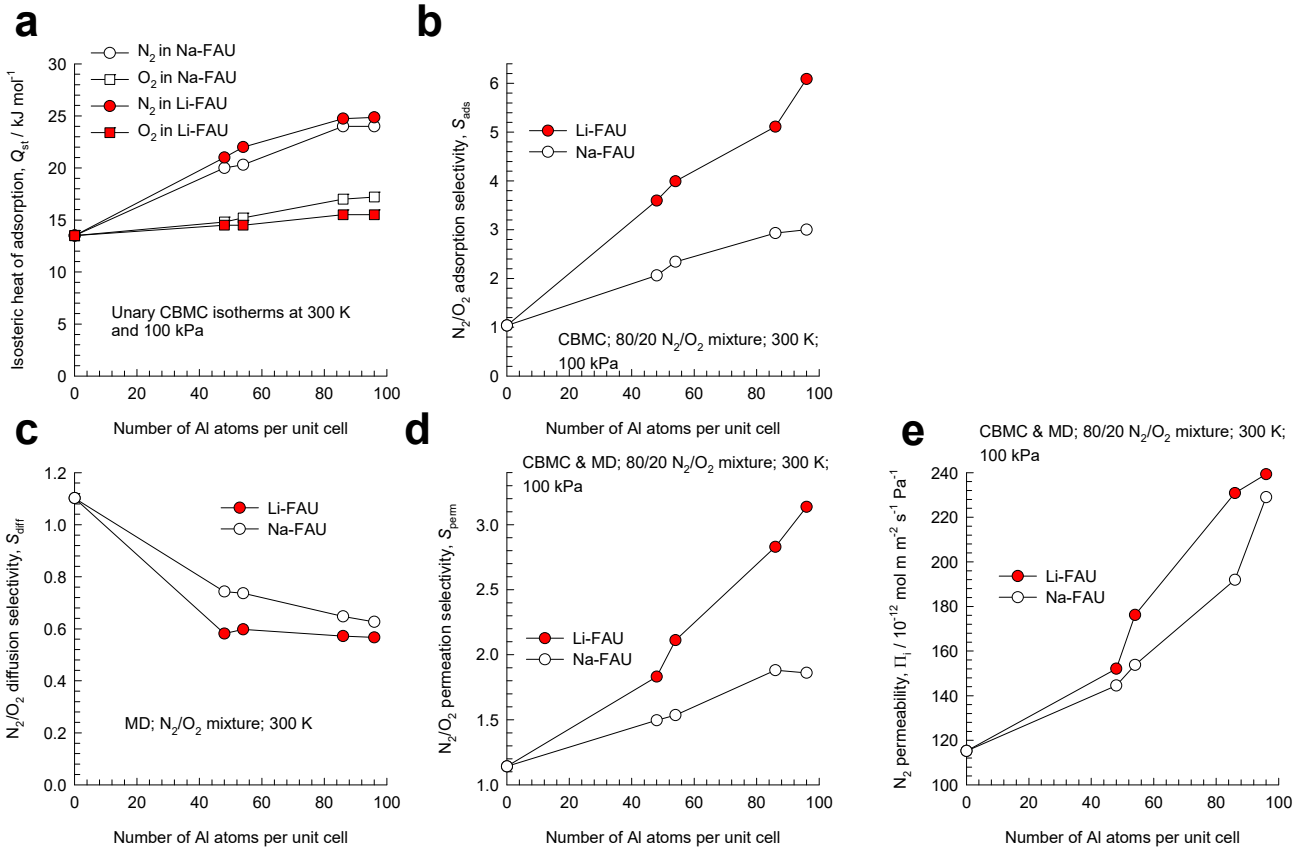

Figure S81. Comparison of the (a) isosteric heats of adsorption, (b) adsorption selectivity, (c) diffusion selectivity, (d) permeation selectivity, and (e) nitrogen permeabilities for 80/20 N_2/O_2 separations using Li-exchanged and Na-exchange FAU zeolites, with different Al contents per unit cell: 0, 48, 54, 86, and 96.

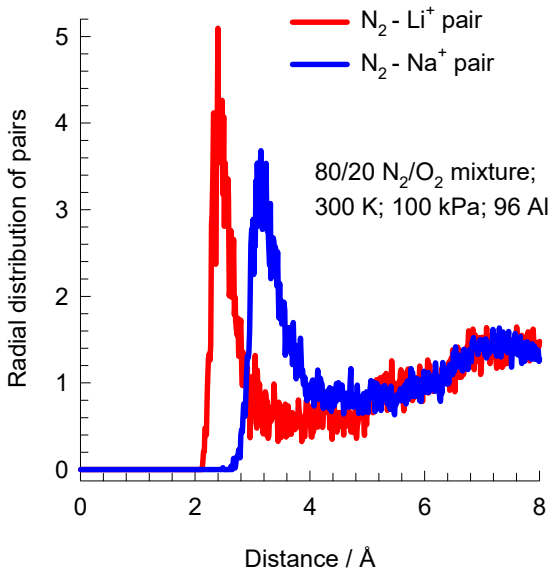

Figure S82. Radial distribution functions for N_2-Li^+ and the N_2-Na^+ pairs for 80/20 N_2/O_2 mixture adsorption in Li-FAU(96Al) and Na-FAU(96Al) at 100 kPa, and 300 K.

12 Nomenclature

Latin alphabet

A	surface area per kg of framework, $m^2\ kg^{-1}$
b_A	dual-Langmuir-Freundlich constant for species i at adsorption site A, $Pa^{-\nu A}$
b_B	dual-Langmuir-Freundlich constant for species i at adsorption site B, $Pa^{-\nu B}$
$[B]$	inverted Maxwell-Stefan diffusivity matrix, $m^{-2}\ s$
$Đ_i$	Maxwell-Stefan diffusivity for molecule-wall interaction, $m^2\ s^{-1}$
$Đ_i(0)$	Maxwell-Stefan diffusivity at zero-loading, $m^2\ s^{-1}$
$Đ_{ij}$	Maxwell-Stefan exchange coefficient, $m^2\ s^{-1}$
$D_{i,self}$	self-diffusivity of species i, $m^2\ s^{-1}$
f_i	partial fugacity of species i, Pa
f_t	total fugacity of bulk fluid mixture, Pa
$[I]$	Identity matrix with elements δ_{ij}, dimensionless
n	number of species in the mixture, dimensionless
N_i	molar flux of species i with respect to framework, $mol\ m^{-2}\ s^{-1}$
p_i	partial pressure of species i in mixture, Pa
p_t	total system pressure, Pa
P_i^0	sorption pressure, Pa
q_i	component molar loading of species i, $mol\ kg^{-1}$
$q_{i,sat}$	molar loading of species i at saturation, $mol\ kg^{-1}$
q_t	total molar loading in mixture, $mol\ kg^{-1}$
Q_{st}	isosteric heat of adsorption, $J\ mol^{-1}$
$\mathbf{r}_{l,i}(t)$	position vector for molecule l of species i at any time t, m

Nomenclature

R	gas constant, 8.314 J mol^{-1} K^{-1}
S_{ads}	adsorption selectivity, dimensionless
S_{diff}	diffusion selectivity, dimensionless
S_{perm}	permeation selectivity, dimensionless
T	absolute temperature, K
u_i	velocity of motion of adsorbate species *i* with respect to the framework material, m s^{-1}
V_p	accessible pore volume, m^3 kg^{-1}
x_i	mole fraction of species *i* in adsorbed phase, dimensionless
y_i	mole fraction of species *i* in bulk gas phase, dimensionless
z	distance coordinate, m

Greek alphabet

δ	thickness of membrane, m
δ_{ij}	Kronecker delta, dimensionless
γ_i	activity coefficient of component *i* in adsorbed phase, dimensionless
$[\Lambda]$	matrix of Maxwell-Stefan diffusivities, m^2 s^{-1}
μ_i	molar chemical potential of component *i*, J mol^{-1}
π	spreading pressure, N m^{-1}
θ	fractional occupancy, dimensionless
Θ_i	loading of species *i*, molecules per unit cell
$\Theta_{i,sat}$	saturation loading of species *i*, molecules per unit cell
Θ_t	total mixture loading, molecules per unit cell
ν	exponent in Langmuir-Freundlich isotherm, dimensionless
Π_i	membrane permeability of species *i*, mol m m^{-2} s^{-1} Pa^{-1}
ρ	framework density, kg m^{-3}

Nomenclature

Φ	surface potential, mol kg^{-1}

Subscripts

1	referring to component 1
2	referring to component 2
i	referring to component *i*
t	referring to total mixture
sat	referring to saturation conditions
δ	referring to conditions at downstream face of membrane

13 References

(1) Materials for Separation Technologies: Energy and Emission Reduction Opportunities. U.S. Department of Energy, Energy Efficiency and Renewable Energy, 2005.

(2) Yang, R. T. *Adsorbents: Fundamentals and Applications*. John Wiley & Sons, Inc.: Hoboken, New Jersey, 2003; pp 1-410.

(3) Ruthven, D. M. *Principles of Adsorption and Adsorption Processes*. John Wiley: New York, 1984; pp 1-433.

(4) Sircar, S.; Myers, A. L. *Gas Separation by Zeolites, Chapter 22*. Handbook of Zeolite Science and Technology; Edited by S.M. Auerbach, K.A. Carrado and P.K. Dutta, Marcel Dekker: New York, 2003.(

(5) Krishna, R.; van Baten, J. M. In silico screening of metal-organic frameworks in separation applications. *Phys. Chem. Chem. Phys.* **2011**, *13*, 10593-10616. https://doi.org/10.1039/C1CP20282K.

(6) Krishna, R.; van Baten, J. M. In Silico Screening of Zeolite Membranes for CO_2 Capture. *J. Membr. Sci.* **2010**, *360*, 323-333.

(7) Krishna, R.; van Baten, J. M. Describing Mixture Diffusion in Microporous Materials under Conditions of Pore Saturation. *J. Phys. Chem. C* **2010**, *114*, 11557-11563.

(8) Krishna, R.; van Baten, J. M. Diffusion of alkane mixtures in zeolites. Validating the Maxwell-Stefan formulation using MD simulations. *J. Phys. Chem. B* **2005**, *109*, 6386-6396.

(9) Krishna, R.; van Baten, J. M. Insights into diffusion of gases in zeolites gained from molecular dynamics simulations. *Microporous Mesoporous Mater.* **2008**, *109*, 91-108.

(10) Krishna, R. Describing the Diffusion of Guest Molecules inside Porous Structures. *J. Phys. Chem. C* **2009**, *113*, 19756-19781. https://doi.org/10.1021/jp906879d.

(11) Krishna, R. Diffusion in Porous Crystalline Materials. *Chem. Soc. Rev.* **2012**, *41*, 3099-3118. https://doi.org/10.1039/C2CS15284C.

(12) Ryckaert, J. P.; Bellemans, A. Molecular dynamics of liquid alkanes. *Faraday Discuss. Chem. Soc.* **1978**, *66*, 95-106.

(13) Dubbeldam, D.; Calero, S.; Vlugt, T. J. H.; Krishna, R.; Maesen, T. L. M.; Smit, B. United Atom Forcefield for Alkanes in Nanoporous Materials. *J. Phys. Chem. B* **2004**, *108*, 12301-12313.

(14) Kumar, A. V. A.; Jobic, H.; Bhatia, S. K. Quantum effects on adsorption and diffusion of hydrogen and deuterium in microporous materials *J. Phys. Chem. B* **2006**, *110*, 16666-16671.

(15) Makrodimitris, K.; Papadopoulos, G. K.; Theodorou, D. N. Prediction of permeation properties of CO_2 and N_2 through silicalite via molecular simulations. *J. Phys. Chem. B* **2001**, *105*, 777-788.

(16) García-Pérez, E.; Parra, J. B.; Ania, C. O.; García-Sánchez, A.; Van Baten, J. M.; Krishna, R.; Dubbeldam, D.; Calero, S. A computational study of CO_2, N_2 and CH_4 adsorption in zeolites. *Adsorption* **2007**, *13*, 469-476.

(17) Kiselev, A. V.; Lopatkin, A. A.; Shul'ga, A. A. Molecular statistical calculation of gas adsorption by silicalite. *Zeolites* **1985**, *5*, 261-267.

(18) Frenkel, D.; Smit, B. *Understanding Molecular Simulations: From Algorithms to Applications*. 2nd Edition, Academic Press: San Diego, 2002; pp

(19) García-Sánchez, A.; Ania, C. O.; Parra, J. B.; Dubbeldam, D.; Vlugt, T. J. H.; Krishna, R.; Calero, S. Development of a Transferable Force Field for Carbon Dioxide Adsorption in Zeolites. *J. Phys. Chem. C* **2009**, *113*, 8814-8820.

(20) Fu, Y.; Liu, Y.; Yang, X.; Li, Z.; Zhao, C.; Jiang, L.; Zhang, C.; Wang, H.; Yang, R. T. Thermodynamic analysis of molecular simulations of N_2 and O_2 adsorption on zeolites under plateau special conditions. *Appl. Surf. Sci.* **2019**, *480*, 868-875. https://doi.org/10.1016/j.apsusc.2019.03.011.

(21) Fu, Y.; Liu, Y.; Li, Z.; Zhang, Q.; Yang, X.; Zhao, C.; Zhang, C.; Wang, H.; Yang, R. T. Insights into adsorption separation of N_2/O_2 mixture on FAU zeolites under plateau special conditions: A molecular simulation study. *Sep. Purif. Technol.* **2020**, *251*, 117405. https://doi.org/10.1016/j.seppur.2020.117405.

(22) Myers, A. L.; Prausnitz, J. M. Thermodynamics of Mixed Gas Adsorption. *A.I.Ch.E.J.* **1965**, *11*, 121-130.

(23) Talu, O.; Myers, A. L. Rigorous Thermodynamic Treatment of Gas-Adsorption. *A.I.Ch.E.J.* **1988**, *34*, 1887-1893.

(24) Siperstein, F. R.; Myers, A. L. Mixed-Gas Adsorption. *A.I.Ch.E.J.* **2001**, *47*, 1141-1159.

(25) Krishna, R.; Van Baten, J. M. Elucidation of Selectivity Reversals for Binary Mixture Adsorption in Microporous Adsorbents. *ACS Omega* **2020**, *5*, 9031-9040. https://doi.org/10.1021/acsomega.0c01051.

(26) Krishna, R.; Van Baten, J. M. Using Molecular Simulations for Elucidation of Thermodynamic Non-Idealities in Adsorption of CO_2-containing Mixtures in NaX Zeolite. *ACS Omega* **2020**, *5*, 20535-20542. https://doi.org/10.1021/acsomega.0c02730.

(27) Krishna, R.; Van Baten, J. M. Water/Alcohol Mixture Adsorption in Hydrophobic Materials: Enhanced Water Ingress caused by Hydrogen Bonding. *ACS Omega* **2020**, *5*, 28393-28402. https://doi.org/10.1021/acsomega.0c04491.

(28) Krishna, R.; Van Baten, J. M. Investigating the Non-idealities in Adsorption of CO_2-bearing Mixtures in Cation-exchanged Zeolites. *Sep. Purif. Technol.* **2018**, *206*, 208-217. https://doi.org/10.1016/j.seppur.2018.06.009.

(29) Krishna, R. Occupancy Dependency of Maxwell−Stefan Diffusivities in Ordered Crystalline Microporous Materials. *ACS Omega* **2018**, *3*, 15743-15753. https://doi.org/10.1021/acsomega.8b02465.

(30) Smith, W.; Forester, T. R.; Todorov, I. T. The DL_POLY Molecular Simulation Package. http://www.cse.clrc.ac.uk/msi/software/DL_POLY/index.shtml, Warrington, England, March 2006.

(31) SARA Computing & Networking Services. https://subtrac.sara.nl/userdoc/wiki/lisa/description, Amsterdam, 16 January 2008.

(32) Skoulidas, A. I.; Sholl, D. S.; Krishna, R. Correlation effects in diffusion of CH_4/CF_4 mixtures in MFI zeolite. A study linking MD simulations with the Maxwell-Stefan formulation. *Langmuir* **2003**, *19*, 7977-7988.

(33) Chempath, S.; Krishna, R.; Snurr, R. Q. Nonequilibrium MD simulations of difusion of binary mixtures containing short n-alkanes in faujasite. *J. Phys. Chem. B* **2004**, *108*, 13481-13491.

(34) Krishna, R.; van Baten, J. M. Onsager coefficients for binary mixture diffusion in nanopores. *Chem. Eng. Sci.* **2008**, *63*, 3120-3140.

(35) Hansen, N.; Keil, F. J. Multiscale modeling of reaction and diffusion in zeolites: from the molecular level to the reactor. *Soft Mater.* **2012**, *10*, 179-201.

(36) Krishna, R.; van Baten, J. M. An Investigation of the Characteristics of Maxwell-Stefan Diffusivities of Binary Mixtures in Silica Nanopores. *Chem. Eng. Sci.* **2009**, *64*, 870-882.

(37) Krishna, R.; van Baten, J. M. Unified Maxwell-Stefan Description of Binary Mixture Diffusion in Micro- and Meso- Porous Materials. *Chem. Eng. Sci.* **2009**, *64*, 3159-3178.

(38) Krishna, R.; van Baten, J. M. Investigating the Influence of Diffusional Coupling on Mixture Permeation across Porous Membranes *J. Membr. Sci.* **2013**, *430*, 113-128.

(39) Krishna, R.; Baur, R. Modelling Issues in Zeolite Based Separation Processes. *Sep. Purif. Technol.* **2003**, *33*, 213-254.

(40) Krishna, R. Thermodynamically Consistent Methodology for Estimation of Diffusivities of Mixtures of Guest Molecules in Microporous Materials. *ACS Omega* **2019**, *4*, 13520-13529. https://doi.org/10.1021/acsomega.9b01873.

(41) van Baten, J. M.; Krishna, R. Entropy effects in adsorption and diffusion of alkane isomers in mordenite: An investigation using CBMC and MD simulations. *Microporous Mesoporous Mater.* **2005**, *84*, 179-191. https://doi.org/10.1016/j.micromeso.2005.05.025.

(42) Krishna, R.; van Baten, J. M. Describing binary mixture diffusion in carbon nanotubes with the Maxwell-Stefan equations. An investigation using molecular dynamics simulations. *Ind. Eng. Chem. Res.* **2006**, *45*, 2084-2093.

(43) Krishna, R.; van Baten, J. M. Influence of segregated adsorption on mixture diffusion in DDR zeolite. *Chem. Phys. Lett.* **2007**, *446*, 344-349.

(44) Krishna, R.; van Baten, J. M. Segregation effects in adsorption of CO_2 containing mixtures and their consequences for separation selectivities in cage-type zeolites. *Sep. Purif. Technol.* **2008**, *61*, 414-423. https://doi.org/10.1016/j.seppur.2007.12.003.

(45) Krishna, R.; van Baten, J. M. A molecular dynamics investigation of the diffusion characteristics of cavity-type zeolites with 8-ring windows. *Microporous Mesoporous Mater.* **2011**, *137*, 83-91. https://doi.org/10.1016/j.micromeso.2010.08.026.

(46) Krishna, R.; van Baten, J. M. Maxwell-Stefan modeling of slowing-down effects in mixed gas permeation across porous membranes. *J. Membr. Sci.* **2011**, *383*, 289-300. https://doi.org/10.1016/j.memsci.2011.08.067.

(47) Krishna, R.; Baur, R. Analytic solution of the Maxwell-Stefan equations for multicomponent permeation across a zeolite membrane. *Chem. Eng. J.* **2004**, *97*, 37-45.

(48) Krishna, R.; van Baten, J. M. Investigating cluster formation in adsorption of CO_2, CH_4, and Ar in zeolites and metal organic frameworks at sub-critical temperatures. *Langmuir* **2010**, *26*, 3981-3992.

(49) Krishna, R.; van Baten, J. M. Highlighting a variety of unusual characteristics of adsorption and diffusion in microporous materials induced by clustering of guest molecules. *Langmuir* **2010**, *26*, 8450-8463.

(50) Krishna, R.; Van Baten, J. M. How Reliable is the Ideal Adsorbed Solution Theory for Estimation of Mixture Separation Selectivities in Microporous Crystalline Adsorbents? *ACS Omega* **2021**, *6*, 15499–15513. https://doi.org/10.1021/acsomega.1c02136.

(51) Krishna, R.; van Baten, J. M.; Baur, R. Highlighting the Origins and Consequences of Thermodynamic Nonidealities in Mixture Separations using Zeolites and Metal-Organic Frameworks. *Microporous Mesoporous Mater.* **2018**, *267*, 274-292. http://dx.doi.org/10.1016/j.micromeso.2018.03.013.

(52) Robeson, L. M. The upper bound revisited. *J. Membr. Sci.* **2008**, *320*, 390-400.

(53) Ruthven, D. M.; Farooq, S.; Knaebel, K. S. *Pressure swing adsorption*. VCH Publishers: New York, 1994; pp 1-352.

(54) Farooq, S.; Ruthven, D. M.; Boniface, H. A. Numerical-Simulation of a Pressure Swing Adsorption Oxygen Unit. *Chem. Eng. Sci.* **1989**, *44*, 2809-2816.

(55) Rama Rao, V.; Farooq, S.; Krantz, W. B. Design of a Two-Step Pulsed Pressure-Swing Adsorption-Based Oxygen Concentrator. *A.I.Ch.E.J.* **2010**, *56*, 354-370.

(56) Rama Rao, V. *Adsorption based portable oxygen concentrator for personal medical applications*. Ph.D. Dissertation, National University of Singapore, Singapore, 2011.

(57) Ritter, J. A. Development of Pressure Swing Adsorption Technology for Spaceflight Oxygen Concentrators. http://www.dsls.usra.edu/meetings/hrp2010/pdf/Friday/Ritter.pdf, NASA Human Research Program, Houston, 2010.

(58) Arora, A.; Faruque Hasan, M. M. Flexible oxygen concentrators for medical applications. *Sci. Rep.* **2021**, *11*, 14317. https://doi.org/10.1038/s41598-021-93796-3.

(59) Vemula, R. R.; M.D., U.; Kothare, M. V. Experimental design of a “Snap-on” and standalone single-bed oxygen concentrator for medical applications. *Adsorption* **2021**, *27*, 619-628. https://doi.org/10.1007/s10450-021-00299-8.